The Accretion Process in Neutron-star Low-mass X-ray Binaries

by

Dacheng Lin

B.S., University of Science and Technology of China (2003)

Submitted to the Department of Physics
in partial fulfillment of the requirements for the degree of

Doctor of Philosophy

at the

MASSACHUSETTS INSTITUTE OF TECHNOLOGY

September 2009

Author . . . .
Department of Physics
July 27, 2009

Certified by . . . .
Ronald A. Remillard
Principal Research Scientist
Thesis Supervisor

Certified by . . . .
Deepto Chakrabarty
Professor of Physics
Thesis Co-supervisor

Accepted by . . . .
Thomas J. Greytak
Lester Wolfe Professor of Physics
Associate Department Head for Education

The Accretion Process in Neutron-star Low-mass X-ray Binaries

by

Dacheng Lin

Submitted to the Department of Physics
on July 27, 2009, in partial fulfillment of the
requirements for the degree of
Doctor of Philosophy

Abstract

There had been long-standing fundamental problems in the spectral studies of accreting neutron stars (NSs) in low-mass X-ray binaries involving the X-ray spectral decomposition, the relations between subtypes (mainly atoll and Z sources), and the origins of different X-ray states. Atoll sources are less luminous and have both hard and soft spectral states, while Z sources have three distinct branches (horizontal(HB)/normal(NB)/flaring(FB)) whose spectra are mostly soft.

I analyzed more than twelve-year *RXTE* observations ($\sim$ 2500 in total) of four atoll sources Aql X–1, 4U 1608–522, 4U 1705–44, and 4U 1636–536. I developed a hybrid spectral model for accreting NSs. In this model, atoll hard-state spectra are described by a single-temperature blackbody (BB), presumed to model emission from the boundary layer where the accreted material impacts the NS surface, and a strong Comptonized component, modeled by a cutoffpl power law (CPL). Atoll soft-state spectra are described by two thermal components, i.e., a multicolor disk (MCD) and a BB, with additional weak Comptonized component, modeled by a single power law. I found that the accretion disk in most of the soft state is truncated at a constant value, most probably at the innermost stable circular orbit (ISCO), predicted by general relativity. This allows us to derive upper limits of magnetic fields on the NS surface of the above four atoll sources. The apparent emission area of the boundary layer is small, $\sim$1/16 of the whole NS surface, but is fairly constant, spanning the hard and soft states. All this was not seen if the classical models for thermal emission plus high Comptonization were used instead. By tracking the accretion rate onto the NS surface, I inferred a strong mass jet in the hard state. My study of 4U 1705–44 using broadband spectra from *Suzaku* and *BeppoSAX* supported the above results.

From my spectral study of the above four atoll sources, I also found that in a part of the soft state with frequent occurrences of kilohertz quasi-periodic oscillations (kHz QPOs), the accretion disk appears to be truncated at larger radii than in other parts of the soft state where the disk is presumably truncated at the ISCO. Thus the production of kHz QPOs in accreting NSs should be closely related to the behavior of the accretion disk. It is well known that the kHz QPO amplitude spectrum tracks the BB, even though we see no changes in the BB spectral evolution track when kHz QPOs are present. The simplest interpretation is that accretion oscillations are imparted in the inner disk and then seen as the waves impact the NS surface in the boundary layer.

The transient XTE J1701-462 (2006-2007) is the only source known to exhibit properties of both the Z and atoll types. I carried out the state/branch classifications of all the $\sim$900 RXTE observations. The Z-source branches evolved substantially in the X-ray color-color diagram during this outburst. In the decay, the HB, NB and FB disappeared successively, with the NB/FB transition evolving to the atoll-source soft state. Spectral analyses using my new spectral model show that the inner disk radius maintains at a nearly constant value, presumably at ISCO, when the source behaves as an atoll source in the soft state, but increases with accretion rates when the source behaves as a Z source at high luminosity. We interpreted this as local Eddington limit effects and advection domination in the accretion disk. The disks in the two Z vertices probably represent two stable accretion configurations, and we speculate that the lower (NB/FB) vertex represents a standard thin disk and the upper (HB/NB) vertex a slim disk. The changes in the accretion rate are responsible for movement of Z-source branches and the evolution from one source type to another. However, the three Z-source branches are caused by three mechanisms that operate at a roughly constant accretion rate. The FB is an instability tied to the Eddington limit. It is formed as the inner disk radius temporarily decreases toward the ISCO. The NB is traced out mostly due to changes in the boundary layer emission area, as a result of the system transiting from a standard thin disk to a slim disk. The HB is formed with the increase in Comptonization, consistent with strong radio emission detected from this branch.

Thesis Supervisor: Ronald A. Remillard
Title: Principal Research Scientist

Thesis Co-supervisor: Deepto Chakrabarty
Title: Professor of Physics

Acknowledgments

It is the most worthwhile journey to have written this work, during which I harvest knowledge, love, and friendship, and eventually reach this milestone of my life. Here I would like to make the acknowledgments to my mentors, colleagues, friends, and family, without whom, this thesis would be impossible.

First, I would like to express my deepest appreciation to my advisor, Ronald A. Remillard. His help includes many aspects, and the impact on my life is invaluable. It is not often that one finds an advisor who not only always finds time to give expert guidance to research projects but also care about his common life, including learning of English and understanding of American culture, which is essential for me, an international student here in the United States. I am also indebted to other MIT RXTE group members, i.e., Hale V. Bradt, Alan M. Levine, and Edward H. Morgan, for their great help.

Second, my special thanks go to Jeroen Homan, who is my another constant collaborator at MIT. He has made his support available in a number of ways. There are also a lot of other collaborators who I would like to show my gratitude to. They include Jeffrey E. McClintock and Ramesh Narayan and other members in their group at Harvard CFA, Diego Altamirano, Tomaso M. Belloni, Rudy Wijnands, etc. I would also like to thank my thesis committee members Deepto Chakrabarty, Saul A. Rappaport, and Joshua N. Winn for their instructions during my preparation for this thesis.

Also, I would like to thank all astrograds, both former and current, for the help and happiness they brought to me in the past six years. They include Lindy Blackburn, Jeff Blackburne, Ben Cain, Josh Carter, Aidan Crook, Tamer Elkholy, Will Farr, Joel Fridriksson, Jake Hartman, Miriam Krauss, Ryan Lang, Adrian Liu, Ying Liu, Jinrong Lin, Jared Markowitz, Michael Matejek, Madhusudhan Nikku, En-Hsin Peng, Leslie Rogers, Robyn Sanderson, Leo Stein, Michael Stevens, Pranesh Adhyan Sundararajan, Molly Swanson, Sarah Vigeland, Chris Williams, and Philip Zukin. Several current and past post-doctors, such as Li Ji and Yangsen Yao, also help me a lot. Thank you.

In addition, I thank a lot of friends, from those who share their happiness in common life with me to those in the Ashdown House Executive Committee and the MIT Graduate Student Council in the same year as me. I learned a lot from them.

Last, but not the least, I have many thanks to my family. In particular, I thank my wife, Yaning Li, for her incredible support and love. I also thank my mother, brothers, sister and sisters-in-law for their long-term understanding, support and love.

Contents

List of Figures

List of Tables

Chapter 1

Introduction

This thesis is dedicated to the study of accretion physics in low-mass X-ray binaries (LMXBs), in which a neutron star (NS) or a stellar-mass black hole (BH) accretes matter from a low-mass companion star through an accretion disk. Intense X-ray emission is released from the inner accretion disk and/or the boundary layer produced by impact of the accretion flow on the NS surface. LMXBs are important cosmic laboratories for studying the properties of strong gravitational fields and dense matter. X-ray spectral studies of the BHs are in an advanced stage, e.g., spin parameters have been derived from relativistic accretion disk models for several BHs [e.g., Shafee et al., 2006]. NS binaries show many spectral differences from the BHs, and their spectral studies can provide additional valuable information on accretion processes and the nature of the NSs. However, progress had been impeded by the long-standing ambiguity about the spectral decomposition for the NSs. The work of this thesis devises a new way to model the spectra of weakly magnetized bright NS LMXBs, and offers new physical interpretations of spectral evolution of different subclasses.

In this introduction, I will first describe the general properties of X-ray binaries in §1.1. I then describe different classes of LMXBs.

1.1 X-ray binary systems

A normal star is supported against its strong gravity by pressure of interior hot gas heated by nuclear burning. As all the nuclear energy is exhausted, it has to collapse to a much denser state. The end product is a compact object, which can be a white dwarf (WD), a NS or a BH, depending on the mass (M). A WD is supported by electron degeneracy pressure, and has mass believed to be below the Chandrasekhar limit, about 1.4 $M_\odot$ ($M_\odot$ is the mass of the sun hereafter), and radius about a few thousand kilometer. A NS is supported by neutron degeneracy pressure, and has mass believed to be between 1.4 and 3 $M_\odot$ and radius 10 to 20 km. If the compact object has mass above 3 $M_\odot$, there is no known force to support it, and it might be a singularity, or a quantum element of unknown size. Such a compact object is called a BH. In practical terms, the size of a BH is characterized by its event horizon, which is $2GM/c^2 \approx 3M/M_\odot$ km, where M is the BH gravitational mass, G is the gravitation constant, and c is the light speed in vacuum.

After formation, compact objects will simply cool off and lose energy, and they will become almost invisible relics if left isolated. They can become spectacular objects, i.e., strong emitters, again if there is mass accretion onto them. X-ray binaries are the class bright X-ray sources associated with accreting NSs or BHs. In an X-ray binary, high rates

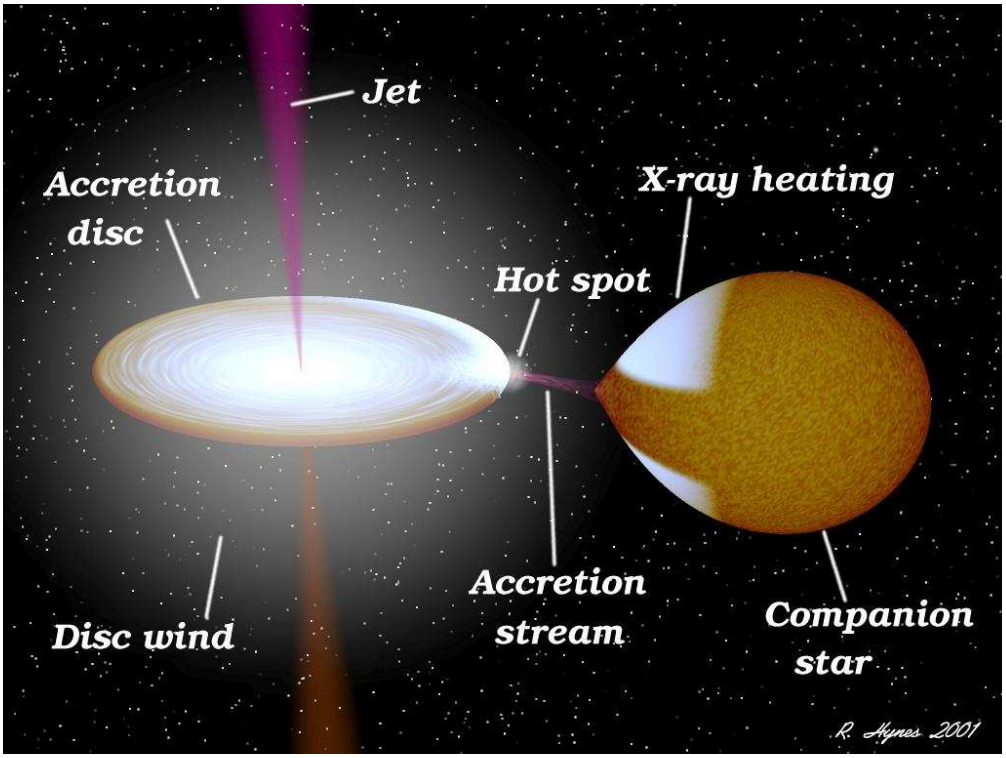

Figure 1-1: Artist's impression of a low-mass X-ray binary [Rob Hynes 2001].

of mass accretion ($\dot{M}$) from the companion to the compact object can be transient or persistent. A significant amount of gravitational energy is transformed into thermal energy as the mass from the companion spirals through the accretion disk toward the compact object. Observations show that the inner disk reached temperatures $\gtrsim 1$ keV, and most of the photons are released in X-rays. A more quantitative description of this scenario is given in Chapter 3. X-ray astronomy started with the discovery of the X-ray binary Sco X–1 in 1960s [Giacconi et al., 1962]. Since then, more than 200 X-ray binaries have been discovered [Guseĭnov et al., 2000]. Our understanding of these sources have been significantly improved in the past decade by the launch of X-ray telescopes with unprecedented capabilities, such as the *Rossi X-ray Timing Explorer* (*RXTE*), *BeppoSAX*, the *Chandra* X-ray observatory, XMM-Newton, and *Suzaku*. I refer to Shapiro and Teukolsky [1983], Lewin et al. [1997], Frank et al. [2002], Lewin and van der Klis [2006] for basic concepts and reviews of X-ray binaries. Figure 1-2 shows some sample X-ray long-term light curves from ASM onboard *RXTE* . They are from seven NS X-ray binaries, which will be studied in detail in this thesis.

Optical studies of X-ray binaries can reveal the physical properties of the companion [Charles and Coe, 2006]. The mass of the companion is one of the most important factors determining the properties of X-ray binaries. If the mass of the companion is massive ($\gtrsim 10M_\odot$), the X-ray binaries are called high-mass X-ray binaries (HMXBs). Otherwise, if the mass of the companion is $\lesssim 2M_\odot$, they are called low-mass X-ray binaries (LMXBs). Because the companion is small, the two stars in LMXBs must be close to each other in order to transfer substantial mass from the NS or BH to the companion. The mass

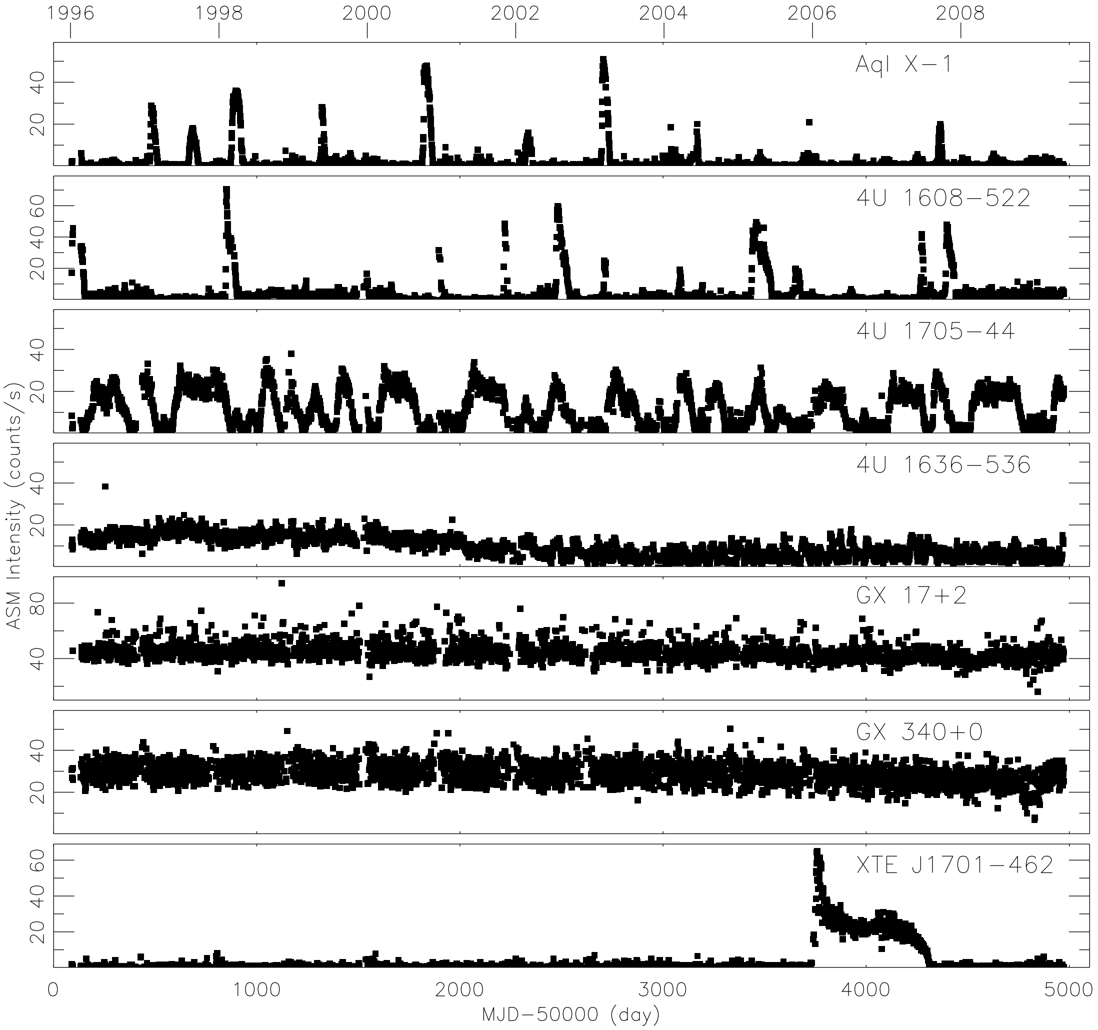

Figure 1-2: The X-ray long-term light curves of seven NS X-ray binaries observed by *RXTE*/ASM. These sources will be studied in detail in this thesis.

transfer in LMXBs is normally through the inner Lagrangian point as the companion fills its Roche lobe (Figure 1-1). HMXBs, which mostly have giant or supergiant O and B stars as the companions, can also transfer mass via filling their Roche lobes. However, most HMXBs transfer mass via a vigorous stellar wind, in which case the separation between the companion and the compact object can be large.

The lifetimes of HMXBs are short, $\sim 10^5 - 10^7$ yr, as they are determined by the evolution timescales of the high-mass companions. On the other hand, the lifetimes of LMXBs are longer, $\sim 10^7 - 10^9$ yr, and they are determined by the mass-transfer process governed by binary evolution [Tauris and van den Heuvel, 2006]. Thus, HMXBs are found mostly near the Galactic plane, where young massive stars lie, while LMXBs are found mostly towards the Galactic center and in globular clusters. It is believed that a HMXB is formed as the massive companion survived the supernova explosion of its primary, while a LMXB is probably formed via gravitational capture of a NS or BH in the places with high number density of stars, such as the Galactic center and globular clusters. The NS in LMXBs can also be formed by the accretion-induced collapse of a WD. The NS in HMXBs mostly appears as an accretion-powered pulsar, while most NS LMXBs show weak or absence of periodic pulsations.

1.2 Physics in X-ray binaries: why we study them

X-ray binaries provide important cosmic settings for us to study accretion physics. The characteristics of emission from X-ray binaries, from radio to X-ray, or even gamma ray photon energies, vary with the mass accretion rate ($\dot{M}$), and depend on many physical parameters, especially the nature of the compact object (NS or BH), its mass, the magnetic fields, and the spin of the compact object. We are still developing our understanding of accretion physics, and there are a wide variety of interesting accretion phenomena, such as jets and quasi-periodic X-ray oscillations with limited understanding as to how they depend on the physical parameters.

X-ray binaries also provide unique opportunities to probe the effects of general relativity and the properties of dense matter. The general relativistic effects around the NS and BH are many orders of magnitude stronger than those probed by other tests of general relativity [Psaltis, 2004]. The interior of the NS is denser than atomic nuclei and occupies an environment distinct from both the early Universe and current terrestrial experiments [Hands, 2001].

Here, I briefly introduce one area at the cutting edge of studies of X-ray binaries, i.e., the measurement of BH spin parameters a_* [Remillard and McClintock, 2006], in order to show the progress that we have made thus far in study of X-ray binaries. There are several ways that have been used to measure the BH spin parameters, especially the continuum spectral fitting and Fe K line profile. The main idea for the method of continuum spectral fitting is that the spectral fitting can give the information of the radius R_{in} of the inner edge of the accretion disk, which can be assumed to be the innermost stable orbit R_{ISCO} predicted by general relativity. R_{ISCO} depends only on the BH mass and spin a_* [Zhang et al., 1997, Gierliński et al., 2001]. Therefore, the estimated size of the inner accretion disk can constrain the BH spin if the mass is known from binary dynamics. The spectra used in such studies are normally taken from the thermal state, where the disk emission in the form of radiated heat dominates the spectra. The assumption of R_{in} to be R_{ISCO} is based on the phenomenon that the inferred R_{in} from the spectral fitting is roughly constant over

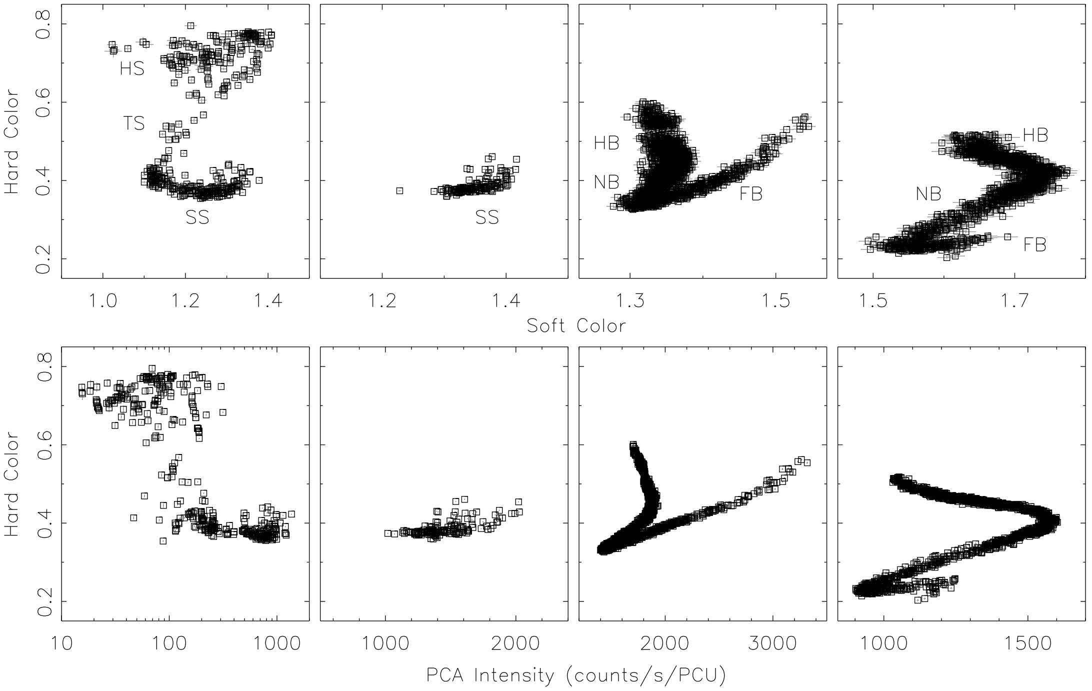

Figure 1-3: The sample CDs (upper panels) and HIDs (lower panels) of NS X-ray binaries. The panels for the columns from the left to the right correspond to the atoll source 4U 1705–44, the "GX" atoll source GX 9+1, the Sco-like Z source GX 17+2, and the Cyg-like Z source GX 340+0, respectively. The data are all from *RXTE*/PCA. The data of atoll sources span more than ten years, and exposure for each data point is up to 4 ks. Data of GX 17+2 are from 1999 October 3–12, and those of GX 340+0 are from 2001 January 11–15, with exposure for each data point 128 s. The annotations HS, TS, and SS refer to the hard, transitional, and soft states of atoll sources, respectively, while the annotations HB, NB, and FB refer to the horizontal, normal, and flaring branches of Z sources respectively. See §1.5 for more information.

some range of luminosity, which is believed to be the signature of $R_{\rm ISCO}$. Such a technique requires many system parameters such as the orbital inclination, distance and BH mass to be well known and involved considerations of many effects such as general relativity and spectral hardening. The Galactic LMXB GRS 1915+105 is measured to have spin parameter $a_* > 0.98$ [McClintock et al., 2006].

The BH spin measurement based on Fe K line profile comes from the consideration that the relativistic beaming and gravitational redshift can serve to distort the emission line profile [Miller, 2007]. The extent of this distortion depends on the inner disk radius $R_{\rm in}$, and the fitting of Fe K line can constrain the value of $R_{\rm in}$. By assuming $R_{\rm in}$ to be $R_{\rm ISCO}$, a_* can be obtained if the BH mass is known, as above. The Fe line emission is believed to be the response of an accretion disk to irradiation by an external source of hard X-rays, which is sometimes seen in the spectra of X-ray binaries. The spin of XTE J1650-500 is suggested to be nearly the maximum using this technique [Miller et al., 2002, Miniutti et al., 2004].

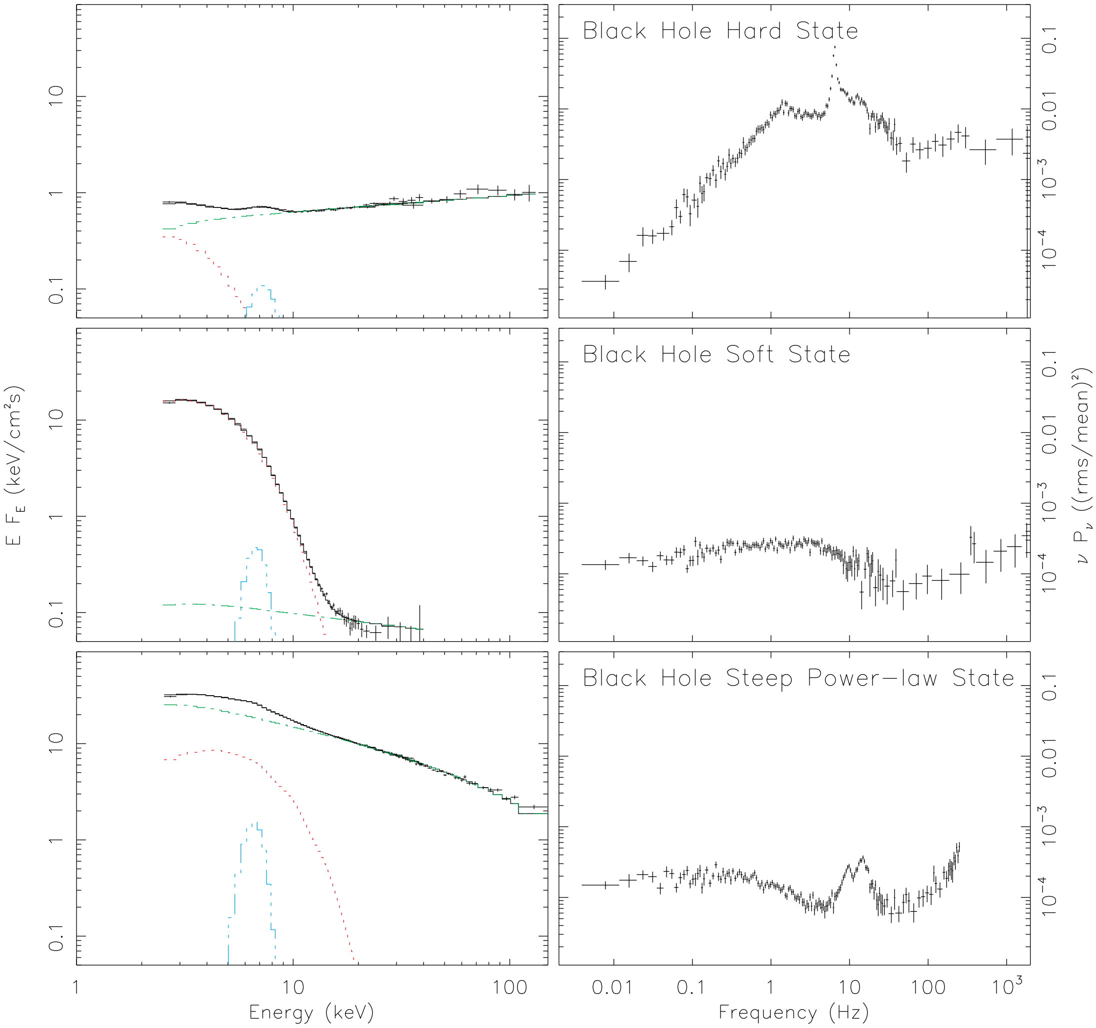

Figure 1-4: The sample unfolded energy spectra (left panels) and power density spectra (right panels) of the BH X-ray binary GRO J1655–40 in different X-ray spectral states. The energy spectra are fit with a multi-color disk (red dotted line), a simple power-law or a cutoff power-law (green dot-dashed line), and a Gaussian Fe line (cyan double-dot-dashed line). The total model fit is shown as a black solid line. Both the energy and power density spectra have been rebinned to improve the signal to noise ratio. The data for top to bottom panels are from observations of *RXTE* on 1997 August 14, 1997 March 24, 1996 August 29, respectively.

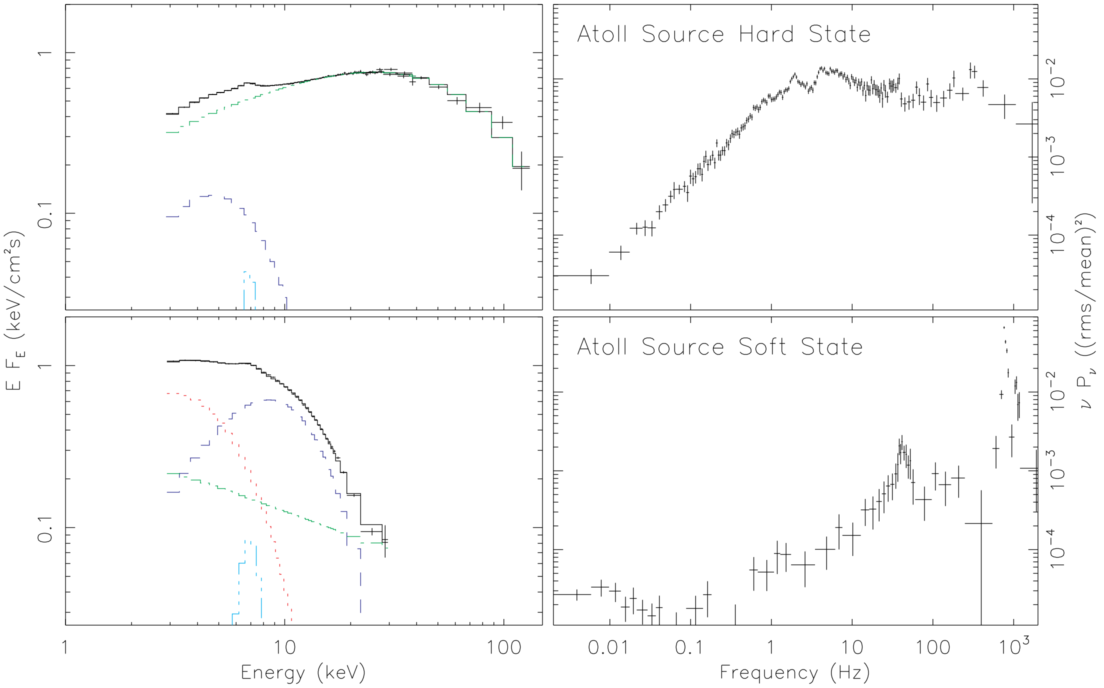

Figure 1-5: The same as Figure 1-4, but for the atoll source 4U 1636–536. Compared with the BH cases, the energy spectral models also include a single-temperature blackbody (blue dashed line). The data for upper and lower panels are from observations of *RXTE* on 2006 March 22 and 2001 April 30, respectively.

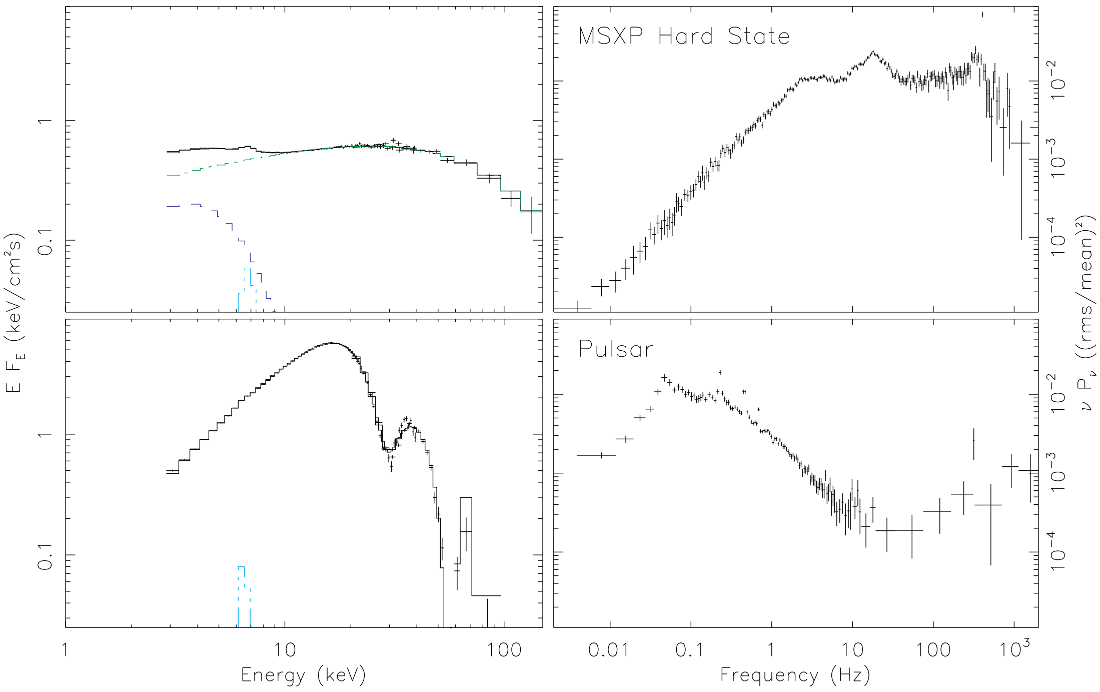

Figure 1-6: The same as Figure 1-5, but for the millisecond and slow accretion-powered X-ray pulsars SAX J1808.4–3658 (upper panels; 2002 October 18) and V 0332+53 (low panels; 2005 February 13). The energy spectrum from V 0332+53 is fitted with a cutoff power-law with the cyclotron resonant lines modeled by three Gaussian absorption lines. Only the total model plus the Gaussian Fe line is shown for this source.

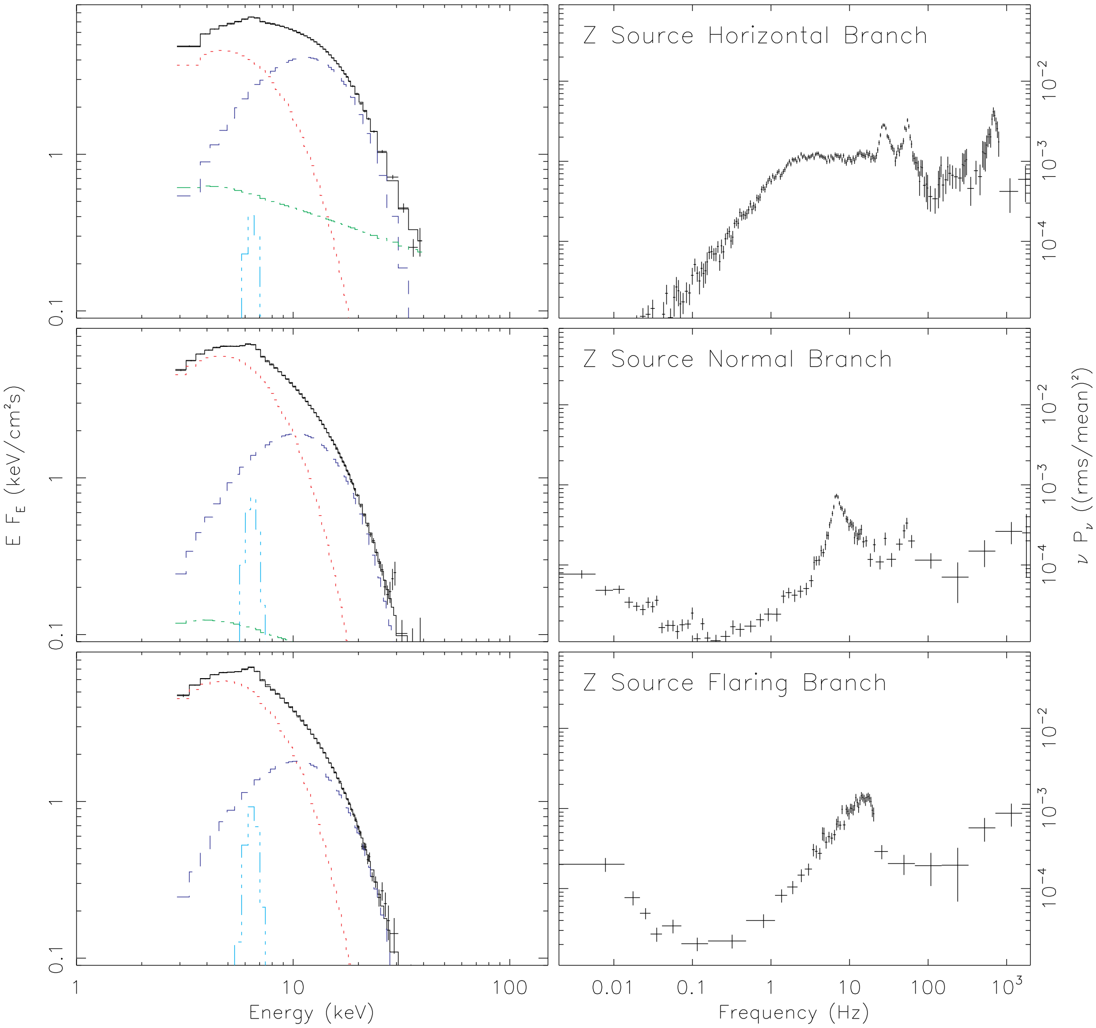

Figure 1-7: The same as Figure 1-5, but for the Z source GX 17+2. The data for top to bottom panels are from observations of *RXTE* on 1999 October 5, 1998 August 7, 1999 October 11, respectively.

1.3 Techniques used to study X-ray binaries

The information of X-ray binaries is gained from studies of the photons that they emit. The wavelength coverage extends both from radio to X-rays, and to gamma rays. The spectral and timing properties are utilized to understand the source spectral evolution and to reveal the physical parameters. I describe below the techniques that are normally used in the X-ray band. Currently we cannot resolve the LMXBs using direct imaging techniques in X-rays. Thus the techniques used to study them naturally fall into two categories, spectral and timing studies.

The spectral studies include both photometric analyses and spectral fitting methods. In the photometric analyses, X-ray colors are used. An X-ray color is a hardness ratio between the photon counts in two different energy bands and is a rough measure for spectral slope. Two X-ray colors are normally used, i.e., soft and hard colors. They correspond to lower and higher ranges, respectively, where the energy bands are defined. For example, in this thesis, the soft color is defined as the ratio of the counts in the (3.6–5.0)/(2.2–3.6) keV bands, and the hard color is the ratio in the (8.6–18.0)/(5.0–8.6) keV bands. By defining these two colors over appropriate timescales, we can track X-ray spectral variations. The conventional practice is to show a color-color diagram (CD), with the hard color vs. the soft color, and a hardness-intensity diagram (HID), with one color vs. the intensity, i.e., the sum of the count rates in the four bands. Different source types normally display different patterns in the CD or HID. Their patterns normally correspond to several source states or branches. Some examples of CD/HIDs for different types of sources are presented shown in Figure 1-3, using the above definition of colors. I note that the CD/HID is typically combined with timing properties (e.g., power density spectra; see below) so that the source states/branches can be distinguished more effectively.

The spectral fitting method is used in order to obtain more physically meaningful interpretations of the X-ray spectra and evolution. Spectra can be accumulated based on time bins (time-resolved spectra) or their positions in the CD/HID (color-resolved spectra). In either way, a single spectrum is intended to characterize a particular condition. Then the spectra are fit against physical models to obtain the physical parameters. This is often carried out using the X-ray spectral fitting package XSPEC, which is distributed by NASA and includes many theoretical models [Arnaud, 1996]. Compared with the photometric method, the spectral fitting method heavily depends on the models used, and in some cases, different models lead to very different results, which is called model degeneracy (see, e.g., Chapter 4).

The left panels of Figures 1-4–1-7 show the sample spectral fit of the energy spectra from different classes of X-ray binaries in different spectral states/branches. It can be seen that X-ray binaries typically show a composite spectrum, i.e., several spectral components needed to explain the whole spectrum. The continuum spectral components for X-ray binaries can be broadly grouped into two classes, i.e., thermal and non-thermal. In this thesis, the thermal components specifically refer to a single temperature blackbody (BB), or a composite of multicolor blackbody such as a multicolor disk (MCD). Non-thermal components typically have a wide energy range, extending into hard X-rays and have a flatter spectral energy distribution than thermal components. The most common non-thermal component seen in X-ray binaries is Comptonization emission. In this thesis, Comptonization refers to the inverse Compton scattering, i.e., photon energies are boosted due to interaction of photons with energetic electrons. More detailed description of X-ray emission mechanisms is presented in Chapter 3.

Timing studies provide information on the properties of rapid variabilities. X-ray emission from X-ray binaries is stochastic process, and the mathematical tool used mostly is Fourier analysis. The Fourier power spectrum of the X-ray count time series measures that variance as a function of Fourier frequency ν in terms of the power density $P_\nu(\nu)$. Several broad features are normally seen in a typical power density spectrum, and they are believed to correspond to different types of noises. There are sometimes components in the power density spectrum which show discrete peaks. When such features are resolved and thought to arise from non-coherent processes, they are called quasi-periodic oscillations (QPOs). For X-ray pulsars (coherent modulations with some smearing in frequency due to the binary motion or spin changes), the peak at their spin frequency can be extremely sharp, sometimes with width $\ll$1 Hz. The right panels of Figures 1-4–1-7 show the sample power density spectra from different classes of X-ray binaries in different spectral states/branches. The timing study involves investigation of how different power density spectral components vary as source spectra evolve, with the goal to understand their origins.

1.4 BH and NS X-ray binaries

Based on the nature of the compact object, X-ray binaries are classified into NS and BH types. So far, we cannot obtain direct evidence of the event horizon to prove the existence of BHs. Thus, the classifications of NS and BH X-ray binaries are mostly based on empirical methods attached to theoretical arguments. The strongest evidence for BHs is currently considered to be the measurement of a gravitational mass for a compact object larger than the upper limit in mass for a NS. The upper bound of the NS mass is $\sim 3\ M_\odot$ [Rhoades and Ruffini, 1974]. This approach is carried out by measuring the binary mass function, $f \equiv P_{\rm orb} K_2^3/2\pi G = M \sin^3 i/(1+q)^2$, where $P_{\rm orb}$ is the orbital period, K_2 is the half-amplitude of the velocity curve of the companion, M is the mass of the compact object, i is the orbital inclination angle, and q is the ratio of the masses of the companion to the compact object. The mass function gives the lower limit of the mass of the compact object, through optical observations of velocity curves of the companions.

The classification of a compact object in the X-ray binary into a NS is warranted if coherent pulsations or type I X-ray bursts are detected. The coherent pulsations, which are at the spin frequency of the NS, is believed to be due to the channeling of accreting material along magnetic field line onto the magnetic poles that are misaligned with the NS rotation axis. The focusing of accretion at the magnetic poles produces hot spots, which rotate in and out of view and cause pulsations. BHs cannot produce a magnetic field to channel the accreting material. There are also no hot spots because a solid surface is required to make them. Type I X-ray bursts (or superbursts) are another signature of a NS, because they are believed represent violent nuclear burning as the accreting material is compressed and heated. Again this requires a solid surface to store the accreted H and He until detonation occurs. The differences in spectral/timing properties are also invoked to distinguish NS and BH X-ray binaries [e.g., Done and Gierliński, 2003, Sunyaev and Revnivtsev, 2000]. However, on the whole remarkable spectral and timing similarities exist between NSs and BHs, especially in low luminosity states (see Figures 1-4–1-5).

The BH X-ray binaries are mostly LMXBs, but several of them are known to be HMXBs [McClintock and Remillard, 2006]. Their continuum energy spectra mostly exhibit a composite shape consisting of a thermal and a nonthermal component. The thermal component is well modeled by a multi-color disk, while the nonthermal component is usually modeled by a power-law model (Figure 1-4). There are three dominant active emission states for BH X-ray binaries: thermal, hard, and steep power-law [Remillard and McClintock, 2006]. Roughly speaking, the hard state is dominated by the power-law component with initial photon index around 1.7, while the thermal state is dominated by the thermal disk emission. The important characteristics of the steep power-law state are that the initial photon index of the power-law component is around 2.5 (much higher than that in the hard state), and that there are often strong QPOs (Figure 1-4).

The NS X-ray binaries can be classified based on whether they pulse or show type I X-ray bursts. Coherent pulsations are observational manifestation of strong magnetic field in the compact object. The classical accretion-powered pulsars are those with spin periods of the order of one second or more, and they are called slow accretion-powered pulsars (compared with millisecond pulsars). They are commonly seen in HMXBs, and this is because HMXBs are young systems and their magnetic fields are not expected to evolve away from its high birth value due to accretion. LMXBs mostly are old systems, and their prolonged phase of accretion is thought to have suppressed the magnetic fields of the NS [Psaltis, 2004]. One sample of energy and power density spectra of the slow accretion-powered X-ray pulsar V 0332+53 (with spin period 4.375 s) is shown in the lower panels in Figure 1-6. Clear cyclotron absorption lines are seen. The millisecond accretion-powered X-ray pulsars are one special class of LMXBs that have magnetic field strong enough to produce coherent pulsations at their fast spin frequencies ($v > 100$ Hz). It should be noted that whether the magnetic field is strong enough to produce coherent pulsations depends the accretion rate too. In the millisecond accretion-powered pulsars, the magnetic field is about 10^8 G, much lower than 10^{12} G often seen in slow accretion-powered pulsars, but their accretion rates are low on the whole too, among the lowest in the known LMXB population. The energy spectra of millisecond accretion-powered pulsars are mostly hard (Figure 1-6).

The weakly magnetized accreting NSs are mostly found in LMXBs. They can be classified into Z and atoll sources [Hasinger and van der Klis, 1989]. They will be focus of this thesis. Thus their properties will be presented in the next section in more detail. Weakly magnetized accreting NSs normally show type I X-ray bursts, but generally no strong coherent pulsations, except the millisecond accretion-powered pulsars.

1.5 Weakly magnetized NS LMXBs

Z and atoll sources are the two main classes of weakly magnetized NS LMXBs. They are classified based on their X-ray spectral and timing properties [Hasinger and van der Klis, 1989, van der Klis, 2006]. They were named after the patterns that they trace out in the CDs or HIDs [Hasinger and van der Klis, 1989]. Figure 1-3 shows the CD/HIDs of two atoll sources (first two columns) and two Z sources (last two columns). It should be noted that atoll sources originally were thought to have only atoll patterns in the CD/HIDs, but with extensive coverage by *RXTE* , some atoll sources can have Z-like patterns [Muno et al., 2002, Gierliński and Done, 2002a], such as those in the first column in Figure 1-3. However, Z and atoll sources are still two distinct classes with differences in many aspects. Their patterns have different orientation, color ranges, evolution timescales. Z sources typically radiate at luminosities close to Eddington luminosity ($L_{\rm EDD}$), while atoll sources cover a lower and larger luminosity range (∼0.001–0.5 $L_{\rm EDD}$). Furthermore, the spectra of Z sources are very soft on all three branches of the "Z", whereas the spectra of atoll sources are soft at high luminosities, but hard when they are faint (Figures 1-5 and 1-7). Properties like the rapid

X-ray variability and the order in which the branches are traced out are also different for the two classes [Barret and Olive, 2002, van Straaten et al., 2003, Reig et al., 2004, van der Klis, 2006]. As denoted in Figure 1-3, the upper, diagonal and lower branches of the Z-shaped tracks for Z sources are called horizontal, normal and flaring branches (HB/NB/FB), respectively, while for atoll sources, they are called the hard, transitional and soft states (HS/TS/SS), respectively (or extreme island, island, and banana states, respectively). As will be shown in §5, the differences between Z and atoll sources are due to their different mass accretion rates.

Atoll sources include ordinary atoll sources and "GX" atoll sources. "GX" atoll sources include GX 3+1, GX 9+1, and GX 9+9 (GX 13+1 is sometimes included in this class, but it shows some peculiar behavior) [van der Klis, 2006]. They are all in the galactic bulge and are all persistent, with luminosity believed to be roughly higher than ordinary atoll sources. "GX" atoll sources are only observed in the soft state thus far. Some ordinary atoll sources are persistent (e.g., 4U 1636–53 and 4U 1705–44), while the others are transient (e.g., Aql X–1 and 4U 1608–52; Figure 1-2).

As mentioned above, Z sources have three distinct branches. Based on the shape and orientation of their branches, the six classical Z sources were further divided into two subclasses [Kuulkers et al., 1994]: Cyg-like (Cyg X-2, GX 340+0, and GX 5-1) and Sco-like (Sco X-1, GX 17+2, and GX 349+2; Figure 1-3). In addition to movement along the "Z" tracks, the Z tracks themselves display slow shifts and shape changes in CDs/HIDs. These so-called secular changes are most apparent in Cyg X-2. XTE J1701–462 is a new transient accreting NS X-ray binary, with a long outburst in 2006–2007 (Figure 1-2). It exhibited both Z source and atoll source behavior.

One of the most important tasks of understanding accreting NSs is to reveal the origin of their spectral evolution. This includes not only the origin of different states/branches, but also the origin of secular changes of Z source tracks and transformation of source types. To achieve this, we need to have a correct spectral model for these systems. However, the spectral modeling of accreting NSs has been controversial for a long time [see Barret, 2001, for a review].

1.6 Organization and content of thesis

The main focus of this thesis is on the spectral evolution of weakly magnetized accreting NS X-ray binaries. They include both Z and atoll sources. This investigation considers the spectral decomposition problem of these systems, the physical origin of spectral evolution, and the transformation from one source type to the other.

Chapter 2 introduces the X-ray observatories *RXTE* , *Suzaku*, and *BeppoSAX*, and their data analysis methods. They will be used extensively in this thesis.

Chapter 3 describes in more detail some fundamental accretion physics and the X-ray emission mechanisms relevant to X-ray binaries.

Chapter 4 is a published paper on the spectral modeling for atoll sources, concentrating on two transients Aql X–1 and 4U 1608–52. I compare different models that have been used for these systems and come up with a new way to model the spectra of these systems. The new model is shown to describe the spectral evolution of atoll sources better in terms of some desirability criteria, including $L_X \propto T^4$ evolution for the multicolor disk (MCD) component, and the similarity to black holes (BHs) for correlated timing/spectral behavior.

Chapter 5 examines our new spectral model (Chapter 4) to the highly variable atoll source 4U 1705–44 using the extended soft X-ray sensitivities of *Suzaku* and *BeppoSAX*.

Chapter 6 applies our new spectral model on two persistent atoll sources 4U 1636–536 and 4U 1705–44. In this paper, I examine the soft state more carefully by comparing the results from the part of the soft state with kHz QPOs detected with those from other parts. Because this difference from Chapter 4, I also include Aql X–1 and 4U 1608–52 in this chapter. The conclusions in this chapter are mostly the same as those in Chapter 4, but I also find a close relation between the kHz QPOs and the accretion disk.

Chapter 7 is a published paper on the spectral evolution of XTE J1701–462. Physical interpretations are given for the 3 branches of Z sources, and I explain the cause of the transformation between Z and atoll types.

In Chapter 8, I present the study of type I X-ray bursts from XTE J1701–462 and estimate the distance to this system.

In Chapter 9, I study the Sco-like Z source GX 17+2 in order to see whether our interpretations of Z tracks of XTE J1701–462 apply to persistent Z sources.

I summarize our study results of NS X-ray binaries and present the complete picture of their spectral evolution and transformation of source types in Chapter 10. The conclusions are presented in Chapter 10.

Chapter 2

X-ray Observatory and Data Analyses

In this chapter I briefly describe the *Rossi X-ray Timing Explorer*, *Suzaku*, and *BeppoSAX*, which are the X-ray observatories that provide the data used in this thesis. I will describe the relevant data reduction techniques that are common to the detailed studies reported in the later chapters.

2.1 The *Rossi X-ray Timing Explorer*

The *Rossi X-ray Timing Explorer* [*RXTE* , Bradt et al., 1993] is an X-ray mission, which features unprecedented time resolution in combination with moderate spectral resolution to explore the variability of X-ray sources. It was launched on December 30, 1995 from NASA's Kennedy Space Center by a Delta II rocket into its intended low-earth circular orbit at an altitude of 580 km, corresponding to an orbital period of about 90 minutes, with an inclination of 23°. A diagram of the *RXTE* is shown in Figure 2-1, with three major instruments labeled, i.e., the Proportional Counter Array [PCA; Jahoda et al., 1996], the High Energy X-ray Timing Experiment [HEXTE; Rothschild et al., 1998], and the All-Sky Monitor [ASM; Levine et al., 1996]. The PCA and the HEXTE are collimated (non-focusing) pointed instruments, while the ASM is a coded-mask imaging instrument designed to survey the sky with a wide viewing angle. *RXTE* has been carrying out science observations for more than 12 years, far surpassing its required lifetime of two years.

2.1.1 Instruments

The PCA is an array of five Proportional Counters Units (PCUs) with a large total collecting area of 6500 cm^2. It can detect sources as faint as 0.1 mCrab. It only carries out pointed observations, with the FWHM spatial resolution confined to be 1° by the collimator. It is sensitive to energy range 2.5–60 keV with energy resolution $< 18\%$ at 6 keV. The PCA has been well calibrated, based on observations of the Crab Nebula. The data can be collected at time resolution of 1 μs. The PCA data, which are processed by the Experiment Data System before telemetered, are collected in a variety of modes corresponding to different combinations of time and energy resolution in order to stay within the mission's telemetry limit. However, there are two modes, known as 'standard1' and 'standard2', that are made for every observation. Standard1 data contain 0.125-s full-energy-band light curves for

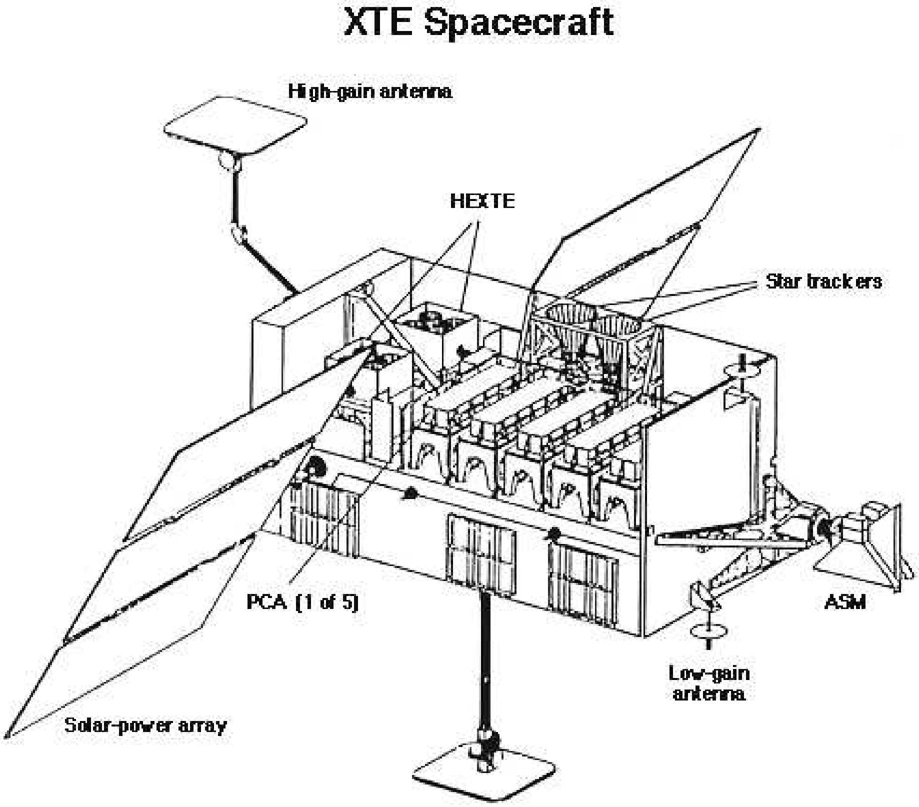

Figure 2-1: Diagram of the *RXTE* spacecraft, with major instruments labeled. Figure courtesy of the NASA High Energy Astrophysics Science Archive Research Center/Goddard Space Flight Center (HEASARC/GSFC).

every PCU and for different types of instrument background rates. Standard2 data has a time resolution of 16s and 129 energy channels covering the full energy range of the PCA detectors. Some of the PCUs suffer breakdown and trip off if they are not regularly "rested". This means that any individual observation may contain data from 1 to 5 operating PCUs.

The HEXTE is composed of two clusters (A and B) consisting of four "phoswich" scintillation detectors each. These two clusters rock on and off the source along mutually orthogonal directions for realtime background measurements. Cluster A started experiencing rocking problems in 2006, and since then it was fixed in the on-source position. The detectors are sensitive to high-energy X-rays from 15-250 keV. The energy resolution is 15% at 60 keV. The FWHM spatial resolution for the HEXTE is also 1°. Each cluster has collecting area of 800 cm^2. The time resolution can be as high as 8 μs. The HEXTE has one standard mode that is used for every observation. This mode has 16-s time resolution and 64 spectral channels.

The ASM consists of three wide-angle shadow cameras equipped with proportional counters with a total collecting area of 90 cm^2. It scans about 80% of the sky every 90 minutes, with additional gaps if the satellite orbit crosses through the South Atlantic Anomaly. It can monitor sources of 30 mCrab or brighter, and have spatial resolution of $3' \times 5'$. The ASM standard products consist of light curves and color measurements for each of the ∼566 sources (at the present time) in the ASM catalogue.

2.1.2 Data Analyses

The studies of X-ray binaries rely on their spectral and timing information and involve creation of light curves, energy spectra, color diagrams, and power density spectra, etc., on appropriate timescales. The data analyses typically start with filtering of the data for proper observing conditions, accumulate data over energy/time bins, and transform in ways depending the types of data products, and finally compare/fit them with spectral/timing models as needed. Most observatories, including *RXTE* , *Suzaku* and *BeppoSAX*, provide main data products in the FITS (Flexible Image Transport System) format. They can be analyzed using the FTOOLS software package, which is part of the HEAsoft provided by NASA's High Energy Astrophysics Science Archive Research Center (HEASARC). FTOOLS provides general and mission-specific tools to manipulate FITS files. In the following I describe the procedures used in most part of this thesis to reduce data from *RXTE* . I will start with the PCA first.

Some standard criteria were used to filter the PCA data: the earth-limb elevation angle was required to be larger than 10°, and the spacecraft pointing offset was required to be $< 0.02°$. For faint observations, we additionally excluded data within 30 minutes of the peak of South Atlantic Anomaly passage or times with large trapped electron contamination. In most part of this thesis, the focus is on spectral evolution, and only the persistent emission due to gravitational accretion is relevant. Emission due to stable nuclear burning might present, but is negligible compared with the persistent emission due to gravitational accretion (Chapter 3). Sometimes, however, the source emission can be dominated by unstable nuclear burning leading to type I X-ray bursts, which occurs over very short intervals (a few seconds to minutes). Such intervals should be excluded. In this thesis, I exclude data of 20 seconds before and 200 seconds after type I X-ray bursts [see Remillard et al., 2006a].

To create PCA spectra, "standard 2" data were normally used. As the PCA is a collimated instrument and is always pointed at the source during an observation, the background is not directly available, but is estimated by models, which are provided by the PCA team. As suggested by the PCA team, I used appropriate faint/bright background models when the source had intensity lower or higher than 40 counts/s/PCU, respectively. The integration time for each spectrum depends on source variability. It can be one spectrum for each observation, or one spectrum for several observations, or several spectra for one observation. When necessary, the integration time can be selected based on positions in the CD/HIDs. In order to carry out spectral fitting and because of PCA response varying with time, I create and select response files appropriate to the time of each spectrum that is analyzed.

The hard/soft colors used in the CD/HIDs are based on PCA spectra. Soft and hard colors were defined as the ratios of the background-subtracted counts in the (3.6–5.0)/(2.2–3.6) keV bands and the (8.6–18.0)/(5.0–8.6) keV bands, respectively [Muno et al., 2002]. We normalized the raw count rates from each PCU with the help of observations of the Crab Nebula. For each PCA gain epoch, we computed linear fits (vs. time) to normalize the Crab count rates to target values of 550, 550, 850, and 570 counts/s/PCU in these four energy bands. The CD/HIDs using PCA data presented in this thesis are all normalized in this way.

In timing analyses, the common mathematical tool is the power density spectra calculated through discrete Fourier transform. PCA data instead of HEXTE data are normally used for timing analyses, since accreting NSs emit photons most intensely at energies below 20 keV. Data with high time resolutions are necessary in order to probe rapid variability. Thus binned or event mode data, instead of standard mode data, are used for this purpose. Detailed calculation of power density spectra is presented in the Appendix A. They are normally Leahy-normalized and have Poisson noise subtracted. The deadtime correction is also necessary for sources with high intensity. The resulting power density spectra can be fit with model consisting of different noise components and QPOs. The power continuum can be integrated over some frequency range (0.1-10 Hz in this thesis) to obtain the fractional root-mean-square values, to characterize source variability in that frequency range.

In this thesis, the HEXTE data are only used to create spectra that have integration time matching that of PCA spectra. The background spectra can be directly made from off-source observation data. Most of observations of Cluster A after 2006 only have on-source observation data due to rocking problems, and the background should be estimated using the `hextebackest` tool. It is based on the off-source observations of Cluster B. The deadtime correction for HEXTE data is made using the program provided by the HEXTE team. The response file for each cluster of the HEXTE has been the same throughout the *RXTE* mission and is provided directly by the HEXTE team.

2.2 *Suzaku*

Suzaku [Mitsuda et al., 2007] is Japan's fifth X-ray astronomy mission and was launched in August 2005. The goal of this mission is to carry out high resolution spectroscopy and wide-band observations of high energy astronomical phenomena. It covers the energy range 0.2–600 keV with the two instruments, i.e., X-ray CCDs [X-ray Imaging Spectrometer; XIS;0.2–12 keV Koyama et al., 2007], and the hard X-ray detector [HXD; 10–600 keV Takahashi et al., 2007]. Suzaku also carries a third instrument, an X-ray micro-calorimeter (X-ray Spectrometer; XRS), but the XRS lost all its cryogen before routine scientific observations could begin. The XISs and HXD are imaging and collimated instruments respectively. Broadband spectral feature and high energy resolution of this X-ray observatory make it

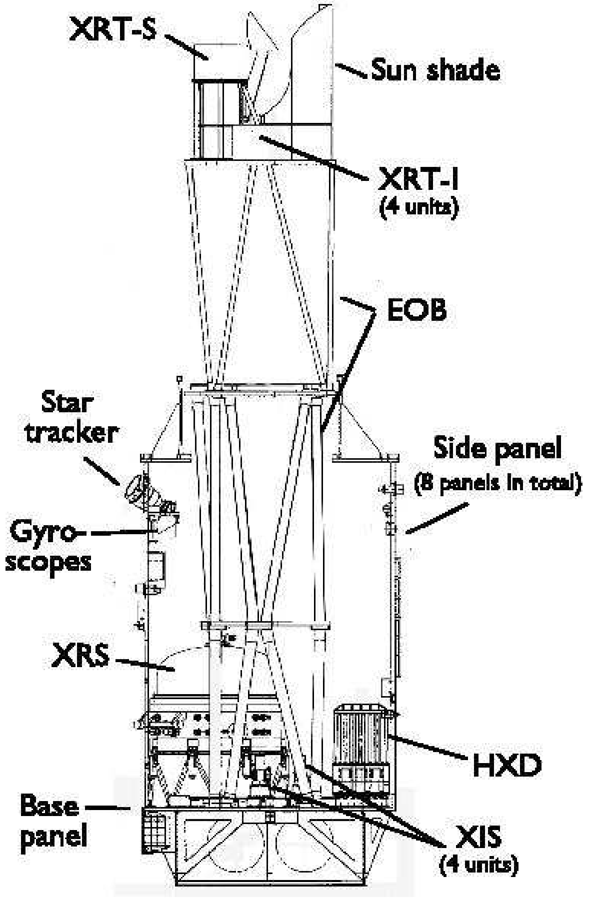

Figure 2-2: Diagram of the *Suzaku* spacecraft, with major instruments labeled [Mitsuda et al., 2007].

highly suitable for X-ray binary studies.

2.2.1 Instruments

XISs

The *Suzaku* X-ray CCD instrument consists of four XIS cameras. They employ X-ray sensitive silicon charge-coupled devices (CCDs), which are operated in a photon-counting mode. In general, X-ray CCDs operate by converting an incident X-ray photon into a charge cloud, with the magnitude of charge proportional to the energy of the absorbed X-ray. This charge is then shifted out onto the gate of an output transistor via an application of time-varying electrical potential. This results in a voltage level (often referred to as "pulse height") proportional to the energy of the X-ray photon.

The four Suzaku XISs are named XIS0, 1, 2 and 3, each located in the focal plane of an X-ray Telescope. XIS2 has not been used for scientific observations since November 2006, due to a large amount of charge leakage. XIS1 uses a back-illuminated CCDs, while the other three use front-illuminated CCDs. The CCD performance gradually degrades in space due to the radiation damage. This is because of the accumulation of charge traps that are produced by cosmic-rays. One of the important features of the XIS is the capability to inject small amounts of charge to the pixels. Periodic charge injection is quite useful to fill the charge traps, and to make them almost harmless. This method is called the spaced-row charge injection (SCI), and the SCI has been adopted as a standard method since AO-2 to cope with the increase of the radiation damage.

There are two different kinds of on-board data processing modes for XISs, i.e., the Clock and Editing modes. The Clock modes describe how the CCD clocks are driven, and this determines the exposure time, exposure region, and time resolution. The Clock modes include normal modes, which is explained in more detail below, and Parallel Sum Mode, in which the pixel data from multiple rows are summed in the Y-direction on the CCD, and the sum is put in the Pixel RAM as a single row. The Editing modes specify how detected events are edited, and this determines the format of the XIS data telemetry. One example of edit modes is the 5×5 observation mode, in which all the pulse heights of the 25 pixels centered at the event center are sent to the telemetry. There are also 3×3 and 2×2 observation modes.

In the Normal Clock mode, the Window and Burst options can be specified, otherwise all the pixels on the CCD are read out every 8 seconds. The Window and Burst options are important when observing bright X-ray binaries, because the pile-up problem can be reduced by faster readout times. Pile-up occurs when more than one photon strikes in the same or adjacent pixels in one CCD readout frame. The Window option allows shorter exposure times by reading out more frequently only a portion of the CCD. The full CCD has 1024×1024 pixels. When the Window width is 256×1024 pixels (1/4 Window), the exposure time becomes a quarter of that without the Window option (i.e., 2 s), and the Pixel RAM is filled with the data from four successive exposures. Similarly, there can be 1/8 or 1/32 Window options. In the Burst option, an extra deadtime t is introduced for every exposure. If the pixel is read out, say, every 2 s for 1/4 Window, the live time is 2-t s in every exposure. The Burst and Window options are independent and may be used simultaneously. They can effectively reduce the pile-up problem. For example, the XIS team expects that a point source as bright as 12.5 counts/s/XIS can be observed with the pile-up problem being negligible if neither options are specified. Then if the 1/N Window option and deadtime of t s for the Burst option are specified, a point source as bright as $12.5\times N \times 8/(8 - Nt)$ counts/s/XIS can be observed with the pile-up problem being negligible.

HXD

The HXD is a hard X-ray scintillating instrument, and has a main purpose to extend the bandpass of the Suzaku observatory to the highest feasible energies, thus allowing broadband studies of celestial objects. The HXD sensor is a compound-eye instrument, consisting of 16 main detectors. Each unit actually consists of two types of detectors: a GSO/BGO phoswich counter, and 2mm-thick PIN silicon diodes located inside the well, but in front of the GSO scintillator. The PIN diodes are mainly sensitive below $\sim$ 60 keV, while the GSO/BGO phoswich counter (scintillator) is sensitive above $\sim$ 40keV. The HXD features an effective area of $\sim$ 160 cm^2 at 20 keV, and $\sim$ 260 cm^2 at 100 keV. The energy resolution is $\sim$ 4.0 keV (FWHM) for the PIN diodes, and $7.6/\sqrt{E}\%$ (FWHM) for the scintillators, where E is energy in MeV. The HXD time resolution is 61 μs.

2.2.2 Data Analyses

The extraction of light curves or spectra of XISs can be done within the program xselect provided by FTOOLS. As this thesis deals with X-ray binaries and they can be treated as point sources, one spatial region on the CCD measures the source, while a different other region away from the source position can be used to measure the background. A radius of 250 pixels ($260''$) of the circular source extraction region can ensure that 99% of the flux of a point source is included. For bright sources, the background region can be significant contaminated by source emission, but in this case, background subtraction might be unnecessary, as the source is so much brighter than the background. As the response of XISs varies with time, response files close in time to each spectrum must be created, and we used the `xisrmfgen` and `xissimarfgen` provided by the XIS team to accomplish this task.

When the sources are bright, the XIS CCDs can still experience serious event pile-up, even when the Window and Burst options are used. Normally, the center region with serious pile-up should be excluded. In this thesis, I estimated the pile-up fraction of each CCD pixel using two publicly available tools `aeattcor.sl` and `pileup_estimate.sl`. Their results were used to exclude regions with the local pile-up fraction $> 5\%$. For more information of both tools, we refer to the website http://space.mit.edu/CXC/software/suzaku/.

The extraction of light curves or spectra for the HXD/PIN and the HXD/GSO can also be carried out in xselect program in FTOOLS. The procedures are very similar between the PIN and GSO, and I here describe them for the HXD/PIN only. As it is a collimated instrument, no spatial extraction region needs to be specified. The background includes two parts, i.e., the cosmic X-ray background and the non X-ray background. The non X-ray background is distributed to users as simulated event files tailored to each observation. The cosmic X-ray background can be simulated based on the typical cosmic X-ray background model using XSPEC. The response files for the HXD/PIN are provided by the HXD team for different instrument setting epochs.

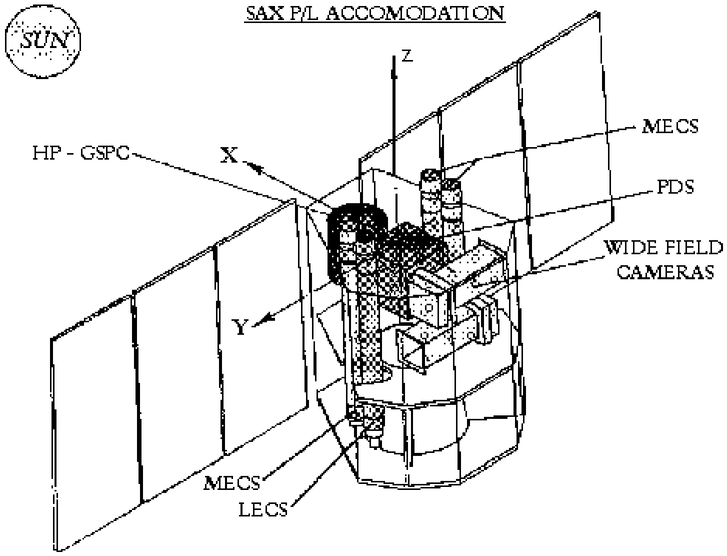

Figure 2-3: Diagram of the *BeppoSAX* spacecraft, with major instruments labeled [Boella et al., 1997a].

2.3 *BeppoSAX*

BeppoSAX was a past X-ray mission which operated from 1996 April 30 till 2002 April 30. It was a program of the Italian Space agency with participation of the Netherlands Agency for Aerospace programs. One of its important goals was to make broad band spectroscopy of different classes of X-ray sources, with the energy coverage 0.1–300 keV. It carried four narrow field instruments (Figure 2-3): the Low Energy Concentrator Spectrometer [0.1–10 keV, LECS; Parmar et al., 1997], the Medium Energy Concentrator Spectrometer [1.3–10 keV, MECS; Boella et al., 1997b], the High Pressure Proportional Gas Scintillation Counter [8–50 keV, HPGSPC; Manzo et al., 1997], and the Phoswich Detection System [15–300 keV, PDS; Frontera et al., 1997]. The LECS and MECS are imaging instruments, while the HPGSPC and PDS are collimated instruments. The HPGSPC had operation problems and has no data publicly available. Thus below I only focus on the other three instruments. *BeppoSAX* also carried two coded mask proportional counters (Wide Field Cameras, WFC; Figure 2-3), that provide access to large regions of the sky in the range 2–30 keV. Each WFC has a field of view of $20^\circ \times 20^\circ$ (FWHM) with a resolution of $5'$. In this thesis, the WFC is not used and thus is not described in detail.

2.3.1 Instruments

LECS and MECS

The MECS is a set of three identical grazing incidence telescopes with a double-cone geometry. The detectors were position sensitive gas scintillation proportional counters in their focal planes. Three units are named as MECS1, 2, 3. They have total effective area 150 cm^2 at 6 keV, FOV $56'$ in diameter, angular resolution $1.2'$ at 6 keV, and energy resolution depending on energy E as $8 \times (E/6\mathrm{keV})^{-0.5}\%$ (FWHM). MECS1 did not operate for very long, and there are no data available after 1997 May 7.

The LECS had only one unit and was almost identical to the MECS units, except that it had a thinner window that allows photons with lower energies down to 0.1 keV to pass through. High background contamination made the LECS data above 4 keV unusable. The LECS has total effective area 22 cm^2 at 0.28 keV, FOV $37'$ in diameter, angular resolution $3.5'$ at 0.25 keV, and energy resolution depending on energy E as $8 \times (E/6\mathrm{keV})^{-0.5}\%$ (FWHM).

PDS

The PDS detector consisted of 4 actively shielded NaI(Tl)/CsI(Na) phoswich scintillators, with a total geometric area of 795 cm^2 and a field of view of 1.3° (FWHM). The total effective area was 600 cm^2 at 80 keV, and the energy resolution was slightly better than 15% at 60 keV.

Great care was taken to minimize the PDS background level. The detector materials were selected with low residual radioactivity. The phoswich technique provides an efficient active shielding of the NaI(Tl) detector over 2π solid angle, the lateral AC shielding system provides a rejection of the unwanted photons and charged particles, the AC top shield provides an efficient rejection of charged particles, in particular electrons.

The observation strategy of the PDS was very similar to *RXTE*/HEXTE. It continuously monitored background and source+background sky positions by rocking with both collimators in a cyclic law faction. While one of the two collimators pointed to the source the other one pointed to a blank (non source-contaminated) sky position for background measurement. During each cycle, positions of the two collimators were swapped: the one pointing to the source was moved to monitor the background and vice versa.

2.3.2 Data Analyses

The data analyses of the LECS, MECS and PDS were carried out using the program xselect provided by FTOOL. The response files for spectral analyses were provided by the instrument teams, but for the imaging instruments LECS and MECS, only some particular circular extraction regions ($8'$, $6'$, etc. in radius) should be used, and the particular selection for a given observation depends on the brightness of the source.

The background of the LECS and MECS varied with the position of the detector. Thus, the simple use of the background extraction regions to estimate the background was not feasible. One standard method is to use the 'blank field' observations. Briefly, the background was extracted from the 'black field' observations using the source extraction region and was rescaled by comparing the count rates in a background region from the 'black field' observations and the source observation. For the LECS, this only works for the faint observation, as the bright source contaminates the background region. It does not work for sources located at low galactic latitudes either, as these sources have Galactic ridge emission background that is not included in the 'black field' observations. Parmar et al. [1999] provided another method that worked for these cases, i.e., sources that are bright and/or in the low galactic latitudes. This method was based on the quantitative estimates of how the source emission contaminated the background region and how the background varied with the position of the detector. This method was used in this thesis, as our sources are all bright and at low galactic latitudes.

The PDS was a collimated instrument with cyclic on and off-source observations. Thus the background of the PDS can be directly estimated from the off-source observations.

However, there is one additional analysis requirement for the PDS data prior to spectral extraction, i.e., screening for “spikes”. These events were due to single particle hits that illuminated one crystal and created fluorescence cascades. As they normally resulted in momentary higher count rates than most sources, spikes can be excluded by excluding high intensity intervals.

Chapter 3

Accretion Physics and X-ray Emission Mechanisms

3.1 Accretion physics

One of the main differences between an X-ray binary and an isolated compact object is that material from the companion can accrete onto the compact object through the Roche lobe or stellar wind. As the members of binaries orbit around each other, the accreting material possesses angular momentum relative to the compact object and tends to form an accretion disk. It is one main common X-ray emission component in X-ray binaries. For weakly magnetized NS LMXBs, the class of X-ray binaries studied in this thesis, the accreting material is expected to finally impact the surface of the NS, and we will show evidence suggesting that the hot accreting gas forms an equitorial belt, which is illustrated in Figure 3-1. There are possibly other significant emission components, such as a jet and a corona of hot tenuous gas (Figure 3-1), although not all of these components mentioned above might be present simultaneously. This section is devoted to describe accretion physics relevant to this thesis.

3.1.1 Spherically symmetric accretion and Eddington luminosity

We start with the simple case of spherical accretion, i.e., symmetric radial infall, and introduce the concept of Eddington limit. For a body of mass M and radius r_*, the gravitational potential energy released by the accretion of a mass m onto its surface is (in Newtonian approximation)

$$\Delta E_{\rm acc} = GMm/r_*, \tag{3.1}$$

where G is the gravitation constant. For a NS with $M = 1.4M_\odot$ and $r_* = 10$ km, $\Delta E_{\rm acc} = 0.21mc^2$, where c is the speed of light. For comparison, the nuclear energy released from burning hydrogen to helium is

$$\Delta E_{\rm nuc} = 0.007mc^2, \tag{3.2}$$

about one thirtieth of gravitational potential energy released. Burning to heavier elements such as Fe increases a little more release of nuclear energy, changing 0.007 to 0.009 in the above expression. Thus accretion onto NSs or BHs can be powerful emitters, with luminosity $L_{\rm acc} \sim GM\dot{M}/r_*$ ($\dot{M}$ is the mass accretion rate), if the gravitational potential energy is converted in some way into electromagnetic radiation.

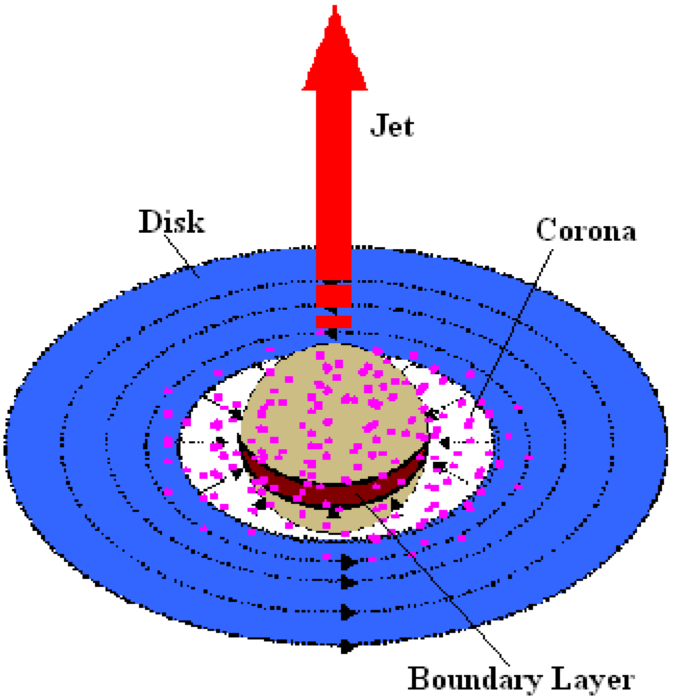

Figure 3-1: The main X-ray emission components in weakly magnetized NS LMXBs. The relative importance of these components varies with different X-ray states.

The wavelength of emission in accreting systems can be estimated as follows. If it is emitted as a blackbody spectrum (see §3.2.1) uniformly over area $4\pi r_*^2$, the blackbody temperature would be

$$T_{\rm bb} = (L_{\rm acc}/4\pi r_*^2\sigma)^{1/4}, \tag{3.3}$$

where σ is the Stefan-Boltzmann constant. An accretion rate of $\dot{M} = 10^{16}$ g s^{-1} is typically seen in close binary systems. If we assume that all of its available gravitational energy is converted to heat, then $T_{\rm bb}$ would be about 1 keV for the NS case (using $M = 1.4M_\odot$ and $r_* = 10$ km), with the spectrum strongest in the X-ray band (i.e., 1–10 keV). Applying the above argument to the WD case ($M \sim M_\odot$, $r_* \sim 5000$ km), it can be found that the emission is strongest in the ultraviolet region. Thus binaries with strong X-ray emission probably contain NSs or BHs, instead of WDs.

There is an upper limit, i.e., the Eddington limit, for the radiation that the accretion system can have, whereby there are so many photons experiencing Thomson scattering interactions with infalling particles, mainly free electrons, that the net outward force can stop the accretion process. The scattering cross-section for the proton is much smaller than that for the electron, but the attractive electrostatic Coulomb force between electrons and protons are strong enough that stopping of electrons requires stopping of protons too. Thus we can treat the accreting particles as electron-proton pairs, assuming that accreting material is mainly hydrogen and is fully ionized. Each pair at a radial distance r has a total gravitational force $GM(m_{\rm p} + m_{\rm e})/r^2 \approx GMm_{\rm p}/r^2$, but also experiences an outward radiation force equal to the rate at which it absorbs momentum $\sigma_{\rm T}S/c$. Here $\sigma_{\rm T} = 6.7 \times 10^{-25}$ cm^2 is the Thomson scattering cross-section, and S is the radiant energy flux and is equal to $L/4\pi r^2$ if spherical symmetry is assumed. The accretion would be stopped if these two forces balance each other, i.e., $GMm_\mathrm{p}/r^2 = \sigma_\mathrm{T} L/4\pi c r^2$, and we obtain the Eddington luminosity

$$L_\mathrm{Edd} = 4\pi G M m_\mathrm{p} c/\sigma_\mathrm{T} \approx 1.26 \times 10^{38} (M/M_\odot) \text{ erg s}^{-1}. \tag{3.4}$$

If the accreting material is pure helium, each nucleus has two extra neutrons and has nearly four times the mass of a proton, while the radiation pressure would act on two free electrons. Thus the Eddington luminosity would be larger. More generally, we can assuming the mass fraction of hydrogen to be X and that the accreting material consists of hydrogen and helium. Then the Eddington luminosity becomes

$$L_\mathrm{Edd} = 8\pi G M m_\mathrm{p} c/(1+X)\sigma_\mathrm{T} \approx 2.51 \times 10^{38} (M/M_\odot)/(1+X) \text{ erg s}^{-1}. \tag{3.5}$$

The above canonical Eddington luminosity (Equation 3.5) is given under the assumption of spherical symmetry and in the Newtonian limit. It is independent of the radial distance. The relativistic Eddington luminosity for a local observer at r is instead given by [see e.g., Shapiro and Teukolsky, 1983, p396; nonrotational compact object case],

$$L_\mathrm{Edd,rel}(r) = [8\pi G M m_\mathrm{p} c/(1+X)\sigma_\mathrm{T}][1 - 2GM/rc^2]^{-1/2} = [8\pi G M m_\mathrm{p} c/(1+X)\sigma_\mathrm{T}](1+z). \tag{3.6}$$

In the above expression, $1+z = [1 - 2GM/rc^2]^{-1/2}$ is the redshift factor. It has a value of almost 1.31 at the surface of the NS with $M = 1.4 M_\odot$ and $r_* = 10$ km. The extra factor $1+z$ comes from the relativistic correction of the gravity force. The corresponding Eddington luminosity measured by a distant observer is

$$L_\mathrm{Edd,rel,\infty} = [8\pi G M m_\mathrm{p} c/(1+X)\sigma_\mathrm{T}][1 - 2GM/rc^2]^{1/2} = [8\pi G M m_\mathrm{p} c/(1+X)\sigma_\mathrm{T}]/(1+z). \tag{3.7}$$

The Eddington limit can also refer to the accretion rate $\dot{M}$, and in this case it represents the accretion rate when the accretion luminosity reaches L_Edd. It can also provide a reference scale for the flux and the temperature. The Eddington flux is $F_\mathrm{Edd} = L_\mathrm{Edd}/4\pi r^2$, or $F_\mathrm{Edd,rel} = L_\mathrm{Edd,rel}/4\pi r^2$, at a spherical emitting surface with radius r. The corresponding relativistic value measured by a distant observer is $F_\mathrm{Edd,rel,\infty} = L_\mathrm{Edd,rel,\infty}/4\pi D^2$, where D is the distance of the source. The Eddington temperature at a spherical emitting surface with radius r is the effective temperature corresponding to the Eddington flux, i.e., $\sigma T_\mathrm{Edd} = F_\mathrm{Edd}$, or $\sigma T_\mathrm{Edd,rel} = F_\mathrm{Edd,rel}$. The (relativistic) Eddington temperature observed by a distant observer is related to the above local values by correcting for the redshift of photons and is in fact a color temperature for the distant observer [Goldman, 1979, Marshall, 1982, Lewin et al., 1993]

$$\begin{aligned} T_\mathrm{Edd,rel,\infty} &= f_\mathrm{c} \left(\frac{1}{4\pi\sigma r^2} \frac{8\pi G M m_\mathrm{p} c}{(1+X)\sigma_\mathrm{T}} (1+z)^{-3} \right)^{1/4} \\ &= (2.10 \text{ keV}) f_\mathrm{c} \left(\frac{M}{M_\odot} \right)^{1/4} \left(\frac{r}{10 \text{ km}} \right)^{-1/2} \left(1 - \frac{M}{M_\odot} \frac{2.95 \text{ km}}{r} \right)^{3/8} (1+X)^{-1/4}, \end{aligned} \tag{3.8}$$

where I have included color correction factor f_c due to Compton scattering normally seen in X-ray binaries (§3.2). Using $r = r_* = 10$ km, $M = 1.4 M_\odot$, and $f_\mathrm{c} = 1.4$ [Madej et al., 2004], I obtain $T_\mathrm{Edd,rel,\infty}$=2.20, 2.28, and 2.61 keV for X=1.0, 0.7, and 0.0, respectively.

3.1.2 The standard thin disk

The standard thin disk refers to a specific type of accretion disk which is geometrically thin and optically thick. Such systems can be described in cylindrical coordinates (r,ϕ,z), with the coordinate center being the center of the compact object, the disk in the plane of $z = 0$, and the rotation in the ϕ-direction. I will limit to the case of the Newtonian limit in this and the next section. The relativistic accretion disk will be described in §3.1.6.

First a simple picture of the formation of accretion disk is described. Most LMXBs accrete material through Roche lobe (in contrast, mostly through capture of the stellar wind for HMXBs). This can occur when the secondary evolves and increases its radius or the binary separation shrinks so that the gravitational force of the primary is strong enough to attract the outer layers of the secondary. The material mostly flows though the inner Lagrange point L_1 where the gravity forces from both members are equal in absolute value. The particles there are presumably pushed by pressure forces and thus have a velocity about the sound of the speed toward the primary. In the perpendicular direction, their velocity in most cases are much larger, due to orbital motion of the binary system. It can thus be assumed that the particles are released from rest at L_1, with a given angular momentum with respect to the primary. Due to the influence of the secondary, these particles will not have circular orbits, but assume elliptical orbits. With a lot of particles, or a continuous stream, it will intersect itself. Some energy should be dissipated, and the stream will tend to follow a circular orbit under a given angular momentum. This orbit (circularization radius) can be shown to be so close to the primary that the stream is mostly under the influence of the primary. With some dissipative processes (see below), which result in the loss of energy and angular momentum, the streams can spiral slowly inwards toward the primary through a series of approximately circular orbits and form an accretion disk.

The accretion disks extract gravitational potential energy and convert it into radiation. This can happen due to viscous torques. The precise nature of the relevant viscosity is still poorly understood. However, considerable progress has been achieved in some areas despite this lack of knowledge, mostly because theories can be scaled to observations without having an accurate knowledge of the efficiency, which depends on the elusive knowledge of the absolute values of the mass accretion rates and viscosity. The rough picture of how viscosity plays role in the accretion disk can be described as follows. In the accretion disk, the material roughly follows Keplerian rotation and thus moves with different angular velocity at different radii. Due to such differential rotation, the motion of particles in the radial direction implies transportation of momentum and exertion of torque by the inner part of the disk to the outer part. The force is in the ϕ-direction and is given by, per unit area,

$$\sigma_{r\phi} \sim -\rho\tilde{v}\lambda r\Omega', \tag{3.9}$$

where ρ is the density, $\tilde{v}$ is the speed of the motion that transports the momentum, λ is the mean free path, and Ω is the angular velocity, with the derivative respective to r denoted by Ω'. There is still debate on what kind of motion of the particles that transports the momentum and creates the viscosity that we refer to here. The molecular viscosity (with λ and $\tilde{v}$ being the mean free path and the thermal speed respectively) turns out to be far too weak to bring about the viscous dissipation and angular momentum transport that we require in the accretion disk. The turbulent motion is one candidate, with λ and $\tilde{v}$ being the size and turnover velocity of the largest turbulent eddies. Currently the most promising mechanism to produce the turbulence that we need for the accretion disk is the magnetorotational instability [MRI; Balbus and Hawley, 1991, Chandrasekhar, 1960, Velikhov, 1959]. This will be discussed in more detail in §3.1.6. It should be noted that the simple α-description of accretion disk might not be valid any more if the turbulence is produced by the magnetorotational instability. Considering that the size of the largest turbulent eddies cannot exceed the disk thickness H and that the turnover velocity is unlikely to be supersonic, the viscosity has been written as follows [Shakura and Syunyaev, 1973],

$$\nu = \lambda\tilde{v} = \alpha c_{\rm s} H, \tag{3.10}$$

where $c_{\rm s}$ is the sound speed. In this α-prescription of viscosity, we expect $\alpha \lesssim 1$, with values of 0.1 or 0.01 being often used in the literature. It should be noted that this does not mean that we know more about viscosity in this prescription. There is also no reason to believe that α is constant throughout the disk. Under the thin disk assumption, we can view the disk as a two dimensional flow. The torque exerted by the outer ring on the inner one is

$$\tau(R) = 2\pi r \nu \Sigma r^2 \Omega', \tag{3.11}$$

where $\Sigma = \rho H$ is the surface density.

In the following, the emission spectrum of the accretion disk will be derived, under the assumption that the disk is geometrically thin, optically thick and in the steady state, with the angular frequency assuming the Keplerian value $\Omega = \Omega_{\rm K} \equiv (GM/r^3)^{1/2}$ and the radial velocity v_r being small. Thus the specific angular momentum is $\sqrt{GMr}$, and the specific dynamic energy (kinetic plus gravitational energy) is $-GM/2r$. The mass accretion is given as $\dot{M} = 2\pi\Sigma v_r$. Consider an annulus of the disk with the outer radius $r + {\rm d}r$ and the inner radius r. In the steady state, there is no change of the angular momentum for this annulus of the disk, so input angular momentum plus the torque at $r + {\rm d}r$ is equal to that at r and thus is constant, i.e.,

$$\left(\tau + \dot{M} r^2 \Omega\right)_{r+{\rm d}r} = \left(\tau + \dot{M} r^2 \Omega\right)_r = {\rm const.} \tag{3.12}$$

Suppose there is a radius r_0 where the torque τ is zero, and then we have

$$\tau + \dot{M} r^2 \Omega = \dot{M} r^2 \Omega(r_0). \tag{3.13}$$

The main function of the viscous stress is to convert the kinetic energy into heat. Assume that the luminosity of that annulus of the disk is ${\rm d}L$, which should be equal to input dynamic energy plus the work by the viscous torque per unit time, again from the steady state assumption. Thus

$${\rm d}L = \left\{\dot{M}(-GM/2r) + \tau\Omega\right\}_{r+{\rm d}r} - \left\{\dot{M}(-GM/2r) + \tau\Omega\right\}_r = \dot{M}{\rm d}(-GM/2r) + {\rm d}(\tau\Omega) \tag{3.14}$$

Using Equation 3.13 and assuming blackbody radiation from both the top and the bottom of the annulus with area $2\pi r{\rm d}r$, we have

$${\rm d}L = \frac{3}{2}\frac{GM\dot{M}}{r^2}\left[1 - \left(\frac{r_0}{r}\right)^{1/2}\right]{\rm d}r = (4\pi r{\rm d}r)\sigma T^4, \tag{3.15}$$

where σ is the Stefan-Boltzmann constant. Thus the blackbody temperature depends on radius as

$$T = \left\{ \frac{3GM\dot{M}}{8\pi r^3 \sigma} \left[1 - \left(\frac{r_0}{r} \right)^{1/2} \right] \right\}^{1/4} . \tag{3.16}$$

Two comments follow. First, in the derivation above, the exact form of the viscosity is not required. This is surprising, but is also important as the form of the emission spectrum and its dependence on $\dot{M}$, r, etc. are known, even though the viscosity is poorly understood at present. Second, r_0 can be inner radius of the disk, and this can be due to innermost stable circular orbit (ISCO), prescribed by general relativity (in the derivation above, however, we only assume Newtonian approximation). If the disk is truncated by the solid surface of the compact object, there should be a boundary layer just outside the surface of the compact object (Figure 3-1). Within this boundary layer, the angular frequency Ω of the accreting material should decrease to the surface angular frequency. Thus there is a maximum of Ω near the surface, where the viscosity torque is zero as Ω' is zero (Equation 3.11). Thus r_0 is the radius where the maximum of Ω is achieved. It can be shown that this is very close to the surface of the compact object. Thus r_0 can be simply assumed to be the radius of the compact object. In summary, r_0 in Equation 3.16 can be ISCO or the radius of the compact object r_* ($r_0 \approx r_*$) if r_* is outside its ISCO.

3.1.3 The magnetorotational instability

In the last section, the unknown nature of the viscosity was parametrized by a coefficient α. Now it is widely recognized that MRI can lead to turbulence that can transport the angular momentum in the accretion disk. We refer to Balbus [2003] for a review.

The physics of MRI is not complicated and can be explained using mechanical analogy. Consider a Keplerian accretion disk in the presence of a weak axial magnetic field. The magnetic field has the magnetic tension acting on two radially neighboring fluid elements. This magnetic tension can be imagined as a massless spring. As in a Keplerian accretion disk the inner fluid element has a larger angular frequency than the outer one ($\mathrm{d}\Omega/\mathrm{d}r < 0.0$), the inner fluid element is then forced by the spring to slow down and thus reduce its angular momentum and move to a lower orbit. In contrast, the outer fluid element is forced by the spring to spring up, increase its angular momentum, and move to an outer orbit. The above process will increase the separation of the above two fluid elements, and so does the spring tension. Thus the process runs away. It should be noted that the angular transport is not some nonlinear consequence of this instability but is the very cause of the linear instability.

With recognition of the presence of MRI in accretion disks, there is a question of whether the standard thin accretion is still valid. Recently, Shafee et al. [2008] carried out three-dimensional general relativistic magnetohydrodynamic simulations of a geometrically thin accretion disk around a nonspinning black hole (the relativistic accretion disk will be addressed later). They found that the specific angular momentum profile of the inflowing magnetized gas deviated by less than 2% from that of the standard thin disk model.

3.1.4 Local Eddington limit in the accretion disk

In §3.1.1, the derivation of the Eddington luminosity was given for the case of spherical accretion (Equation 3.5). In the Newtonian limit, both the gravity and the radiation forces vary as r^{-2}, and such a critical luminosity is a single value applying to the whole space. Due to special geometry of the accretion disk, the Eddington limit can be reached locally. In a standard thin disk, the locally generated luminosity varies as r^{-3}, and radiation pressure most effectively moves matter in the vertical direction, while the vertical component of gravity force roughly varies as r^{-2}, if we assume that the thickness of the disk scales linearly with r ($H \propto r^{9/8}$ for the α-disk). At large $\dot{M}$, one can imagine that the inner part of the disk can reach the local Eddington limit, while at fairly outside, the disk can still be a standard thin disk, producing thermal radiation.

Thus there is a transition zone, outside of which the standard disk is still valid and inside of which the radiative force overcomes the gravity and the standard picture of the thin disk is violated. The radius of the transition zone ($r_{\rm cr}$) can be roughly derived as follows. The gravity force on a pair of electron-proton in the vertical direction is $-GMzm_{\rm p}/(r^2+z^2)^{3/2}$, where $m_{\rm p}$ is the proton mass, while the radiation force is $\sigma_{\rm T}F/c$, where F is the radiative flux in the vertical direction and is $F = \sigma T^4 = [3GM\dot{M}/(8\pi r^3)][1-(r_0/r)^{1/2}]$ (Equation 3.16). Suppose that when $z = kr$ the gravity force in the vertical direction reaches maximum, which is $-[GMm_{\rm p}/r^2][k/(1+k^2)^{3/2}]$. The critical radius is obtained when the above two forces are equal,

$$\frac{r_0}{r_{\rm cr}}\left[1-\left(\frac{r_0}{r_{\rm cr}}\right)^{1/2}\right] = \frac{L_{\rm Edd}}{GM\dot{M}/r_0}\frac{2k}{3(1+k^2)^{3/2}}, \tag{3.17}$$

where $L_{\rm Edd}$ is Equation 3.5. The left-hand side of the above equation achieves the maximum of 4/27 when $r_{\rm cr} = 9r_0/4$. Using $k = 1/\sqrt{2}$ in the Newtonian limit [McClintock et al., 2006], we see that when $GM\dot{M}/r_0$, which is roughly the luminosity for the NS case, exceeds $\sqrt{3}L_{\rm Edd} \approx 1.73L_{\rm Edd}$, there should be some inner parts of the disk reaching the local Eddington limit. The above k value of $1/\sqrt{2}$ seems too large for the disk to be qualified as a geometrically thin disk. If we use $k = 0.1$, the critical value of $GM\dot{M}/r_0$ becomes about 0.44 $L_{\rm Edd}$.

The quantitative picture for the part of the disk inside $r_{\rm cr}$ is quite uncertain. It is possible that the disk inside $r_{\rm cr}$ is slim-disk like, where there is little mass loss and photon trapping takes place. The photon trapping effect refers to the situation when the mass accretion timescale is shorter than the mean travel time for photons to reach the surface to radiate away so that photons are trapped inside the accreting material and go together onto the compact object (advection dominated). It is also possible that there is significant mass outflow, along the vertical direction, as there the radiation pressure force overcomes the gravity force. In reality, there might be both the mass loss and the photon trapping simultaneously, as supported by simulations [e.g., Ohsuga and Mineshige, 2007].

3.1.5 Accretion timescales

In the following several important timescales in the accretion disk are introduced. They are dynamical, viscous and thermal timescales [Frank et al., 1985]. The dynamical timescale is the shortest characteristic timescale of the disk

$$t_\phi \sim r/v_\phi \sim \Omega^{-1}, \tag{3.18}$$

where v_ϕ is the azimuthal velocity. If there are flares on the surface of the disk, it will produce quasi-periodic oscillations corresponding to the above timescale in the emission and can be present in the power density spectra of the emission light curve. The timescale corresponding to perturbations in the z-direction of the disk is $t_z = H/c_{\rm s}$ and can be shown to be just about t_ϕ. The viscous timescale $t_{\rm visc} \sim r/v_r$ gives the timescale on which matter diffuses through the disk under the effect of the viscous torque. The thermal timescale $t_{\rm th}$

is the timescale for re-adjustment to thermal equilibrium, and can be defined as the heat content divided by the dissipation rate per unit disk area. Under the α-prescription, the above timescales can be shown to have the following numerical values [Frank et al., 1985, Equation 5.69]:

$$
\begin{aligned}
t_\phi &\sim t_z \sim \alpha t_{\rm th} \sim 0.1 \left(\frac{M}{M_\odot}\right)^{-1/2} \left(\frac{r}{10~{\rm km}}\right)^{3/2}~{\rm ms} \\
t_{\rm visc} &\sim 3\alpha^{-4/5} \left(\frac{\dot{M}}{(10^{16}~{\rm g/s})}\right)^{-3/10} \left(\frac{M}{M_\odot}\right)^{1/4} \left(\frac{r}{10~{\rm km}}\right)^{5/4}~s.
\end{aligned}
\tag{3.19}
$$

Thus the dynamical and thermal timescales are of the order of milliseconds in the accretion disk around the NS, while the viscous timescale is of the order of seconds.

3.1.6 The relativistic accretion disk

For an accretion disk around the compact objects (NSs and BHs), the general relativistic effects must present. One of the most important effects is the presence of the ISCO, prescribed by the general relativity. For a nonspinning compact object, the ISCO is at a radius of $R_{\rm ISCO} = 6GM/c^2$, i.e., three times of the Schwarzschild radius $R_{\rm s} = 2GM/c^2$. For a black hole with an extreme spin (spin parameter $a_* = 1$), $R_{\rm ISCO} = R_{\rm s}$. In a standard thin disk (not magnetized), the torque is expected to be zero at the ISCO. Therefore the smallest inner radius of a standard thin disk is at the ISCO. The continuum spectral modeling indicates a constant apparent inner disk radius for some black holes over about one order of magnitude variation in luminosity in the black hole soft state. This has been suspected to be the signature of the presence of the ISCO and has been used to infer the spin of black holes (Chapter 1). Under the description of the magnetohydrodynamical turbulence (due to MRI; see above), it is possible that there is still torque at the ISCO, i.e., the disk is not truncated at the ISCO. Shafee et al. [2008] showed that for a geometrically thin disk around a nonspinning black hole, the magnetic torque at the radius of the ISCO is only $\sim$2% of the inward flux of angular momentum at this radius. Thus, the ISCO can still be assumed to be the smallest inner disk radius for a geometrically thin disk. It should be noted that the effect of the ISCO on the observable properties of the accretion disk is gone, or not obvious, when the accretion rate is high, because the particles at the inner disk will be far from following Keplerian motion.

The general relativistic effects on the emission spectrum from the accretion disk around the compact object should be very important too. The redshift factor $1 + z$ is 1.22 at the ISCO. The spectral models for the accretion disk around the compact object should includes all relativistic effects, such as gravitational redshift, frame dragging, Doppler boosting, light bending, and self-irradiation of the disk [Li et al., 2005, Davis and Hubeny, 2006], which will be discussed more in §3.2.1.

3.1.7 ADAF and slim disk

In the above, we just concentrate on the standard disk which is geometrically thin and optically thick. They correspond to modest accretion rates. At a very low accretion rate, the disk is supposed to be in the optically-thin advection-dominated state, i.e., optically-thin ADAF [e.g., Ichimaru, 1977, Narayan and Yi, 1994]. In such an accretion flow, the radiation is very inefficient, and the energy transport is dominated by advection. The flow is quasi-spherical, and the gas rotates at much less than the Keplerian angular velocity. The gas temperature is very high, nearly virial. The emergent spectrum is non-thermal, often with a strong Comptonization component. A jet might be present in such an accretion flow, due to its large thermal energy. Such a model is often used to explain the hard-state spectra in X-ray binaries.

At high accretion rates (of the order of the Eddington limit), the accretion flow should be optically thick ADAF or slim disk. As in the optically thin ADAF, such an accretion flow is cooled by advection, a phenomenon known as photon-trapping effect, and thus is relatively radiatively ineffective [Abramowicz et al., 1988]. However, because of its high optical depth, it emits thermal-like spectra. The luminosity from such a disk is around the Eddington luminosity. To fit the spectra from a slim disk, a common method is to have the local disk temperature $T(r)$ proportional to r^{-p}, with p left free in the fit. The value of p is 0.75 for the standard disk model (Equation 3.16), and is smaller when radial advection is important [Okajima et al., 2006].

3.1.8 The boundary layer

The final fate of the accreting material is different for different types of the compact object in X-ray binaries. For the BH systems, the accreting material will plunge into the event horizon. For the NS systems, the accreting material will fall onto the surface of the NS, but the picture can be complicated by the presence of the magnetic field. Under the weak magnetic field assumption, the picture of how the accretion disk joins with the surface of the NS can depends, in part, on whether the NS is larger than the ISCO or not. The surface lies within the ISCO for most NSs with “soft” equations of state and outside the ISCO for NSs with “stiff” equations of state [Kluzniak and Wagoner, 1985]. If the NS is larger than the ISCO, the boundary layer would be part of the accretion disk and can be roughly defined to be within the radius where the angular frequency Ω achieves its maximum (such that Ω', and thus the viscosity torque, is zero; Equation 3.11). The detailed structure of the boundary layer, its evolution with the accretion rate, and the spectral properties still need a lot of studies. Here we briefly review some results from some theoretical studies. We will assume that the boundary layer is an equatorial belt, as in most studies [see, however, Inogamov and Sunyaev, 1999].

Sibgatullin and Sunyaev [2000] derived simple approximation formulas illustrating the dependence of the efficiency of energy release in the accretion disk and in the boundary layer on the NS spin frequency for various NS equations of state (The ISCO can be inside or outside the NS surface, depending on parameters chosen). The ratio of the luminosity of the boundary layer to that of the accretion disk always increases with decrease in the spin frequency. For a spin frequency of 0.5 kHz, which is typical in the NS LMXBs, the luminosity of the boundary layer is about comparable to that of the accretion disk in most of the NS equations of state that they addressed.

When the accretion disk extends to the surface of the NS, the boundary layer will be dynamically coupled to the accretion disk closely. One of the models for this case is by Popham and Sunyaev [2001]. They modeled the boundary layer as part of the disk, using the slim disk equations, which contain terms that allow for large deviations from the standard thin Keplerian disk with efficient cooling. In the modeling Newtonian approximation is made. Using slim disk equations a simplified, one-dimensional geometry to the boundary layer is applied in such model, which is a poor approximation as radial structure changes dramatically, similar to the vertical direction. With these problems borne in mind, this model predicts a hot, optically thin boundary layer with emergent X-ray spectrum very hard at low accretion rates, and at high accretion rates, the boundary layer is optically thick and can produce a quasi-Planckian spectrum. The extent of the boundary layer increases with the accretion rate.

When the accretion disk is truncated by the ISCO which is well outside the NS surface, the boundary layer should be dynamically well decoupled from the accretion disk (Figure 3-1). One of the models for such a case is by Kluzniak and Wilson [1991]. Accreting material crosses the 'gap' between the disk and the star in free fall and then strikes the NS surface at a shallow angle, creating a hot equatorial accretion belt with a temperature inversion. At low accretion rates, the accretion flow through the gap is optically thin to X-rays escaped from the boundary layer, and the emergent spectrum can be hard. However, it should be noted that this depends on the angle of the incidence of the infalling matter assumed. For large angles of incidence, the emission from the boundary layer can be close to blackbody spectra [Alme and Wilson, 1973].

The width of the belt is about the 1 km or less (for accretion rates not too large), but it depends on the thickness of the infalling flow Kluzniak and Wilson [1991]. Abramowicz et al. [1978] shows the existence of the cusp of the equipotential surface with the presence of the ISCO, resulting in the sharp cusp on the inner edge of the accreting disk. Thus the thickness of the disk can be forced to be small near the ISCO, until the inner part of the disk reaches the local Eddington limit (at this point, the radial velocity of the accretion flow is large so that the ISCO effect is negligible).

Inogamov and Sunyaev [1999] modeled the boundary layer in a quite different way from others. In their models, the accreting material touches the NS surface with Keplerian rotation velocity and is decelerated by friction against the dense, slowly rotating neutron star surface. The energy release takes place on the stellar surface in a latitudinal belt whose width increases with the accretion rate. In such a model, the boundary layer is treated as part of the star rather than part of the disk. There are two latitudinal rings of enhanced brightness, which are symmetric about the equator in the upper and lower hemispheres and shift from the equatorial zone to higher latitudes as the accrete rate increases. The radiating belt broadens as the accretion rate increases. The extra high frequency noise near 1 kHz seen only in the power density spectrum of the accreting NS (not in the BHs) can be attributed to such a spreading layer [Sunyaev and Revnivtsev, 2000].

In all the above models, the magnetic field is assumed to be dynamically unimportant. To see how weak the magnetic field should be to have the above pictures relevant, we can compare the Alfvén radius r_{A}, the radius at which the magnetic pressure is roughly the sum of the ram and gas pressure, with the radius of the NS. It is roughly [Frank et al., 1985, Equation 6.20]

$$r_{\mathrm{A}} \sim 15 k_{\mathrm{A}} \left(\frac{M}{M_{\odot}}\right)^{1/7} \left(\frac{r_{*}}{10\ \mathrm{km}}\right)^{10/7} \left(\frac{L}{10^{37}\ \mathrm{erg/s}}\right)^{-2/7} \left(\frac{B}{10^{8}\ \mathrm{G}}\right)^{4/7}\ \mathrm{km}, \tag{3.20}$$

where B is the magnetic field strength at the surface of the NS and k_{A} is the correction from the spherical accretion to the disk accretion and is about 0.5. Thus, if the magnetic field is weaker than 10^{8} G, it would become dynamically unimportant if the luminosity is above about 10^{37} erg/s.

3.2 X-ray emission mechanisms

In the following I introduce the typical spectra seen in the X-ray binaries and explain their emission mechanisms. Only the blackbody and inverse Compton scattering spectra are extensively used in this thesis. Others are included for completeness. In X-ray wavelength, the radiation is normally treated as photons, instead of waves. A photon is characterized by its energy $h\nu$, where h is Planck constant and ν is its frequency, and its direction. Its momentum is given as $p = h\nu/c$. Many processes can produce/absorb photons or modify their properties (energy and/or direction).

3.2.1 Blackbody radiation and multicolor disk blackbody

Blackbody radiation

Thermal radiation, radiation emitted by matter in thermal equilibrium, is common in astrophysics. Blackbody radiation is a special form of thermal radiation, which itself is in thermal equilibrium. The emitting material should be optically thick, and the photons are scattered, absorbed, and re-emitted, many times prior to being emitted from the surface. The specific intensity is given as (unit: W m^{-2} Hz^{-1} sr^{-1})

$$I(\nu,T) = \frac{2h\nu^3}{c^2}\frac{1}{\mathrm{e}^{h\nu/kT}-1}, \tag{3.21}$$

where k is Boltzmann constant. We see that the shape and the magnitude of the specific intensity are uniquely specified when the temperature is defined. It is possible to have a gray body which emits a spectrum of blackbody shape but of less intensity, but this is not blackbody radiation. We can calculate the flux from a blackbody surface of unit area

$$F = \int_{\theta=0}^{\pi/2}\int_{\phi=0}^{2\pi}\int_{\nu} I(\nu,T)\cos\theta\sin\theta \mathrm{d}\nu\mathrm{d}\theta\mathrm{d}\phi = \sigma T^4, \tag{3.22}$$

where $\sigma = \frac{2\pi^5k^4}{15c^2h^3} = 5.670^{-8}$ W m^{-2} K^{-4}, the Stefan-Boltzmann constant. The radiation pressure inside the blackbody medium is

$$P = \int_{\theta=0}^{\pi/2}\int_{\phi=0}^{2\pi}\int_{\nu} \frac{I(\nu,T)}{c}2\cos^2\theta\sin\theta \mathrm{d}\nu\mathrm{d}\theta\mathrm{d}\phi = \frac{aT^4}{3}, \tag{3.23}$$

where $a \equiv 4\sigma/c$.

The peak power happens at ν_{peak} with $h\nu_{\mathrm{peak}} = 2.82kT$, a relation known as Wien Displacement Law. At frequencies significantly less than the peak frequency, the blackbody function varies linearly with the temperature and quadratically with frequency (Rayleigh-Jeans law):

$$I(\nu,T) \approx \frac{2k}{c^2}\nu^2T. \tag{3.24}$$

At frequency $h\nu \gg kT$, we have Wien's law:

$$I(\nu,T) = \frac{2h\nu^3}{c^2}\mathrm{e}^{-h\nu/kT} \tag{3.25}$$

The blackbody specific intensity (or flux σT^4) is the maximum that can be emitted by

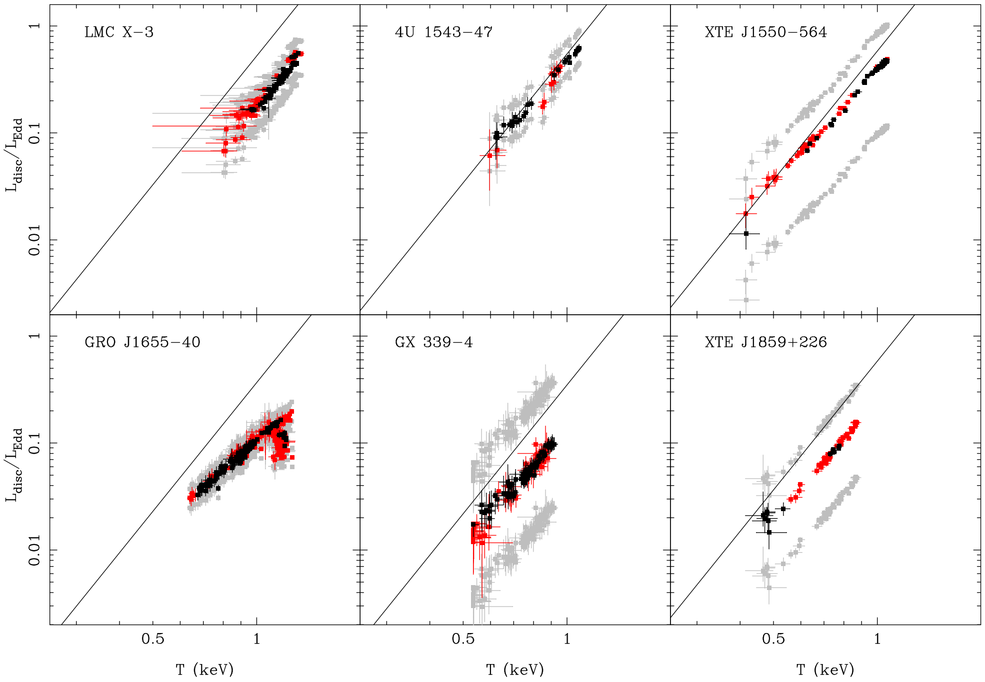

Figure 3-2: Luminosity versus inner disk temperature from the fit of DISKBB to the soft-state spectra of several BH X-ray binaries [Done et al., 2007]. Gray points show the range of uncertainty due to mass and distance estimates. The solid lines are $L \propto T^4$ lines.

a thermal source. The blackbody specific intensity is therefore sometimes called the blackbody limit of specific intensity. As will be introduced below (Bremsstrahlung spectrum), the optically thin emission has a relation: $I(\nu, T) \propto g(\nu, T) n_e n_i \Lambda T^{-1/2} \exp(-h\nu/kT)$ (see Equation 3.30). When the densities of the ions and electrons increase and the cloud is still optically thin, the intensity measured will increase. To some point, it will become optically thick to low frequency, and specific intensity there will reach the blackbody limit. With the increase of the densities, the higher and higher frequencies reach this limit. Finally the cloud becomes optically thick at all frequencies of interest and the spectrum has become identical to the blackbody function.

Here I introduce the concepts of the color temperature T_c and the effective temperature T_eff. T_c characterizes the spectral shape of a spectrum. It can be obtained by fitting the spectral data to a blackbody curve without regard to the magnitude. T_eff is obtained by equating σT_eff^4 to the actual total flux emitted at the source. The ratio of the color temperature to the effective temperature by definition is the color correction factor $f_\mathrm{c} = T_\mathrm{c}/T_\mathrm{eff}$.

The blackbody spectrum with a temperature varying with time is one of the characteristics of type I X-ray bursts. The emission from the boundary layer on the accreting NS can also resemble the blackbody spectrum when the accretion rate is not too low.

Multicolor disk blackbody

The standard accretion disk, which is geometrically thin and optically thick, also emits a blackbody spectrum at each radius whose temperature depends on the radius as Equa-

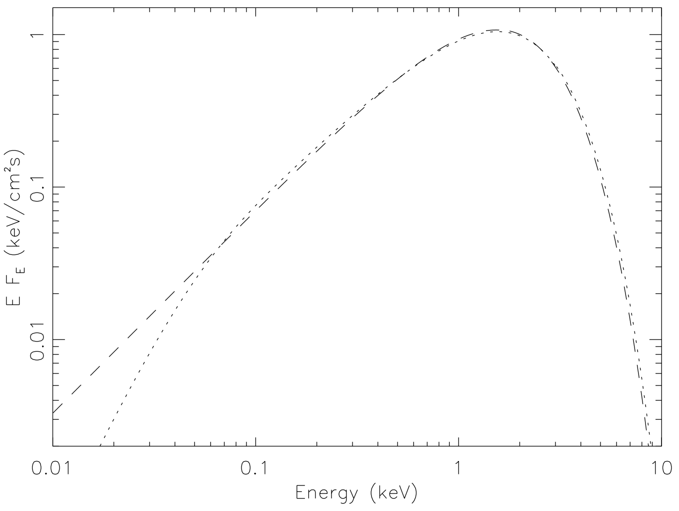

Figure 3-3: Comparison between two XSPEC thermal models DISKBB (dashed line) and DISK (dotted line).

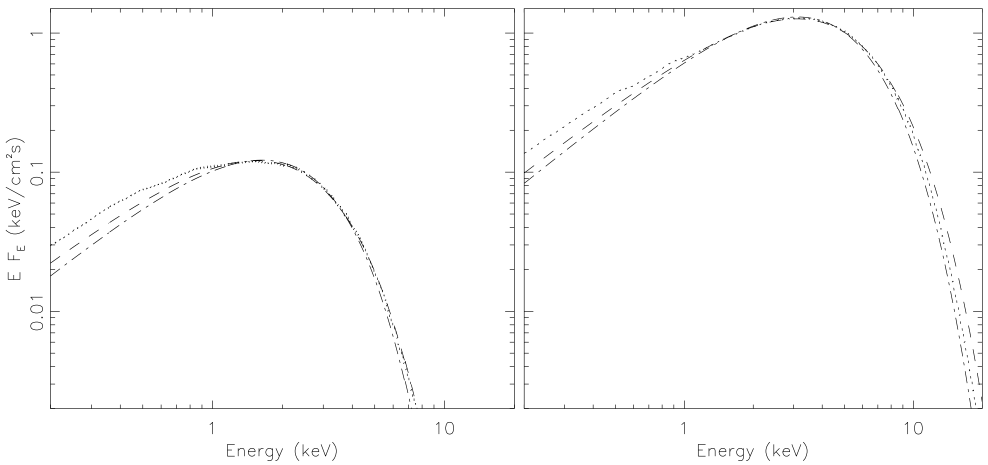

Figure 3-4: Comparison of DISKBB (dot-dashed lines) with relativistic disk models BHSPEC (dotted lines) and KERRBB (dashed lines). The spectra on the left and on the right correspond to $\log(L/L_{\rm Edd}) = -1.5$ and -0.5, respectively.

tion 3.16. Neglecting the term $1-(r_0/r)^{1/2}$ in Equation 3.16, we have $T \propto r^{-3/4}$. The observed spectrum would be

$$F = \frac{\cos\theta}{D^2}\int_{r_{\rm in}}^{r_{\rm out}} 2\pi r I(\nu, T){\rm d}r = \frac{8\pi r_{\rm in}^2\cos\theta}{3D^2}\int_{T_{\rm out}}^{T_{\rm in}}\left(\frac{T}{T_{\rm in}}\right)^{-11/3} I(\nu, T)\frac{{\rm d}T}{T_{\rm in}}, \tag{3.26}$$

where θ is the disk inclination with respect to the line of sight, D is the distance, and the subscripts 'in' and 'out' denote the quantities at the inner and outer boundaries of the disk. Equation 3.26 is implemented as DISKBB in XSPEC, and is also called MCD in this thesis. There are only two parameters for this model, i.e., $T_{\rm in}$ and $r_{\rm in}^2\cos\theta/D^2$. The luminosity of the disk is

$$L_{\rm disk} = \int_{r_{\rm in}}^{r_{\rm out}} 4\pi r\sigma T^4(r){\rm d}r \cong 4\pi r_{\rm in}^2\sigma T_{\rm in}^4, \tag{3.27}$$

assuming $r_{\rm out} \gg r_{\rm in}$. Accreting systems impose a boundary condition on $r_{\rm in}$, e.g., for black holes, the disk is truncated at a constant radius of the ISCO (§3.1.6), and we have $L_{\rm disk} \propto T_{\rm in}^4$ (Figure 3-2). This thesis will show that this also seems to be true for a specific class of accreting NSs, i.e, atoll sources, as well.

The model DISK in XSPEC implements Equation 3.16 without neglecting the term $1-(r_0/r)^{1/2}$. This model requires four parameters, i.e., $L/L_{\rm Edd}$ ($L_{\rm Edd}$ is Equation 3.5 with $X = 0.7$), M, r_0, and $2\cos\theta/D^2$. The disk luminosity is $L = GM\dot{M}/2r_0$. The difference between models DISK and DISKBB is minor when fitting actual spectra, and their parameters can be related as follows. $T_{\rm in}$ in model DISKBB is about the maximum temperature in Equation 3.16, which is $(3GM\dot{M}/8\pi\sigma r_0^3)^{1/4}6^{3/2}7^{-7/4} = 1.285(L/L_{\rm Edd})^{1/4}(10\ {\rm km}/r_0)^{1/2}$ keV and is obtained at $r = (49/36)r_0$, while $r_{\rm in} = (7/3)^{1/2}(7/6)^3 r_0$ [Kubota et al., 1998]. Figure 3-3 shows the spectra of models DISKBB and DISK. For model DISK, I assume $M = 1.4M_\odot$, $L = 0.1L_{\rm Edd}$, r_0 at ISCO, $\theta = 0.0$, and $D = 10$ kpc. For model DISKBB, the parameters are obtained using the above relations. From Figure 3-3, we see that significant differences between these two models are only seen below 0.1 keV, an energy range that few X-ray detectors are designed for. Thus neglecting the term $1-(r_0/r)^{1/2}$ in Equation 3.16 is practical, and model DISKBB, which is simpler, is often used.

The real disk spectrum from X-ray binaries should experience strong relativistic effect due to the extreme compactness of the NSs/BHs. There is also the question of radiative transfer, where there is expected to be a hot disk atmosphere that can Comptonize the photons coming out of the disk and modify the disk spectrum. The two commonly used and more realistic disk spectral models are KERRBB [Li et al., 2005] and BHSPEC [Davis and Hubeny, 2006] in XSPEC. Model KERRBB includes all relativistic effects, such as gravitational redshift, frame dragging, Doppler boosting, light bending, and self-irradiation of the disk. Model BHSPEC does not include self-irradiation. One main difference between KERRBB and BHSPEC is the treatment of the hardening effect. KERRBB uses a color-corrected blackbody prescription with the hardening factor being one of its key parameters, while BHSPEC uses stellar atmospheres-like calculations of disk annuli to self-consistently calculate the vertical structure and radiative transfer. Both models have the accretion rate/luminosity and the spin parameter as their key fit parameters.

To compare DISKBB with BHSPEC and KERRBB, I simulated two spectra using model BHSPEC and *Suzaku* responses, with $\log(L/L_{\rm Edd}) = -1.5$ and -0.5, respectively. The other parameters are $M = 1.4M_\odot$, a_*=0 (spin parameter), $\theta = 60°$, $D = 10$ kpc, and the viscosity parameter $\alpha = 0.1$. Then both spectra are fit with KERRBB and DISKBB for the energy range 1.0–10 keV. The results are shown in Figure 3-4. On the whole model, DISKBB can well describe the high energy part of the spectra obtained from simulation of the relativistic models, and this can help us to monitor spectral changes when the mass and distance of the compact object are unknown. The values of $r_{\rm in}$ of DISKBB from fitting the above spectra differ about 10% while the luminosity differs by one order of magnitude. Thus it is nearly constant. However, to relate the best-fitting parameter of DISKBB to the real system parameter, a series of corrections are required [Zhang et al., 1996].

3.2.2 Inverse Compton Scattering

Compton scattering refers to the process in which high energy photons ($h\nu$ comparable to or larger than $m_{\rm e}c^2 = 511$ keV, where $m_{\rm e}$ is the electron mass) will transfer a portion of its momentum and energy to the electron. In the opposite sense, inverse Compton scattering refers to the process in which high-energy electrons transfer momentum to lower-energy photons, boosting the photons to higher energies. The spectrum is generally quite complicated, and mostly depends on the temperature or energy distribution of the seed photons, the temperature, the optical depth τ, and the geometry of the hot plasma. The energy would be changed after emerging from the hot plasma by a factor called Compton y parameter. For the case of non-relativistic thermal electrons, this parameter is given as,

$$y = \frac{4kT_e}{m_e c^2} \max(\tau, \tau^2). \tag{3.28}$$

In this thesis, and also in the X-ray astronomy, inverse Compton scattering is normally referred to as Comptonization. Comptonization is expected to be commonplace in X-ray binaries, because accretion disks are usually accompanied by a hot corona [Shakura and Syunyaev, 1973]. In this thesis, the Comptonization model is approximated by one of the following: a broken power-law model (bknpower in XSPEC, hereafter BPL), a cutoff power-law model (cutoffpl in XSPEC, hereafter CPL), or the Comptonization model by Titarchuk [1994] (CompTT in XSPEC). The CompTT model computes the Comptonization of a Wien input spectrum of seed photons by a hot (single temperature) plasma with a uniform covering geometry. On the other hand, the BPL or CPL model can be considered as a functional approximation for Comptonization under complex conditions or in combination with another radiation process like synchrotron radiation.

3.2.3 Bremsstrahlung

Here I limit the discussion to the thermal Bremsstrahlung emission from an optically thin plasma. A plasma is a cloud of ionized atoms or molecules. To maintain an ionized condition, the plasma must be sufficiently hot. The radiation arises when electrons are accelerated in near collisions with ions and thereby emit photons. In an electron-ion near collision, the less-massive electron undergoes a large acceleration and radiate some of its energy. The emissivity is given by (unit: W m^{-3} Hz^{-1}),

$$j(\nu, T)\ {\rm d}\nu = C_1 g(\nu, T, Z) Z^2 n_e n_i \frac{e^{-h\nu/kT}}{T^{1/2}}\ {\rm d}\nu \tag{3.29}$$

where $C_1 = 6.8 \times 10^{-51}$J m^3 K$^{1/2}$, n_e and n_i are the number densities of electrons and ions respectively, and Z is the atomic number of the ion. The Gaunt factor, $g(\nu, T, Z)$ is a slowly varying function of ν that derives from the exact quantum-mechanical calculation of the electron-ion collisions. If $Z = 1$ and the plasma cloud is uniform, the intensity is

$$I(\nu, T) = \frac{C_1}{4\pi} g(\nu, T) \frac{\exp^{-h\nu/kT}}{T^{1/2}} \Lambda n_e^2, \tag{3.30}$$

where Λ is the extent of the plasma along the light of sight. The Bremsstrahlung spectrum is often seen in the hot gas that envelopes clusters of galaxies.

3.2.4 Synchrotron Emission

Synchrotron radiation is electromagnetic radiation, similar to cyclotron radiation, but generated by the acceleration of ultrarelativistic (i.e., moving near the speed of light) charged particles through magnetic fields. The volume emissivity for the case of a power-law distribution of electrons (with index p) is given by,

$$j(\nu)\mathrm{d}\nu \propto B^{(1-p)/2} \nu^{(p+1)/2}. \tag{3.31}$$

Synchrotron radiation is commonly seen in pulsars. However, this thesis primarily deals with non-pulsing X-ray binaries where synchrotron radiation is not important.

Chapter 4

Evaluating Spectral Models and the X-ray States of Neutron-Star X-ray Transients

Abstract

We analyze the X-ray spectra of the neutron-star (NS) X-ray transients Aql X-1 and 4U 1608-52, obtained with *RXTE* during more than twenty outbursts. Our aim is to properly decompose the spectral components and to study their evolution across the hard and soft X-ray states. We test commonly used spectral models and evaluate their performance against desirability criteria, including $L_X \propto T^4$ evolution for the multicolor disk (MCD) component, and similarity to black holes (BHs) for correlated timing/spectral behavior. None of the classical models for thermal emission plus Comptonization perform well in the soft state. Instead, we devise a hybrid model: for the hard state a single-temperature blackbody (BB) plus a broken power-law (BPL) and for the soft state two thermal components (MCD and BB) plus a constrained BPL. This model produces $L_X \propto T^4$ tracks for both the MCD and BB, and it aligns the spectral/timing correlations of these NSs with the properties of accreting BHs. The visible BB emission area is very small ($\sim 1/16$ of the NS surface), but it remains roughly constant over a wide range of L_X that spans both the hard and soft states. We discuss implications of a small and constant boundary layer in terms of the presence of an innermost stable circular orbit that lies outside the NS. Finally, if the BB luminosity tracks the overall accretion rate, then we find that the Comptonization in the hard state has surprisingly high radiative efficiency, compared to MCD emission in the soft state. Alternatively, if we assume that the radiative efficiency of a jet in the hard state must be less than the MCD efficiency in the soft state, while relaxing presumptions about the accretion rate, then our results may suggest substantial mass outflow in the jet.

This chapter is adapted from the paper "Evaluating Spectral Models and the X-Ray States of Neutron Star X-Ray Transients" by Dacheng Lin, Ronald A. Remillard, & Jeroen Homan, published in The *Astrophysical Journal*, 2007, Vol. 667, p. 1073–1086.

4.1 Introduction

In low-mass X-ray binaries (LMXBs), a neutron star (NS) or stellar-mass black hole (BH) accretes matter from a Roche-lobe filling, low-mass companion star through an accretion disk. X-rays are produced by the inner accretion disk and/or the boundary layer formed by impact of the accretion flow with the NS surface. The luminous and weakly magnetized NS LMXBs are classified into atoll and Z sources based on their X-ray spectral and timing properties [Hasinger and van der Klis, 1989]. In a color-color diagram, Z sources trace out roughly Z-shaped tracks within hours to a day or so. Their X-ray spectra are normally soft in all three branches of the "Z", i.e., most of the flux is emitted below 20 keV. Atoll sources, however, show more dramatic spectral changes, albeit on longer time scales (days to weeks); their spectra are usually soft at high luminosities and hard when they are faint.

Recently, it was found that some atoll sources can also exhibit Z-shaped tracks in the color-color diagram when they are observed over a large range of luminosity [Muno et al., 2002, Gierliński and Done, 2002a]. However, it was noted by several authors [Barret and Olive, 2002, van Straaten et al., 2003, Reig et al., 2004, van der Klis, 2006] that the properties of atoll sources (e.g., rapid X-ray variability, the order in which branches are traced out) are very different from those of the Z sources. The spectral states of atoll sources in the upper, diagonal and lower branches of these Z-shaped tracks are often referred to as the "extreme island", "island", and "banana" states/branches, respectively. However, in this paper we will use the terms "hard", "transitional", and "soft" states, respectively.

The spectral modeling of accreting NSs has been controversial for a long time [see Barret, 2001, for a review]. In the soft state, the spectra are generally described by models that include a soft/thermal and a hard/Comptonized component. Based on the choice of the thermal and Comptonized components, there are two classical models, often referred to as the *Eastern* model [after Mitsuda et al., 1989] and the *Western* model [after White et al., 1988]. In the *Eastern* model, the thermal and Comptonized components are described by a multicolor disk blackbody (MCD) and a weakly Comptonized blackbody, respectively. In the *Western* model, the thermal component is a single-temperature blackbody (BB) from the boundary layer and there is Comptonized emission from the disk. The color temperature for the thermal component (i.e., the temperature at the inner disk radius $kT_{\rm mcd}$ for a disk model or $kT_{\rm bb}$ for a boundary layer model) is typically in the range of $\sim$ 0.5–2.0 keV [e.g., Barret et al., 2000, Oosterbroek et al., 2001, Di Salvo et al., 2000a, Iaria et al., 2005]. For the Comptonized component, the same authors reported a plasma temperature of $\sim$ 2–3 keV and a large optical depth of $\sim$ 5–15 in the soft state (for a spherical geometry).

In the hard state, the spectra are dominated by a hard/Comptonized component, but a soft/thermal component is generally still required [Christian and Swank, 1997, Barret et al., 2000, Church and Balucińska-Church, 2001, Gierliński and Done, 2002b]. The thermal component can be either a BB or a MCD, but the latter seems to be ruled out by the inferred inner disk radii that are unphysically small. The color temperature of this component is typically $\lesssim$ 1 keV [e.g., Barret et al., 2003, Church and Balucińska-Church, 2001]. The inferred plasma electron temperature of the Comptonized component is typically a few tens of keV and its optical depth is $\sim$ 2–3 in the hard state (for a spherical geometry). The hard state of atoll sources is considered by some authors to be associated with a steady jet [e.g., Fender, 2006, Migliari and Fender, 2006]. The inverse Compton spectrum could then arise from the base of the jet, and synchrotron emission would contribute seed photons and perhaps a secondary contribution to the X-ray spectrum [Markoff et al., 2005].

In the past, various approaches have been made to further our understanding of X-ray spectra of accreting NSs. These include: (1) spectral surveys of a large number of sources, covering a wide range of luminosities [Church and Balucińska-Church, 2001, Christian and Swank, 1997], (2) detailed studies of a large number of observations from a single outburst of a NS X-ray transient [Gierliński and Done, 2002b, Maccarone and Coppi, 2003b, Maitra and Bailyn, 2004], (3) Fourier frequency resolved X-ray spectroscopy [Gilfanov et al., 2003, Olive et al., 2003], and (4) comparisons of spectral and timing properties to those of BH LMXBs, to understand which features might be the result of the presence/absence of a solid surface [Wijnands, 2001, Barret, 2001, Done and Gierliński, 2003]. However, a general consensus on the appropriate X-ray spectral model for the various subtypes and states of accreting NSs has not been achieved.

In this paper we present an extensive study of a large number of observations of two NS transients Aql X-1 and 4U 1608-52, using data obtained with the *Rossi X-ray Timing Explorer* [*RXTE* , Bradt et al., 1993], during more than twenty individual outbursts. There are several advantages of using this archive. First, it allows us to compare the evolution of spectral properties of different outbursts systematically. Second, we can examine the behavior of a specific spectral component with changes in accretion rate, capitalizing on the wide range in luminosity exhibited by these atoll-type transients. Third, compared with surveys using just a few observations but many sources, we can reduce the problems due to our poor knowledge of the parameters of the sources (e.g., the distance, inclination, and absorption).

The goal of this paper is to find a spectral model that can well describe the X-ray spectra of NS X-ray transients. Although the NS X-ray transients often change luminosity by several orders of magnitude and show substantial diversity in outbursts, their well organized color-color and color-intensity diagrams clearly show that their spectral evolution tracks are narrow and thus repeatable. This compels the efforts to unlock spectral models for NS systems to explain the well-behaved sources in terms of accretion physics, and also to further investigate the differences and similarities between BHs and NSs.

Aql X-1 and 4U 1608-52 have been classified as atoll sources [Hasinger and van der Klis, 1989, Reig et al., 2000]. Recently, Reig et al. [2004] and van Straaten et al. [2003] analyzed the general timing properties of these two sources. Here we will concentrate on their spectral properties. We describe our data reduction scheme in §4.2 and show the long-term light curves and color-color diagrams in §4.3. We perform and evaluate detailed spectral modeling in §4.4. In §4.5, we compare timing properties with BHs in order to further evaluate the spectral models. We argue that a particular model is most suitable for these NS transients, and then we further explore the ramifications of this model for X-ray states and the physical properties of accretions in §4.6 and §4.7. Finally we give our summary and discussion.

4.2 Observations and data reduction

For our analysis, we used all of the available *RXTE* observations of Aql X-1 and 4U 1608-52 prior to 2006 January 1. Data were analyzed from the Proportional Counter Array [PCA; Jahoda et al., 1996] and the High Energy X-ray Timing Experiment [HEXTE; Rothschild et al., 1998] instruments. We utilized the best-calibrated detector units of each instrument, which are Proportional Counter Unit 2 (PCU 2) for the PCA and Cluster A for the HEXTE, and we extracted the average pulse-height spectra, one for each *RXTE* observation. All spectral extractions and analyses utilized the FTOOLS software package version 6.0.4. Some standard criteria were used to filter the data: data of 20 seconds before and 200 seconds after type I X-ray bursts were excluded [see Remillard et al., 2006a]; the earth-limb elevation angle was required to be larger than 10°; the spacecraft pointing offset was required to be $< 0.02°$. For faint observations, we additionally excluded data within 30 minutes of the

Table 4.1. X-ray Sources and Observations Prior to 2006 January 1

Source name	number of total/used observations	Time of total/used observations (ks)	$N_{\rm H}$ (10^{22}cm^{-2})	Distance (kpc)
Aql X-1	393/333	1402/1252	0.5	5
4U 1608-52	523/459	1310/1204	1.0	3.6

peak of South Atlantic Anomaly passage or with large trapped electron contamination.

We only considered observations that yielded data from the PCA, HEXTE and relevant spacecraft telemetry. Only observations with PCA intensity (background subtracted) larger than 10 counts/s/PCU were used. We required the exposure of the spectra to be larger than five minutes for faint observations (source intensity lower than 40 counts/s/PCU) and two minutes for bright observations. Appropriate faint/bright background models were used when the source had intensity lower or higher than 40 counts/s/PCU. For the PCA, the spectra were extracted from "standard 2" data collection mode and the response files were created so that they were never offset from the time of each observation by more than 20 days. For the HEXTE, the program HXTLCURV was used for spectral extraction, background subtraction, and deadtime correction. Finally, we applied systematic errors of 0.8% for PCA channel 0–39 (about below 18 keV) and 2% for PCA channel 40–128 [Kreykenbohm et al., 2004, Jahoda et al., 2006]. No systematic errors were applied for HEXTE data. A summary of the observations and other source properties is given in Table 4.1. All further analyses and spectral fits were uniformly applied to each selected observation.

4.3 Light curves and color-color diagrams

The long-term light and color curves of Aql X-1 and 4U 1608-52 are shown in Figure 4-1. This figure combines data from the PCA and the *RXTE* All-Sky Monitor [ASM; Levine et al., 1996]. Typically, outbursts start in the hard state, evolve to the soft state, and finally return to the hard state during the decay. However, outbursts can be quite different from each other, e.g., in amplitude and duration. Moreover, in some outbursts the source did not enter the soft state.

For each observation we calculated X-ray colors, in a manner similar to Muno et al. [2002]. Soft and hard colors were defined as the ratios of the background-subtracted counts in the (3.6–5.0)/(2.2–3.6) keV bands and the (8.6–18.0)/(5.0–8.6) keV bands, respectively. We normalized the raw count rates from each PCU with the help of observations of the Crab Nebula. For each PCA gain epoch, we computed linear fits (vs. time) to normalize the Crab count rates to target values of 550, 550, 850, and 570 counts/s/PCU in these four energy bands. The normalized color-color and color-intensity diagrams in Figure 4-2 resemble those in Muno et al. [2002], although our figure includes more data and we used a different normalization scheme for the softest energy bands. Although these two sources are atoll sources, their tracks in the color-color diagrams are Z-shaped, owing to their large range of luminosities. We combined the hard color and PCA intensity to pragmatically define the source states as shown in Figure 4-2. The hard state has a hard color > 0.65 (Aql X-1) or > 0.6 (4U 1608-52); the soft state has a PCA intensity > 400 counts/s/PCU and a hard

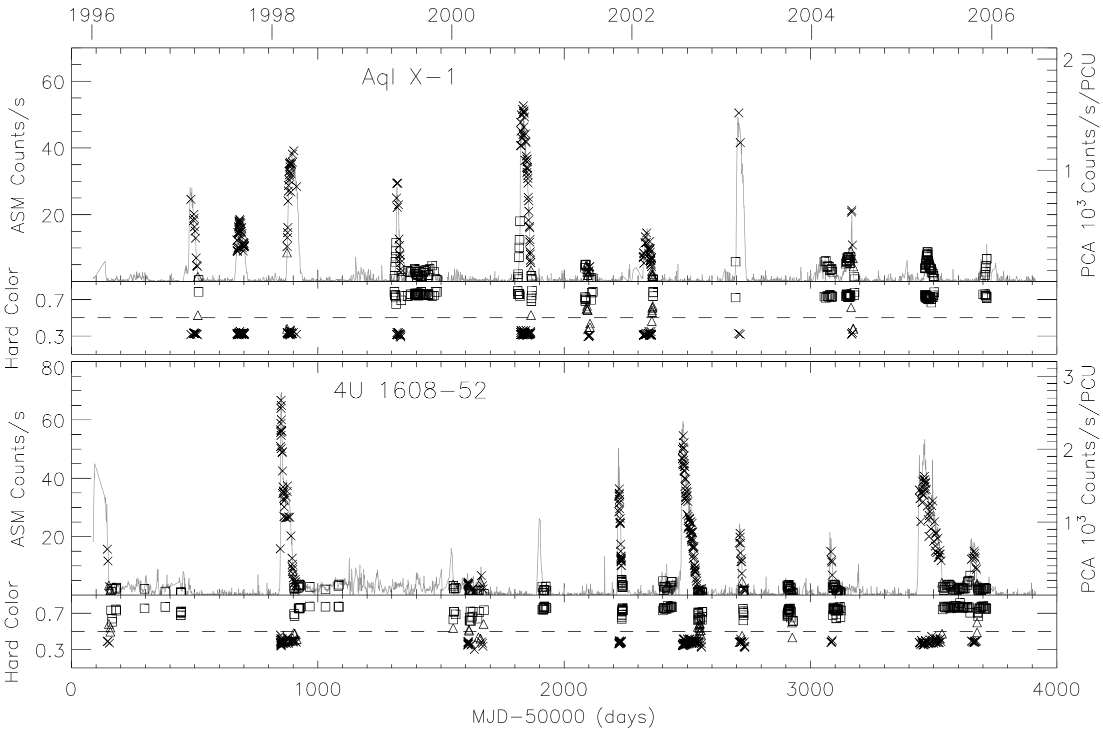

Figure 4-1: Long-term light and color curves of Aql X–1 and 4U 1608–52, showing a large variety of outburst properties. Grey solid lines are from *RXTE* ASM and discrete symbols are from PCA observations representing different spectral states: hard (square), transitional (triangle), and soft (cross). The dashed line (hard color = 0.5) is a reference to help distinguish the different states.

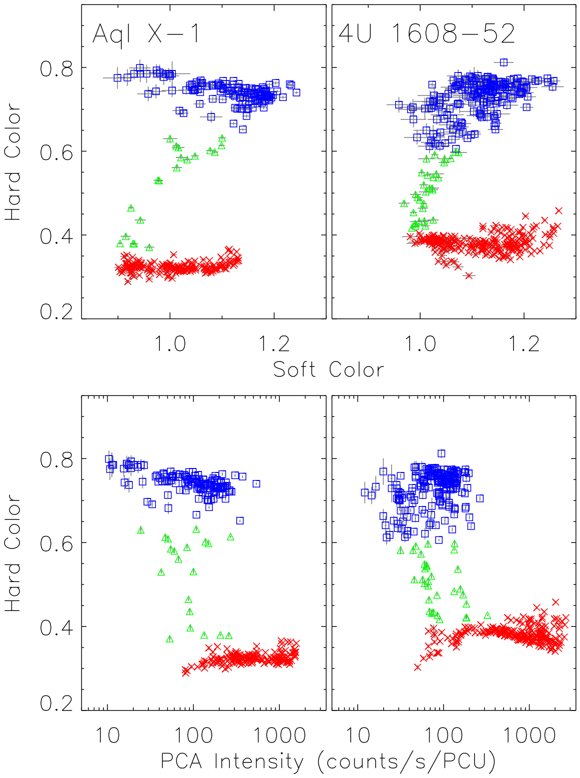

Figure 4-2: Normalized color-color and color-intensity diagrams of Aql X–1 and 4U 1608–52 from ten years of pointed *RXTE* PCA observations. The PCA intensity is the total count rate from PCU2. The hard, transitional, and soft states are represented by blue squares, green triangles, and red crosses, respectively. The uncertainties are at 1 σ confidence and are normally smaller than the symbol size.

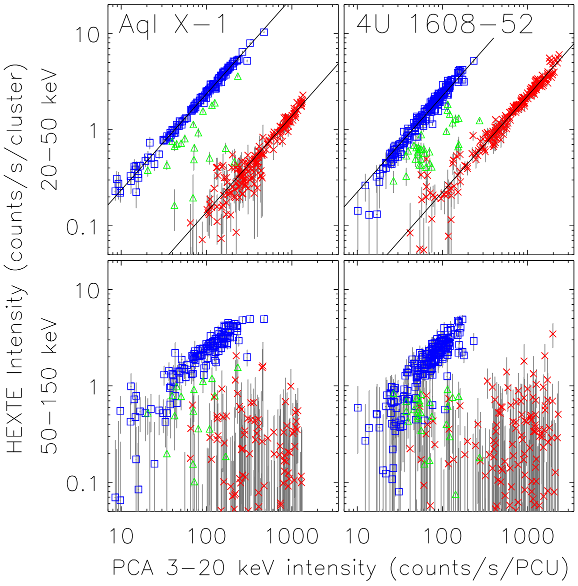

Figure 4-3: The HEXTE intensity in two hard energy bands versus the PCA intensity at 3–20 keV. The solid lines show linear fits for these measurements. The hard and soft states appear increasingly different when they are compared using more widely spaced energy bands.

color < 0.5 or a PCA intensity < 400 counts/s/PCU and a hard color < 0.36 (Aql X-1) or < 0.41 (4U 1608-52). All of the remaining observations are referred to as the transitional state. For all figures in this paper, the hard, transitional, and soft states are represented by blue squares, green triangles, and red crosses, respectively. We note that strong hysteresis is observed in both sources, that is, the hard-soft transition generally occurs at higher X-ray flux compared to the soft-hard transition [e.g., Maccarone and Coppi, 2003a]. The transitional-state observations are mostly from the decay phases of the outbursts, since the rise is often sparsely covered.

Figure 4-3 shows the relation of source intensities in more widely spaced energy bands. The top panels are the HEXTE 20–50 keV intensity versus the PCA 3–20 keV intensity. The most striking aspect of these panels is that there are two nearly linear tracks corresponding to the soft and hard states. The bottom panels are the HEXTE 50–150 keV intensity versus the PCA 3–20 keV intensity. We can still see the linear track in the hard state, but the sources are generally not detected above 50 keV in the soft state.

While the light curves in Figure 4-1 show substantial diversity in outburst amplitude and duration for a given source, Figures 4-2 and 4-3 show that the superposition of all observations on color-color and color-intensity diagrams shows well organized spectral states and very common behaviors in these two sources. The aim of this paper is to capitalize on this organization and the comprehensive *RXTE* data archive, in order to determine the best way to model the X-ray spectra across these different states.

Table 4.2. The spectral models

	Hard State			Soft/Transitional State		
Model #[a]	Description	$\chi^2_\nu(\sigma)$[b]	Problems[c]	Description	$\chi^2_\nu(\sigma)$[b]	Problems[c]
1	BPL+MCD	0.93(0.21),0.88(0.16)	R	BPL+MCD	0.99(0.38),1.07(0.36)	R L P
$2_{\rm cold}$	CompTT+MCD	1.00(0.28),0.90(0.17)	R	CompTT+MCD	1.04(0.39),0.93(0.25)	R L P
$2_{\rm hot}$	CompTT+MCD	...	R	CompTT+MCD	...	L P
3	BPL+BB	0.94(0.21),0.90(0.17)	—	BPL+BB	1.06(0.41),1.24(0.49)	P
$4_{\rm cold}$	CompTT+BB	0.99(0.24),0.93(0.19)	—	CompTT+BB	0.95(0.33),0.90(0.25)	P
$4_{\rm hot}$	CompTT+BB	...	T	CompTT+BB	...	T P
5[d]	...	...	...	MCD+BB	1.23(0.36),1.17(0.38)	...
6	BPL+BB	0.94(0.21),0.90(0.17)	—	MCD+BB+CBPL	1.15(0.30),1.02(0.27)	—

Note. — All models also include an interstellar absorption component and a Gaussian line. The notations BPL, MCD, BB and CompTT refer the bknpower, diskbb, bbodyrad, and comptt models in XSPEC, respectively. CBPL is a constrained BPL with the break energy $E_{\rm b}$ fixed at 20 keV and the initial photon index Γ_1 forced to be smaller than 2.5. "..." means that the information is not available or meaningless because the corresponding model does not work. "—" means that none of the four problems listed in §4.4.2 is found to apply to the corresponding model/spectral state.

[a] The subscripts cold and hot denote the cold-seed-photon models and hot-seed-photon models, respectively.

[b] The mean χ^2_ν and standard deviation. The two columns are for Aql X–1 and 4U 1608–52, respectively.

[c] See §4.4.2 for the meanings of these characters.

[d] Only observations in the soft state are fitted with this model. The mean χ^2_ν for this model is from observations with source intensity > 800 counts/s/PCU.

4.4 Spectral modeling

4.4.1 Spectral models and assumptions

In this work, we fitted the X-ray spectra of Aql X-1 and 4U 1608-52 with several different models. The PCA and HEXTE pulse-height spectra were fitted jointly over the energy range 2.6–23.0 keV and 20.0–150.0 keV, respectively, allowing the normalization of the HEXTE spectrum, relative to the PCA spectrum, to float between 0.7 and 1.3. For soft-state observations, HEXTE spectra were used up to 50 keV because the flux at higher photon energies was negligible (Figure 4-3).

In the typical description of the NS continuum spectra, some form of pure thermal radiation is often combined with another radiation process, commonly presumed to be some form of Comptonization, although synchrotron radiation might also be involved (§1). Hereafter, we simply refer to emission other than the pure thermal radiation as the "Comptonized" component. Two forms of thermal radiation were considered: BB and MCD models (bbodyrad and diskbb in XSPEC respectively). The BB model provides the color temperature ($kT_{\rm bb}$) and the apparent radius ($R_{\rm bb}$; isotropic assumption) of the BB emission area, while the MCD model provides the apparent inner disk radius ($R_{\rm mcd}$) and the color temperature at the inner disk radius ($kT_{\rm mcd}$).

As for the modeling of the Comptonized component, we considered both a broken power-law model (bknpower in XSPEC, hereafter BPL) and the Comptonization model by Titarchuk [1994] (CompTT in XSPEC). The CompTT model computes the Comptonization of a Wien input spectrum of "seed photons" by a hot (single temperature) plasma with a uniform covering geometry. On the other hand, the BPL component can be considered as a

Table 4.3. Best-fitting parameters of two sample spectra

Data	Model	kT_s keV	kT_e keV	τ	$kT_\mathrm{mcd}, kT_\mathrm{bb}$ keV	$N_\mathrm{mcd}, N_\mathrm{bb}$	χ^2_ν(d.o.f)
Hard-state sample	CompTT+MCD(cold)	$\lesssim 0.35$	$14.3^{+1.0}_{-0.9}$	$6.07^{+0.36}_{-0.36}$	$1.79^{+0.07}_{-0.08}$	$1.7^{+0.3}_{-0.3}$	1.49(78)
Hard-state sample	CompTT+MCD(hot)	$1.16^{+0.08}_{-0.12}$	$15.5^{+1.2}_{-1.0}$	$5.54^{+0.32}_{-0.32}$	$1.00^{+0.05}_{-0.09}$	$44.8^{+17.2}_{-10.7}$	1.32(78)
Hard-state sample	CompTT+BB(cold)	$\lesssim 0.4$	$15.0^{+1.0}_{-0.9}$	$2.53^{+0.14}_{-0.14}$	$1.21^{+0.04}_{-0.04}$	$8.9^{+1.7}_{-1.5}$	1.25(78)
Hard-state sample	CompTT+BB(hot)	$1.03^{+0.12}_{-0.18}$	$16.6^{+1.3}_{-1.1}$	$2.24^{+0.14}_{-0.14}$	$0.67^{+0.05}_{-0.05}$	$227.9^{+63.1}_{-44.0}$	1.59(78)
Soft-state sample	CompTT+MCD(cold)	$\lesssim 0.5$	$2.5^{+0.1}_{-0.1}$	$16.6^{+8.5}_{-2.5}$	$1.70^{+0.08}_{-0.06}$	$68.7^{+22.6}_{-15.7}$	1.27(53)
Soft-state sample	CompTT+MCD(hot)	$1.02^{+0.02}_{-0.03}$	$2.6^{+0.1}_{-0.1}$	$10.1^{+0.3}_{-0.3}$	$\lesssim 0.7$	...	0.95(53)
Soft-state sample	CompTT+BB(cold)	$\lesssim 0.5$	$2.5^{+0.1}_{-0.1}$	$6.08^{+0.25}_{-0.29}$	$1.24^{+0.04}_{-0.04}$	$164.1^{+27.9}_{-25.4}$	1.07(53)
Soft-state sample	CompTT+BB(hot)	$1.02^{+0.03}_{-0.04}$	$2.6^{+0.1}_{-0.1}$	$4.66^{+0.16}_{-0.16}$	$\lesssim 0.5$	...	0.95(53)

Note. — The detailed information of these two spectra are given at the beginning of §4.4.2 and their unfolded spectra are shown in Figures 4 and 5. The notations "cold" and "hot" refer to the cold and hot-seed-photon models respectively (see §4.4.2). For CompTT+MCD models, a spherical geometry was assumed for CompTT component, while for CompTT+BB models, a disk geometry was assumed instead. N_mcd and N_bb are normalizations (in unit of km^2 at distance 10 kpc) of MCD and BB, respectively.

functional approximation for Comptonization under complex conditions or in combination with another radiation process like synchrotron radiation. We gave these two models an equal opportunity to handle the effects of Comptonization when we tested different kinds of spectral decomposition. Thus BPL or CompTT was combined with BB and/or MCD in a variety of ways, as summarized in Table 4.2. The BPL model has four parameters: two photon indices, a break energy (E_b) and a normalization parameter. The CompTT model is parametrized by the seed-photon temperature (kT_s), the plasma electron temperature (kT_e), the optical depth (τ), a parameter describing the geometry of the Comptonizing cloud (either spherical or disk-like), and a normalization parameter.

All models also included a Gaussian line. Its central line energy was constrained to be between 6.2–7.3 keV, targeting the Fe line 6.4 keV [Asai et al., 2000]. The average best-fitting value was ~ 6.6 keV for both sources. The intrinsic width of the Gaussian line (σ) was fixed at 0.1 keV. This is consistent with the *ASCA* result of Church and Balucińska-Church [2001]. The PCA has energy resolution ~ 1 keV, limiting the need for a precise value. An interstellar absorption component was also included with the hydrogen column fixed at $N_\mathrm{H} = 0.5 \times 10^{22}$ cm^{-2} for Aql X-1 [Church and Balucińska-Church, 2001] and 1.0×10^{22} cm^{-2} for 4U 1608-52 [Penninx et al., 1989]. Since no eclipses or absorption dips have been observed, the two sources are likely not high-inclination systems and we assumed their binary inclinations to be 60°. We scaled the luminosity and radius related quantities using distances of 5 kpc for Aql X-1 [Rutledge et al., 2001] and 3.6 kpc for 4U 1608-52 [Natalucci et al., 2000], unless indicated otherwise.

4.4.2 Comptonized + thermal two-component models

The problem of model degeneracy

First we consider models with two continuum components: one is Comptonized and the other is thermal (Models 1–4 in Table 4.2). It turns out that the spectral fitting is inherently non-unique. To illustrate the contribution of each component and the problem of model degeneracy, we use two observations of Aql X-1. One is a hard-state observation on

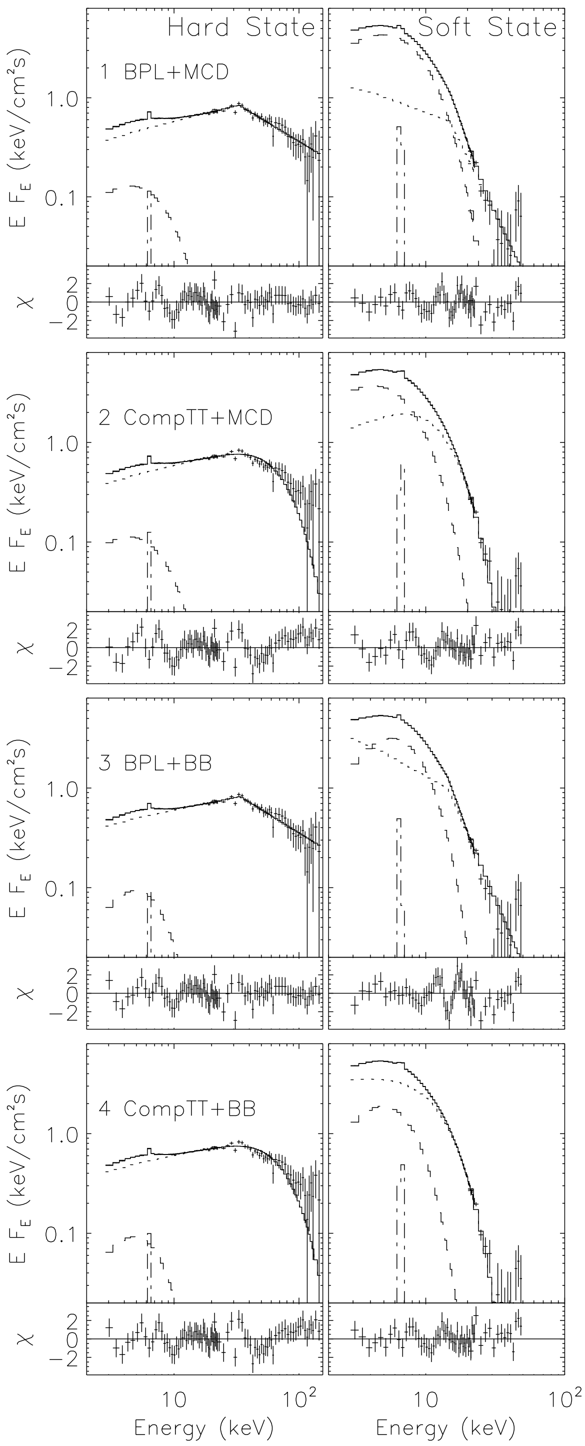

Figure 4-4: The unfolded spectra and residuals of two sample observations of Aql X–1 using different kinds of models. One is in the hard state and the other in the soft state. The panels for models with CompTT are from spectral fits with seed-photon temperatures $\lesssim$ 0.5 keV (cold-seed-photon models). The total model fit is shown as a solid line, the Comptonized component as a dotted line, the thermal component as a dashed line, and the Gaussian line as a dot-dashed line.

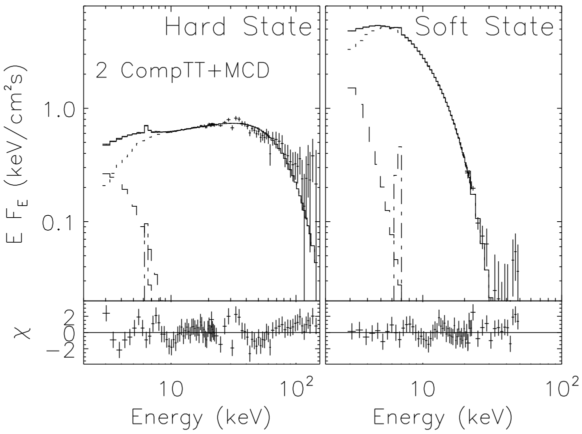

Figure 4-5: The unfolded spectra and residuals of two sample observations of Aql X–1 with best-fitting $kT_\mathrm{s} \gtrsim 1$ keV using Model CompTT+MCD (hot-seed-photon model). The total model fit is shown as a solid line, the Comptonized component as a dotted line, the thermal component as a dashed line, and the Gaussian line as a dot-dashed line.

2004 February 21 (hard color 0.73, intensity 178.5 counts/s/PCU), the other is a soft-state observation on 2000 October 27 (hard color 0.33, intensity 1262 counts/s/PCU).

Figures 4-4 and 4-5 show the unfolded spectra of these two observations using different Comptonized + thermal models. All models give acceptable spectral fits, despite the fact that the spectra each contain well over 10^6 counts. Figure 4-4 shows that there is not only degeneracy from the choice of the thermal component (i.e., BB or MCD), but also from the choice of the Comptonized component (i.e., BPL or CompTT). Moreover, even if we choose Model CompTT+MCD or CompTT+BB, there are still two competing χ^2 minima, one with best-fitting $kT_\mathrm{s} \lesssim 0.5$ keV and the other with best-fitting $kT_\mathrm{s} \gtrsim 1$ keV. Their corresponding unfolded spectra can be seen in Figures 4-4 and 4-5, respectively. Table 4.3 gives the detailed results using the CompTT+MCD and CompTT+BB models for our two representative spectra. Hereafter, we call models with best-fitting $kT_\mathrm{s} \gtrsim 1$ keV "hot-seed-photon models" and models with best-fitting $kT_\mathrm{s} \lesssim 0.5$ keV "cold-seed-photon models". Hot-seed-photon models require that the modeling of the Comptonized component takes into account the spectral curvature expected from having the seed photons close to the observed bandpass [Done et al., 2002]. We note that the temperature of the chosen thermal component increases and its normalization decreases significantly when the seed-photon model flips from the hot to cold solution, for a given observation.

Examination of the other observations shows that this seed-photon problem is quite general. CompTT+MCD and CompTT+BB models (Table 4.2) yield two solutions each: photon temperature $kT_\mathrm{s} \gtrsim 1$ keV and $kT_\mathrm{s} \lesssim 0.5$ keV. The inferred parameters of the thermal component are also quite different (Table 4.3 and references following). For the soft-state observations, the inferred temperature of the thermal component is typically > 1 keV for the cold-seed-photon models [e.g., Barret et al., 2000, Oosterbroek et al., 2001, White et al., 1988]. Otherwise, if the hot-seed-photon models are used, the temperature of the thermal component is normally < 1 keV and thus less than kT_s [e.g., Di Salvo et al., 2000a,b, Iaria et al., 2005]. For the hard-state observations, if BB is used as the thermal component, the size of the BB emission area is typically very small, ~ 2 km, for the cold-seed-photon models [e.g., Barret et al., 2003, Church and Balucińska-Church, 2001, Gierliński and Done, 2002b].

However, with the hot-seed-photon models, the BB emission area can be comparable to the size of the NS [e.g., Barret et al., 2000, Natalucci et al., 2000, Guainazzi et al., 1998]. Replacement of BB with MCD in cold-seed-photon models yields very small inner disk radii as already found by other authors (see references in §1). We also point out that many of the references cited above made use of broad band spectra from *BeppoSAX*. This means that the seed-photon problem is also present for instruments that have extended low-energy spectral coverage (see also Farinelli et al. [2005]). We also analyzed the *BeppoSAX* observations of Aql X-1 and 4U 1608-52 and found the same problem to be present.

The low-energy limit of PCA is 2.3–3.0 keV, depending on the gain setting epoch. We cannot constrain $kT_{\rm s}$ in the cold-seed-photon models because the peak energy flux of the seed-photon spectrum (Wien approximation) is at $3kT_{\rm s} \lesssim 1.5$ keV. On the other hand, for the hot-seed-photon models, the fits to PCA spectra produce a cool thermal component in the soft state making it is difficult to constrain the temperature and normalization of this component, and sometimes the thermal component is even not required [Gierliński and Done, 2002b].

Efforts to resolve model degeneracy

As outlined in the previous section, there is a degeneracy in X-ray spectral models for NS LMXBs. The problem is based on the fact that acceptable fits (χ^2_ν criteria) can be obtained for either the hard or soft states by using any combination of two ambiguous components: a thermal spectrum (BB or MCD) plus a Comptonized component (BPL, hot-seed CompTT, or cold-seed CompTT). The various models convey (very) different pictures for the structures and energetics of NS accretion.

In our descriptions of various model details, we have begun to mention arguments that have been offered to evaluate competing models in terms of physical implications derived from the fitted spectral results. This strategy of performance-based evaluations of spectral models is most effective when there is a self-consistency issue at stake. Multiple evaluation criteria will help us to choose a spectral model that may be superior in overall suitability. Useful considerations can involve single parameters, spectral evolution, and the relationship between the hard and soft states. The comparison between the atoll sources and BHs can provide further constraints on this choice. Below we list one such consideration used in the literature, followed by three considerations offered in this paper. We describe them in term of problems that are encountered in a particular model/spectral state, and we track these problems in the fourth and seventh columns of Table 4.2.

1. "R" problem: the inner disk radius in models with MCD is too small, i.e., much less than the size of the NS [Church and Balucińska-Church, 2001, Gierliński and Done, 2002b].

2. "L" problem: $L_{\rm mcd} \propto T^4_{\rm mcd}$ (i.e., constant inner disk radii) for MCD component is not satisfied for any meaningful range of luminosity in the soft state; We note that BH systems do show $L_{\rm mcd} \propto T^4_{\rm mcd}$ when they are in the soft (thermal) state [Kubota and Done, 2004].

3. "T" problem: $kT_{\rm s} > kT_{\rm bb}$ in models with BB; if we attribute the BB component to the boundary layer and accept that the boundary layer should have a higher temperature than the disk [Mitsuda et al., 1989, Popham and Sunyaev, 2001], $kT_{\rm s}$ seems unlikely to be larger than $kT_{\rm bb}$.

4. "P" problem: the Comptonization fraction is not consistent with the power density spectrum, assuming that a comparison of atoll sources and BHs in timing properties is relevant. We will explain this in more detail in §4.5.

In the definition of the "L" problem, we use the phrase "over some range of luminosity" in recognition of the possibility that the disk may deviate from the MCD's geometric assumptions, as do BH accretion disks at high $L_{\rm mcd}$ [Kubota and Done, 2004]. To help evaluate the "R" problem, we inferred the NS radii of our two sources from the spectral fitting to Type I X-ray bursts (denoted as $R_{\rm burst}$). During the decay phase of some bursts, an approximately constant burst emission area is derived when temporal series of the burst are fitted with a BB model after subtracting the average persistent emission to isolate the burst from other radiation components. Such an emission area is expected to be roughly similar to the apparent size of the NS [Lewin et al., 1993]. Our fits using PCA data gave $R_{\rm burst} \sim 8$ km for Aql X-1 and ~ 7.2 km for 4U 1608-52 (at distances in Table 4.1), which are consistent with previous results [e.g., Koyama et al., 1981, Nakamura et al., 1989]. However, we note that these values are given without any corrections, e.g., hardening factors and surface occultation by the inner disk. These issues are further discussed in §4.6.

Model fit results

We fitted the observations of Aql X-1 and 4U 1608-52 using Models 1–4 in Table 4.2. The PCA does not allow us to gain meaningful constraints on the properties of the (cool) thermal components using the hot-seed-photon models, as explained above. Thus, for models with CompTT, we just show results of cold-seed-photon solutions. In these models, $kT_{\rm s} \ll kT_{\rm e}$ ($kT_{\rm e}$ is typically 2–3 keV in the soft state and several tens of keV in the hard state), and $kT_{\rm s}$ is far below the PCA energy limit. Thus, the Wien approximation of the input seed photon is valid.

The top four rows in Figures 4-6, 4-7 and 4-8 show the fit results for the commonly used Comptonized + thermal models. They correspond to Models 1, $2_{\rm cold}$, 3, and $4_{\rm cold}$ in Table 4.2, where we also list the mean χ^2_ν values. The errors represent 90% confidence limits for a single parameter, and the circled points are those with relatively large errors. There is not only strong similarity between these two sources, but also strong similarity between the results of these four models. The extreme difference of the hard and soft states can also be seen in these plots.

Figure 4-6 shows the variation of the color temperature of the thermal components ($kT_{\rm bb}$ for BB and $kT_{\rm mcd}$ for MCD) with the PCA intensity. All four models show that the temperature of the thermal components of both sources increases with intensity in the hard state. In contrast, the temperature is almost constant (for models with BPL) or decreases (for models with CompTT) with increasing luminosity in the soft state.

Figure 4-7 shows the luminosity of the thermal component versus its color temperature, $kT_{\rm bb}$ or $kT_{\rm mcd}$. For reference, we also show the lines for constant radius, assuming $L_{\rm X} = 4\pi R^2 \sigma T^4$. The NS radii (§4.4.2) are shown with dotted lines in this figure. The dashed lines correspond to $R = 1.9$ km and 1.3 km for Aql X-1 and 4U 1608-52, respectively; they are derived from the fit to the BB radius values obtained from Model 6 (see below). With increasing luminosity in the respective thermal component, $R_{\rm mcd}$ or $R_{\rm bb}$ increases in the soft state. For the case of MCD-related Models 1 and $2_{\rm cold}$, this behavior in the soft state contradicts the basic prediction of the accretion disk model and warrants the "L" problem in Table 4.2. Besides, from the comparison with the $R_{\rm burst}$ lines, we find that the inner

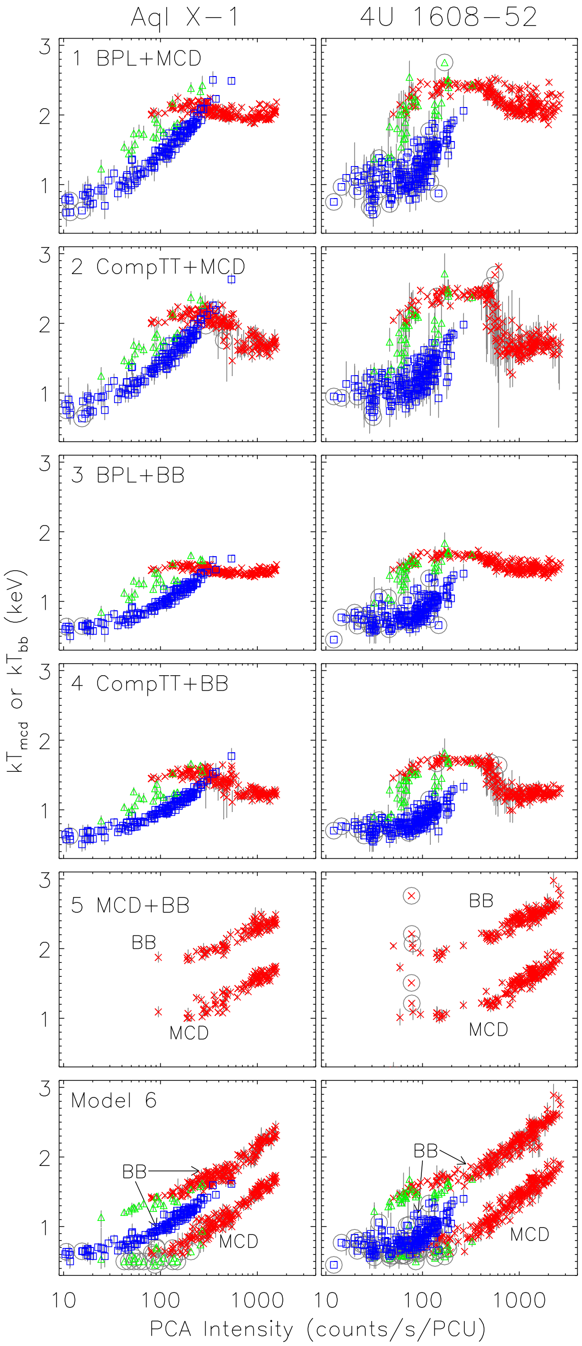

Figure 4-6: Variation of the temperature of the thermal component (kT_{bb} for BB and kT_{mcd} for MCD) with the PCA intensity. Cold-seed-photon solutions are shown for Models with CompTT.

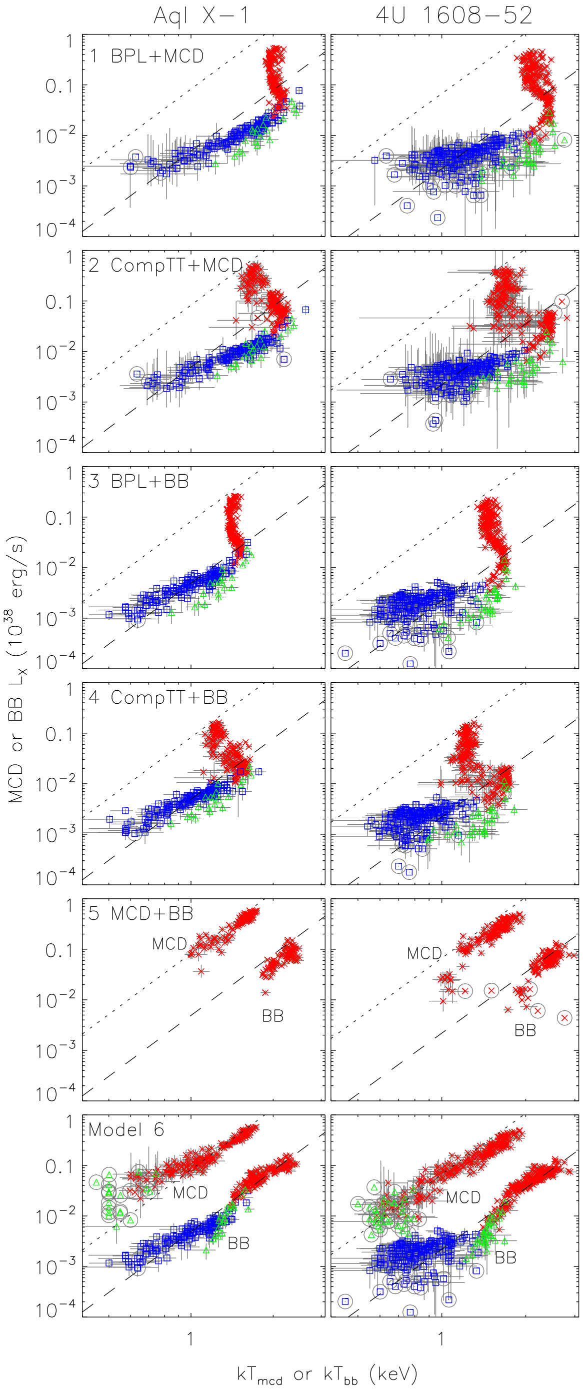

Figure 4-7: The luminosity of the thermal component versus its characteristic temperature. Models 5 and 6 produce luminosity evolution for BB and MCD components in the soft state (red crosses) that are nearly parallel to reference lines, which show $L_X \propto T^4$ with constant emitting surface area. The dotted lines correspond to the NS burst radii (§4.4.2) and the dashed lines correspond to $R = 1.9$ km and 1.3 km for Aql X–1 and 4U 1608–52, respectively, assuming $L_X = 4\pi R^2 \sigma T^4$.

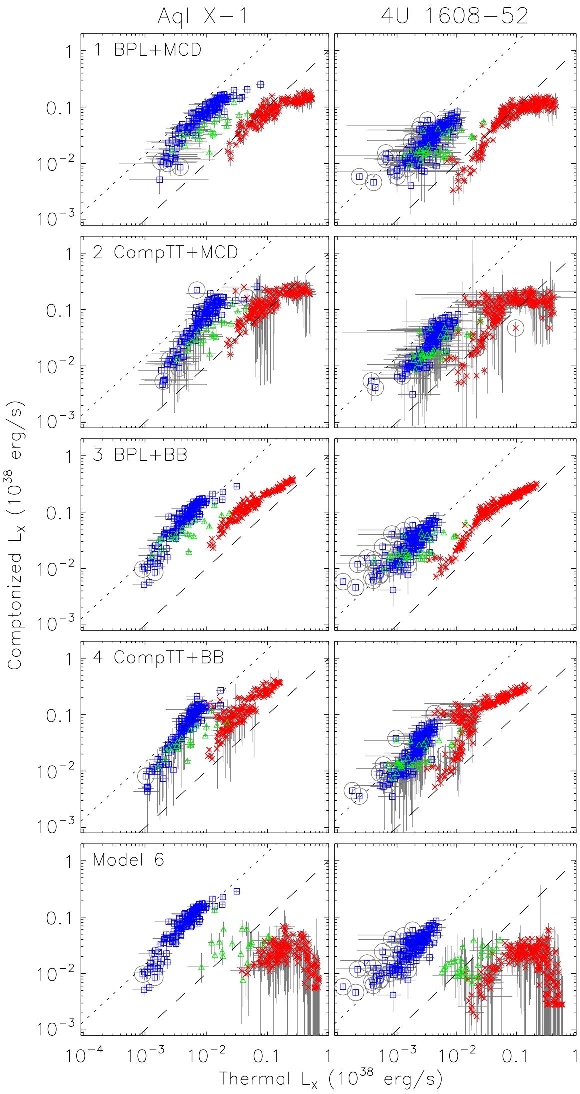

Figure 4-8: The luminosity of the Comptonized component versus the luminosity of the thermal component(s). The dashed and dotted lines are for reference. They connect the points where the ratio of the luminosities of the thermal component and the Comptonized component is 1.0 and 0.07, respectively. The latter is a typical value for the hard state.

disk radius $R_{\rm mcd}$ in the hard state and some part of the soft state is simply too small, even after taking into account expected correction factors (see §4.6). This is consistent with the results of Gierliński and Done [2002b] and Church and Balucińska-Church [2001]. Thus, the "R" problem also applies to these two models.

For BB-related Models 3 and $4_{\rm cold}$, the luminosity evolution of the effective radius is tied to the evolution of the boundary layer, which is much less certain. This is why the "L" problem is not applied to the BB component in Table 4.2. If we attribute the thermal component BB to the boundary layer, it would imply that the boundary layer is measured with almost constant surface area in the hard state, but it spreads out with constant color temperature in the soft state. One possible explanation for the constant color temperature during the spreading of the boundary layer is that the local flux reaches the Eddington limit. The spreading layer model [Suleimanov and Poutanen, 2006] predicts that the color temperature of the boundary layer is ~ 2.4 keV for a NS with $R_{\rm ns} = 15$ km and $M = 1.4 M_\odot$ and solar composition of the accreting matter (smaller $R_{\rm ns}$ would predict higher value). A problem with this interpretation for our results of Model 3 or $4_{\rm cold}$ is that the critical value of the temperature for area expansion is ~ 1.5 keV. Higher temperatures are only seen during Type I X-ray bursts from these two sources with maxima normally > 2.5 keV. Thus, the critical value of the temperature ~ 1.5 keV from Models 3 and $4_{\rm cold}$ does not match expectations for boundary layer spreading. We will show later that these two models are also disfavored from strong similarities of the timing properties between BH and NS LMXBs.

In Figure 4-8 we investigate the luminosity evolution of the Comptonized component (BPL or CompTT) versus the thermal component(s) (BB or MCD or their sum if both are used). For the thermal component the bolometric luminosity is used while for the Comptonized component we integrated from 1 keV to 200 keV for CompTT and from 1.5 keV to 200 keV for BPL. The 1.5 keV lower limit for the BPL integration is chosen so that this component does not extend below the temperature of the MCD in the soft state, i.e., when the BPL is steep and the lower limit matters. The errors of the luminosity of BPL, CompTT and MCD primarily depend on the uncertainties in their respective normalizations. In Figure 4-8 we also show two reference lines: dashed and dotted. They connect the points where the ratio of the luminosities of the thermal component and the Comptonized component is 1.0 and 0.07, respectively. The latter is a typical value for the hard state. In both the hard and soft states, the luminosity of the Comptonized component increases with the luminosity of the thermal component, but the two states follow different tracks. In the soft state, the luminosities of these two components are relatively close to each other, while in the hard state, the luminosity of the thermal component is only $\sim 10\%$ of the Comptonized component.

The uncertainties for the thermal-component luminosity from the hot-seed-photon models are quite large from PCA data in the soft state. However, hot-seed-photon models with BB as the thermal component have the "T" problem (§4.4.2). Hot-seed-photon models with MCD as the thermal component have the "L" problem in the soft state [Gierliński and Done, 2002b, Done et al., 2002] and the "R" problem in the hard state from our investigation (not shown).

Since the luminosity evolution of the thermal component in the soft state is either in violation of the basic model (MCD) or, at best, suspicious (BB), we continued to investigate alternative models such as those in the next section.

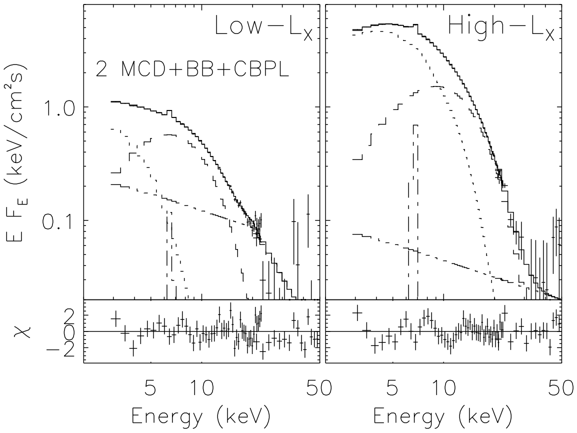

Figure 4-9: The unfolded spectra and residuals of two sample soft-state observations of Aql X–1 using Model 6. The total model fit is shown as a solid line, the MCD component as a dotted line, the BB component as a dashed line, the CBPL component as a dot-dot-dashed line, and the Gaussian line as a dot-dashed line. The high-L_X observation is the same as the sample soft-state observation seen in Figures 4-4 and 4-5. The low-L_X observations is on 1999 June 3 (hard color 0.32, intensity 243 counts/s/PCU).

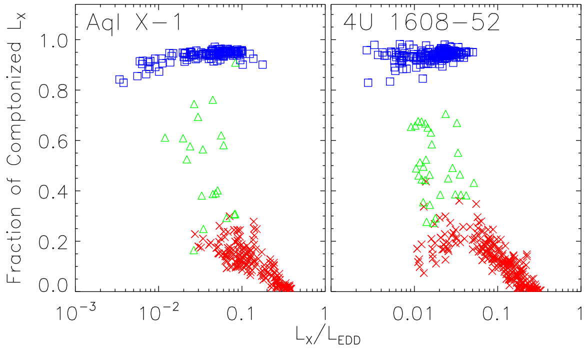

Figure 4-10: The fraction of Comptonized luminosity versus the total luminosity, using Model 6. $L_{\rm EDD} = 1.8 \times 10^{38}$ erg/s, assuming $M_{\rm ns} = 1.4M_\odot$ for both sources.

4.4.3 Double thermal models

Early analyses of NS spectra in the soft state considered the possibility that we might detect thermal components from both the disk and boundary layer [Mitsuda et al., 1984]. This "double thermal" model (i.e., MCD+BB or Model 5 in Table 4.2) was applied to the soft-state observations of Aql X-1 and 4U 1608-52, and the results are shown in the fifth row of panels in Figures 4-6 and 4-7. Data points for this model are omitted when χ^2_ν is > 2 (only for this model). It turns out that this model works very well in the soft state when the luminosity is high, but with the decreasing luminosity, χ^2_ν becomes large. Either source gives a mean $\chi^2_\nu \sim 1.2$ and ~ 3.5 for observations with source intensity > 800 counts/s/PCU and < 500 counts/s/PCU, respectively (also see Table 4.2). However, Model 5 is remarkably successful in its implication that the disk and the boundary layer both remain at constant sizes for a substantial range of luminosity (Figure 4-7). Moreover, the inferred size of the boundary layer is close to that inferred by Models 3 and $4_{\rm cold}$ for the hard state. The failure of Model 5 for soft-state observations at lower luminosity is apparently due to small levels of Comptonization, since the fit residuals are pointing chronically positive at photon energies above 15 keV (PCA data).

Given the interesting luminosity evolution for the soft state with Model 5 (no Comptonization), we added a *weakly Comptonized* component, while continuing to assume that both the MCD and BB are visible in the soft state. The difficulty here is how to model weak Comptonization by adding a third component. Freely adding a BPL or CompTT component is obviously not feasible, because BPL or CompTT plus one thermal component is sufficient to model the entire spectrum as shown by Models 1–4. As a first attempt, we tried several forms of constrained CompTT (e.g., couple $kT_{\rm s}$ to $kT_{\rm bb}$ or $kT_{\rm mcd}$; force $kT_{\rm e} > 10$ keV; or do both), but the fits always yielded large fractions of Comptonization for low-luminosity observations in the soft state. This problem could be due to RXTE's lack of low-energy coverage.

On the other hand, we found that the entire soft state remains weakly Comptonized if we adopt the following constrained BPL (CBPL) model: the break energy is fixed at 20 keV (the best-fitting break energy is typically > 20 keV in the hard state and is ~ 15 keV in the soft state from Models 1 and 3), and the initial photon index is required to be ≤ 2.5 [a typical initial photon index in the soft state of BHs is also about 2.5; Remillard and McClintock, 2006]. Therefore, we define Model 6 as follows: the hard state is still modeled by BPL+BB (no BPL constraints; same as Model 3 for the hard state) and the soft/transitional states are modeled by MCD+BB+CBPL. Figure 4-9 shows the unfolded spectra of two soft-state observations using this model, one at low luminosity and the other at high luminosity.

The bottom row of panels of Figures 4-6, 4-7 and 4-8 show the results obtained for Model 6. Figure 4-6 shows that with the increase in the intensity, $kT_{\rm bb}$ increases both in the hard and soft states, with the tracks that are clearly separated. The BB temperature reaches a maximum ~ 2.5 keV for Aql X-1 and ~ 3.0 keV for 4U 1608-52, similar to the peak temperatures of Type I X-ray bursts from these two sources [Koyama et al., 1981, Nakamura et al., 1989, Galloway et al., 2008]. The temperature at the inner disk radius $kT_{\rm mcd}$ increases from ~ 0.5 to 2.0 keV, also correlated with the intensity.

In Figure 4-7, we see that Model 6 remarkably produces results where $L_{\rm X} \propto T^4$ for both the MCD and BB components in the soft state. Furthermore, the inferred emission areas of the boundary layer from the hard and soft states have essentially the same value. The emission area of the boundary layer is small compared with the size of the NS. We realize that the size of the BB emission area slightly increases with decreasing luminosity in the hard state, especially for 4U 1608-52. However, we note that the BB curve lies well below the line of $R_{\rm burst}$ at all luminosities.

In Figure 4-8, we show the luminosity of the Comptonized component versus the total luminosity of the double thermal components. The behavior in the soft state for Model 6 is quite different from that in the first four models. Here, with increasing luminosity of the thermal components (i.e. $L_{\rm bb} + L_{\rm mcd}$), the luminosity of the Comptonized component first increases and then decreases. At the highest luminosities, the Comptonized component is negligible, as implied by the success of Model 5 in the same region. Figure 4-10 shows the fraction of the Comptonized luminosity versus the total luminosity. It looks similar to the color-intensity diagram in Figure 4-2, suggesting that the hard color tracks the degree of Comptonization fairly well.

It should be noted that there are other kinds of weak-Comptonization approximations like constrained power-law (photon index < 2.5) or constrained cutoff power-law (photon

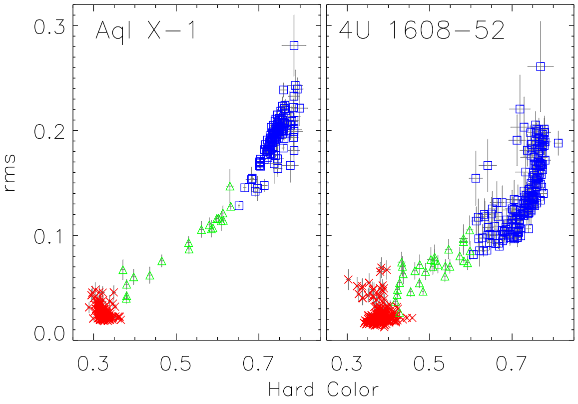

Figure 4-11: The integrated rms power in the power density spectrum (0.1–10 Hz and energy band 2–40 keV) versus the hard color.

index < 2.5 and cutoff energy > 10 keV) that gave results for the soft state that are similar to those obtained using CBPL. For the hard state, Figures 6–8 show that the Model 4_{cold} (CompTT+BB) gives similar results to Model 6 in terms of the properties of the thermal component and the fraction of Comptonization. Model 6 is successful, but there are no claims that it is either a unique solution to the problem, nor an adequate depiction of Comptonization other than the estimate for the fraction of energy related to Comptonization.

4.5 Timing properties and comparison with black holes

Compared to Models 1–4, the use of a double thermal model + CBPL (i.e., Model 6) for Aql X-1 and 4U 1608-52 produces dramatically different results for the luminosity evolution of the thermal components in the soft state and for the implied significance of Comptonization in the soft state.

There are strong similarities in timing properties between the BH and NS LMXBs (see, e.g., Wijnands [2001]), which can be used to further assess these differences. In Figure 4-11, we show the integrated root-mean-square (rms) power in the power density spectrum (0.1–10 Hz and energy band 2–40 keV) versus the hard color for Aql X-1 and 4U 1608-52. The two sources show very similar timing properties. The rms, normalized as a fraction of the source's mean count rate, is very small ($\lesssim 0.05$) in the soft state, and the values increase with the hard color progressing through the transitional and hard states. The rms versus hard-color relations from Figure 4-11 can be compared with similar plots for BHs in Remillard and McClintock [2006] (panels g in their Figures 4–9). Based on such a comparison we conclude that, when considered in a model-independent manner, the way in which the strength of the X-ray variability changes as a function of spectral hardness is very similar for BHs and our two NS transients. Since the hard color effectively traces the fractional contribution of the thermal and Comptonized components to the X-ray spectrum in BH systems, it is interesting to see which of our spectral models conserves this similarity when rms is plotted versus the fractional contribution of the thermal component(s).

In Figure 4-12 we present such a plot for the same 6 BH binaries analyzed by Remillard and McClintock [2006]. Two different integration limits were investigated for the thermal

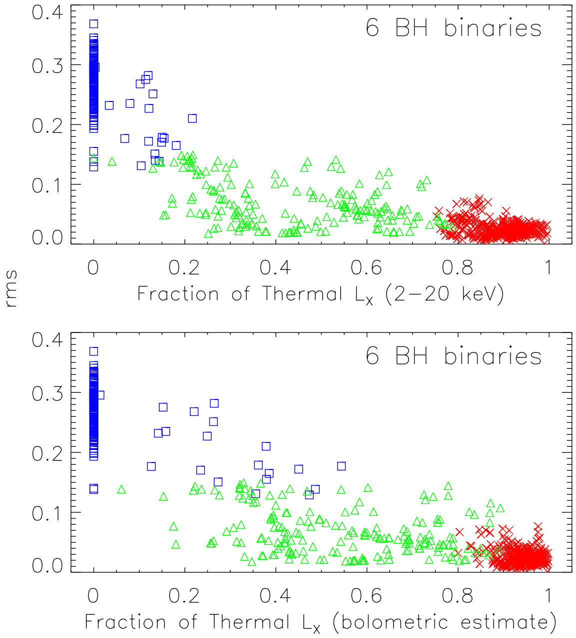

Figure 4-12: The integrated rms power versus the fraction of luminosity contained in the thermal (MCD) component for 6 black hole systems.

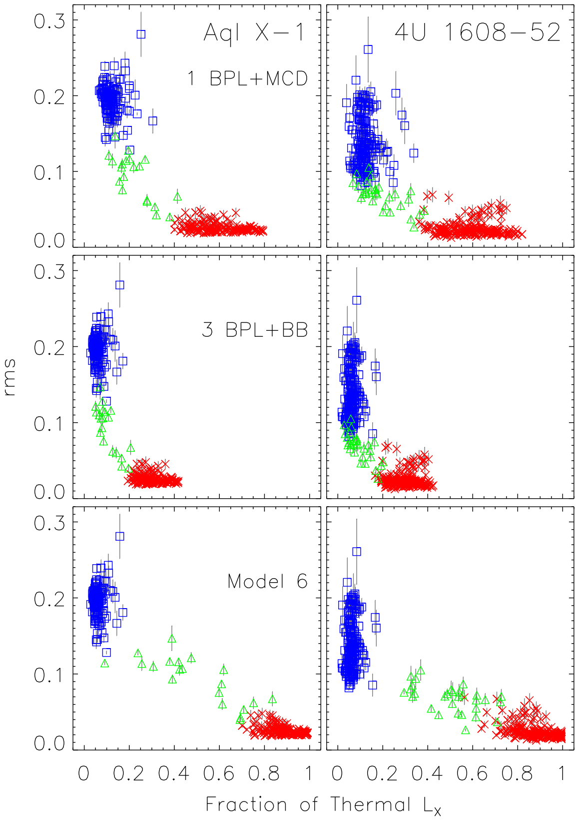

Figure 4-13: The rms versus the fraction of luminosity contained in BB and/or MCD components as evaluated for different spectral models.

and Comptonized luminosities, but the overall behavior was insensitive to our exact choice. It can be seen that for BHs in the soft state, the luminosity fraction of the thermal component is quite high ($\gtrsim 75\%$) and the rms is very small $\lesssim 0.05$. For Aql X-1 and 4U 1608-52 we plot the rms versus the fraction of thermal luminosity for Models 1, 3, and 6 in Figure 4-13. Note that in case of Model 6 the sum of MCD and BB was used to determine the fractional contribution of the thermal components. Comparing Figures 4-12 and 4-13 one can see that only Model 6 reproduces the same dependence of rms on fractional thermal luminosity for Aql X-1 and 4U 1608-52, as for the six BHs. In Models 1 and 3, the luminosity fraction of the thermal component can be as low as 40% and 20%, respectively, while continuing to show very low values of rms power. Similar results are obtained for Models 2 and 4 (cold and hot included for both cases). Hence, for the models outlined in Table 4.2 only Model 6 links weak Comptonization with low rms power, as is clearly evident in the properties of BHs. Models 1–4 for the soft state are therefore described as having the "P" problem (see §4.4.2 and Table 4.2).

4.6 Physical interpretations of model 6 for thermal components

Since Model 6 has many attractive advantages over the other models, we further explore its implications in terms of the physical properties of the accretion flow in both the hard and soft states.

There is a well known difficulty in deriving true radii from the apparent dimensions (i.e., $R_{\rm bb}$, $R_{\rm burst}$, and $R_{\rm mcd}$ extracted from model components of the X-ray spectrum BB, $\rm BB_{burst}$, and MCD, respectively). Nevertheless, the small value of $R_{\rm bb}$ and the nearly constant values of $R_{\rm bb}$ and $R_{\rm mcd}$ across a large range in luminosity motivate cautious efforts to discuss physical interpretations.

If we assume the BB emission area to be a latitudinally symmetric equatorial belt, then the BB emission area of the belt should be

$$A_{\rm belt} = 4\pi N_{\rm bb} D_{\rm 10kpc}^2 f^4 k(i,\delta)\ {\rm km}^2, \tag{4.1}$$

where $N_{\rm bb} = R_{\rm bb}^2/D_{\rm 10kpc}^2$ is the normalization of the BB component (isotropic assumption), f represents a spectral hardening factor (sometimes expressed as the ratio of the color to effective temperature), and k is a geometrical correction factor taking into account the emitting geometry and any occultations by the accretion stream. The k factor depends on the disk inclination (i), the latitude range (from the NS equator) of surface emission (δ). We note that this factor is also strongly dependent on the properties of the occulting accretion stream. Unless otherwise indicated, we assume a geometrically thin but optically thick accretion stream so that the half belt on the other side of the accretion stream is invisible to the observer. To have some sense of this k factor, we give two examples: $k(i=60^\circ, \delta=10^\circ) = 1.69$, and $k(i=60^\circ, \delta=90^\circ) = 1.33$. From this perspective, the area of the NS, e.g., for Aql X-1 in this study is:

$$A_{\rm ns} = 4\pi N_{\rm burst} D_{\rm 10kpc}^2 f^4 k(i,\delta=90^\circ)\ {\rm km}^2, \tag{4.2}$$

assuming that the entire NS surface is radiating (using the asymptotic value of $R_{\rm burst}$ late in the burst). This expression conveys the difficulty in gaining accurate inferences of NS sizes from X-ray burst measurements. The raw values for $R_{\rm burst}$ given in §4.4.2 ignore f

and k.

Perhaps of greater interest is the effort to understand a key measurement result of this paper: $R_{\rm bb}/R_{\rm burst} \simeq 0.25$ ($N_{\rm bb}/N_{\rm burst} \simeq 1/16$) for Aql X-1. If we assume that the f values cancel in these different applications of the BB model and use the fact $A_{\rm belt}/A_{\rm ns} = \sin\delta$, we obtain

$$\sin\delta \quad = \quad \frac{N_{\rm bb}k(i,\delta)}{N_{\rm burst}k(i,\delta=90^\circ)} = \frac{k(i,\delta)}{16k(i,\delta=90^\circ)}. \tag{4.3}$$

In this case, the $R_{\rm bb}/R_{\rm burst}$ value is equivalent to an equatorial belt with a half-angle of $\delta_{\rm belt} \simeq 9^\circ$ for $i = 30^\circ$, or $\delta_{\rm belt} \simeq 6^\circ$ for $i = 60^\circ$. We stress that this scaling estimate ignores the annular half width of the occulting stream ($\delta_{\rm stream}$) itself. A more realistic estimate is $\delta_{\rm belt} \gtrsim \delta_{\rm stream} + 6^\circ$ for $i = 60^\circ$, implying $k \gg 1$.

Regardless of the details of δ, we must confront the implication of measuring $N_{\rm bb}/N_{\rm burst} \sim 1/16$, noting that $N_{\rm burst}$ is the asymptotic value that should screen out effect of the radius expansion and momentary disruption in the occulting stream (§4.4.2). How is it possible that accreting NSs could maintain an almost uniformly small area of BB emission through hard and soft states that span such a wide range in luminosity (i.e., 0.005 to 0.5 $L_{\rm EDD}$)? Such simple results suggest a picture in which a geometrically thin accretion stream feeds a rather well-defined impact zone, where the accreting gas may efficiently release energy before spreading over the remainder of the NS surface. Since the scale height of the inner accretion disk is expected to increase with the accretion rate, it is difficult to understand our results without the help of an inner-most stable circular orbit (ISCO). As illustrated for BHs, the effective potential of an ISCO creates a pinch on the vertical structure of the accretion stream that can suppress variations in the scale height of the inner disk [Abramowicz et al., 1978]. To the extent that Model 6 remains viable with further scrutiny, the small size of $R_{\rm bb}$ over a large range in luminosity should be examined as a means to infer that these NSs lie within their ISCOs. This may provide another observational link to general relativity, while providing potential constraints on the NS equation of state.

The ability of Model 6 to restore the expected luminosity evolution of the MCD component motivates efforts to compare the MCD radius and relative luminosity to the results determined for the BB component. In Figure 4-7, it is evident that the raw values of $R_{\rm mcd}$ are only slightly less than the values of $R_{\rm burst}$ (dotted line) for Aql X-1 and 4U 1608-52. Given the uncertainty in the different correction factors that must be applied, respectively, to the disk and the burst radii in order to derive physical sizes, our results may still be consistent with expectations framed by the preceding discussion, i.e., that $R_{\rm ns} < R_{\rm isco} \lesssim R_{\rm disk}$.

The comparison of BB and MCD luminosities is a trickier topic. The apparent luminosity of the boundary layer ($L_{\rm bb}$) is about one third of that of the disk ($L_{\rm mcd}$) in the soft state, neglecting the weak Comptonization. In contrast, we might expect $L_{\rm bb} \gtrsim L_{\rm mcd}$ if the boundary layer is inside the NS ISCO, as sketched above, where the accreting material may impact the surface with a large relative velocity that includes a component along the radial path. We note, however, that while $L_{\rm mcd}$ is estimated in a true bolometric sense, this is not the case for $L_{\rm bb}$. We need to correct $L_{\rm bb}$ by $k(i,\delta)$ (Equation 4.1) due to the geometry of the boundary layer and occultation by the accretion stream. For Aql X-1, it is $\simeq 1.7$ ($i = 60^\circ$) or $\simeq 2.6$ ($i = 30^\circ$), and these factions can become much larger if $\delta_{\rm stream} \sim \delta_{\rm belt}$, as noted above. We conclude that there is considerable uncertainty in our final results as to whether the total energy losses at the boundary layer are less than the total bolometric luminosity of the other spectral components.

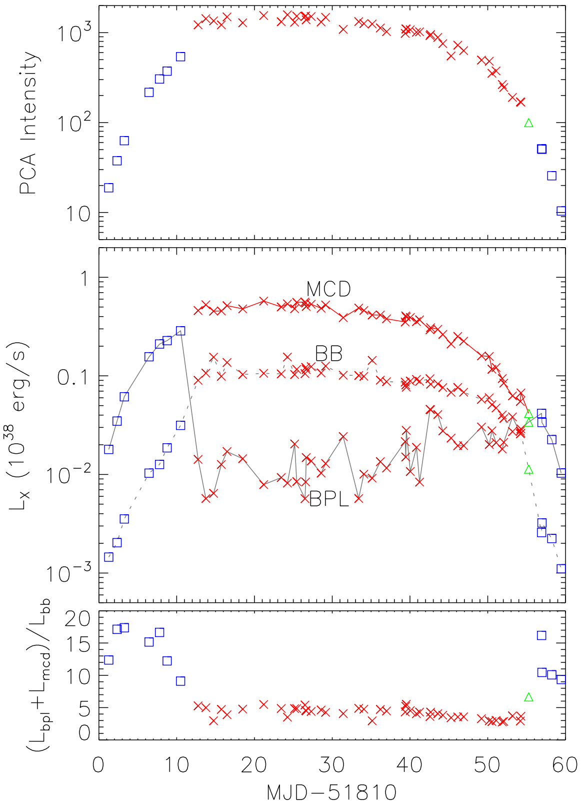

Figure 4-14: The luminosity evolution of different spectral components (middle panel) during the 2000 outburst of Aql X–1, as viewed with Model 6. Blue, green, and red symbols denote hard, transitional, and soft states, as done previously. Note that the MCD component (points connected by a solid red line) is not directly visible with the PCA in the hard state. The top panel shows the PCA count rate (2-30 keV). The bottom panel shows the ratio: $(L_{\rm bpl} + L_{\rm mcd})$ / $L_{\rm bb}$, and the value is clearly highest in the hard state, when Comptonization appears to dominate the X-ray spectrum.

4.7 Physical consequences of model 6 for the hard state

Figure 4-14 shows the luminosity evolution with time during a well-covered outburst of Aql X-1 in 2000. The light curve of this outburst is shown on the top panel. The middle panel shows the luminosity evolution of each spectral component, using our hybrid Model 6, where the BPL and MCD dominate the apparent luminosity of the hard and soft states, respectively. The bolometric BB luminosity ($L_{\rm bb}$) curve resembles the total luminosity curve, and it provides a reference measurement that allows us to further compare the hard and soft states. The ratio of BPL (isotropic) and MCD (bolometric) luminosities ($L_{\rm bpl} + L_{\rm mcd}$) to $L_{\rm bb}$ is shown in the bottom panel. We note that the values of this ratio are elevated, in part, by the k factor described for Eq. 1. Nevertheless the high luminosity of the hard state, relative to $L_{\rm bb}$, is apparent in the bottom panel of Figure 4-14.

To compare the hard and soft state luminosities in a more global manner, Figure 4-15 shows ($L_{\rm bpl} + L_{\rm mcd}$) versus $L_{\rm bb}$ for all of the *RXTE* observations of Aql X-1 and 4U 1608-52. The behavior of these two sources is quite similar. The hard and soft states are largely separated by vertical lines near $L_{\rm bb} \sim 10^{36}$ erg/s (uncorrected). Here, the hard-

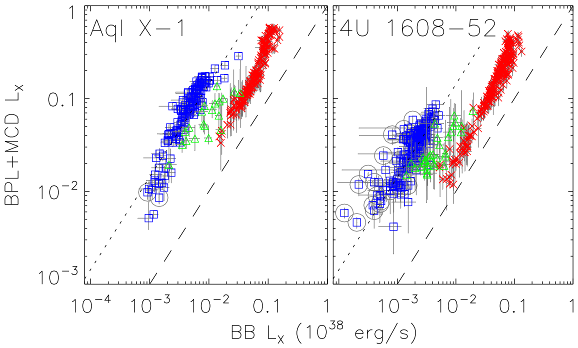

Figure 4-15: The luminosity of non-BB components (i.e., BPL+MCD) versus the luminosity of the BB component. At the transitional BB luminosity that separates hard and soft states, the hard-state BPL appears to be very luminous compared to the soft-state MCD. The two reference lines, dashed and dotted lines, connect the points where the ratio of the luminosities of the BB component and the non-BB components is 1.0 and 0.07, respectively.

state values for $(L_{\rm bpl} + L_{\rm mcd})$ are clearly higher than those for the soft state, by a factor of ~ 6. For the hard state, the vertical axis represents Comptonization, since 90% of the total luminosity in the hard state is due to $L_{\rm bpl}$. In the soft state, the vertical axis is effectively the disk luminosity. On the horizontal axis, we assume that $L_{\rm bb}$ represents emission from the boundary layer, and we can then use the nearly constant value of $R_{\rm bb}$ across the hard and soft states to motivate the presumption that $L_{\rm bb}$ quantifies the mass accretion rate onto the NS surface. Using these assumptions, there are still different ways to interpret Figure 4-15.

First, if we further assume that the total accretion rate $(\dot{M})$ flows into a boundary layer with constant $\delta_{\rm belt}$, then $L_{\rm bb}$ effectively tracks $(\dot{M})$, and we can compare hard and soft states in terms of their radiation efficiency. Unlike $L_{\rm bb}$, $L_{\rm mcd}$ and $L_{\rm bpl}$ are not expected to require large correction factors, although the origin of the BPL is very uncertain. We would then conclude from Figure 4-15 that Comptonization in the hard state has higher radiative efficiency than thermal disk emission in the soft state, and this occurs across a wide range in the accretion rate. This idea is a radical departure from expectations.

Alternatively, we can refrain from making assumptions about $\dot{M}$, and choose a line of constant $(L_{\rm bpl} + L_{\rm mcd})$ in Figure 4-15. Quite generally, then, one would conclude that less mass reaches the NS surface in the hard state, compared to the soft state, for a given level of luminosity on the vertical axis. This might suggest that the majority of the mass flow is disrupted from the normal path to the NS in the hard state. Given the expectation for radio jets in the hard state of accreting NS LMXBs [e.g., Fender, 2006, Migliari and Fender, 2006], this could further imply that a significant fraction of mass accretion in the hard state is redirected to outflow in the jet. The energy source for this scenario could be problematic.

Finally, it is also possible that some of our preliminary assumptions are incorrect. Changes in accretion geometry across the state boundary, e.g., from correlated jumps in $\delta_{\rm belt}$ and δ_{stream}, would be one way to invalidate the assumption that $L_{\rm bb}$ uniformly tracks the NS surface accretion rate across both states. All of these ideas need to be investigated for other sources and in different ways.

4.8 Summary and discussion

We have analyzed ten years of *RXTE* observations of two NS X-ray transients, Aql X-1 and 4U 1608-52, through more than twenty individual outbursts. Although there is much variety in these outbursts, the spectral and timing properties are well organized, as has been demonstrated in previous investigations [Muno et al., 2002, Gierliński and Done, 2002a]. It is also well known that several different models may adequately fit the X-ray spectra of NS LMXBs, while each one may convey very different physical implications, e.g., the temperatures and sizes of the emitting regions. We therefore attempted to design performance-based criteria for evaluating these models, hoping to gain insights on a model's self consistency, while taking advantage of the large data archive for these two atoll-transient prototypes.

Among these criteria, there is an important quantity, which is the energy fraction for Comptonization, i.e., how much energy is directly visible as pure thermal radiation and what remaining fraction is diverted and expressed as inverse Compton radiation. This quantity is interesting from an accretion-energetics point of view. It can be calculated from any of these models, and furthermore, it is the gateway for comparing NSs and BHs in terms of the relationship between energetics and the measured timing properties.

First we examined the classical two-component models with a Comptonized component (BPL or CompTT) and a thermal component (MCD or BB). We confirmed that many combinations can describe the X-ray spectra successfully. Moreover there are two possible seed-photon solutions for models that utilize CompTT, a problem that is also present for instruments with extended low-energy coverage like *BeppoSAX*. In the soft state, the two-component models behaved poorly for a variety of reasons shown in Table 4.2, Figure 4-7, and Figures 4-12–4-13. We then progressed to consider a double-thermal model (MCD+BB) for the soft state, and we found a need to account for weak Comptonization at the low-L_{X} end of the soft-state track. We then devised a hybrid "Model 6" in which the hard state is modeled by BB+BPL while the soft state is modeled by MCD+BB+CBPL, where the third component is a constrained BPL ($E_{\mathrm{b}} = 20$ keV and $\Gamma_1 \leq 2.5$) that can assume the role of weak Comptonization.

It turns out that Model 6 offers three great advantages over the classical Comptonized + thermal Models. (1) It produces an $L_{\mathrm{X}} \propto T^4$ relation for both the MCD and BB in the soft state with a sufficiently large value for the inner disk radius (compared to the NS radius inferred from Type I bursts). (2) The emission area of the BB extends from the hard to the soft state with essentially the same value. (3) The fraction of Comptonization inferred by this model is also consistent with that for BHs for given values of rms power in the power density spectra. When BH binaries are in the thermal state, the Comptonization fractions in the energy spectra are very low and the rms power is also very low, rms < 0.05. Atoll sources in the soft state show similar rms values, but only Model 6 implies low Comptonization for the soft state.

With regard to previous investigations of NS X-ray spectra (§1), our Model 6 splices together the Western model for the hard state (BB + a heavily Comptonized disk) and a three-component model for the transitional and soft states (BB + MCD + constrained BPL) that represents a BB plus a very weakly Comptonized disk. The soft-state portion of this model was heavily influenced by the original version of the Eastern model (Mitsuda et al. 1984). We further note that low Comptonization solutions ($\tau \sim 1$; $kT_{\mathrm{e}} > 20$ keV) for the soft state were derived with a two-component Eastern model for 4U 1608-52 with *Tenma* data (Mitsuda et al. 1989), and these are the closest results that we can find to those (soft state) of Model 6.

The ad hoc scheme in Model 6 to handle weak Comptonization with the CBPL component for the soft state is obviously a topic that needs further work. Model 6 for the soft state is a three-component continuum model. We did not try to test three-component models in an open-handed manner. Instead, we focused on low-Comptonization solutions, progressing from the success of Model 5 (no Comptonization). The CBPL used in this paper is just one possible solution; our investigation showed that constrained power-law with photon index < 2.5 or constrained cutoff power-law with photon index < 2.5 and cutoff energy > 10 keV would also produce similar results to those obtained with the CBPL. As other alternatives, we tried to add a constrained version of CompTT to the two thermal components, by coupling $kT_{\rm s}$ to $kT_{\rm bb}$ or $kT_{\rm mcd}$, or requiring $kT_{\rm e} > 10$ keV, or doing both. However, the fits always yielded very strong Comptonization in the low-luminosity soft state, but the fit residuals for Model 5 suggested that only weak Comptonization is present in the low-luminosity soft state. This could be due to the limited low-energy coverage of RXTE data. We investigated *BeppoSAX*, which has extended low-energy coverage, for possible new insight. Unfortunately, each X-ray source has only one soft-state observation from *BeppoSAX*, and both of them are at high luminosity. Future observations with broad-band instruments like *Suzaku* could be important to this issue. As for the hard state, Model 6 uses BB+BPL. Replacement of BPL with CompTT does not change our conclusions for the properties of the BB component and the fraction of Comptonization as long as the cold-seed-photon solution is used.

There is a question of whether we could also see a thermal disk in the hard state, where the trend from Figure 4-8 would imply $kT_{\rm mcd} \lesssim 0.5$ keV. Such disks have in fact been observed in the hard state of a number of BH X-ray transients [Miller et al., 2006a,b, Rykoff et al., 2007], with instruments that have better sensitivity at low energies than RXTE. However, being able to detect these components in NSs is not only a matter of low-energy sensitivity. One also needs a relatively low interstellar absorption. Moreover, in NSs a disk would not be the only thermal component contributing around 0.5 keV, since there is also emission from the boundary layer, and it is difficult to disentangle the contribution from the two components at low luminosities when the spectrum is not dominated by these thermal components.

If the boundary layer is an equatorial belt of BB emission, then Model 6 implies that the visible surface area of the belt remains nearly constant, with $N_{\rm bb}/N_{\rm burst} \sim 1/16$, over a wide range in $L_{\rm X}$ (0.005–0.5 $L_{\rm Edd}$). Current theories predict that the geometry and physical processes in the boundary layer should vary significantly with $L_{\rm X}$ [e.g., Inogamov and Sunyaev, 1999, Popham and Sunyaev, 2001, Kluzniak and Wagoner, 1985], and some observations have been interpreted in such a manner [Church et al., 2002]. Our results are much simpler than expected, suggesting that a geometrically thin accretion stream impacts a rather well-defined surface area, where the gas radiates efficiently before spreading over the NS. This scenario would seem to require that the NS lies within its ISCO, which pinches the vertical structure of the accretion stream [Abramowicz et al., 1978] as it flows toward the NS. This topic must be investigated in further detail.

Chapter 5

Suzaku and *BeppoSAX* X-ray Spectra of the Persistently Accreting Neutron-Star Binary 4U 1705-44

Abstract

We report the spectral modeling of 4U 1705–44 using the broad-band spectra made by *Suzaku* in 2006–2008 and by *BeppoSAX* in 2000. The soft-state continuum spectra are modeled by two thermal components, one of which is a multicolor accretion disk and the other is a single-temperature blackbody to describe the boundary layer, with additional weak Comptonization using a simple power law or the SIMPL model by Steiner et al. The hard-state continuum spectra are modeled by a single-temperature blackbody for the boundary layer plus strong Comptonization, modeled by a cutoff power law. While we are unable to derive reliable conclusions about the physical properties of the disk in the hard state, the accretion disk in the soft state seems to approximately follow $L \propto T^{3.2}$. The deviation from $L \propto T^4$ might be caused by two main factors: a luminosity-dependent spectral hardening factor, and/or real change of the inner disk radius in the some part of the soft state. The boundary layer is consistent with $L \propto T^4$, with an apparent emission area about 1/14 of the surface of the neutron star. Based on the disk and boundary layer behavior, we infer that the accretion disk for most of our soft-state observations is truncated by the ISCO, rather than by the surface of the NS. If this interpretation is correct, the magnetic field on the surface of the NS in 4U 1705–44 is estimated to be less than about 1.9×10^8 G. Broad relativistic Fe lines are also detected in each spectrum and are modeled with the diskline model. The strength of the Fe lines is found to correlate well with the boundary layer emission in the soft state. In the hard state, the Fe lines seem to be due to illumination of the accretion disk by the strong Comptonization emission.

5.1 Introduction

There are two main classes of luminous and weakly magnetized neutron stars (NSs) in low-mass X-ray binaries (LMXBs), i.e., atoll and Z sources, named after the patterns that they trace out in X-ray color-color diagrams (CDs) or hardness-intensity diagrams (HIDs) [Hasinger and van der Klis, 1989, van der Klis, 2006]. Atoll sources have lower luminosities (∼0.001–0.5 L_{EDD}) than Z sources and have two distinct X-ray states, i.e., hard (energy spectra are roughly flat with power-law photon index near 1.7) and soft states (energy spectra follow exponential decrease above ∼10 keV), plus a "transitional" state between these two. The hard, transitional and soft states of atoll sources are also often referred to as the "extreme island", "island", and "banana" states/branches, respectively. Z sources only have soft spectra, but there are three distinct branches with different spectral and timing behaviors. Recently, Lin et al. [2009b, Chapter 7] and Homan et al. [2009] analyzed a transiently accreting NS, XTE J1701-462, which changed from the Z-source to the atoll-source behavior as the outburst decayed from near/super Eddington luminosity (L_{EDD}) to almost quiescence. These results confirmed that the behavior differences are due to their different mass accretion rates.

The spectral modeling of NS LMXBs has been controversial for a long time [see Barret, 2001, for a review]. The continuum of soft spectra in both atoll and Z sources are generally described by two-component models that include a soft/thermal and a hard/Comptonized component [e.g., Barret et al., 2000, Oosterbroek et al., 2001, Di Salvo et al., 2000a, Iaria et al., 2005], and there have been two classical models, often referred to as the *Eastern* model [after Mitsuda et al., 1989] and the *Western* model [after White et al., 1988], with different choices of the thermal and Comptonized components. In the *Eastern* model, the thermal and Comptonized components are described by a multicolor disk blackbody (MCD) and a Comptonized blackbody, respectively. In the *Western* model, the thermal component is a single-temperature blackbody (BB) from the boundary layer, and there is Comptonized emission from the disk. In the hard state, the spectra are dominated by a hard/Comptonized component, but a soft/thermal component is generally still required [Christian and Swank, 1997, Barret et al., 2000, Church and Balucińska-Church, 2001, Gierliński and Done, 2002b]. Lin et al. [2007b, Chapter 4] implemented the commonly used two-component models for two classical transient atoll sources, i.e., Aql X-1 and 4U 1608-52, and outlined the problem of model degeneracy for accreting NSs, not only from the choices of the thermal components, but also from the detailed description of Comptonized components (i.e., the scattering corona geometry, the seed photon temperature, etc.). The physical interpretation of the spectral evolution of these atoll sources from different models are also very different from each other. However, none of the tested models produce results similar to those of black-hole X-ray binaries, i.e., $L_{\mathrm{X}} \propto T^4$ tracks for the MCD component and weak Comptonization for the soft-state spectra [Remillard and McClintock, 2006].

Lin et al. [2007b, Chapter 4] devised a hybrid model for atoll sources: a BB to describe the boundary layer plus a broken power law for the hard state, and two strong thermal components (MCD and BB) plus a constrained broken power law (when needed) for the soft state. This choice for the soft state offers a weak-Comptonization solution that differs from the strong Comptonization solution of the two-component models that had previously dominated the literature. The results of the application of the hybrid model can be summarized as follows: both the MCD and BB evolve approximately as $L_{\mathrm{X}} \propto T^4$, the spectral/timing correlations of these NSs are aligned with the properties of accreting black holes, and the visible BB emission area is very small but roughly constant over a wide range of L_{X} that spans both the hard and soft states. Lin et al. [2009b] applied this X-ray spectral model to XTE J1701-462, and results similar to the above were also obtained for the observations when the source showed the atoll-source behavior. Deviations of the MCD from the $L_{\mathrm{X}} \propto T^4$ track were observed with the inner disk showing a luminosity-dependent radius expansion when the source was bright and behaved as a Z source. This was interpreted as an effect of the local Eddington limit.

The hybrid spectral model is still empirical, especially the modeling of Comptonization.

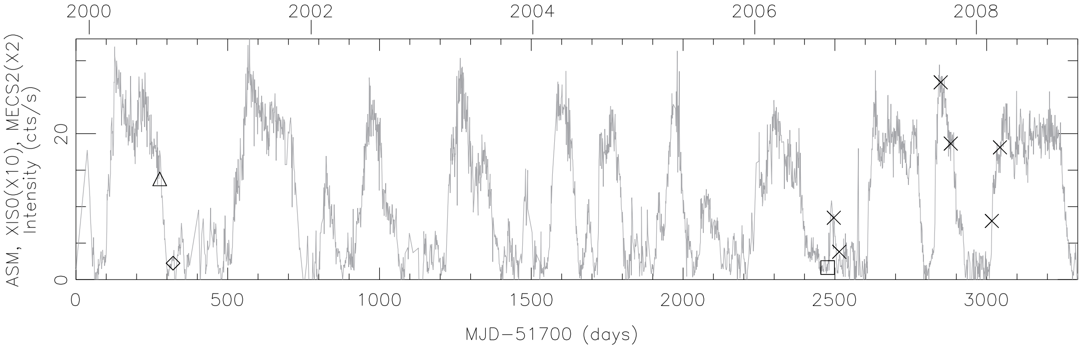

Figure 5-1: The long-term *RXTE* /ASM light curve of 4U 1705–44. Discrete symbols represent different spectral states from different pointed observatories: *BeppoSAX*/*Suzaku* hard state (diamond/square) and *BeppoSAX*/*Suzaku* soft state (triangle/cross).

Moreover, this model has only been applied thus far to extensive data obtained with the *Rossi X-ray Timing Explorer* (*RXTE*). It has two pointing instruments, which cover the energy range from ∼2.5 to 250 keV. However, there is quite significant emission from X-ray binaries below this energy range, as the characteristic temperatures of the thermal components are normally below 3 keV. Thus it is important to test this model using broadband spectra that extend to photon energies below the sensitivity range of *RXTE* .

In this paper we investigate the bright atoll source, 4U 1705-44, which was observed seven times in 2006-2008 by *Suzaku* [Mitsuda et al., 2007]. One of the important features of *Suzaku* is its broad energy band (0.2–600 keV). We also analyzed two observations of 4U 1705-44 made with *BeppoSAX* (0.1–300 keV) in 2000. Both *Suzaku* and *BeppoSAX* additionally provide better energy resolutions than *RXTE* (∼ 2%, 8%, 18% at 6 keV (FWHM) respectively), and this capability can be used to better resolve the broad Fe emission lines. Broad Fe lines are commonly seen in X-ray binaries and provide another tool for investigating the accretion flow around compact objects [e.g., Miller, 2007, Cackett et al., 2008a, 2009c].

4U 1705-44 has been classified as an atoll source [Hasinger and van der Klis, 1989]. Timing studies, including the findings of kilohertz quasi-periodic oscillations (kHz QPOs), have been carried out for this sources using observations with *RXTE* [Ford et al., 1998, Barret and Olive, 2002, Olive et al., 2003]. Spectral studies of this source have also been carried out, using different kinds of X-ray detectors and spectral models [e.g., Barret and Olive, 2002, Di Salvo et al., 2005, Fiocchi et al., 2007, Piraino et al., 2007, Homan et al., 2009, Reis et al., 2009, Di Salvo et al., 2009]. Several of these authors also reported detection of a broad relativistic Fe line from this source. In this paper we will concentrate on the spectral properties of this source. We describe our data reduction scheme in §5.2, and also present the long-term light curves and color-color diagrams. We perform detailed spectral modeling in §5.3, for which we provide our physical interpretations in §5.4. Finally we give our summary and discussion.

5.2 Observations and data reduction

The long-term light curve of 4U 1705-44 is shown in Figure 5-1. The gray solid line is from the *RXTE* All-Sky Monitor [ASM; Levine et al., 1996], and we can see that the source displays persistent X-ray emission, with one or two strong intensity cycles per year. These

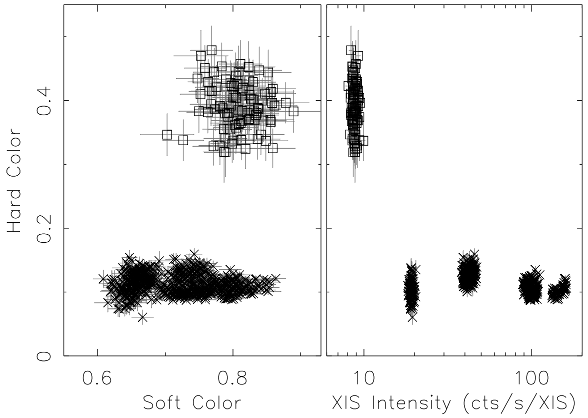

Figure 5-2: Color-color and hardness-intensity diagrams of 4U 1705–44 based on *Suzaku* observations in 2006–2008, with bin size 128 s. The squares are from observation 401046010, and the crosses from the other observations. For the definitions of the colors, see the text. One-σ statistical error bars are also shown.

Table 5.1. The Suzaku observations of 4U 1705–44 in 2006–2008

Observation ID	401046010	401046020	401046030	402051010	402051020	402051030	402051040
Spectral ID	*suz*1	*suz*2	*suz*3	*suz*4,*suz*5	*suz*6	*suz*7	*suz*8
Observation Date	2006/08/29	2006/09/18	2006/10/06	2007/09/05	2007/10/08	2008/02/20	2008/03/18
Exposure of XIS/PIN (ks)[a]	10.1/13.0	12.7/12.1	13.0/12.2	2.1/8.0	3.9/14.5	18.4/17.3	2.9/10.94
XIS Detectors Analyzed	0 1 2 3	0 1 2 3	0 1 2 3	0 1 3	0 1 3	0 1 3	0 1 3
Window Option	1/4	1/4	1/4	1/4	1/4	1/4	1/4
Exposure in Burst Option (s)	1.6	2.0	2.0	0.5	0.5	2.0	0.5
XIS0 Count Rate (cts/s)[b]	17.1	87.7	39.4	279.1	192.7	82.8	187.2
Soft Color[c]	0.81 ± 0.03	0.73 ± 0.01	0.65 ± 0.02	0.79 ± 0.01,0.83 ± 0.01	0.73 ± 0.02	0.66 ± 0.01	0.78 ± 0.02
Hard Color[c]	0.39 ± 0.03	0.13 ± 0.01	0.10 ± 0.01	0.10 ± 0.01,0.11 ± 0.01	0.10 ± 0.01	0.12 ± 0.01	0.11 ± 0.01
Radius of Central Region With >5% pile-up (pixels)[d]	0	55	32	52	39	60	35
Radius of Central Region With >10% pile-up (pixels)[d]	0	39	21	35	24	42	24
Spectral state	hard	soft	soft	soft	soft	soft	soft

[a] The dead time and burst clock options have been taken into account. All XIS detectors have the same exposure time, and the values given are for one detector only.

[b] Total time-averaged count rates, including central regions typically with serious pile-up.

[c] The values of colors are the average values corresponding to each spectrum, with one-σ error bars included.

[d] The values vary among different XIS detectors and can differ from the values given by up to 3 pixels.

cycles correspond to state-transition cycles [Homan et al., 2009]. Discrete plot symbols show the time and spectral states during different pointed observations. The data reduction and spectral analyses are described below.

5.2.1 *Suzaku* data

Suzaku made seven observations of 4U 1705-44 in 2006–2008. The detailed information of these observations is given in Table 5.1. Both the X-ray Imaging Spectrometer [0.2–12 keV, XIS; Koyama et al., 2007] and the Hard X-ray Detector [10–600 keV, HXD; Takahashi et al., 2007] instruments were used during these observations. There are four XIS detectors, numbered as 0 to 3, and each has a 1024×1024-pixel X-ray-sensitive CCD at the focus of each of the four X-ray telescopes. The CCD in XIS1 is back-illuminated, and the CCDs in the other three XIS detectors are front-illuminated. The effective area of the three front-illuminated CCDs in XIS0, XIS2 and XIS3 are very similar, but the back-illuminated

CCD has an increased effective area at low energies (<1 keV) with a small decrease at higher energies. XIS2 was damaged in 2006 November, and its data are analyzed only for the first three observations. The HXD instrument includes both PIN diodes (10–70 keV) and GSO scintillators (30–600 keV). Both the PIN and GSO are collimated (non-focusing) instruments.

As 4U 1705-44 is normally a bright X-ray source, observations of this source with the XIS are affected by the pile-up problem, i.e., when more than one photon strikes in the same or adjacent pixels in one CCD readout frame. Observers often use the so-called window and burst options to reduce this problem. All of these seven observations were made using 1/4 window (Table 5.1), in which the CCD was read out every 2 s (compared with the usual 8-s read-out time), but only recording data from a 256×1024-pixel strip. With the burst option, the exposure time per frame can be reduced further by introducing a dead time. Table 5.1 gives the live exposure time per frame in the burst option adopted for each observation.

Even with both window and burst options utilized, most XIS observations of 4U 1705-44 still suffer from event pile-up in the image center. To solve this problem, we excluded the image center from the event extraction region, and the events were extracted from an annular region to obtain the energy spectra. In order to determine the radius of the central exclusion region, we took the following steps to estimate the pile-up fraction, i.e., the ratio of events lost via grade or energy migration to the events expected in the absence of pile-up, at different positions of the CCD. First, we applied the publicly available tool `aeattcor.sl` by John E. Davis to obtain a new attitude file. This tool corrects the effects of thermal flexing of the *Suzaku* spacecraft and obtains more accurate estimate of the spacecraft attitude. For all our seven observations, the above attitude correction produced sharper PSF images. We then applied the new attitude file and updated the XIS event files using the FTOOL `xiscoord` program. Finally, we used the publicly available tool `pileup_estimate.sl` by Michael A. Nowak to estimate the pile-up fraction at different positions of the CCD.

In Table 5.1 we list the radii of the central circular regions that contain most of the XIS CCD pixels with local pile-up fractions that exceed 5% and 10%, respectively. They vary with observations, due to different intensity levels and different burst options adopted for each observation. The unfiltered pile-up fractions integrated over the whole CCDs are about 10–15% for all observations except for the observation 401046010 (∼3%). We used annular regions to extract spectra (circular regions are used for observation 401046010). The outer radii of the annular regions were set to be about 110 pixels, which is limited by the 1/4 window option. Two cases of inner radii are used, corresponding to 5% and 10% pile-up exclusion regions. The integrated pile-up fractions of all annular regions are ∼3% and ∼5%, corresponding to excluding local 5% and 10% pile-up regions, respectively. Using the models for the soft-state spectra, which include MCD and BB components, we find that the spectral fitting results using 10% pile-up exclusion regions show systematic decrease in the soft-component (MCD) flux and increase in the hard-component (BB) flux, by about 3%, compared with the results using 5% pile-up exclusion regions. The differences in most cases are about within the error bars at 90%-confidence level, and the conclusions of this paper hold for either case. For simplicity, we only show results using the 5% pile-up exclusion regions below.

4U 1705-44 is in the direction toward the Galactic ridge, and the background consists of non-X-ray (particle) background, absorbed cosmic X-ray background, and Galactic ridge emission. Even though our source can be regarded as a point source, there is no background region for us to estimate the background. This is because the PSF of the XIS is so spread out and our source during these seven observations was so bright that the source emission dominates over the background (1–10 keV) over the whole 1/4 window. For the background region of two $250'' \times 230''$ boxes at the two ends of 1/4 window ($\sim 250''$ from the image center), the count rate was found to increase roughly linearly (∼1.7%) with the total count rate over the whole window. Using the above background region of our faintest observation 401046010, we found that the background in general is smaller than the statistical error bars of the spectra extracted from annular regions described above at any energy within 1.0–10 keV. It is typically $< 0.6\%$, but can be as high as 1–4% around 1.0 and 10 keV for faint observations 401046010 and 401046030.

We estimated the background spectra as follows. The non-X-ray background varies with time, and we estimate it using the `xisnxbgen` tool, based on the night Earth data by *Suzaku*. For the X-ray background, including the cosmic X-ray background and Galactic ridge emission, we used observation 100026030 by *Suzaku*. It is specific for observing the background emission around the supernova remnant RX J1713-3946, and the pointing direction of this observation has a $184''$ offset from 4U 1705-44. We used a circular region with a radius of 400 pixels to extract the background emission and subtracted the non X-ray background estimated by the `xisnxbgen` tool to obtain the X-ray background. Using the background files thus obtained, we find that the spectral fitting results are almost identical to the cases without background subtractions, and the values of χ^2 are decreased by values < 4 (with degree of freedom typically > 1000; the maximum is achieved for the faintest observation 401046010).

The response files of the XIS for each observation were generated using the `xisresp` script which uses the `xisrmfgen` and `xissimarfgen` tools (specifying 1% accuracy). They take into account the time variation of the energy response and the specific extraction region for each observation and each XIS detector and used the calibration files released in 2009 April. The shape of the spectra from XIS0, XIS2 and XIS3 on the whole are very similar, but the normalizations are not always consistent with each other at a 90% confidence level, based on our spectral fitting. This is consistent with the current flux calibration uncertainty of small extraction regions, as in our case. Thus we did not choose to add the spectra together, but fit them separately instead, by introducing relative normalizations.

We also extracted the PIN spectra. The non X-ray and cosmic X-ray backgrounds are taken into account. The non X-ray background is calculated from the background event files distributed by the HXD team. The cosmic X-ray background is from the model by Boldt [1987], and its flux is about 5% of the background for PIN. The response files provided by the HXD team were used. The GSO data were not used, considering the large uncertainty of calibration and low signal to noise ratios above 40 keV.

The CD/HID of these observations are shown in Figure 5-2. We defined soft and hard colors as the ratios of the count rates in the (3.6–5.0)/(2.2–3.6) keV bands and the (11.0–20.0)/(5.0–8.6) keV bands, respectively. The count rates of the lowest three energy bands were from all XIS detectors except XIS2 using the whole 1/4 window CCD (i.e., no pile-up region excluded) and having deadtime in burst option corrected. XIS2 was not used for this because it was not on for all observations. The energy band 11.0–20.0 keV was from the PIN with the background subtracted and the deadtime correction made. The CD and HID of seven *Suzaku* observations are shown in Figure 5-2, using 128-s data. The intensity shown is from the energy band 2.2–8.6 keV. Two type I X-ray bursts were found in observation 402051010, and data around them are not included in Figure 5-2 or our spectral analysis. The data points with hard color larger than 0.2 (square symbols) are all from observation 401046010, indicating that only this observation was in the hard state

Table 5.2. The *BeppoSAX* observations of 4U 1705–44

Observation ID Spectral ID	21292001 *sax*1	21292002 *sax*2
Observation Date	2000/08/20	2000/10/03
Exposure of LECS/MECS/PDS (ks)	20.6/20.7/9.1	14.6/14.5/6.4
MECS2 Count Rate (cts/s)	27.6	4.5
Spectral state	soft	hard

while all other observations (cross symbols) were in the soft state.

In the CD/HID, most observations show little variation, and we calculated one spectrum for each observation, except for observation 402051010. This observation is the brightest and shows two intensity levels (∼200 and ∼240 counts/s/XIS (2.2–8.6 keV)). We created two corresponding spectra, as we found that their best-fitting spectral parameters are not consistent with each other at the 90% confidence level (§5.3). In the end, we have eight spectra from *Suzaku* observations, and they are denoted as *suz*1–*suz*8 hereafter (Table 5.1). We rebinned the spectra by factors of 2 and 4 for energies below and above 2.55 keV, respectively, and further rebinning was made so that every bin has at least 40 counts and χ^2 minimization criterion can be used in our spectra fitting.

5.2.2 *BeppoSAX* data

There are two pointed observations of 4U 1705-44 with *BeppoSAX*, one on 2000 August 20 in the soft state and the other on 2000 October 3 in the hard state [Table 5.2; Fiocchi et al., 2007]. The publicly available data are from three narrow field instruments: the Low Energy Concentrator Spectrometer [0.1–10 keV, LECS; Parmar et al., 1997], the Medium Energy Concentrator Spectrometer [1.3–10 keV, MECS; Boella et al., 1997b], and the Phoswich Detection System [15–300 keV, PDS; Frontera et al., 1997]. There are three MECS units (MECS1, 2, 3), but no data from MECS1 are available during these two observations. Thus we used only data from MECS2 and 3. We extracted two spectra, one for the soft-state observation and the other for the hard-state observation, and they are denoted as *sax*1 and *sax*2 hereafter (Table 5.2). The LECS and MECS data were extracted from circular regions of $8'$ radius centered on the source position. As our source is in the direction of the Galactic ridge, we cannot use “blank fields” measurement for background subtraction for the LECS. Instead, we used the semi-annuli method [Parmar et al., 1999]. For the MECS, the Galactic ridge emission should not be important as its Be window filters out a lot of low energy emission [Boella et al., 1997b]. Thus we used the “blank fields” method for the MECS as described in the instrument analysis guide. The PDS spectra were also extracted, with the background rejection method based on fixed Rise Time thresholds. The background of PDS spectra was obtained using observations during off-source intervals. All the spectra for each instrument were finally rebinned using the publicly available template files to sample the instrument resolution with the same number of channels at all energies.

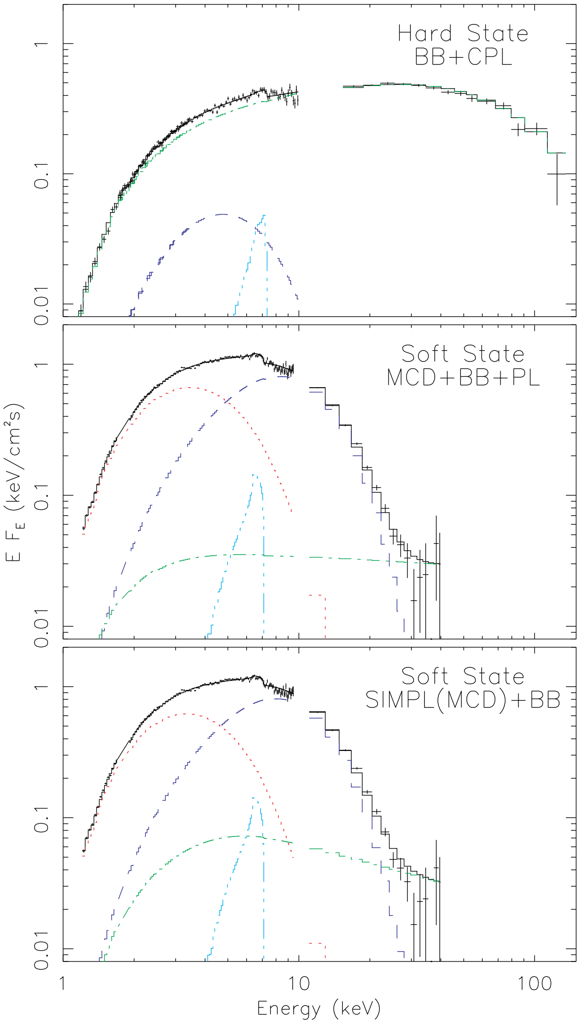

Figure 5-3: Example of unfolded spectra from different states using different models. The total model fit is shown as a black solid line. The MCD component (if included) is shown by a red dotted line, the BB component by a blue dashed line, the PL/CPL/SIMPL component by a green dot-dashed line, and the Fe line (modeled by the diskline model) by a cyan triple-dot-dashed line. For the SIMPL(MCD)+BB model, the MCD component shown is the unscattered part, and the plotted SIMPL component refers to the scattered part.

5.3 Spectral modeling

5.3.1 Spectral models and assumptions

We fit all ten spectra, *suz*1–*suz*8 from *Suzaku* (two from observation 402051010), and *sax*1–*sax*2 from *BeppoSAX*. For *Suzaku*, we jointly fit spectra from XIS0, XIS1, XIS2 (when available), XIS3 and the PIN. We used the energy bands with good calibration and high signal to noise ratios for each instrument: 1.2–1.7 and 1.9–9.5 keV for all XIS detectors, and 11.0-40.0 keV for the PIN. The normalization for each instrument is left free. The spectral fit results quoted later are all referenced to XIS0, as it has the best flux calibration. For *BeppoSAX* spectra, we jointly fit the LECS, MECS2, MECS3, and PDS. We utilized the 1.0–3.5 keV energy band for the LECS, 1.7–10.0 keV for the MECS, and 15.0–40.0 keV for the PDS (15.0–150.0 keV for the hard-state spectrum *sax*2). Their normalizations are also left free, but that of PDS relative to MECS was constrained to the range 0.77–0.93, a 90% confidence interval provided by the instrument analysis guide. The spectral fit results quoted later are all referenced to MECS2 (results from MECS3 differ by $< 2\%$). The fit of the Crab Nebula from the MECS using a single power law gives the photon index 2.1 and normalization 9.23, while the XIS gives 2.1 and 9.55, respectively. Thus the normalizations from both observatories appear to differ by less than 5%.

For the soft-state spectra, we tested three models for the continuum spectra: MCD+BB, MCD+BB+PL, and, SIMPL(MCD)+BB, respectively, where PL is a power law and SIMPL is a simple Comptonization model by Steiner et al. [2008]. MCD (diskbb in XSPEC) has two parameters: one is the temperature $kT_{\rm MCD}$ at the apparent inner disk radius $R_{\rm MCD}$, and the other is the normalization $N_{\rm MCD} \equiv (R_{\rm MCD,km}/D_{\rm 10kpc})^2 \cos i$, where $D_{\rm 10kpc}$ is the distance to the source in unit of 10 kpc and i is the disk inclination. BB (bbodyrad in XSPEC) assumes an isotropic blackbody spherical surface with radius $R_{\rm BB}$ and has two parameters, i.e., the temperature $kT_{\rm BB}$ and the normalization $N_{\rm BB} \equiv (R_{\rm BB,km}/D_{\rm 10kpc})^2$. PL is parametrized by the photon index of power law $\Gamma_{\rm PL}$ and the normalization $N_{\rm PL}$ (photons keV^{-1} cm^{-2} s^{-1} at 1 keV). SIMPL (in XSPEC12) is an empirical convolution model of Comptonization in which a fraction of the photons from an input seed spectrum is scattered into a power-law component. This model has only two free parameters, i.e., the photon power-law index $\Gamma_{\rm SIMPL}$ and the scattered fraction $f_{\rm SC}$. In addition, there is a flag parameter to control whether all the scattered photons are up-scattered in energy or are both up- and down-scattered. We assumed that the Comptonization seed photons are from the disk, and we specified that all the scattered photons are up-scattered in energy. We found that inclusion of down-scattering only changed our results within error bars. The best-fitting photon power-law index $\Gamma_{\rm SIMPL}$ turns out to be high (> 4) in most cases, a regime where the model is not suitable [Steiner et al., 2008]. Thus we constrained $\Gamma_{\rm SIMPL}$ to be less than 2.5, a value typically seen in the black-hole cases. No constraint on $\Gamma_{\rm PL}$ in the PL model was used, and the best-fitting values are all less than 2.5.

All models included an absorption component (we use model wabs in XSPEC). A large range of the value of hydrogen column density $N_{\rm H}$ ((1.2–2.4) $\times 10^{22}$ cm^{-2}) were reported in the literature [e.g., Di Salvo et al., 2005, Piraino et al., 2007, Fiocchi et al., 2007], probably due to different energy bands and/or different spectral models used. We started with modeling the soft-state continuum spectra, i.e., excluding the Fe line region 4.2–8.2 keV, to estimate $N_{\rm H}$. We first fit the seven *Suzaku* soft-state continuum spectra with models SIMPL(MCD)+BB and MCD+BB+PL, with the parameter of $N_{\rm H}$ left free. The model SIMPL(MCD)+BB gives an average of $N_{\rm H} = 1.67 \times 10^{22}$ cm^{-2}, with the standard deviation and averaged error bar 0.03 and 0.01 $\times 10^{22}$ cm^{-2}, respectively (The error bars are at 90% confidence level through out this paper, unless otherwise indicated). The model MCD+BB+PL gives a consistent, but slightly larger and less constrained, value ($N_{\rm H} = 1.74 \times 10^{22}$ cm^{-2}, with the standard deviation and averaged error bar 0.07 and 0.04 $\times 10^{22}$ cm^{-2}, respectively). The *BeppoSAX* soft-state spectrum gives $N_{\rm H} = (1.67^{+0.01}_{-0.02}) \times 10^{22}$ cm^{-2} with model SIMPL(MCD)+BB, and $(1.78 \pm 0.11) \times 10^{22}$ cm^{-2} with model MCD+BB+PL. Since these two values are consistent within errors, we used the better constrained value of $N_{\rm H}$, i.e., 1.67×10^{22} cm^{-2}, in the final spectral fitting of soft-state spectra.

The two hard-state continuum spectra *sax*2 and *suz*1 were fit with a BB plus a Comptonized component. We tested three choices of the Comptonization component: a broken power law (BPL; bknpower in XSPEC), a cut-off power law (CPL; cutoffpl in XSPEC), and the Comptonization model by Titarchuk [1994] (CompTT in XSPEC). BPL has two power laws connected at the break energy. CPL has an additional parameter, i.e., the cutoff energy $E_{\rm cut}$, compared with PL. CompTT is an analytic model describing Comptonization of soft photons in a hot plasma. We found model CPL+BB performs the best, followed by BPL+BB and CompTT+BB, in terms of the χ^2 values. Using spectrum *sax*2, which extends to 150 keV (instead of 40 keV for spectrum *suz*1), and assuming $N_{\rm H} = 1.67 \times 10^{22}$ cm^{-2}, we obtained the values of χ^2/ν 151.7/131, 193.7/130, and 342.7/130 for models CPL+BB, BPL+BB and CompTT+BB, respectively (excluding the Fe line region 4.2–8.2 keV). The order of performance of these models remains the same if we left $N_{\rm H}$ free, and also when we analyzed spectrum *suz*1. The spectral parameters of the BB from these models are in general similar (the temperature $kT_{\rm BB} \sim 1$ keV, and the normalization $N_{\rm BB} \lesssim 20$), and the Comptonization fractions are all above 90%. Below we adopt the results from model CPL+BB.

The fit of the CPL model to the *BeppoSAX* hard-state 15.0–150.0 keV spectrum (the BB contributes little at energies above 15.0 keV) gives a cutoff energy of 46 ± 7 keV. The cutoff energy cannot be well constrained from spectrum *suz*1, for which we used energies only up to 40 keV. Thus we fixed the cutoff energy to be 46 keV when we fit spectra *sax*2 and *suz*1. The best-fitting $N_{\rm H}$ from model CPL+BB is about 1.9×10^{22} cm^{-2} (the average from both spectra *sax*2 and *suz*1). The larger inferred $N_{\rm H}$ from the hard-state spectra than that from the soft-state spectra might be a systematic effect of different ways of handling the Comptonization at the low energy; here we simply used the power-law form extending to low energy [see also Steiner et al., 2008]. We present results for the hard state using both $N_{\rm H} = 1.9$ and 1.67×10^{22} cm^{-2}.

There are strong broad Fe lines in all spectra [see also Reis et al., 2009]. They were either modeled by broad Gaussian lines or by the diskline (included in XSPEC) model [Fabian et al., 1989]. The diskline model describes line emission from a relativistic accretion disk. Its parameters are: the line energy $E_{\rm line}$ in unit of keV, the power law dependence of emissivity (β), the disk inner and outer radii in units of GM/c^2 (G is the gravitation constant, M the mass of the compact object, and c the light speed), the disk inclination i, and the normalization (photons cm^{-2} s^{-1}). Figure 5-3 shows some examples of unfolded spectra at different states using different models, with the Fe lines modeled by the diskline model. The top panel shows the hard-state spectrum *sax*2 using model CPL+BB. The lower two panels show the soft-state spectrum *suz*2 using models MCD+BB+PL and SIMPL(MCD)+BB, respectively.

We scaled the luminosity and radius related quantities using a distance of 7.4 kpc [Haberl and Titarchuk, 1995], unless indicated otherwise. The flux and its error bars are all calculated over an energy band of 0.001–200 keV (1.5-200 keV for CPL/PL components) using

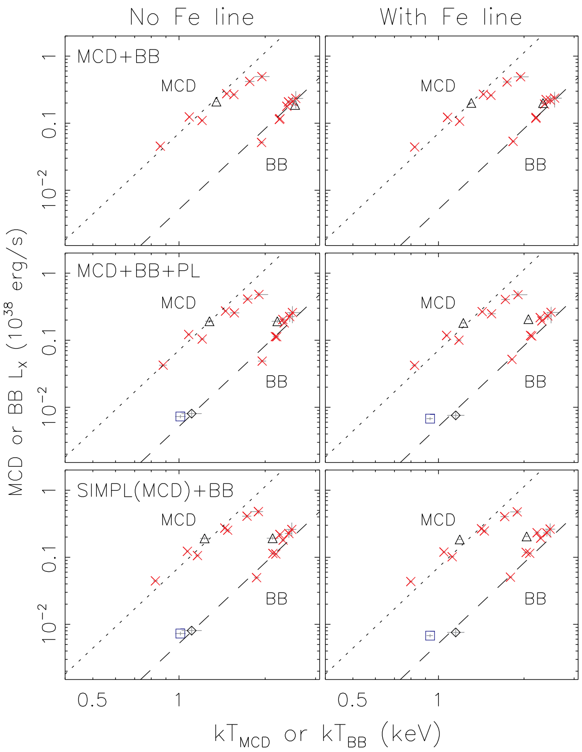

Figure 5-4: The luminosity of the thermal components versus their characteristic temperatures. The panels in the left column show the results of the fit with the Fe line region (4.2–8.2 keV) excluded, while the panels in the right column show the fitting results with the Fe line modeled by the diskline model. The symbols in each panel denote different spectral states and different observatories: *BeppoSAX* hard (black diamond) and soft (black triangle) states, and *Suzaku* hard (blue square) and soft (red crosses) states. For the case of Model SIMPL(MCD)+BB, the MCD component shown refers to the original seed spectrum (i.e., before scattering). The dotted lines correspond to the NS burst radius of 7.4 km (see the text), and the dashed lines correspond to $R = 2.0$ km, assuming $L_X = 4\pi R^2 \sigma T^4$.

the cflux model in XSPEC12. As there is little emission of the thermal components outside the above energy band, the values are essentially bolometric for thermal components. For the MCD component, we assume the inclination to be 30°, from the fitting of Fe lines (see below).

5.3.2 Spectral fit results

The spectral fitting results of the thermal components (MCD and BB) from all tested models are shown in Figure 5-4, and results of all spectral components from some models are tabulated in Tables 5.3 (MCD+BB+PL+diskline; soft state), 5.4 (SIMPL(MCD)+BB+diskline; soft state), and 5.5 (CPL+BB+diskline; hard state). The panels on the left in Figure 5-4 show the results of the fit with the Fe line region 4.2–8.2 keV excluded, while those on the right show the corresponding results with Fe lines fit by the diskline model. The red crosses and the black stars are for soft-state spectra *suz*2–*suz*8 and *sax*1, respectively, and the panels from the top to the bottom correspond to continuum models MCD+BB, MCD+BB+PL, and SIMPL(MCD)+BB respectively. For model SIMPL(MCD)+BB, the MCD component shown is the original value before scattering. The blue squares and the black diamonds are

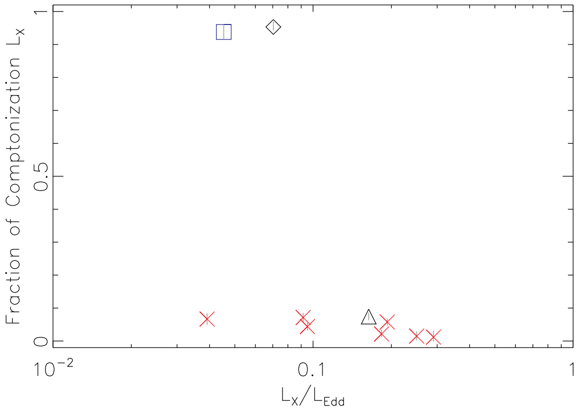

Figure 5-5: The energy fraction of Comptonized luminosity versus the total luminosity, from model MCD+BB+PL.

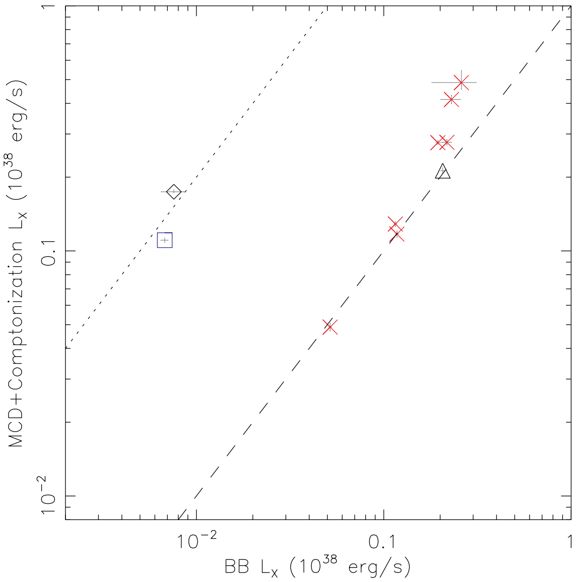

Figure 5-6: The luminosity of the MCD component plus Comptonization versus the BB luminosity. The results are from model MCD+BB+PL+diskline, and thus the Comptonization is modeled by PL. Model SIMPL(MCD)+BB+diskline gives similar results. The dashed and dotted lines mark the ratios of 1 and 0.05 of the BB luminosity versus the MCD component plus Comptonization luminosity, respectively.

Table 5.3. Spectral modeling results of soft-state observations using MCD+BB+PL+diskline

	$kT_{\rm MCD}$ (keV)	$N_{\rm MCD}$	$kT_{\rm BB}$ (keV)	$N_{\rm BB}$	$\Gamma_{\rm PL}$	$N_{\rm PL}$	$E_{\rm line}$ (keV)	β	EW (ev)	$\chi^2_\nu(\nu)$	$L_{\rm X,Edd}$
suz3	$0.82^{+0.01}_{-0.02}$	111^{+10}_{-5}	$1.81^{+0.02}_{-0.03}$	$6.77^{+0.65}_{-0.33}$	$2.05^{+0.19}_{-0.30}$	$0.015^{+0.012}_{-0.009}$	$6.52^{+0.07}_{-0.06}$	$-4.40^{+0.43}_{-0.50}$	165^{+44}_{-32}	1.15(2485)	0.039 ± 0.001
suz2	1.18 ± 0.02	63 ± 4	$2.11^{+0.03}_{-0.04}$	$8.46^{+0.85}_{-0.60}$	$2.10^{+0.12}_{-0.15}$	0.044 ± 0.015	$6.75^{+0.06}_{-0.03}$	$-4.21^{+0.23}_{-0.46}$	208^{+25}_{-26}	1.18(2570)	0.092 ± 0.002
suz7	1.07 ± 0.01	110^{+4}_{-5}	2.13 ± 0.03	$7.99^{+0.53}_{-0.48}$	$2.11^{+0.17}_{-0.25}$	0.028 ± 0.016	$6.78^{+0.04}_{-0.06}$	$-4.55^{+0.41}_{-0.37}$	202^{+27}_{-20}	1.24(1949)	0.095 ± 0.001
sax1	$1.22^{+0.03}_{-0.02}$	98^{+6}_{-8}	$2.07^{+0.03}_{-0.02}$	$15.98^{+0.77}_{-1.17}$	$1.93^{+0.18}_{-0.27}$	$0.051^{+0.039}_{-0.031}$	$6.85^{+0.11}_{-0.17}$	$-4.71^{+0.70}_{-0.86}$	223^{+40}_{-28}	1.43(189)	0.164 ± 0.003
suz6	$1.43^{+0.02}_{-0.01}$	78 ± 2	$2.31^{+0.01}_{-0.03}$	$9.69^{+0.55}_{-0.27}$	$1.50^{+2.80}$	$0.004^{+0.006}_{-0.001}$	$6.80^{+0.06}_{-0.05}$	$-3.37^{+0.30}_{-0.36}$	190^{+21}_{-39}	1.23(1913)	0.183 ± 0.003
suz8	$1.54^{+0.05}_{-0.04}$	54 ± 5	2.28 ± 0.04	$11.42^{+1.33}_{-1.29}$	$2.10^{+0.13}_{-0.19}$	0.075 ± 0.034	$6.69^{+0.04}_{-0.05}$	$-3.42^{+0.35}_{-0.25}$	204^{+12}_{-39}	1.17(1910)	0.193 ± 0.006
suz4	$1.72^{+0.06}_{-0.05}$	56 ± 5	2.43 ± 0.07	$9.44^{+2.21}_{-2.00}$	$1.50^{+0.66}$	$0.004^{+0.020}_{-0.004}$	$6.61^{+0.09}_{-0.08}$	$-2.86^{+0.40}_{-0.62}$	119^{+36}_{-41}	1.09(1756)	0.250 ± 0.012
suz5	$1.9^{+0.14}_{-0.09}$	44^{+6}_{-8}	$2.49^{+0.16}_{-0.09}$	$9.59^{+3.30}_{-4.33}$	$1.50^{+3.16}$	$0.003^{+0.040}_{-0.003}$	$6.84^{+0.13}_{-0.08}$	$-4.07^{+0.81}_{-2.05}$	135^{+47}_{-34}	1.02(1726)	0.291 ± 0.030

Note. — Listed in order of the source total luminosity. See §5.3.1 for the meaning of each parameter. The normalizations of the MCD and BB models are based on assumption of the distance to the source of 10 kpc. For the diskline model, the inclination is fixed at 30°, and inner disk radius at $6GM/c^2$ (see text). EW is the equivalent width of Fe modeled by the diskline model, but it is not a parameter of the model. The last column is the total luminosity in unit of the Eddington luminosity (§5.3.2), and the error bars are calculated based on simple error propagation from individual spectral components.

Table 5.4. Spectral modeling results of soft-state observations using SIMPL(MCD)+BB+diskline

	$kT_{\rm MCD}$ (keV)	$N_{\rm MCD}$	$kT_{\rm BB}$ (keV)	$N_{\rm BB}$	$\Gamma_{\rm SIMPL}$	$f_{\rm SC}$	$E_{\rm line}$ (keV)	β	EW (ev)	$\chi^2_\nu(\nu)$	$L_{\rm X,Edd}$
suz3	0.80 ± 0.01	130^{+6}_{-5}	1.79 ± 0.02	$6.90^{+0.43}_{-0.31}$	$2.50_{-0.12}$	$0.06^{+0.05}_{-0.01}$	$6.52^{+0.07}_{-0.06}$	$-4.36^{+0.44}_{-0.54}$	156^{+44}_{-31}	1.14(2485)	0.041 ± 0.001
suz2	1.12 ± 0.02	79^{+4}_{-3}	2.04 ± 0.04	$9.77^{+0.82}_{-0.73}$	$2.50_{-0.12}$	0.06 ± 0.01	6.76 ± 0.05	$-4.36^{+0.31}_{-0.42}$	201^{+26}_{-24}	1.18(2570)	0.096 ± 0.002
suz7	1.05 ± 0.01	122^{+4}_{-3}	2.09 ± 0.03	$8.43^{+0.56}_{-0.49}$	$2.50_{-0.18}$	0.03 ± 0.01	6.78 ± 0.05	$-4.57^{+0.40}_{-0.43}$	198^{+27}_{-26}	1.24(1949)	0.098 ± 0.002
sax1	1.19 ± 0.02	113^{+1}_{-4}	2.04 ± 0.03	$16.73^{+0.92}_{-0.94}$	$2.50_{-0.19}$	$0.05^{+0.01}_{-0.02}$	$6.88^{+0.09}_{-0.14}$	$-4.81^{+0.69}_{-0.95}$	231^{+38}_{-37}	1.39(189)	0.170 ± 0.003
suz6	$1.42^{+0.01}_{-0.02}$	80 ± 2	$2.29^{+0.02}_{-0.03}$	$10.01^{+0.69}_{-0.48}$	$2.50_{-0.61}$	$0.01^{+0.00}_{-0.01}$	$6.80^{+0.07}_{-0.06}$	$-3.35^{+0.40}_{-0.45}$	187^{+20}_{-36}	1.22(1914)	0.185 ± 0.003
suz8	1.45 ± 0.03	68 ± 3	2.22 ± 0.04	$13.48^{+1.37}_{-1.01}$	$2.50_{-0.30}$	0.03 ± 0.01	$6.71^{+0.06}_{-0.07}$	$-3.66^{+0.34}_{-0.37}$	182^{+41}_{-10}	1.17(1910)	0.201 ± 0.004
suz4	1.71 ± 0.05	57^{+5}_{-4}	$2.41^{+0.05}_{-0.07}$	$9.78^{+2.30}_{-1.61}$	$2.43_{-0.38}$	$0.01^{+0.00}_{-0.01}$	$6.61^{+0.12}_{-0.08}$	$-2.90^{+0.48}_{-0.79}$	120^{+34}_{-41}	1.09(1757)	0.251 ± 0.012
suz5	$1.89^{+0.12}_{-0.10}$	45^{+7}_{-6}	2.47 ± 0.09	$9.98^{+3.90}_{-3.28}$	$2.42_{-0.57}$	$0.00^{+0.01}_{-0.00}$	$6.84^{+0.13}_{-0.08}$	$-4.05^{+0.84}_{-2.13}$	133^{+46}_{-27}	1.02(1727)	0.289 ± 0.026

Note. — Same as Table 5.3, but for model SIMPL(MCD)+BB+diskline.

Table 5.5. Spectral modeling results of hard-state observations using BB+CPL+diskline

	$N_{\rm H}$ (10^{22} cm^{-2})	$T_{\rm BB}$ (keV)	$N_{\rm BB}$	$\Gamma_{\rm CPL}$	$N_{\rm CPL}$	$E_{\rm line}$ (keV)	β	EW (ev)	$\chi^2_\nu(\nu)$	$L_{\rm X,Edd}$
suz1	1.67f	$0.93^{+0.01}_{-0.02}$	$18.6^{+1.78}_{-0.60}$	$1.2^{+0.02}_{-0.01}$	0.053 ± 0.002	$6.82^{+0.07}_{-0.06}$	$-4.71^{+0.58}_{-0.72}$	177^{+52}_{-45}	1.13(2476)	0.053 ± 0.001
sax2	1.67f	1.25 ± 0.05	$6.9^{+1.32}_{-1.02}$	1.36 ± 0.01	0.115 ± 0.004	$6.84_{-0.17}$	$-2.5^{+0.93}_{-1.04}$	121^{+127}_{-105}	1.39(206)	0.070 ± 0.001
suz1	1.9f	0.93 ± 0.02	$12.61^{+1.51}_{-1.36}$	1.38 ± 0.01	0.080 ± 0.002	6.82 ± 0.07	$-4.98^{+0.77}_{-1.33}$	146^{+43}_{-41}	1.12(2476)	0.045 ± 0.001
sax2	1.9f	$1.15^{+0.08}_{-0.07}$	$6.15^{+2.00}_{-1.86}$	1.42 ± 0.01	0.138 ± 0.005	$6.93_{-0.22}$	$-3.41^{+1.06}_{-1.29}$	199^{+111}_{-175}	1.12(206)	0.070 ± 0.001

Note. — Same as Table 5.3, but for model BB+CPL+diskline and for the hard-state data. The cutoff energy of the CPL is fixed at 46 keV.

for hard-state spectra *suz*1 and *sax*2, respectively, and the results using model CPL+BB are repeated in the middle and bottom panels (using $N_{\rm H} = 1.9 \times 10^{22}$ cm^{-2}), but not in the top panels (as explained below). The dotted lines in Figure 5-4 correspond to the NS burst radius of $R_{\rm burst} \sim 7.4$ km (at a distance of 7.4 kpc), assuming $L_{\rm X} = 4\pi R^2 \sigma T^4$. The NS radius was derived from spectral fitting to Type I X-ray bursts of this source using *RXTE* data [see also Gottwald et al., 1989]. The dashed lines correspond to $R = 2.0$ km, which is about the average visible BB emission size.

The details of fitting of the Fe line with the diskline model are as follows. We initially did not constrain the disk inclination. The best-fitting values are in the range of 20–30°. However, the line energies tend to reach 6.97 keV, the upper limit allowed by the Fe line. Fixing the disk inclination to be 30° only increases the χ^2 values typically <10 (for $\gtrsim 1000$ degrees of freedom), but most of the best-fitting line energies are in the range of 6.4–6.97 keV. Thus we fixed the disk inclination to be $i = 30°$. For most of the soft-state spectra, the inner disk radius inferred from the diskline model reaches 6 GM/c^2, the innermost stable circular orbit, which is consistent with our continuum modeling (§5.4). Thus in the final fitting, we fix it to be 6 GM/c^2. For the hard-state spectra, the Fe lines are much weaker, and the best-fitting inner disk radius in the diskline model is quite uncertain. The lower error bar reaches 6 GM/c^2 for the two observatories using both $N_{\rm H} = 1.9$ and 1.67×10^{22} cm^{-2}. For simplicity, we then fixed the inner disk radius in the diskline model to be 6 GM/c^2 for the hard-state spectra to derive the final results. The obtained Fe line flux and equivalent width are not sensitive to such details.

From Figure 5-4, we see that the MCD and BB components roughly follow the $L \propto T^4$ tracks (which implies a constant apparent emission area) for all models, with the extent of deviation described in §5.4. The inner disk radius is comparable with the NS radius, while the visible BB emission is about 1/14 of the NS surface in both the hard and the soft states. The $kT_{\rm MCD}$ has values from ∼0.8 to 1.9 keV, and $kT_{\rm BB}$ from ∼1.8 to 2.5 keV. These results are consistent with the results for XTE J1701-462, which shows a much large luminosity range [Lin et al., 2009b]. Results of the MCD and BB components with Fe lines fit with the diskline model in general are consistent with those without the Fe line region excluded in the fit for each continuum model, to within 10% for $N_{\rm MCD}$ and within 20% for the $N_{\rm BB}$. Spectrum *sax*1 gives larger differences ($\sim 40\%$ for $N_{\rm BB}$), probably because of its smaller energy band and lower energy resolution (only five channels above 10 keV and none in the energy band of 10–15 keV).

Detailed investigation of Comptonization follows. The black-hole X-ray binaries show weak Comptonization in the soft/thermal state [Remillard and McClintock, 2006]. The relevance of weak Comptonization models to the soft state of accreting NS is also one of the main differences between our spectral model and the classical two-components models found in the literature (§5.1). Figure 5-5 plots the fraction of Comptonized luminosity versus the total luminosity. The total luminosity is normalized by the Eddington luminosity $L_{\rm EDD}$, which is derived from the type I X-ray bursts showing photospheric radial expansion and corresponds to an average peak flux of about 4×10^{-8} erg cm^{-2} s^{-1} [Galloway et al., 2006]. Figure 5-5 illustrates the results obtained with the model MCD+BB+PL+diskline. It shows that Comptonization only constitutes $< 10\%$ of the emission in the soft state, but $> 90\%$ in the hard state. For the soft-state data, the fraction of Comptonized luminosity decreases with luminosity on the whole. Spectra *suz*4 and *suz*5 have the highest luminosity, and the inclusion of Comptonized components in the fit only marginally improves the χ^2 values, i.e., a reduction < 3 for $\gtrsim 1000$ degrees of freedom. This is also true for model SIMPL(MCD)+BB.

Results of the thermal components between models MCD+BB+PL and SIMPL(MCD)+BB are generally similar, but differences of $> 20\%$ can occur in some cases (e.g., 26% for $N_{\rm MCD}$ from the spectrum *suz*2; compare Table 5.3–5.4). Due to weak Comptonization in the soft state, model MCD+BB in general also gives similar results of the thermal components (e.g., flux differs $< 5\%$ and $N_{\rm BB}$ by $< 20\%$) and acceptable reduced χ^2 values (< 2.0; but 2.1 for *sax*1 with Fe line region fit with model diskline). The largest differences in best-fitting spectral parameters from model MCD+BB compared with those from models MCD+BB+PL and SIMPL(MCD)+BB are from *BeppoSAX* spectrum *sax*1 ($N_{\rm BB}$ differs by $\sim$50%). Due to strong Comptonization in the hard state, fit of model MCD+BB for the hard-state spectra *suz*1 and *sax*2 gives very large values of χ^2 compared with model CPL+BB and very unphysical results (e.g., $N_{\rm MCD} \leq 2$). Thus these results are not shown in the top panels in Figure 5-4.

More details of the fit results of the hard-state spectra follow. Table 5.5 gives the fit results of hard-state spectra using model CPL+BB+diskline. It lists results for two cases, corresponding to $N_{\rm H} = 1.67$ and 1.9×10^{22} cm^{-2} respectively. Using $N_{\rm H} = 1.9 \times 10^{22}$ cm^{-2} tends to give a smaller BB emission area and a higher photon index of the CPL model. It also gives more similar values of the photon index between spectra *sax*2 and *suz*1 than using $N_{\rm H} = 1.67 \times 10^{22}$ cm^{-2}. Both values of $N_{\rm H}$ give high fractions of Comptonization, >90%.

One of our main goals of using the broad-band spectra is to check whether there is still thermal accretion disk emission in the hard state. We tried to include the MCD component in the hard-state spectra (*suz*1 and *sax*2) with model CPL+MCD+BB, with either the Fe modeled with the diskline model or with the Fe region excluded in the fit. $N_{\rm H}$ was either fixed at 1.67 or 1.9 $\times 10^{22}$ cm^{-2}, or left free in the fit. The best-fitting values of $kT_{\rm MCD}$ tend to go below 0.2 keV, with upper limit at a 90%-confidence level < 0.25 keV. The normalizations of the MCD component $N_{\rm MCD}$ are not well constrained but mostly have lower limits > 3000, much larger than the values seen in the soft state. For the cases of $N_{\rm H} = 1.67 \times 10^{22}$ cm^{-2}, we found that $kT_{\rm MCD} < 0.1$ keV and lower limit of $N_{\rm MCD}$ can be zero. Thus, if we assume a physically visible disk, then we cannot exclude either possibility, i.e., that the disk in the hard state might be truncated at a very large radius and/or the temperature is below 0.1 keV. For all cases, the flux of the MCD component is $< 2\%$ of the total flux (absorbed or unabsorbed; 1–200 keV).

The BB component presents in both the hard and soft states, and it can trace the emission from the boundary layer. We can compare this component with the other spectral components to infer different accretion processes in different states. We plot in Figure 5-6 the luminosity of the MCD component plus Comptonization (PL/CPL) versus the BB luminosity from model MCD+BB+PL. Model SIMPL(MCD)+BB gives similar results. The hard-state data (diamond and square symbols) are from model CPL+BB. If we assume the Comptonization energy comes from the accretion disk, Figure 5-6 shows the energy released in the disk versus that released in the boundary layer. The dashed and dotted lines correspond to the ratios of 1 and 0.05 of the BB luminosity versus the MCD component plus Comptonization luminosity, respectively. They are about the average values for the soft- and hard-state observations, respectively. This means that there is a much lower portion of energy released in the boundary layer in the hard state than in the soft state. Similar results were interpreted as a consequence of a strong jet in the hard state in Lin et al. [2007b, Chapter 4].

5.3.3 Relativistic Fe lines

We first fit the Fe line with a Gaussian line. The results of the continuum components on the whole are very similar to those with Fe lines modeled by the diskline model, whose results will be shown below. However, the central line energies tend to reach 6.4 keV or lower. We constrained the central line energy to be within 6.4–6.97 keV (allowed Fe line energies), and obtained the FWHM of about 1.2 keV. The obtained line equivalent width and flux show much larger uncertainty than those obtained using the diskline model. Considering the broad, relativistic feature of the Fe lines from this source [e.g., Reis et al., 2009, Di Salvo et al., 2009], we focus on the results using the diskline model hereafter.

The results of fitting Fe lines with the diskline model are shown in Figure 5-7. For the soft state, we only show results using model MCD+BB+PL for continuum spectra, as model SIMPL(MCD)+BB gives very similar results. The lower eight panels are for soft-state spectra and have been shown (top to bottom) in order of increasing source luminosity. The upper two panels show hard-state spectra that are fit with model CPL+BB. All spectra show a broad feature of the Fe emission line [see also Reis et al., 2009]. Tables 5.3 and 5.4 give the Fe line equivalent width for each soft-state spectrum. Figure 5-8 plots these results using model MCD+BB+PL for the continuum spectra. There is a possible weak trend that the Fe line equivalent width first increases and then decreases with increasing source luminosity, varying between about 120 and 230 eV.

Fe emission lines in X-ray binaries are believed to be the most obvious reaction of an accretion disk to irradiation by an external source of hard X-rays due to a combination of high fluorescent yield and large cosmic abundance [Miller, 2007]. Photons with high energy ($\geq$6.4 keV) can potentially eject an Iron K-shell electron, and de-excitation of the resulting ion can lead to a Kα line photon. To investigate the irradiation source of the Fe lines, we show in Figure 5-9 the dependence of the Fe energy line flux on the BB energy flux (upper panel) and Comptonization (PL/CPL) flux (lower panel). The soft-state data show that the Fe line flux increases monotonically with the BB flux, but has no clear dependence on the Comptonization flux. This might imply that it is the boundary layer emission that illuminates the accretion disk and produces the Fe line [see also Cackett et al., 2009b]. The Fe line energy flux is about 3% of the BB energy flux (solid lines), but the ratio is lower for the lower-luminosity spectra, especially $suz3$ (2%). This is probably because as the BB temperature increases with luminosity, a larger and larger fraction of the BB emission can have photons with energy above the Fe line energy to be available as the Fe line irradiation source. The total visible Fe line photon flux is about 7–8% of the visible BB photon flux above 6.4 keV for all soft-state spectra.

The hard-state data (diamond/square symbols) in Figure 5-9 in the upper panel show that there is much higher Fe line flux relative to the BB continuum in the hard state compared to the soft state. This might indicate that the BB emission is not the only source illuminating the accretion disk to produce the Fe line in the hard state. From the lower panel, we can see that there is strong Comptonization flux (PL/CPL components) available in the hard state. However, using the reference lines and comparing the upper and lower panels, we see that the Comptonization emission is not as efficient as the BB emission to illuminate the accretion disk and produce the Fe line. This can be explained if the Comptonization emission is located farther away from the accretion disk than the boundary layer. We also caution, again, that some BB flux may be screened from the observer's view by the accretion disk.

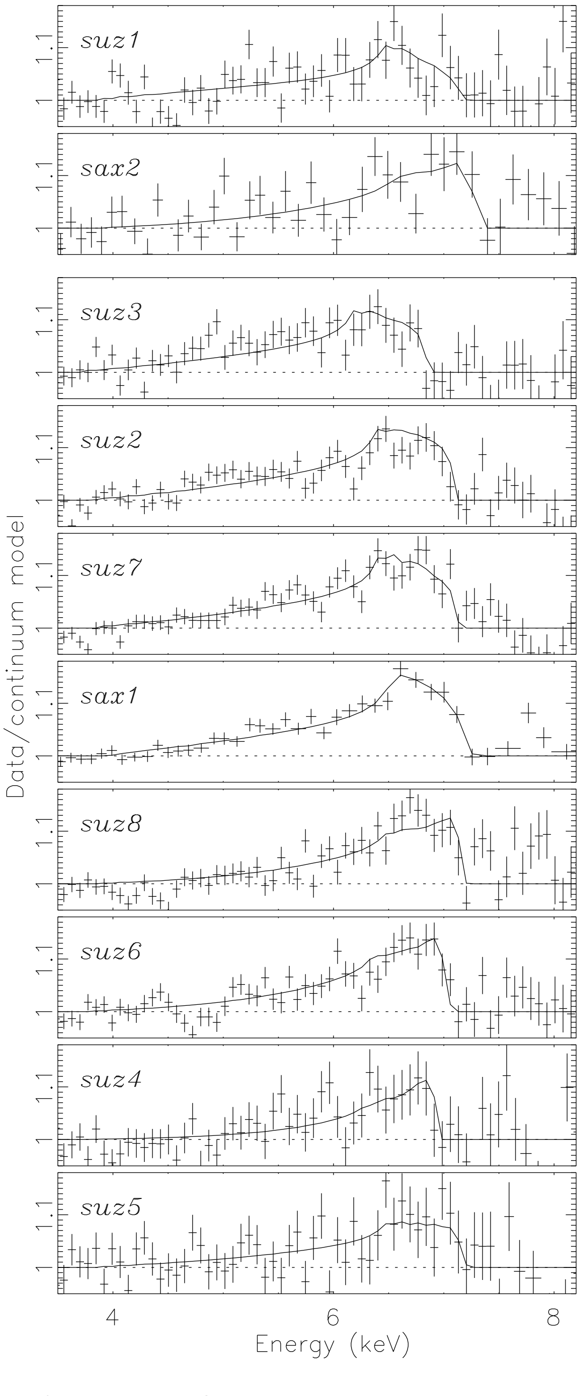

Figure 5-7: Fe lines of all spectra, fit by the diskline model. The upper two panels are for the hard state (spectra *sax*2 and *suz*1), while others for the soft state. The soft-state continuum is fit by model MCD+BB+PL, while model SIMPL(MCD)+BB gives similar results. From top to bottom, the source luminosity increases, except for the hard-state spectra *sax*2 and *suz*1, which are put on the top panels and have luminosities between that of *suz*3 and *suz*2.

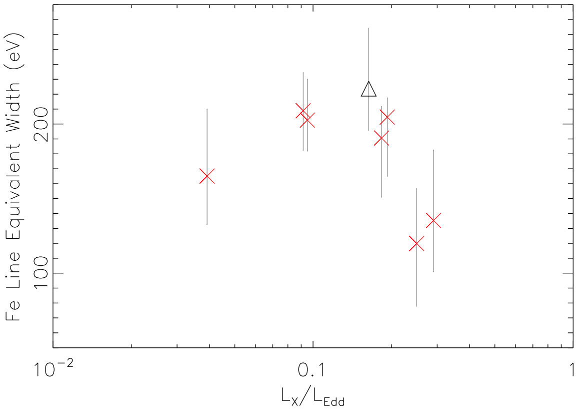

Figure 5-8: The variation of the equivalent width of the Fe lines with the source luminosity, for soft-state data only. The continuum spectra are fit by model MCD+BB+PL, and model SIMPL(MCD)+BB gives quite similar results.

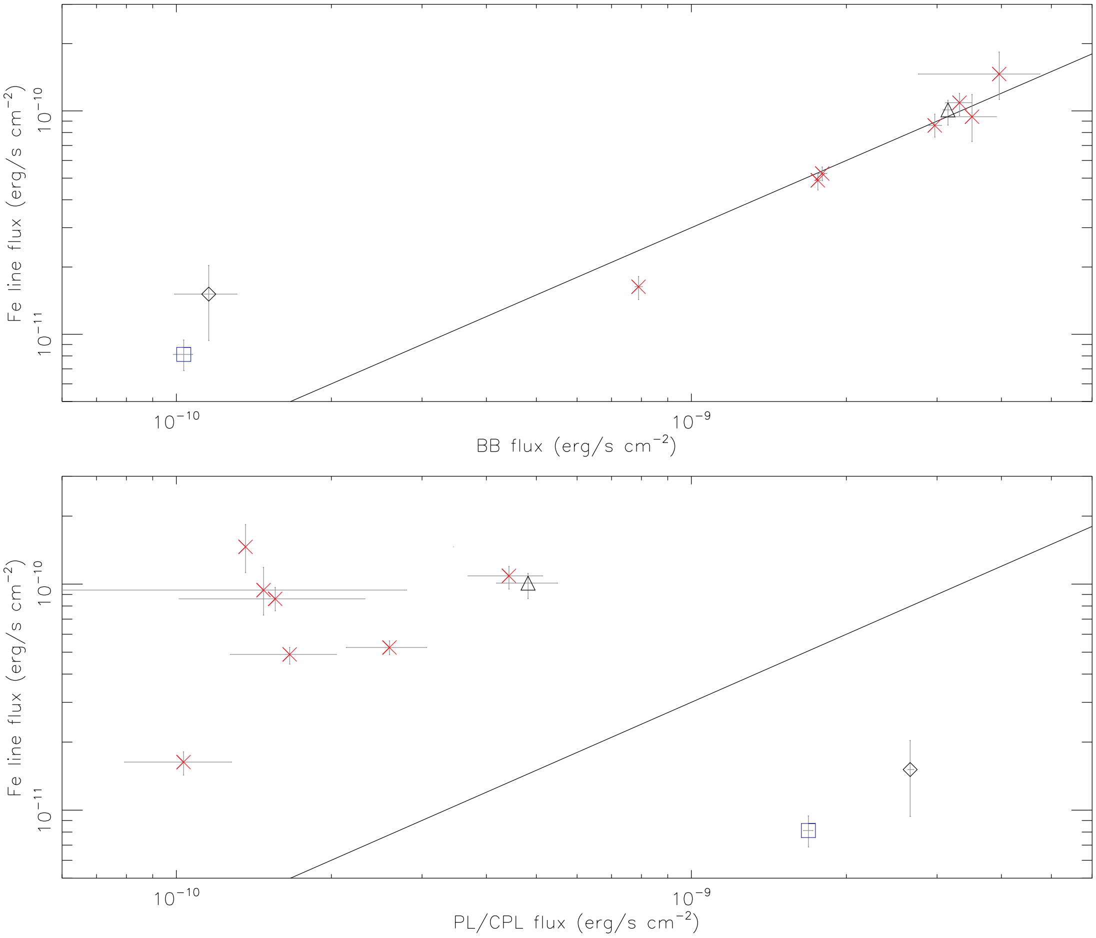

Figure 5-9: Dependence of Fe line flux on the BB flux (upper panel) and Comptonization flux (PL/CPL components; lower panel). The solid lines mark the ratio of 3% of the Fe line flux over the BB flux or the Comptonization flux.

5.4 Discussion

5.4.1 Inner disk radius

In Lin et al. [2007b, Chapter 4], our spectral modeling of two atoll sources, i.e., Aql X-1 and 4U 1608-522, using the MCD+BB model plus weak Comptonization showed the MCD behavior close to the $L_{\rm MCD} \propto T_{\rm MCD}^4$ track. In contrast, classical two-component models resulted in constant or slightly decreasing temperatures of the thermal component (MCD or BB) with increasing luminosity. We note, however, that in that study we used *RXTE* data and the MCD component in the low-luminosity soft state could not be well constrained and the power index of the weak Comptonization had to be imposed to be < 2.5. In this study, we used *Suzaku* and *BeppoSAX* spectra, which extend to energy 1 keV, and the MCD components are well constrained for all soft-state spectra. The power index of the PL component is also well constrained from spectral fit. All this motivates us to evaluate how closely the MCD component follows the $L_{\rm MCD} \propto T_{\rm MCD}^4$ track more quantitatively.

Our spectral modeling of broad-band spectra of 4U 1705-44 shows a track that is flatter than the $L_{\rm MCD} \propto T_{\rm MCD}^4$ relation, with more than an order of magnitude variation in luminosity. There is a slight decrease of $R_{\rm MCD}$ at higher luminosity. Spectral fitting with Comptonization modeled by PL suggests $L_{\rm MCD} \propto T_{\rm MCD}^{3.3\pm0.1}$, while fitting with Comptonization modeled by SIMPL results in $L_{\rm MCD} \propto T_{\rm MCD}^{3.1\pm0.1}$. Such deviations have been seen in several black-hole X-ray binaries, and it is normally believed to be due to the spectral hardening effect, instead of real change in the inner disk radius [Shafee et al., 2006, Davis et al., 2006]. Spectral hardening arises when the electron scattering dominates over absorption as the main opacity source. In such a situation, the local specific flux in the disk appears as a simple dilute blackbody with a color temperature higher than the effective temperature by a factor of $f_{\rm col}$ [Shimura and Takahara, 1995]. This factor slightly increases with luminosity/temperature. Based on a simple analytic estimate of the hardening factor, Davis et al. [2006] suggested a $L_{\rm MCD} \propto T_{\rm MCD}^3$ relation. It should be noted that the extent to which the hardening factor depends on luminosity can vary with inclinations, mass of the compact object, etc. A detailed numeric simulation to obtain how the hardening factor behaves for an accreting NS is worthwhile but is beyond the scope of this paper.

We note that there are possibly other factors causing the above deviation. One is real change of the inner disk radius in some part of the soft state. Lin et al. (2009, in preparation) reports that the inner disk radius appears to be larger in the so-called lower left banana of the soft state than in other parts of the soft state, where the inner disk radius appears to be much more constant. The lower left banana branch, with smallest values of the soft color in the soft state, is associated with frequent occurrences of kHz QPOs [van der Klis, 2006]. Although *Suzaku* has PIN data with high time resolution, low PIN count rates and weakness of kHz QPOs in 4U 1705–44 make it difficult to search for kHz QPOs directly to see whether any of our observations are in the lower left banana. However, based on the soft color, we can see that spectra *suz*3 and *suz*7 are in the leftmost part of the soft state (with the smallest values of the soft color among our *Suzaku* soft-state observations; Table 5.1). The two spectra did have larger best-fitting inner disk radii than other soft-state observations (Tables 5.3–5.4). For example, even though spectra *suz*2 and *suz*7 both have luminosity about 0.1 $L_{\rm Edd}$ (Tables 5.3–5.4), spectrum *suz*7 has a much larger inferred inner disk radius, by about 30% (well above the uncertainty), than spectrum *suz*2. Thus it is possible that *suz*3 and *suz*7 are in the lower left banana. Excluding these two spectra, *Suzaku* soft-state observations suggest a relation approximately of $L_{\rm MCD} \propto T_{\rm MCD}^{3.6}$. It is also possible that the above deviation of our results from the $L_{\rm MCD} \propto T_{\rm MCD}^4$ relation is due to our simple descriptions of the weak Comptonization and the boundary layer.

Modeling using a more realistic spectral model for the accretion disk can potentially address directly whether the inner disk radius is constant and might even obtain its real value. Such a model should not only include all relativistic effects (gravitational redshift, frame dragging, Doppler boosting, light bending, and self-irradiation, etc.), such as the KERRBB model [Li et al., 2005], but also need careful calculation of the disk structure and radiative transfer, such as the BHSPEC model [Davis and Hubeny, 2006]. The illumination of the boundary layer on the disk might also need to be considered. Such a model has not been developed yet. Moreover, such a way of modeling requires fairly accurate information of system parameters such as the mass of the compact object, the inclination, and the distance [McClintock et al., 2006]. In addition, an accurate modeling of the disk also requires accurate modeling of other components, and so the boundary layer, as a simple blackbody description is another concern. Due to the above difficulties, treatments with significant efforts would be required in order to obtain meaningful results.

5.4.2 Constraint on the magnetic field in 4U 1705–44

We perform a rough estimate of the magnetic field in 4U 1705-44, under the assumption that the disk is truncated at the ISCO in our soft-state observations. This requires the magnetic field to be dynamically unimportant for these soft-state observations. That is, the Alfvén radius $r_{\rm A}$, the radius at which the magnetic pressure is roughly the sum of the ram and gas pressure, should be smaller than the ISCO. Based on Equations 6.19–6.20 in Frank et al. [1985], we have

$$r_{\rm A} \sim 7.5 \left(\frac{k_{\rm A}}{0.5}\right) \left(\frac{M_{\rm NS}}{M_\odot}\right)^{1/7} \left(\frac{R_{\rm NS}}{10~{\rm km}}\right)^{10/7} \left(\frac{L}{10^{37}~{\rm erg/s}}\right)^{-2/7} \left(\frac{B}{10^8~{\rm G}}\right)^{4/7}~{\rm km}, \qquad (5.1)$$

where B is the magnetic field strength at the surface of the NS and $k_{\rm A}$ is the correction from the spherical accretion to disk accretion and is about 0.5. This formula assumes a dipole magnetic field. We further assume $M_{\rm NS} = 1.4~M_\odot$ (such that $R_{\rm in} = 12.4$ km), and $R_{\rm NS} = 10$ km. The above expression shows that our obtained value of B will only weakly depend on the NS mass (a power of 1/4). Using $L = 10^{37}$ erg/s, from the faintest soft-state spectrum *suz*2, and the constraint $r_{\rm A} < R_{\rm in}$, we find $B < 1.9 \times 10^8$ G. This limit should be larger by 60% if in fact $R_{\rm in}$ for *suz*2 is larger by 30% (see above). We can also assume that $r_{\rm A}$ is less than $R_{\rm NS}$, which would decrease the above limit by 30%.

5.4.3 The boundary layer

We see that the apparent emission area of the boundary layer, modeled by BB, is roughly constant from the hard to the soft states with the luminosity of the boundary layer covering ~0.003-0.11 $L_{\rm EDD}$. Spectral fitting with Comptonization modeled by PL and Fe lines by the diskline model suggests $L_{\rm BB} \propto T_{\rm BB}^{4.1\pm0.1}$, while fitting with Comptonization modeled by SIMPL results in $L_{\rm MCD} \propto T_{\rm MCD}^{4.2\pm0.1}$ (the above results were obtained with spectrum *sax*1 excluded; $N_{\rm BB}$ from this spectrum is much larger than those from other spectra (Table 5.3–5.4) and varies the most with models (§5.3.2)). The apparent area of the boundary layer is only about 1/14 of the size of the NS, from simple comparison with the size of NS inferred from Type I X-ray bursts. The factor 1/14 might be a little larger due to special geometry of the boundary layer, which is generally believed to be an equatorial belt [Lin et al., 2007b, Chapter 4]. We note that there are scatterings in the inferred apparent emission area of the boundary layer. The fractional variation is about 25%, larger than the typical error bars (10%). Whether this is real or due to instrumental effects is unclear.

Whether the above results imply that the real boundary layer is small and nearly constant depends on the radiative transfer process in the atmosphere above the boundary layer, i.e., the hardening effect as discussed above for the disk spectra. The small BB emission area is reminiscent of the well known spectral modeling problem of the NS thermal emission in quiescence, i.e., the BB fit of its thermal component produced inferred radii too small for theoretical NS size estimate, whereas models taking into account the radiative transfer in the hydrogen atmosphere give radius estimate much closer to theoretical expectation of the size of NSs [e.g., Rutledge et al., 1999]. However, all our observations are quite bright ($\gtrsim 10^{37}$ erg/s), and the emission should be due to active accretion. At such a high accretion rate, a pure hydrogen atmosphere is not expected [Brown et al., 1998], and the above problem might not apply to our case. Our conclusion of small size of the boundary layer is based on the assumption that the modification of the bursting atmosphere on burst emergent spectra is similar to that of the boundary layer emission. This assumption might be valid if most of the heat in the boundary layer is generated in a layer as deep as that for burst nuclear burning. We note that the small inferred size of the boundary layer agrees with the theoretical expectation of most of the boundary layer models at sub-Eddington accretion rates [Kluzniak and Wilson, 1991, Inogamov and Sunyaev, 1999, Popham and Sunyaev, 2001]. Thus it is quite possible that the boundary layer emission area is indeed small for our observations.

If the behavior of the hardening factor for the boundary layer is similar to that for the burst emission, then one might expect little deviation of $L_{\rm BB} \propto T_{\rm BB}^4$ for the boundary layer, as the hardening factor is quite independent of the temperature for burst emission at sub-Eddington limit [Madej et al., 2004, Özel, 2006]. For example, for a NS with mass 1.4 $M_\odot$ and radius 10 km, Table 2 from Madej et al. [2004] suggests an approximate relation of $L_{\rm BB} \propto T_{\rm BB}^{3.7}$ for $T_{\rm BB}$ within 1.1–2.5 keV (most of our observations fall into this range). Thus, our results of the boundary layer closely following $L_{\rm BB} \propto T_{\rm BB}^4$ might imply little change of the real boundary layer emission area for our observations.

Now we combine our results for the accretion disk and the boundary layer to discuss their implication of accretion configuration in 4U 1705-44. From the above, we have seen that the inner disk radius is possibly constant during those soft-state observations (possibly except those in the lower left banana), under the uncertainty of the spectral hardening factor. For the black hole cases, this is normally associated with the ISCO. For the NS cases, there is another possibility, i.e., the accretion disk is truncated by the NS surface. The main difficulty in determining whether the accretion disk is truncated by the NS surface or at the ISCO is that the ISCO is quite close to the surface of the NS. The above two cases can be differentiated if the NS confined inside its ISCO or not can result in quite different spectral evolution behavior of the boundary layer and the accretion disk. If the accretion disk extends all the way down to the surface of the NS, the boundary layer and the disk are dynamically coupled. Popham and Sunyaev [2001] modeled the boundary layer as part of the disk, using the slim disk equations and Newtonian approximation, and found that the transition radius of the accretion disk to the boundary layer increased with the accretion rate. Our results suggest that the increase in the luminosity of the boundary layer and the accretion disk results in increase most in characteristic temperatures, instead of in emission areas, and might suggest that the boundary layer is not fully coupled with the accretion disk. Thus the accretion disk is probably truncated by the ISCO if our spectral model is correct [Lin et al., 2007b, Chapter 4]. The small size of the boundary layer might require that the disk is always geometrically thin. Abramowicz et al. [1978] showed the existence of the cusp of the equipotential surface with the presence of the ISCO, resulting in the sharp cusp on the inner edge of the accreting disk. Thus the thickness of the disk can be forced to be small near the ISCO. All the above pictures need to be confirmed by modeling the accretion disk and boundary layer together, with the general relativistic effects taken into account.

5.5 Conclusion

We have fit the broad-band spectra of 4U 1705-44 obtained with *Suzaku* and *BeppoSAX*. The continuum model for the soft-state spectra consists of double thermal components, one of which is a multicolor accretion disk and the other is a single-temperature blackbody boundary layer, with additional weak Comptonization, modeled by simple power law or by the SIMPL model by Steiner et al. [2008]. The model for the hard-state continuum spectra consists a single-temperature blackbody boundary layer and a strong Comptonization component, modeled by a cutoff power law.

The accretion disk in the soft state seems to approximately follow a $L \propto T^{3.2}$ track. There are two main factors that might act together to cause its deviation from $L \propto T^4$. One is the luminosity-dependent spectral hardening factor. The other is that the inner disk radius is really changed in some part of the soft state. We found no significant contribution of the thermal disk in our hard-state spectra above 1 keV, and the disk might be truncated at a large radius and/or has a low temperature (< 0.1 keV). The boundary layer is consistent with $L \propto T^4$, with emission size about 1/14 of the whole surface of the neutron star. Small size of the boundary layer and no evidence for dynamical coupling between the accretion disk and the boundary layer over more than one order of magnitude change in the luminosity lead us to interpret that the accretion disk is truncated by the ISCO, instead of the surface of the NS. However, detailed numerical simulation with general relativistic effect incorporated is required to confirm this interpretation. Assuming that the disk is truncated by the ISCO, we estimated the magnetic field of in 4U 1705-44 to be less than about 1.9×10^8 G.

Broad relativistic Fe lines are also detected in each spectrum. We modeled them with the diskline model and found that the strength of the Fe line correlates well with the boundary layer emission in the soft state, with the Fe line flux about 3% of the flux from the boundary layer. In the hard state, our results suggest that the Fe lines are due to the strong Comptonization emission. However, the Comptonization emission in the hard state seems to illuminate the accretion disk and produce the Fe line not as efficiently as the boundary layer emission in the soft state, probably because the boundary layer is closer to the accretion disk.

Chapter 6

Spectral Study of Accreting Neutron-Star X-ray Sources and Hint on Origins of Kilohertz Quasi-periodic Oscillations

Abstract

We have analyzed four neutron-star (NS) atoll sources, Aql X-1, 4U 1608-522, 4U 1705-44, and 4U 1636-536, using their observations over more than twelve years with *RXTE*. Their spectra are fit with our new NS spectral model. In this model, the hard-state observations are fit with a strong Comptonized component, described by a cutoff power law, and a thermal (boundary layer) component, described by a single-temperature blackbody (BB). The soft-state observations are fit with two thermal components, i.e., a BB and a multi-color disk (MCD), with additional weak Comptonization described by a constrained power law or the empirical convolution Comptonization model by Steiner et al. (when needed). Different from our previous studies, here we divide the soft state into different parts based on the occurrences of kilohertz quasi-periodic oscillations (kHz QPOs) and positions in the color-color diagram to have a more detailed examination on their spectral behavior. We show that the X-ray spectral evolution in the two persistent sources 4U 1705-44 and 4U 1636-536 are similar to the transients Aql X-1 and 4U 1608-522 in many aspects. We find that the disks for all four sources approximately follow $L \propto T^4$ tracks (constant apparent inner disk radius) in the soft state where no kHz QPOs occur. We also find that the disks seem to truncate at larger radii in the soft state where kHz QPOs occur, indicating a close relation between the kHz QPOs and the accretion disk. Further considering that kHz QPOs are more significant at higher photon energies and are quite probably from the emission from the boundary layer, one possible explanation for kHz QPOs in accreting NSs is that they are due to modulation of the accretion rate into the boundary layer. The boundary layers for all four sources are roughly constant from the hard to the soft state, and their sizes are $\sim$1/16 of the whole NS surfaces, consistent with the study in Lin et al. (2007, Chapter 4).

6.1 Introduction

The luminous and weakly magnetized neutron stars (NSs) in low-mass X-ray binaries (LMXBs) are classified into atoll and Z sources, named after the patterns that they trace out in X-ray color-color diagrams (CDs) or hardness-intensity diagrams (HIDs), based on their X-ray spectral and timing properties [Hasinger and van der Klis, 1989, van der Klis, 2006]. Although extensive coverage by the *Rossi X-ray Timing Explorer* (*RXTE*) has shown that atoll sources can also similar patterns in the CD/HIDs, i.e., Z-like shapes, as Z sources [Muno et al., 2002, Gierliński and Done, 2002a], these two classes are different from each other in shape/orientation of the Z patterns, evolution timescales, luminosity ranges, spectral types and timing properties [Barret and Olive, 2002, van Straaten et al., 2003, Reig et al., 2004, van der Klis, 2006]. Recently Lin et al. [2009b] and Homan et al. [2009] analyzed a transient accreting NS, XTE J1701-462, which showed behavior of a Z source to that of an atoll source as the outburst decayed from near/super Eddington luminosity (L_{Edd}) to almost quiescence, and confirmed that the differences between Z and atoll sources are due to their different mass accretion rates. Atoll sources have lower luminosities, ($\sim$0.001–0.5 L_{Edd}), and have two distinct X-ray states, i.e., hard (significant emission above 20 keV) and soft states, plus the transitional state. The hard, transitional and soft states of atoll sources are also often referred to as the "extreme island", "island", and "banana" states/branches, respectively. The spectra of Z sources are mostly soft, and their upper, diagonal and lower branches of the Z-shaped tracks are called horizontal, normal and flaring branches, respectively. These branches are different from each other in many aspects, such as spectral evolution timescales and fast variability.

The atoll soft state can be further subdivided into the upper banana where the <1 Hz power-law noise dominates, the lower banana where several dominant 10 Hz band limited noises occur, and the lower left banana where twin kilohertz quasi-periodic oscillations (kHz QPOs) are observed. During the decay of XTE J1701-462 in its 2006-2007 outburst, the Z-source horizontal, normal and flaring branches disappeared successively, with the vertex between the normal and flaring branches becoming the atoll lower banana [Lin et al., 2009b, Homan et al., 2009]. The Z-source flaring branch might be just the atoll-source upper banana. However, the flaring branch in XTE J1701-462 is better defined and stronger in the CD/HID than the upper banana seen in typical atoll sources, and the association of the Z-source flaring branch with the atoll-source upper banana still needs further investigation.

Spectral modeling of weakly magnetized accreting NSs has been controversial for decades [see Barret, 2001, for a review]. Compared with black-hole X-ray binaries, there should exist a boundary layer, where the accreted materials impact on the NS surface, in the accreting NSs. X-ray emission from the boundary layer is believed to be comparable to that from the accretion disk. Moreover, they cover energy bands close to each other, $\sim$1–20 keV. All this leads to the main difficulty in decomposing the spectra from accreting NSs. The classical models consist of two continuum components, i.e., a soft/thermal and a hard/Comptonized component [White et al., 1988, Mitsuda et al., 1989, Christian and Swank, 1997, Barret et al., 2000, Oosterbroek et al., 2001, Church and Balucińska-Church, 2001, Di Salvo et al., 2000a, Gierliński and Done, 2002b, Iaria et al., 2005]. The thermal component is normally chosen to be either a single-temperature blackbody (BB) for the boundary layer or a multicolor disk blackbody (MCD). Lin et al. [2007b, hereafter LRH07] implemented the commonly used two-component models for two classical transient atoll sources, i.e., Aql X-1 and 4U 1608-52, and showed strong spectral model degeneracy for accreting NSs, not only from the choices of the thermal components, but also from the detailed description of Comptonized components (the scattering corona geometry, the seed photon temperature, etc.). The pictures of the spectral evolution of these atoll sources are very different from different models. However, none of the tested models produce $L_{\rm X} \propto T^4$ tracks for the thermal component (MCD or BB), and they all result in strong Comptonization, for the soft-state spectra, in contrast with the picture from the black-hole binaries [Remillard and McClintock, 2006].

LRH07 further devised a hybrid model for atoll sources: a BB to describe the boundary layer plus a strong Comptonized component for the hard state, and two strong thermal components (MCD and BB) plus a weak Comptonized component (when needed) for the soft state. The results from this model are very different from those from the classical two-component models (see above), and can be summarized as follows: both the MCD and BB evolve approximately as $L_{\rm X} \propto T^4$, the spectral/timing correlations of these NSs are aligned with the properties of accreting black holes, and the visible BB emission area is very small but roughly constant over a wide range of $L_{\rm X}$ that spans both the hard and soft states. We also applied this model XTE J1701-462, and results similar to the above were also found for the observations in the atoll-source stage. Deviation of the MCD from the $L_{\rm X} \propto T^4$ track was observed with the inner disk showing a luminosity-dependent expansion at high luminosity when the source behaved as a Z source at high luminosity.

In this paper we continue our spectral study of atoll sources using data obtained with the *Rossi X-ray Timing Explorer* [*RXTE* , Bradt et al., 1993], and the goals are manifold. We test our spectral model on two persistent atoll sources 4U 1705-44 and 4U 1636-536 [Hasinger and van der Klis, 1989]. Compared with LRH07, in this study, we have a closer look at the soft state in order to see any different spectral behavior associated with different parts of the soft state (lower left banana, lower banana, and upper banana). As our model is still partially empirical, especially for the Comptonized component, the effect of this component on the spectral fit results will be addressed in more detail, including application of a new Comptonization model, i.e., SIMPL by Steiner et al. [2008]. Considering the above differences from LRH07 and the recent significant improvement of calibration of the Proportional Counter Array [PCA; Jahoda et al., 1996] on board *RXTE* , this study still includes Aql X-1 and 4U 1608-522, which were analyzed in LRH07.

Some detailed timing studies of these four atoll sources, including the findings of kHz QPOs, have been carried out. [e.g., Zhang et al., 1996, Berger et al., 1996, Wijnands et al., 1997c, Ford et al., 1998, Zhang et al., 1998b, Barret and Olive, 2002, van Straaten et al., 2003, Olive et al., 2003, Reig et al., 2004, Barret et al., 2007]. Here we will concentrate on their spectral properties, with analyses of kHz QPOs also included, as they are related to our spectral results. We describe our data reduction scheme in §6.2 and show the long-term light curves and color-color diagrams in §6.3. The spectral variability is given in §6.4. The search of the kHz QPOs for these sources are presented in §6.5. We perform detailed spectral modeling in §6.6. We discuss our spectral results and implications of the origin of kHz QPOs in §6.7. Finally we give our summary.

6.2 Observations and data reduction

For our analysis, we used all of the *RXTE* observations of Aql X-1, 4U 1608-522, 4U 1705-44 and 4U 1636-536 as of 2009 June 30. Data were analyzed from the PCA (2–60 keV) and the High Energy X-ray Timing Experiment [HEXTE;15–250 keV Rothschild et al., 1998] instruments. The PCA has five Proportional Counter Units (PCUs). Their calibration was

Table 6.1. Observations and State Definitions for Each Source

		Aql X-1	4U 1608-522	4U 1705-44	4U 1636-536
Number of total/used observations		476/423	932/807	335/331	1063/1035
Time of total/used observations (ks)		1564/1458	1797/1632	897/897	3339/3315
HS	Def.	HC>0.6	HC>0.6	HC>0.64	HC>0.64
	Time (ks/%)	662/45	828/51	350/39	309/9
TS	Def.	—	—	—	—
	Time (ks/%)	54/4	87/5	61/7	639/19
SS/LLB	Def.	HC≤0.37 & SC≤0.96	HC≤0.41 & SC≤1.06	HC≤0.44 & SC≤1.17	HC≤0.46 & SC≤1.05
	Time (ks/%)	173/12	289/18	136/15	1424/43
SS/LB	Def.	HC≤0.37 & 0.96<SC≤1.0 HC≤0.34 & SC>1.0	HC≤0.41 & 1.06<SC≤1.1 HC≤0.4 & SC>1.1	HC≤0.44 & 1.17<SC≤1.25 HC≤0.39 & SC>1.25	HC≤0.46 & SC>1.05
	Time (ks/%)	509/35	357/22	281/31	857/26
SS/UB	Def.	0.34<HC<0.45 & SC>1.0	0.4<HC<0.5 & SC>1.1	0.39<HC<0.45 & SC>1.25	0.46<HC<0.52 & SC>1.05
	Time (ks/%)	59/4	70/4	69/8	86/3

Note. — Color ranges are given for the hard state (HS), soft state (SS) lower left banana (LLB), lower banana (LB) and upper banana (UB). All of the remaining observations are referred to as the transitional state.

significantly improved (HEAsoft 6.7), and we used data from all PCUs. The HEXTE has two clusters (A and B), and both of them were also used. We used the same standard criteria to filter the data as described in LRH07, and only observations with source count rates $\geq$10 counts/s/PCU were used. Data before 1996 April 15 (PCA epoches 1 & 2) are not used considering bad calibration at low energy. Deadtime corrections for PCA and HEXTE data were also applied.

We created spectra for both the PCA and HEXTE instruments. To avoid large spectra variations, we created pulse-height spectra with integration time required to be $<$4 ks. The observational gap in each spectrum is required to be < 500 s (this is normally smaller than the observation gaps induced by earth occultations and South Atlantic Anomaly passages). For the PCA, the spectra were extracted from "standard 2" data collection mode, and the response files were created so that they were never offset from the time of each observation by more than 20 days. We ignore channels 1–3 (numbering from 1 to 129) and energy above 50 keV for our spectral fitting and applied systematic errors of 0.5% for all channels. We created the HEXTE spectra to match the PCA spectra in observation time. No systematic errors were applied for HEXTE data. A summary of the observations is given in Table 6.1.

In order to classify the spectral states/branches, we calculated the CD/HIDs. We calculated X-ray colors as described in LRH07. We normalized the raw count rates from each PCU using observations of the Crab Nebula, and we defined soft and hard colors as the ratios of the normalized background-subtracted count rates in the (3.6–5.0)/(2.2–3.6) keV bands and the (8.6–18.0)/(5.0–8.6) keV bands, respectively. The values of colors are then averaged over all PCUs. Throughout the paper, all PCA intensity values are normalized and correspond to the sum count rate of these four energy bands. The difference between the normalized intensity and the raw total PCA count rate is normally $<5\%$.

6.3 Light curves and color-color diagrams

Figure 6-1 shows the long-term light and color curves of Aql X-1 and 4U 1608-522 (a) and 4U 1705-44 and 4U 1636-536 (b) in 1996–2009. This figure combines data from the PCA and the *RXTE* All-Sky Monitor [ASM; Levine et al., 1996]. These four sources show quite different long-term accretion behavior during this period. Aql X-1 and 4U 1608-522 show

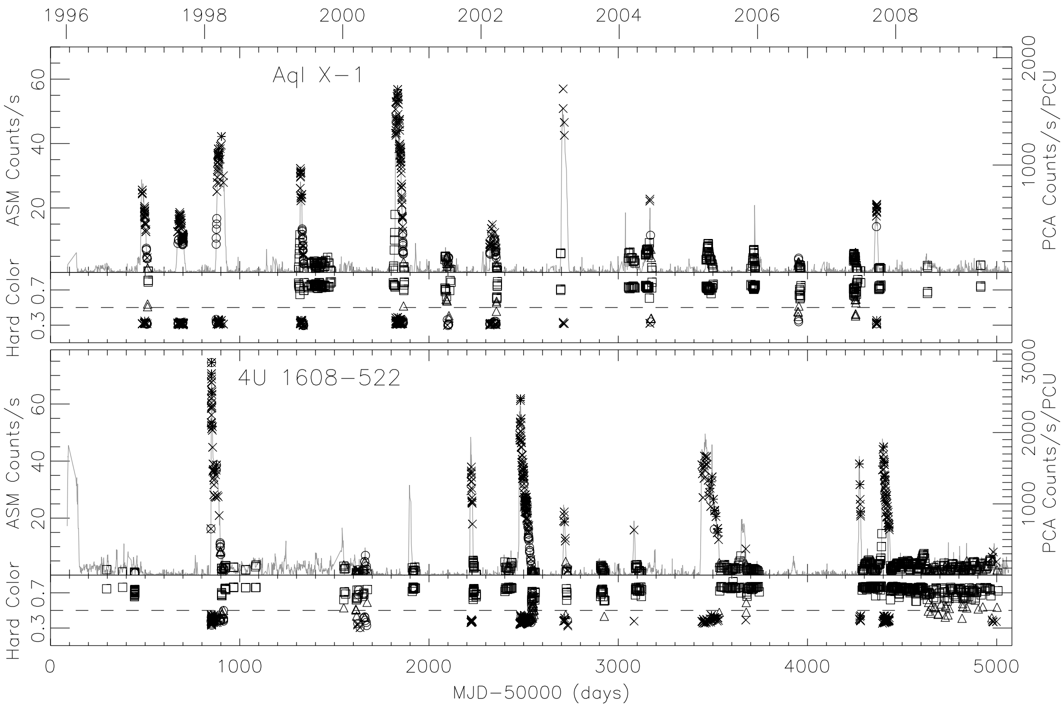

(a)

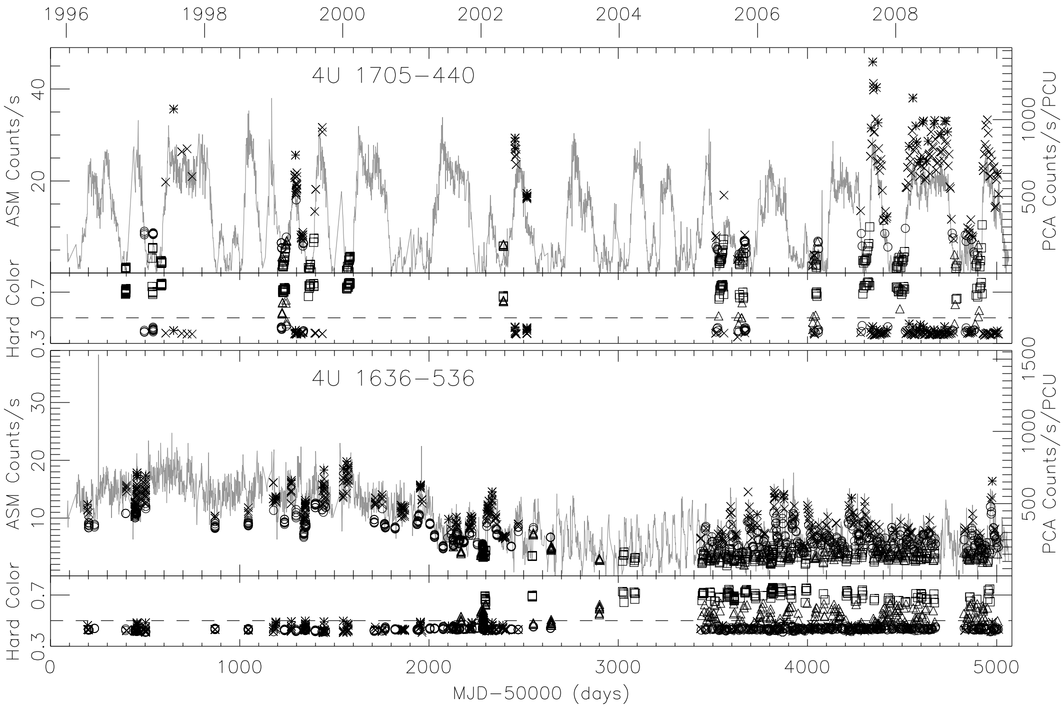

(b)

Figure 6-1: Long-term light and color curves of transient (a; Aql X–1 and 4U 1608–522) and persistent (b; 4U 1705–44 and 4U 1636–536) atoll sources. Grey solid lines are from *RXTE* ASM, and discrete symbols are from PCA observations representing different spectral states (see Figure 6-2). The dashed line (hard color = 0.5) is a reference to help distinguish the different states.

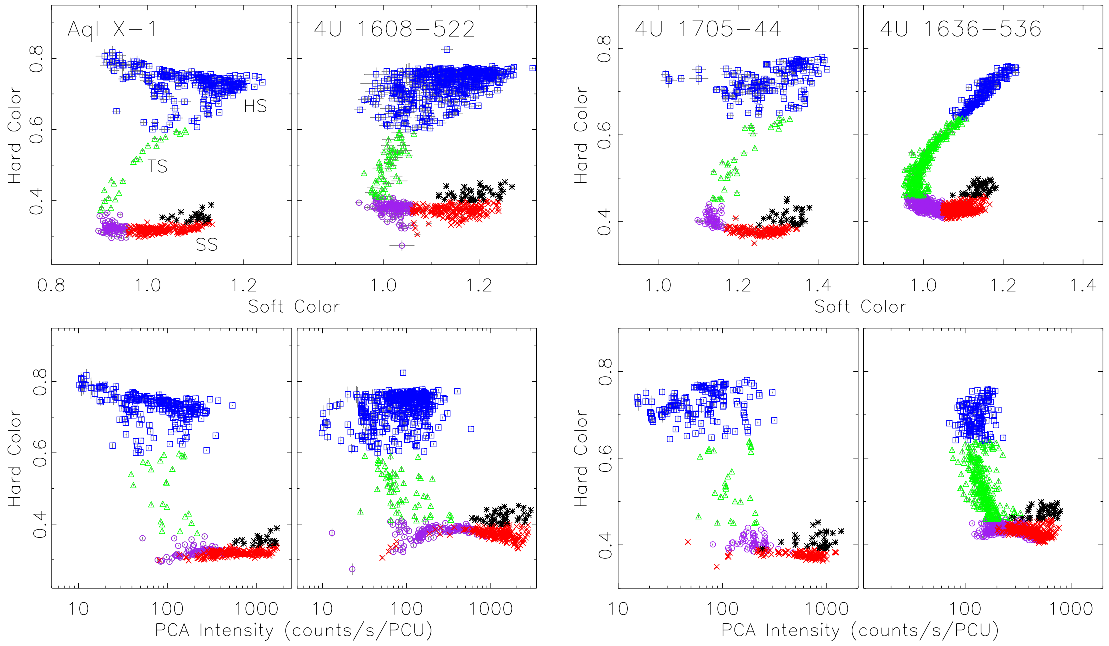

(a) (b)

Figure 6-2: Color-color and hardness-intensity diagrams of transient (a; Aql X–1 and 4U 1608–522) and persistent (b; 4U 1705–44 and 4U 1636–536) atoll sources. The atoll-source states (HS: hard state (blue squares); TS: transitional state (green triangles); SS: soft state (purple circles for lower left banana, red crosses for lower banana, and black stars for upper banana)) are labeled in the color-color diagram of Aql X–1. One-σ uncertainties are also shown and are normally smaller than the symbol size.

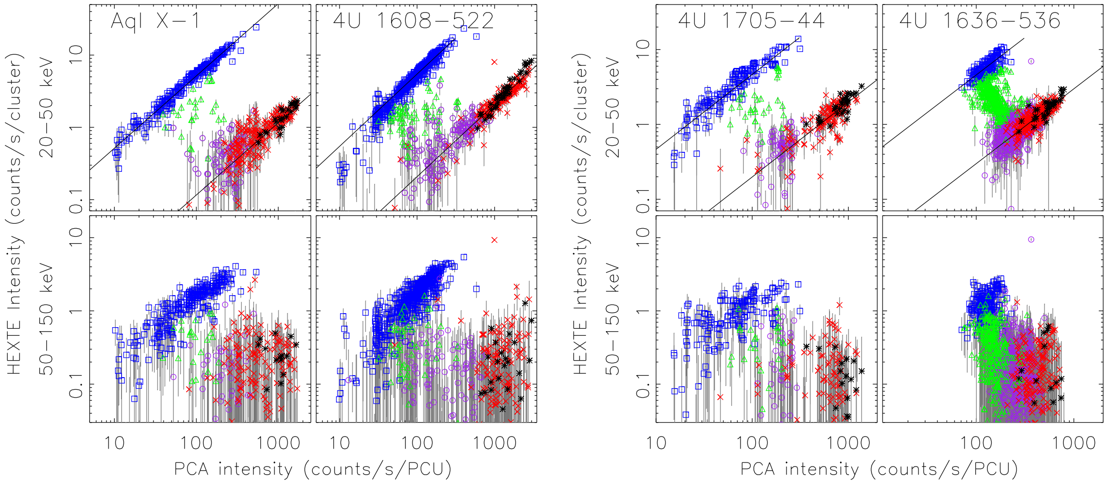

(a) (b)

Figure 6-3: The HEXTE intensity in two hard energy bands versus the PCA intensity. The solid lines show linear fits for these measurements. The hard and soft states appear increasingly different when they are compared using more widely spaced energy bands. The meanings of symbols are the same as Figure 6-2 about one active outburst per year, while at other times, they are almost in quiescence. 4U 1705-44 shows one or two active outbursts every year with durations $\sim 100 - 200$ days, while maintaining weak persistent accretion in the between. The outbursts normally start in the hard state, evolve to the soft state, and finally return to the hard state during the decay. 4U 1636-536 maintains at active accretion from 1996 till 2003, after which the source experiences regular small outbursts. Unlike Aql X-1 and 4U 1608-52, both 4U 1705-44 and 4U 1636-536 maintain at modest accretion in addition to active outbursts in the interval shown in Figure 6-1, with intensity always above 10 counts/s/PCU (2 mCrab).

The CD/HIDs of these four sources are shown in Figure 6-2. Although they are atoll sources, their patterns in the CD/HIDs are Z-shaped, owing to their large range of luminosities. The hard-state track of 4U 1636-536, however, is not as extended as the other three sources. This is due to the fact that 4U 1636-536 was not observed to be in very low hard state; its intensity observed by the PCA is always >50 counts/s/PCU.

We use the CDs to pragmatically define the source states/branches as shown in Figure 6-2. The observations are classified into the hard, transitional, and soft states, with the soft state is further subdivided into the lower left banana, lower banana, and upper banana branches (§6.1). In Table 6.1, we give the color ranges adopted for each state/branch for each source. We first define the three states, with the upper part of the pattern in the CD assigned to be the hard state and the lower part to be the soft state. For the soft state, we then search for kHz QPOs (§6.5) and choose the range of soft color for the lower left banana so that all kHz QPOs found are in this branch. The soft-state observations left are assigned to be lower banana and upper banana. We do not define the color ranges for these two branches based on detailed timing analysis, but base on the fact that the upper banana tends to stay at the lower end of the pattern in the CD and tends to have hard colors higher than those of the lower banana. For all figures in this paper, the hard state, transitional state, soft-state lower left banana, lower banana, and upper banana are represented by blue squares, green triangles, purple circles, red crosses, black stars, respectively. The detailed analysis of how the sources evolve through the CD/HIDs in time and the strong hysteresis (i.e., the hard-soft transition generally occurs at higher X-ray flux compared to the soft-hard transition) present in these sources are beyond the scope of this paper.

As in LRH09, we show the relation of source intensities in more widely spaced energy bands, in Figure 6-3. The top panels are the HEXTE 20–50 keV intensity versus the PCA intensity (2.2–18 keV; §6.2). The most striking aspect of these panels is that there are two nearly linear tracks corresponding to the soft and hard states, with that of the soft state is far below the hard-state one, for all source. The ratio of the HEXTE 20–50 keV intensity versus the PCA intensity for the hard state is > 15 times of that for the soft state for all sources. The bottom panels are the HEXTE 50–150 keV intensity versus the PCA intensity. We can still see the linear track in the hard state, but the sources are generally not detected above 50 keV in the soft state. These results support our classifications of the hard/transitional/soft states above. However, within the bandwidth and statistical capabilities of HEXTE measurements, we cannot see differences in the soft state subdivisions in Figure 6-3.

6.4 Spectral variability

We quantify the spectral variability of these sources, as follows. The spectra that we created as described in §6.2 on average have exposure 2.3, 1.6, 2.1, and 2.2 ks, respectively, for Aql

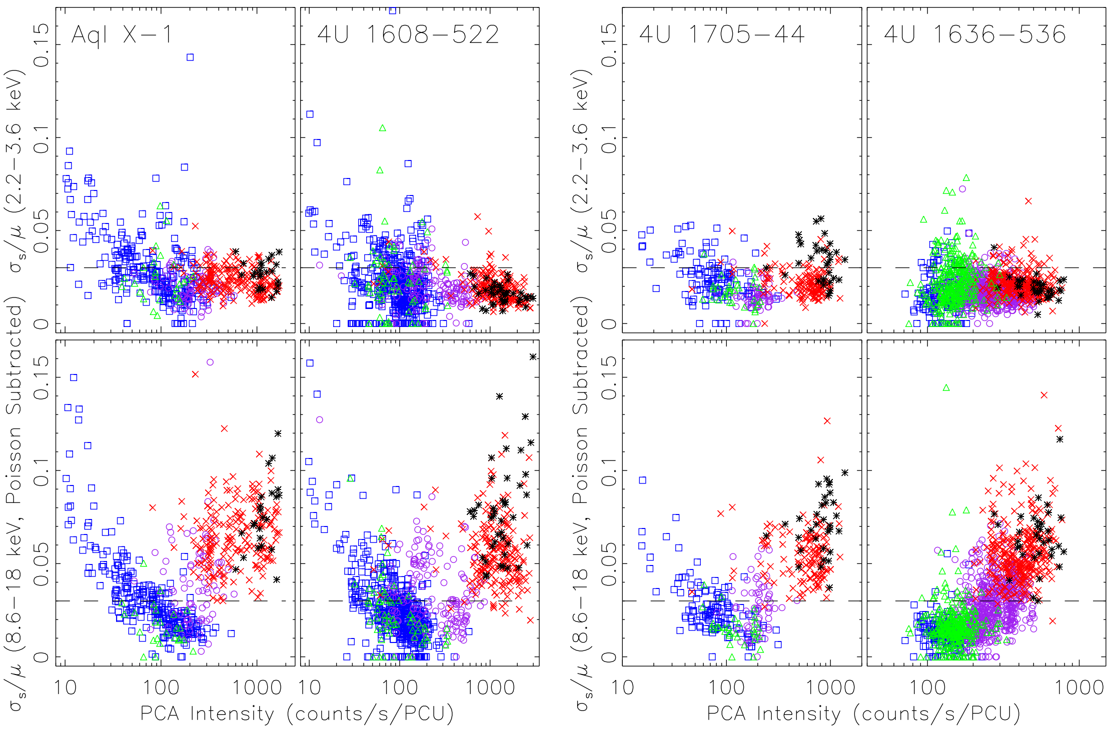

(a) (b)

Figure 6-4: The fractional spectral variations within each spectrum in two energy bands (2.2–3.6 keV and 8.6–18 keV) using quanta of 32-s data. The states/branches are color/symbol-coded, and the Poisson noise is subtracted. Data with negative poison-subtracted variance are assigned to be zero.

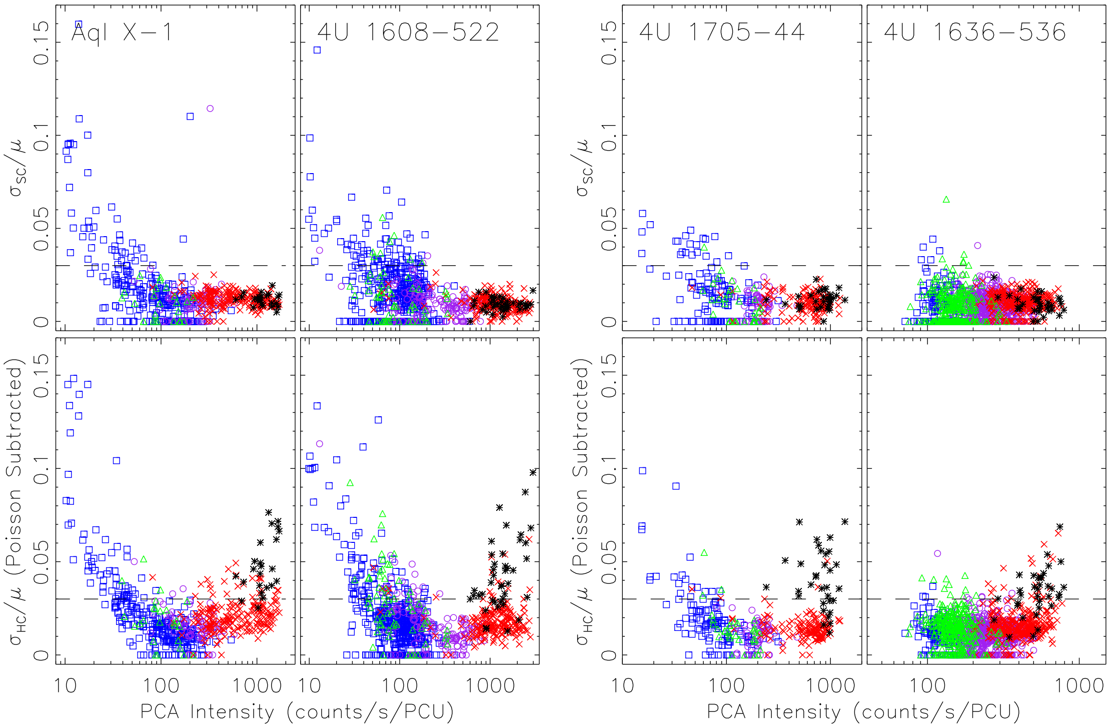

(a) (b)

Figure 6-5: The same as Figure 6-4, but using the soft color (upper panels) and hard color (lower panels).

X-1, 4U 1608-522, 4U 1705-44 and 4U 1636-536. We calculate spectral variations using quanta of 32-s data. we are interested in the source variability (i.e., in excess of statistics). Thus we subtract the sample variance from the variance due to Poisson noise. Finally the Poisson-subtracted sample standard deviation σ is divided by the sample mean μ to obtain the fractional Poisson-subtracted spectral variations σ/μ. We conduct these variance analyses for both intensities and colors.

Figures 6-4 and 6-5 show the fractional Poisson-subtracted spectral variations using the 2.2–3.6 keV and 8.6–18 keV intensities and the soft and hard colors, respectively. We see that the spectral variations characterized by these quantities are generally smaller than 3% (dashed lines). There are two exceptions. One is the hard state at low intensity. The other is the soft state at high intensity, including the lower banana and upper banana, and this is true for all four sources. We note that in the lower banana the 8.6-18 keV intensity shows variations above 3%, while this is not true for the hard color, which means that the spectral variation at high energy comes from the change in the normalization, but not the spectral shape. In the upper banana, both the spectral shape and normalization change above 3%. However, all quantities shown here indicate that the spectral variations for the spectra that we created in §6.2 are almost all $< 10\%$, and they should be able to be used for spectral modeling directly, which we carry out in §6.6.

6.5 Kilohertz quasi-periodic oscillations

These four atoll sources are all shown to exhibit single (Aql X-1 and 4U 1705-44) or twin (4U 1608-522 and 4U 1636-536) kHz QPOs (§6.1). They normally occur around the lower left banana. The frequencies can shift with time. They are around 600–900 Hz (lower kHz QPOs) in the lower left banana and can decrease to < 200 Hz in the transitional state. We also did brief kHz QPO search for each source in order to define the lower left banana for our observations as follows. We created Poisson-noise subtracted power density spectra using (2–40 keV), one per time interval corresponding to energy spectra, using data with fast collection modes. Then the power density spectra were fit with a single power law and one or two Lorentzian functions describing the kHz QPOs over a frequency range of 200–1500 Hz.

The upper limit of the soft color of the lower left banana given in Table 6.1 for each source is defined to about the maximal soft color of the soft-state observations that have kHz QPOs above a three-σ level (in term of the normalization of the Lorentzian function), except for 4U 1705-44. For the lower left banana defined in Table 6.1, we found that Aql X-1, 4U 1608-522, and 4U 1636-536 respectively have 49%, 46%, and 54% of the observations with kHz QPOs above a three-σ level. The kHz QPOs in 4U 1705-44 are much weaker and require much detailed analysis, which is beyond the scope of this paper. Thus the definition of the lower left banana for 4U 1705-44 should be taken as an assumption.

6.6 Spectral modeling

6.6.1 Spectral models and assumptions

In this work, we fit the X-ray spectra of Aql X-1, 4U 1608-522, 4U 1705-44 and 4U 1636-536 with several different models. The pulse-height spectra of five PCUs and two HEXTE clusters were fit jointly over the energy range 2.7–40.0 keV and 20.0–150.0 keV, respectively,

Table 6.2. Physical Parameters Assumed in Spectral Study

	Aql X-1	4U 1608-522	4U 1705-44	4U 1636-536
$N_{\rm H}$ (10^{22} cm^{-2})	0.5	1.0	1.67	0.4
Distance (kpc)	5	3.6	7.4	5.9
Inclination (°)	60	60	30	60
$E_{\rm Fe}$	6.63±0.08	6.62±0.11	6.46±0.05	6.80±0.08
$\sigma_{\rm Fe}$ (keV)	0.3	0.3	0.43	0.43
$R_{\rm burst}$ (km)	8	7.2	7.4	6.5
$<F_{\rm peak}>$ (10^{-9} erg cm^{-2} s^{-1})	89	132	39.3	40
References	a1,a2,a3,d3	b1,b2,d3	c1,c2,c3,d3	a1,d1,d2,d3

Note. — References: a1 Church and Balucińska-Church 2001; a2 Rutledge et al. 2001; a3 Koyama et al. 1981; b1 Penninx et al. 1989; b2 Nakamura et al. 1989; c1 Lin et al. 2009 (in preparation); c2 Haberl and Titarchuk 1995; c3 Gottwald et al. 1989; d1 Fiocchi et al. 2006; d2 Augusteijn et al. 1998; d3 Galloway et al. 2008

allowing the relative normalizations of different instruments to be free. For soft-state observations, HEXTE spectra were used up to 50 keV because the flux at higher photon energies was negligible (Figure 6-3).

In this paper, we continue to fit the spectra of these atoll sources with our hybrid model, i.e., Model 6 in LRH07, but with some minor modifications. This model consists of a BB to describe the boundary layer plus a strong Comptonized component for the hard state, and two strong thermal components (MCD and BB) plus a weak Comptonized component (when needed) for the soft state. The choice of description of the Comptonized component is somewhat empirical and is not unique either. For the hard state, either a broken power law or the Comptonization model by Titarchuk [1994] (CompTT in XSPEC; the seed photon temperature < 0.5 keV) works well, as far as behavior of the BB and fractions of Comptonization are concerned. In our study of broad-band spectra of 4U 1705-44 observed with *Suzaku* and *BeppoSAX* (Lin et al. 2009, in preparation), we found that a cutoff power law (CPL) is better than the above two descriptions for the Comptonization in the hard state, in terms of the values of χ^2. Thus in this paper, we use a CPL to describe the Comptonization in the hard state. In the soft state, the Comptonization is in general very weak, and for simplicity, we fit it with a single power law (PL), with constraint of the photon power-law index $\Gamma_{\rm PL} \leq 2.5$ (2.2 for 4U 1705-44; Lin et al. 2009, in preparation). We note that such a constraint is not necessary for broad-band spectra (Lin et al. 2009, in preparation). In the transitional state, we still fit the Comptonization with a CPL, with constraints of photon power-law index $\Gamma_{\rm CPL} \leq 2.5$ and the cutoff energy $E_{\rm CPL} \geq 20$ keV (see below). We hereafter refer to the above hybrid model as MCD+BB+PL. We note that a MCD is not included in this model for the hard state. This might be because there is no thermal disk in the hard state. The lower energy boundary of the PCA (>2.7 keV) can also make this component invisible in the spectra even if it is present.

The BB model provides the color temperature ($kT_{\rm BB}$) and the apparent radius ($R_{\rm BB}$; isotropic assumption) of the BB emission area, while the MCD model provides the apparent inner disk radius ($R_{\rm MCD}$) and the color temperature at the inner disk radius ($kT_{\rm MCD}$). The CPL model has three parameters: a photon index ($\Gamma_{\rm CPL}$), a cutoff energy ($E_{\rm CPL}$) and a normalization parameter.

In LRH07, we find that a double thermal model of MCD+BB is enough to describe the soft state at high intensity and produce the results of the MCD and the BB close to $L_X \propto T^4$ tracks. Only at the low-intensity soft and transitional states, a weak Comptonization is necessary. The model MCD+BB will also be used to fit the spectra to show what part of observations can still be fit without a PL.

In this paper, we also fit the spectra by fitting the Comptonization in the soft state with a recently developed Comptonization model, i.e., SIMPL by Steiner et al. [2008]. This is an empirical convolution model of Comptonization in which a fraction of the photons in an input seed spectrum is scattered into a power-law component. It requires that the seed spectrum is partially visible and it counts the photons scattered into the power law, so that the original seed spectrum and the lower-energy turnover of the Comptonized power law are self-consistently tracked. These features are not designed into the other Comptonization models described above. This model has only two free parameters, i.e., the photon power-law index Γ and the scattered fraction f_{SC}, in addition to a flag denoting whether all the scattered photons are up-scattered in energy or are both up- and down-scattered. We assume that the Comptonization is from the disk and that the seed photons are from the disk. We specify that all the scattered photons are up-scattered in energy only. We find that inclusion of down-scattering only change our results normally within error bars. We denote this combined model as SIMPL(MCD)+BB. We did not apply SIMPL to the hard and transitional states, as there is no MCD in our model or the MCD is poorly constrained.

In a summary, we will show results for three models: MCD+BB, MCD+BB+PL, and SIMPL(MCD)+BB. All models also included a Gaussian Iron line. Its central line energy E_{Fe} was initially left free in the fit and was then fixed to be the average values in the final fits (Table 6.2). We also fixed the intrinsic width of the Gaussian line σ_{Fe}, with values also given in Table 6.2. As the Fe lines are intrinsically broad from 4U 1705-44 and 4U 1636-536, their values of σ_{Fe} were fixed at a higher value (0.43 keV) than those for Aql X-1 and 4U 1608-522 (0.3 keV). We note that the PCA has energy resolution $\sim$ 1 keV, limiting the need for a precise value of σ_{Fe}. An interstellar absorption component was also included with the hydrogen column fixed; see Table 6.2 and references therein. To estimate the disk luminosity, we need the binary inclinations, which are poorly known for all four systems. Since no eclipses or absorption dips have been observed, these sources are likely not high-inclination systems, and we assumed their binary inclinations to be 60° (30° for 4U 1705-44; Lin et al. 2009, in preparation). We scaled the luminosity and radius related quantities using distances given in Table 6.2, unless indicated otherwise.

6.6.2 Spectral fit results

Figure 6-6 shows the luminosity of the thermal components, i.e., MCD and BB, versus their characteristic temperatures, kT_{BB} or kT_{MCD}. The errors represent 90% confidence limits for a single parameter. For reference, we also show the lines for constant radius, assuming $L_X = 4\pi R^2 \sigma T^4$. The NS radii are shown with dotted lines in this figure. They are inferred from our spectral fitting to Type I X-ray bursts (denoted as R_{burst}), and are consistent with previous studies (see Table 6.2 and references therein). The dashed lines correspond to $R = 2.0$, 1.3, 2.0, and 1.5 km for Aql X-1, 4U 1608-522, 4U 1705-44, and 4U 1636–536, respectively. They are derived from the fit to the BB radius values obtained from model MCD+BB+PL.

The top panels in Figure 6-6 show the results for Model MCD+BB. Only results of

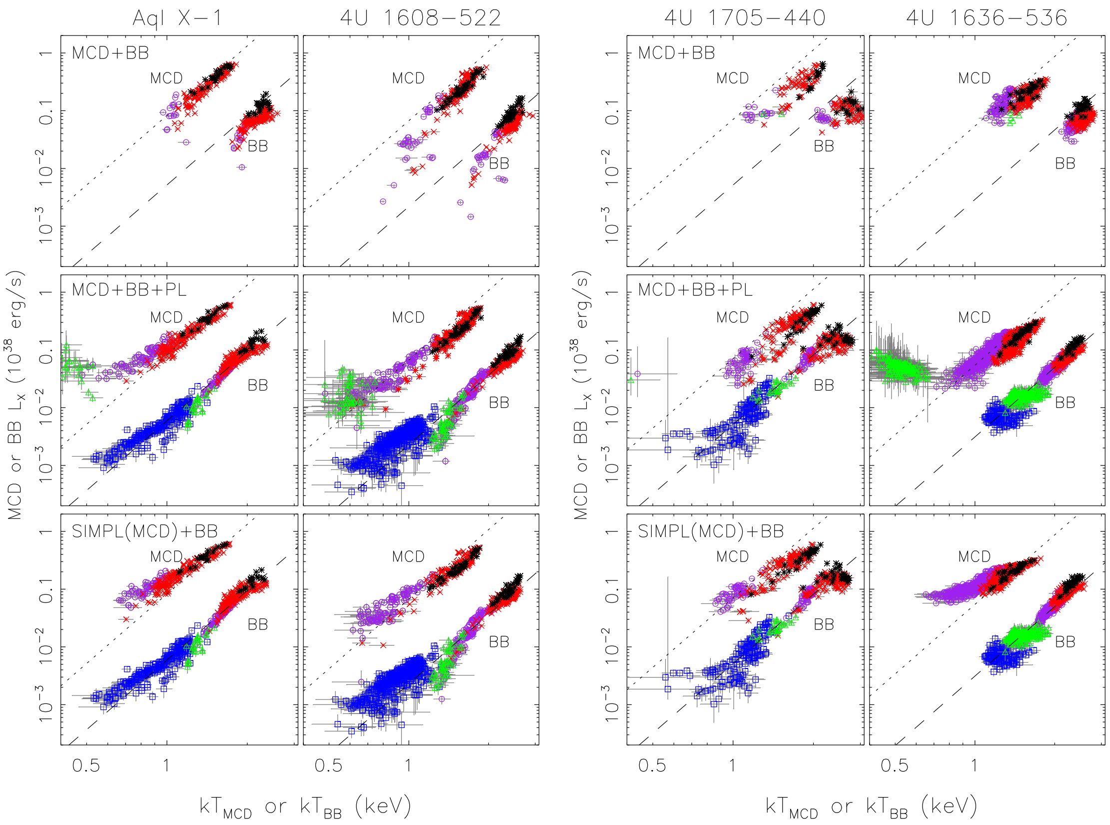

(a)

(b)

Figure 6-6: The luminosity of the thermal components versus their characteristic temperatures. The meanings of the symbols are the same as Figure 6-2. All models produce luminosity evolution for BB and MCD components in most part of the soft state that are nearly parallel to reference dotted/dashed lines, which show $L_X \propto T^4$ with constant emitting surface area. The dotted lines correspond to the NS burst radii (Table 6.2) and the dashed lines correspond to $R = 2.0$, 1.3, 2.0, and 1.5 km for Aql X–1, 4U 1608–522, 4U 1705–44 and 4U 1636–536, respectively, assuming $L_X = 4\pi R^2 \sigma T^4$.

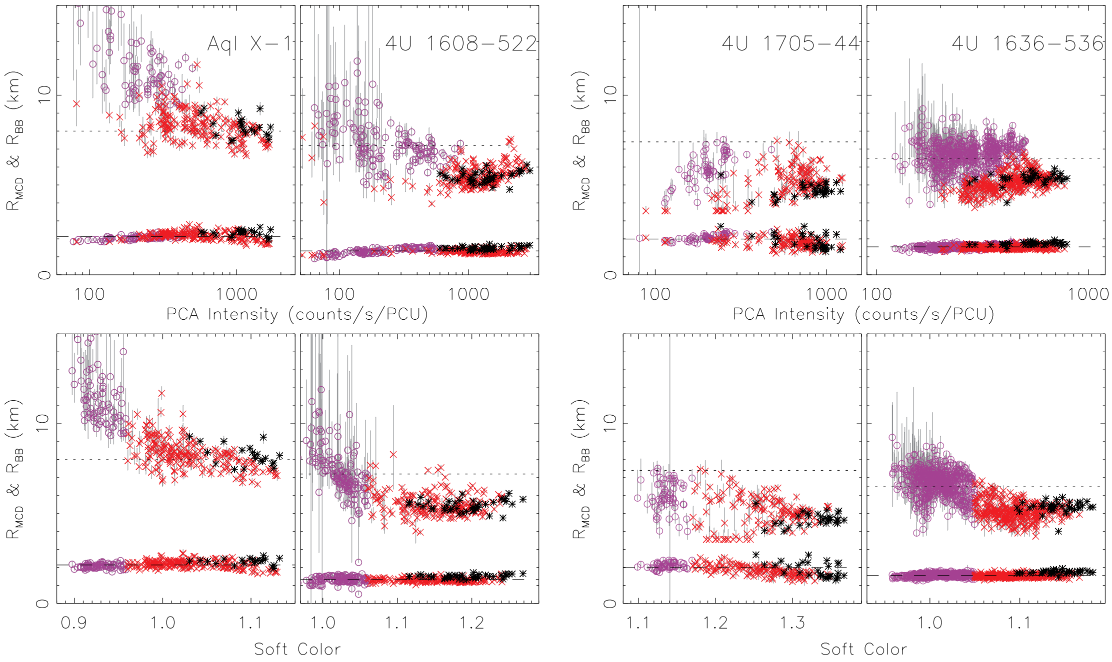

(a) (b)

Figure 6-7: The apparent inner disk radius and size of the boundary layer in the soft state from model MCD+BB+PL. The upper panels show their dependence on intensity, while the lower panels on the soft color. The meanings of the symbols are the same as Figure 6-2, and the reference dotted/dashed lines are the same as those in Figure 6-6.

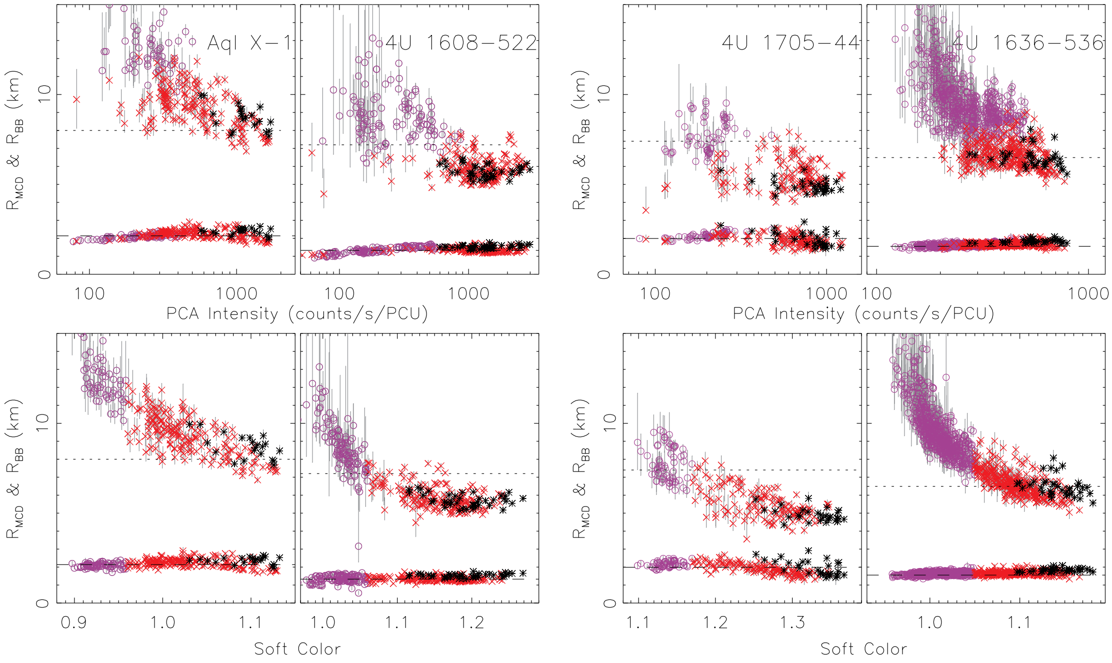

(a) (b)

Figure 6-8: The same as Figure 6-7 but from model SIMPL(MCD)+BB.

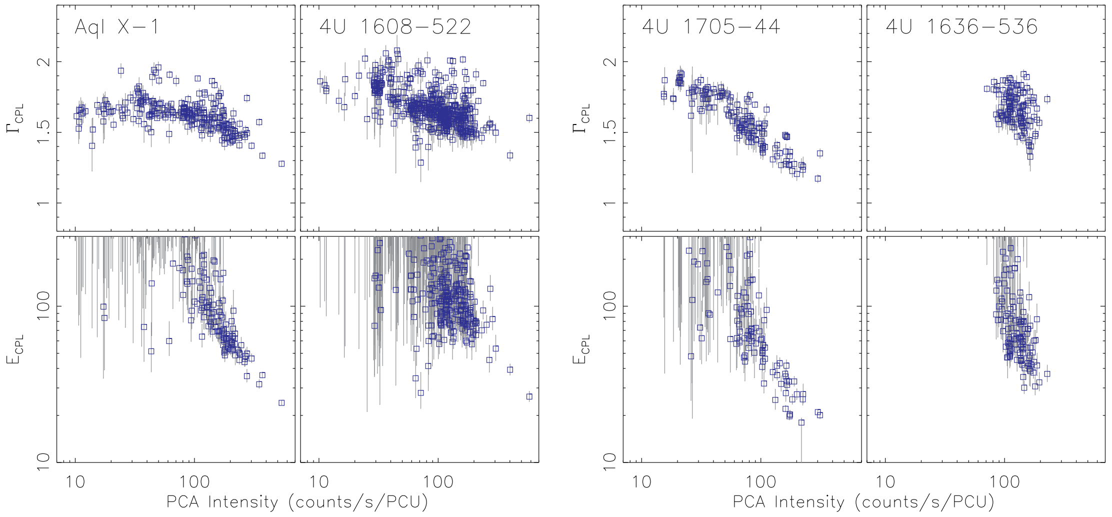

(a) (b)

Figure 6-9: The power-law index and cutoff energy of the cutoff power-law in the fit of atoll-source hard state. The meanings of the symbols are the same as Figure 6-2.

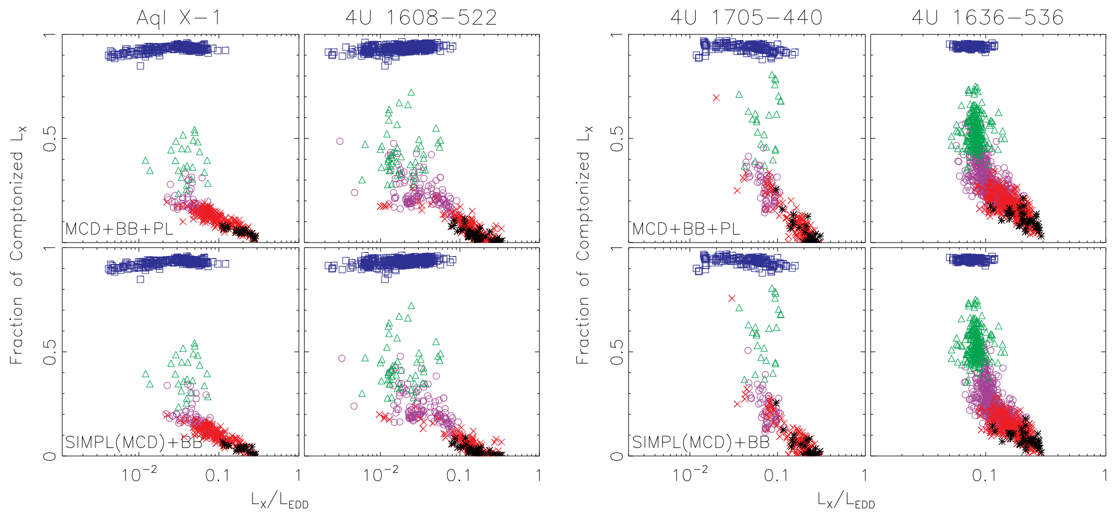

(a) (b)

Figure 6-10: The fraction of Comptonized luminosity versus the total luminosity. The meanings of the symbols are the same as Figure 6-2.

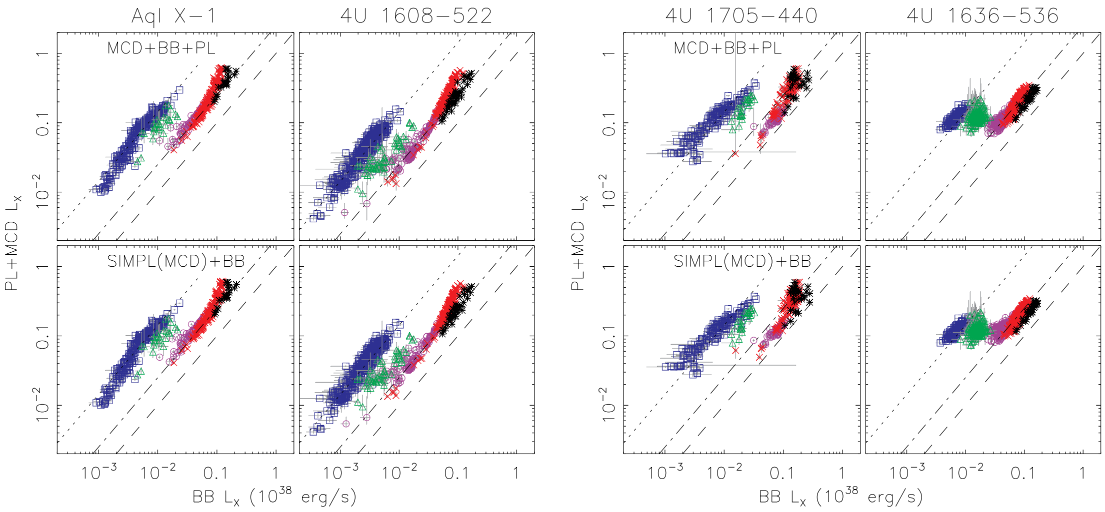

(a) (b)

Figure 6-11: The luminosity of non-BB components (i.e., PL+MCD or SIMPL(MCD)) versus the luminosity of the BB component. At the transitional BB luminosity that separates hard and soft states, the hard-state CPL appears to be very luminous compared to the soft-state MCD. The three reference lines (dashed, dot-dashed, and dotted), connect the points where the ratio of the luminosities of the BB component and the non-BB components is 1.0, 0.4, and 0.07, respectively.

fits with reduced χ^2 values < 2 are shown. We see that the model can only work for the high-intensity soft states, i.e., the lower and upper bananas. However, for those with good fit, the MCD and BB both roughly follow $L_X \propto T^4$ tracks.

The middle panels in Figure 6-6 are for model MCD+BB+PL. For clarity, we only plot data points with small error bars, i.e., if the difference between the upper and lower limits (90% confidence) of the temperatures of the thermal components is <0.7 keV. Data excluded mostly are the MCD component in the transitional state, where the $kT_{\rm MCD}$ is much lower than 1 keV and the MCD cannot be well constrained due to the PCA's limited energy range (> 2.7 keV). We see that both the MCD in the soft state for all four sources mostly follow $L_X \propto T^4$ tracks. However, the detailed behavior seems to be a little complicated when comparing between the lower left banana and other parts of the soft state, which will be probed in more detail below. The inner disk radius for each source is comparable with the NS radius inferred from the bursts, but more quantitative comparison is prohibited by limited information of distance, inclination, and other parameters such as the hardening factors for the disk and burst spectra. The BB also nearly follows $L_X \propto T^4$ tracks for all sources, spanning from the hard to soft states. The apparent BB emission areas are quite small and are only about 1/16 of the size of the NSs (see above).

The bottom panels in Figure 6-6 are for model SIMPL(MCD)+BB. For the hard and transitional states, model MCD+BB+PL is still used (i.e., CPL+BB for the hard state, MCD+BB+CPL for the transitional state). The data for the MCD show the values before Comptonization. On the whole the results using SIMPL(MCD)+BB is similar to those from model MCD+BB+PL, but subtle differences occur, e.g., the best-fitting values of $R_{\rm MCD}$ from this model is systematically larger than those from model MCD+BB+PL.

A closer look at spectral fit results for different parts of the soft state follows, in order to reveal their difference in spectral evolution. We plot in Figure 6-7 the apparent inner disk radius R_{MCD} and the size of the boundary layer (R_{BB}) in the soft state, inferred from model MCD+BB+PL. The upper panels show their dependence on intensity, while the lower panels on the soft color. We note that the hard color is fairly constant in the soft state and that the soft color basically tracks the position in the CD for the soft state. we see in Figure 6-7 that although the inferred R_{MCD} in general have larger uncertainties in the lower left banana than in other parts of the soft state, they on the whole have larger values in the lower left banana than in the lower banana or upper banana, when comparing observations with similar intensity. The plot against the soft color shows that R_{MCD} is rather independent of the soft color in the lower banana and upper banana, but assumes larger values in the lower left banana. It seems that R_{MCD} increases with decrease in the soft color, but we cannot rule out that this is due to the energy band limitation of the instrument. The above results seem to be also supported by model SIMPL(MCD)+BB, as shown in Figure 6-8.

As far as R_{BB} is concerned, it is quite independent of intensity and the soft color, from Figures 6-7–6-8. However, for all sources and from both models MCD+BB+PL and SIMPL(MCD)+BB, R_{BB} seems to be larger in the upper banana than in the lower banana, which might suggest that the difference between the upper banana and the lower banana comes from the boundary layer emission. We note that this difference is just modest, about 20–40% larger for the upper banana in terms of the total apparent BB emission area, depending on sources.

Now we focus on Comptonization, starting with the hard state. We plot in Figure 6-9 the best-fitting values of Γ_{CPL} and E_{CPL} from the CPL model. Γ_{CPL} is roughly constant in the hard state, but slight decrease with increase in intensity is seen, especially for the case of 4U 1705-44. The cutoff energy E_{CPL} is typically large (>100 keV) at low intensity (<100 counts/s/PCU), but decreases with increase in intensity at high intensity. The minimum is about 20–30 keV for all sources. In the transitional state, the Comptonization is still strong for observations close to the hard state, we found that the fit still preferred introduction of cutoff energy, in terms of the values of χ^2. That is why we still use the CPL to describe Comptonization in the transitional state. However, we need constraints of the photon power-law index, similar to the soft state, and the cutoff energy $E_{\mathrm{CPL}} \geq 20$ keV (otherwise it will become smaller than 10 keV when the spectra become soft). Using a single power law tends to obtain smaller normalizations for the BB.

Figure 6-10 shows the fraction of the Comptonized luminosity versus the total luminosity for both model MCD+BB+PL and model SIMPL(MCD)+BB. The total luminosity is normalized by the Eddington luminosity L_{Edd}. The L_{Edd} is derived from the type I X-ray bursts showing photospheric radial expansion. Its corresponding average peak flux $<F_{\mathrm{peak}}>$ for each source is listed in Table 6.2 [Galloway et al., 2008]. For 4U 1636-536, there are two groups of type I X-ray bursts showing photospheric radial expansion, and they have different peak flux. It is possible that the group with high peak flux is due to pure helium burning [Galloway et al., 2006]. Thus we adopt the value from the group with lower peak flux, as this group should have more similar material composition to that of the disk. Figure 6-10 shows that the Comptonization emission contributes more than 90% of the total emission in the hard state, and about less than 70% in the soft state. In the soft state, it decreases with increase in luminosity and is almost zero at high luminosity. From this figure, we also see that the peak luminosity for these sources is about 0.3–0.4 L_{Edd}.

Figure 6-11 shows $L_{\mathrm{PL}} + L_{\mathrm{MCD}}$ (For model SIMPL(MCD)+BB, it is the MCD plus its Comptonization emission) versus L_{BB}. Both models (MCD+BB+PL and SIMPL(MCD)+BB)

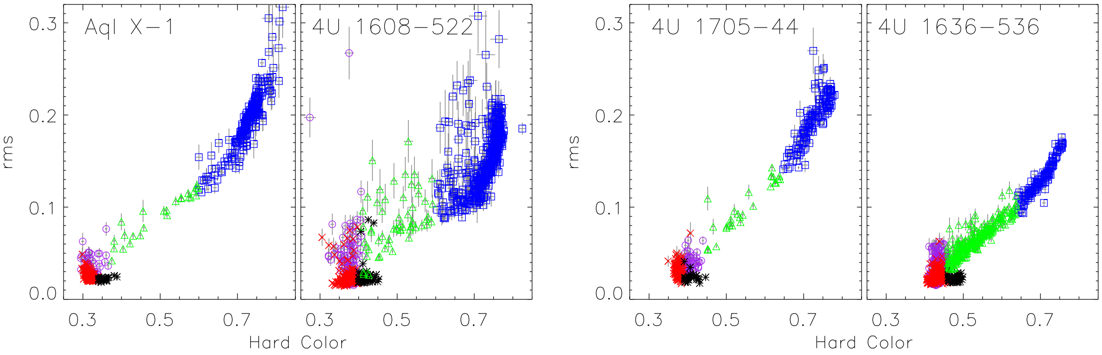

(a) (b)

Figure 6-12: The integrated rms power in the power density spectrum (0.1–10 Hz and energy band 2–40 keV) versus the hard color.

give similar results. The behavior of these four sources also resembles each other. The $L_{\rm PL} + L_{\rm MCD}$ relative to $L_{\rm BB}$ is significantly higher in the hard state than in the soft state. For the hard state, the vertical axis represents Comptonization, since $> 90\%$ of the total luminosity in the hard state is due to $L_{\rm CPL}$. In the soft state, the vertical axis is effectively the disk luminosity. On the horizontal axis, we assume that $L_{\rm BB}$ represents emission from the boundary layer. From the dot-dashed reference line, the BB emission is about 40% of the disk emission in the soft state. We always note in Figures like 6-11 that we expect $L_{\rm bb}$ to track the mass accretion rate reaching the NS surface, with caveats for significant changes in either the radiative efficiency or the viewing geometry, including any obscuration of the boundary layer by the inner disk. Taken at face value, one possible explanation for the relatively low BB emission in the hard state, compared to the soft state, when referenced to $L_{\rm PL} + L_{\rm MCD}$, is substantial mass loss via the hard state jet.

6.7 Timing properties and comparison with spectral fit results

6.7.1 Rapid variability and Comptonization

In Figure 6-12, we show the integrated root-mean-square (rms) power in the power density spectrum (0.1–10 Hz and energy band 2–40 keV) versus the hard color, as in LRH07, where it was shown that Aql X-1 and 4U 1608-522 have similar rms versus hard color relations to BHs [Remillard and McClintock, 2006]. Figure 6-12 shows that this is also true for 4U 1705-44 and 4U 1636-536. The rms, normalized to a fraction of the source's mean count rate, is very small ($\lesssim 0.05$) in the soft state, and the values increase with the hard color progressing through the transitional and hard states. In BH systems, the hard color effectively traces the fractional contribution of the thermal and Comptonized components to the X-ray spectrum in BH systems. The above similarity of the rms versus hard color relations between BH and NS systems motivates examination of whether our spectral models conserves this similarity when rms is plotted versus the fractional contribution of the thermal component(s). This has been shown to be true for Aql X-1 and 4U 1608-522 in LRH07, and we show in Figure 6-13 for all four sources. As shown in Figure 12 in LRH07, for six BHs in the soft state, the luminosity fraction of the thermal component is quite high ($\gtrsim 75\%$) and the rms is very

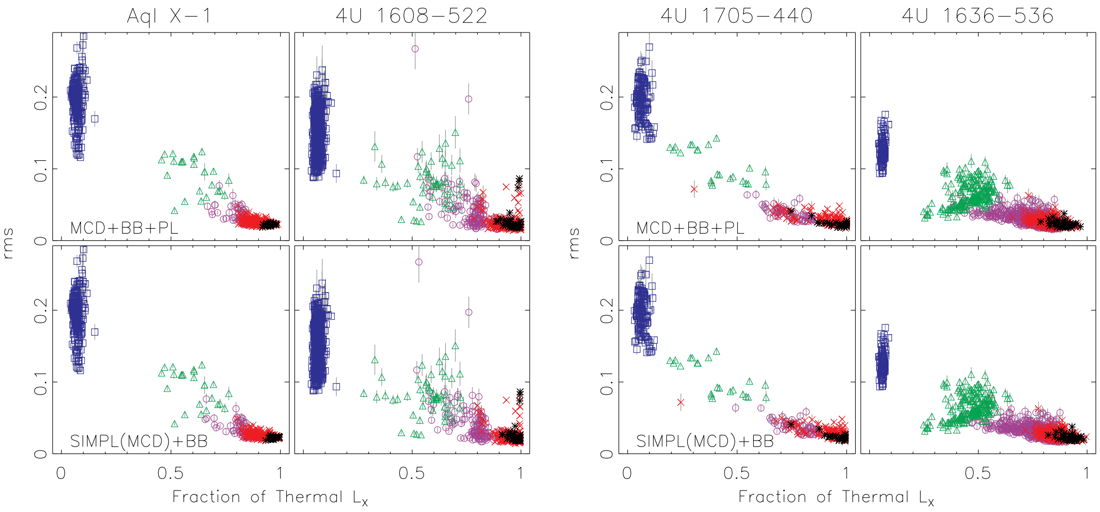

(a) (b)

Figure 6-13: The rms versus the fraction of luminosity contained in BB and/or MCD components as evaluated for different spectral models.

small $\lesssim 0.05$. Comparing Figure 12 in LRH07 and Figure 6-13, one can see that all four NS sources reproduce the same dependence of rms on fractional thermal luminosity as for the six BHs.

6.7.2 Kilohertz quasi-periodic oscillations in the lower left banana

We have seen that the disk seems to truncate at larger radii in the lower left banana of the soft state where kHz QPOs are detected than in the lower banana and upper banana. The apparent inner disk radius $R_{\rm MCD}$ seems quite constant in the lower banana and upper banana. In the lower left banana, the fit results indicate that $R_{\rm MCD}$ appears to increases as the source becomes closer to the transitional state, but we caution the large uncertainties there. We note that occurrences of frequency-shifting kHz QPOs in the lower left banana is special to accreting NSs, as they are not detected in black-hole X-ray binaries [van der Klis, 2006].

The frequent occurrences of kHz QPOs and special disk behavior in the lower banana, compared with other parts of the soft state, suggest that kHz QPOs are tied to distinct spectral changes in which the inner disk appears to be larger than its normal soft-state value. We see no spectral changes tied to the BB component when kHz QPOs are present. On the other hand, it is well known that kHz QPOs in the accreting NS has larger fractional root-mean-square at higher photon energies [van der Klis, 2006]. In their study of 4U 1608-522 and GX 340+0 using Fourier frequency resolved X-ray spectroscopy, Gilfanov et al. [2003] argued that the kHz QPOs in accreting NSs should be from emission from the boundary layer. Based on the above results, one explanation for the kHz QPOs in accreting NSs is that they are due to modulation of the accretion rate into the boundary layer [van der Klis, 2006]. The fast shifting of the kHz QPO frequency (on timescales of hours) and the uncertainties of our spectral fit results in the lower left banana requires a lot of effort to calculate the quantitative relation between the kHz QPO frequency and inner disk radii, which should be important to constrain the kHz QPO models. This will be done in the future.

6.8 Summary and discussion

We have spectrally modeled four (NS) atoll sources, Aql X-1, 4U 1608-522, 4U 1705-44, and 4U 1636-536, using their observations over more than twelve years with *RXTE* . We use the new NS spectral model that we developed in LRH07 and Lin et al. (2009, in preparation). The hard-state observations were fit with a model consisting of a strong Comptonized component, described by a CPL, and a thermal (boundary layer) component, described by a BB. The soft-state observations were fit with two thermal components, i.e., a BB and a MCD, with additional weak Comptonization described by a constrained PL or the empirical convolution Comptonization model by Steiner et al. (when needed). One of the main differences of this study from LRH07 is that we divide the soft state into different parts based on the occurrences of kHz QPOs and positions in the CD to have a more detailed examination on their spectral behavior.

We show that the X-ray spectral evolution in the two persistently accreting NSs 4U 1705-44 and 4U 1636-536 are similar to the transients Aql X-1 and 4U 1608-522 in many aspects. We find that the disks for all four sources approximately follow $L \propto T^4$ tracks (constant apparent inner disk radius) in the soft state where no kHz QPOs occurs. By identifying kHz QPOs, we find that the disks seem to truncate at larger radii in the soft state where kHz QPOs occur, indicating a close relation between the kHz QPOs and the accretion disk. Further considering that kHz QPOs are more significant at higher photon energies and are quite probably from the emission from the boundary layer, one possible explanation for kHz QPOs in accreting NSs is that they are due to modulation of the accretion rate into the boundary layer. The boundary layers for all four sources are roughly constant from the hard to the soft state, and their sizes are $\sim$1/16 of the whole NS surfaces (see also LRH07).

We see that our results are quite robust against the specific choice of the Comptonization model. We have tested a constrained PL and SIMPL in this paper and a constrained broken power law in LRH07 in the soft state, and for the hard state, we test a CPL here and a broken power law and CompTT in LRH07. We see that they infer similar behavior of the thermal components (MCD and BB) and the fraction of Comptonization on the whole (compare the results for Aql X-1 and 4U 1608-522).

Chapter 7

Spectral States of XTE J1701-462: Link between Z and Atoll Sources

Abstract

We have analyzed 866 *RXTE* observations of the 2006–2007 outburst of the accreting neutron star XTE J1701-462, during which the source evolves from super-Eddington luminosities to quiescence. The X-ray color evolution first resembles the Cyg X-2 subgroup of Z sources, with frequent excursions on the horizontal and normal branches (HB/NB). The source then decays and evolves to the Sco X-1 subgroup, with increasing focus on the flaring branch (FB) and the lower vertex of the "Z". Finally, the FB subsides, and the source transforms into an atoll source, with the lower vertex evolving to the atoll soft state. Spectral analyses suggest that the atoll stage is characterized by a constant inner disk radius, while the Z stages exhibit a luminosity-dependent expansion of the inner disk, which we interpret as effects related to the local Eddington limit. Contrary to the view that the mass accretion rate ($\dot{m}$) changes along the Z, we find that changes in $\dot{m}$ are instead responsible for the secular evolution of the Z and the subclasses. Motion along the Z branches appears to be caused by three different mechanisms that may operate at roughly constant $\dot{m}$. For the Sco X-1-like Z stage, we find that the FB is an instability track that proceeds off the lower vertex when the inner disk radius shrinks from the value set by the X-ray luminosity toward the value measured for the atoll soft state. Excursions up the NB occur when the apparent size of the boundary layer increases while the disk exhibits little change. The HB is associated with Comptonization of the disk emission. The Z branches for the Cyg X-2-like stage are more complicated, and their origin is unclear. Finally, our spectral results lead us to hypothesize that the lower and upper Z vertices correspond to a standard thin disk and a slim disk, respectively.

This chapter is adapted from the paper "Spectral States of XTE J1701-462: Link Between Z and Atoll Sources" by Dacheng Lin, Ronald A. Remillard, & Jeroen Homan, published in The *Astrophysical Journal*, 2009, Vol. 696, p. 1257-1277.

7.1 Introduction

Based on their X-ray spectral and timing properties, the luminous and weakly magnetized neutron stars (NSs) in low-mass X-ray binaries (LMXBs) are classified into atoll and Z sources, named after the patterns that they trace out in X-ray color-color diagrams (CDs)

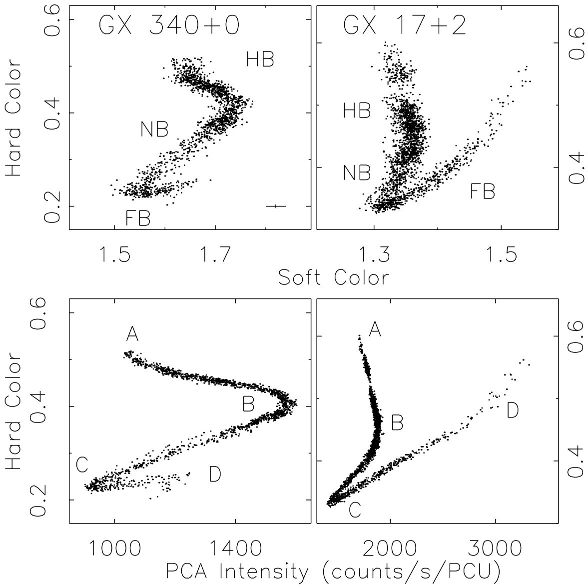

Figure 7-1: CDs and HIDs of the Cyg-like Z source GX 340+0 (MJD 51920–51925) and the Sco-like Z source GX 17+2 (MJD 51454–51464), with bin size 128 s. The typical error bars for the colors are shown in the top left panel; errors in the intensity are negligible. The Z-source branches (HB, NB, and FB) are labeled in the CDs. 'A', 'B', 'C', and 'D' in the HIDs mark key positions in the Z tracks: the left end of HB, HB/NB vertex, NB/FB vertex, and the right end of FB, respectively. Their corresponding spectra are shown in Figure 7-2.

or hardness-intensity diagrams (HIDs) [Hasinger and van der Klis, 1989, van der Klis, 2006]. Z sources typically radiate at luminosities close to Eddington luminosity (L_{EDD}), and they trace out roughly Z-shaped tracks in CDs/HIDs within a few days. Atoll sources cover a lower and larger luminosity range (∼0.001–0.5 L_{EDD}), and they trace out their patterns in CDs/HIDs on longer timescales (days to weeks). Although extensive coverage by the *Rossi X-ray Timing Explorer* (*RXTE*) has shown that atoll patterns can have Z-like shapes [Muno et al., 2002, Gierliński and Done, 2002a], they are different from the Z-source tracks in shape, color ranges, and evolution timescales. Furthermore, the spectra of Z sources are very soft on all three branches of the "Z", whereas the spectra of atoll sources are soft at high luminosities, but hard when they are faint. Properties like the rapid X-ray variability and the order in which the branches are traced out are also different for the two classes [Barret and Olive, 2002, van Straaten et al., 2003, Reig et al., 2004, van der Klis, 2006]. The upper, diagonal and lower branches of the Z-shaped tracks for Z sources are called horizontal, normal and flaring branches (HB/NB/FB), respectively, while for atoll sources, they are called the extreme island, island, and banana states. To stay consistent with our previous work on atoll sources, however, we refer to the atoll branches as hard, transitional and soft states (HS/TS/SS), respectively.

Based on the shape and orientation of their branches, the six classical Z sources were further divided into two subgroups [Kuulkers et al., 1994]: Cyg-like (Cyg X-2, GX 340+0, and GX 5-1) and Sco-like (Sco X-1, GX 17+2, and GX 349+2). We show sample CDs and HIDs for these subgroups in Figure 7-1. The spectra from key positions along the "Z" are shown in Figure 7-2. We also plot the ratios of these spectra at the two ends of each branch

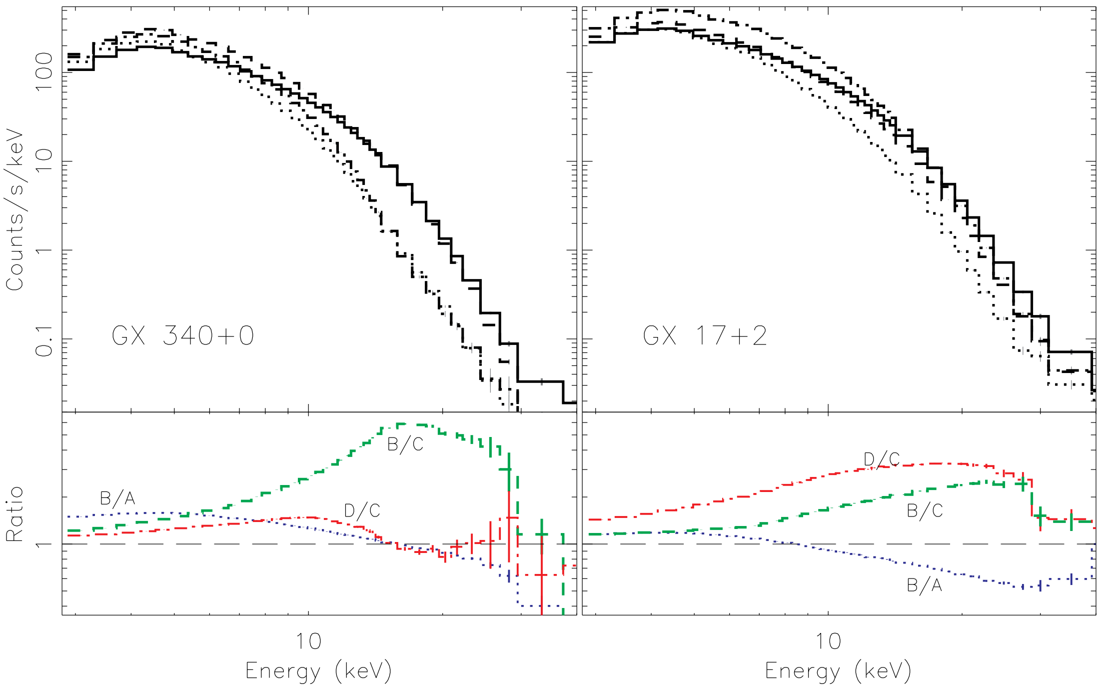

Figure 7-2: PCA spectra of GX 340+0 and GX 17+2 from key positions along their Z tracks. The solid, dashed, dotted, and dot-dashed lines correspond to labels 'A'–'D' in Figure 7-1 respectively. The ratios of the spectra from the two ends of each branch are shown in the bottom panels. Spectra with high total PCA intensity are divided by those with lower total PCA intensity in order to show that on each branch the intensity increases in a different energy range.

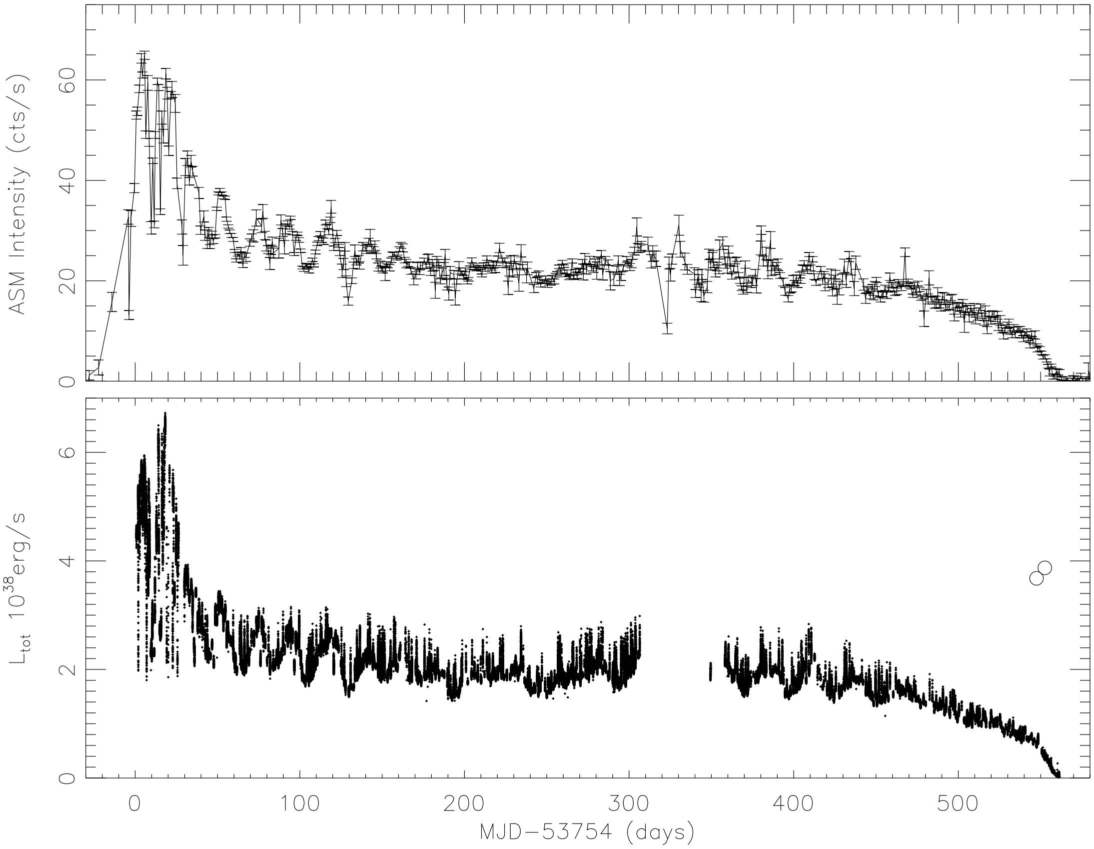

Figure 7-3: Upper panel: the *RXTE* ASM one-day-averaged light curve of XTE J1701–462 during its 2006–2007 outburst; lower panel: the *RXTE* PCA 32-s luminosity curve, from spectral fits with a MCD+BB model and assuming the source distance to be 8.8 kpc and system inclination 70° (§7.4). The two circles mark the peak luminosities (persistent emission subtracted) of two type I X-ray bursts, detected from this source during the decay of the outburst. These two bursts showed photospheric radius expansion, thus indicating the Eddington limit.

(bottom panels) to show that the motion along each Z branch is the result of spectral changes in different energy ranges. The spectral differences between the two subgroups are quite apparent, especially in the case of the FB (red dot-dashed lines in Figure 7-2). Although the branches have the same names for each subgroup, their origins are possibly different. In addition to movement along the "Z" tracks, the Z tracks themselves display slow shifts and shape changes in CDs/HIDs. These so-called secular changes are most apparent in Cyg X-2.

There are several questions regarding the Z sources that remain unanswered: e.g., what is the nature of the Z branches, how do they relate to the spectral states of atoll sources, and how are the two Z subclasses related? A unique opportunity to improve our understanding of Z sources arose with the discovery in 2006 of XTE J1701-462 [Remillard et al., 2006b], the first NS transient to show all the characteristics of a Z source [Homan et al., 2007b]. In the first 10 weeks of its ∼600-day outburst, XTE J1701-462 transformed from a Cyg-like into a Sco-like Z source [Homan et al., 2007b], and during the decay it evolved further into an atoll source [Homan et al., 2007c]. The upper and lower panels of Figure 7-3 show light curves of the outburst, using data from, respectively, the All-Sky Monitor [ASM; Levine et al., 1996] and the Proportional Counter Array [PCA; Bradt et al., 1993, Jahoda et al., 1996] on board *RXTE* . The latter one shows the luminosity as obtained from spectral fits (see §7.4 for more details). The two circles correspond to the peak luminosities of two type I X-ray bursts (persistent emission subtracted) which showed photospheric radius expansion [Lin et al., 2007a, 2009a]. In terms of a single value of Eddington limit (however, see §7.7), we see from this figure that the source reached super-Eddington luminosities during the peak of its outburst, assuming orbital inclination to be 70°.

The large dynamic range in luminosity of XTE J1701-462, from super-Eddington down to near-quiescence, also implies significant changes in the mass accretion rate ($\dot{m}$). This allows one to investigate the relevance of $\dot{m}$ to the questions that we posed above. The study by Homan et al. [2007b] suggests that differences in $\dot{m}$ are responsible for the Z-source subclasses, with the Cyg-like sources accreting at higher rates. Initial results from the end phase of the outburst suggest that the differences between Z and atoll sources are also purely the results of a difference in $\dot{m}$, with a lower $\dot{m}$ for the atoll class [Homan et al., 2007c].

Concerning the role of $\dot{m}$ in the evolution along the Z tracks, we note that results from multi-wavelength campaigns have been interpreted as monotonically increases in $\dot{m}$ from the HB, through the NB, to the FB [e.g., Hasinger et al., 1990, Vrtilek et al., 1990]. However, this classical view is inconsistent with the fact that the X-ray intensity decreases as Z sources move along the NB in the direction of the FB. In recent years, several alternatives have been proposed. Based on the behavior of the 0.1–200 keV flux as reported by Di Salvo et al. [2000b] and on a comparison with black hole systems, Homan et al. [2002] suggested that $\dot{m}$ might be constant along the Z track, with motion along the "Z" being caused by an unknown parameter. Church et al. [2008] used X-ray spectral fits to claim that $\dot{m}$ increases in the direction opposite to the classical view, being lowest on the FB, which is a branch proposed to be driven by unstable nuclear burning. Finally, based on the observed change between Cyg-like and Sco-like Z-source behavior in the NS transient XTE J1701-462, Homan et al. [2007b] proposed that secular changes in Z sources are the result of changes in $\dot{m}$ and that the position along the "Z" is determined by $\dot{m}$ normalized by its long term average. Definitive conclusions on the role of $\dot{m}$ have been hindered by the lack of a spectral model that lets us unambiguously track the evolution of physical components along the Z track.

A major difficulty in interpreting the X-ray spectra of NS LMXBs has been the problem of model degeneracy, i.e., significantly different models providing acceptable fits to the same data [Lin et al., 2007b, Chapter 4, hereafter LRH07]. In the classical framework of two-component models for the continuum spectra of NS LMXBs, one component is thermal, and the other is Comptonized. The thermal component can be either a single-temperature blackbody (BB), used to describe the boundary layer, or a multicolor disk blackbody (MCD), while there are choices for the nature of the Comptonized component, with no clear advantages for any set of combination of these two components. As far as Z sources are concerned, Done et al. [2002], Agrawal and Sreekumar [2003], and D'Aí et al. [2007] used a model of Comptonization plus a MCD to fit the spectra of Cyg X-2, GX 349+2 and Sco X-1, respectively, while Di Salvo et al. [2000b, 2001, 2002] used a model of Comptonization plus a BB for GX 17+2, GX 349+2 and Cyg X-2. The model used by Church et al. [2008] for their study of GX 340+0 also consisted of a BB plus Comptonization, with the latter approximated by a cut-off power law.

In LRH07, we showed for two atoll type transients that the commonly used spectral models for thermal emission plus Comptonization are not favored for the SS, because they fail to satisfy various desirability criteria, such as $L_{\mathrm{X}} \propto T^4$ evolution for the MCD component and similarity to black holes for correlated timing/spectral behavior. In an attempt to solve this, we devised a hybrid model: a BB to describe the boundary layer plus a broken power-law (BPL) for the HS, and two strong thermal components (MCD and BB) plus a constrained BPL (when needed) for the SS. The results from this model are summarized as follows: both the MCD and BB evolve as $L_{\mathrm{X}} \propto T^4$, the spectral/timing correlations of these NSs are aligned with the properties of accreting black holes, and the visible BB emission area is very small but roughly constant over a wide range of L_{X} that spans both the HS and SS. We note that this model is still partially empirical, especially the (constrained) BPL description of Comptonization. We also note that the boundary layer spectrum was reported to be broader than a BB in the Z-source HB and atoll-source SS [Gilfanov et al., 2003, Revnivtsev and Gilfanov, 2006]. However, it is also possible that the broadening is caused by rapid variability of a Comptonized component and its blending with a BB in these states/branches.

Considering the success of this spectral model for atoll sources, we intend to apply it to XTE J1701-462. This unique source was observed on an almost daily basis with *RXTE* during its outburst. In this work, we present a color/spectral analysis of all *RXTE* observations from the 2006–2007 outburst of XTE J1701-462, as part of our campaign to understand this source (Lin et al. 2009a (type I X-ray bursts, Chapter 8); Homan et al. 2009 (transition from a Z to an atoll source); Fridriksson et al. 2009 (quiescence)). The goal of this paper is to improve our understanding of the physical processes that drive the evolution along the Z-source tracks and the link between the Z-source branches and atoll-source states. A description of our data set and reduction techniques is given in §7.2. In §7.3, we present an analysis of the CDs/HIDs. States and branches are classified for the entire outburst, and we study the global evolution of the Z/atoll tracks. Using our state/branch classification, in §7.4 we present our spectral fit results as a function of increasing source luminosity. Each of the Z-source branches and transitions between them (i.e., the vertices) is examined in terms of repeatable patterns in the evolution of spectral parameters. Results of a brief investigation of timing properties are presented in §7.5. In §7.6, we present a physical interpretation of the evolution of the source and some of the branches and vertices of the Z track, and we discuss the role of $\dot{m}$. A comparison with other NS LMXBs is also given. Finally, we summarize our main conclusions in §7.7.

7.2 Observations and data reduction

We analyzed all 866 pointed observations (∼3 Ms) of XTE J1701-462 from the 2006–2007 outburst made with the PCA and the High Energy X-ray Timing Experiment [HEXTE; Rothschild et al., 1998] instruments. For the PCA we only used data from Proportional Counter Unit (PCU) 2, which is the best-calibrated unit. For the HEXTE only Cluster B data were used, because all the observations of this outburst were made after 2006 January, when Cluster A started experiencing frequent problems with rocking between the source and background positions. We used the same standard criteria to filter the data as described in LRH07. Only observations with PCA intensity (background subtracted) larger than 10 counts/s/PCU were considered. Appropriate faint/bright background models were used when the source had intensity lower/higher than 40 counts/s/PCU. Deadtime corrections for PCA and HEXTE data were also applied.

To spectrally model the evolution of the source during the entire outburst, we must create pulse-height spectra on an appropriate timescale. This timescale should be short enough to characterize the spectral evolution, but also long enough to minimize statistical uncertainties. XTE J1701-462 showed rapid spectral variations on some occasions, especially on the FB. To characterize these variations, we created spectra with exposures of 32 s and 960 s, from "standard 2" data of PCU 2. The 960-s spectra were created by combining 30 sequential 32-s spectra with a maximum observational gap <500 s. Although we allow several gaps in a 960-s spectrum, in the end all such spectra have time span <1600 s. Longer observation gaps than 500 s limit the exposure to <960 s. If a spectrum had an exposure <320 s, it was combined with the preceding spectrum if the time gap between them was <500 s; otherwise it was omitted. The final selection of spectra for modeling was based on our understanding of the source variability, using the 32-s and 960-s spectra (see §7.3.4).

Once we had spectra from the PCA for spectral modeling, we created the response file for each spectrum using HEAsoft version 6.4. An investigation of Crab Nebula observations revealed that the low energy channels still showed calibration issues after 2006. Therefore, we used channels 4–50 (numbering from 1 to 129; ∼2.7–23.0 keV) for our spectral fitting and applied systematic errors of 0.8% for channels 5–39 (below 18 keV) and 2% for channels 4 and 40–50. We created the HEXTE spectra to match the PCA spectra in observation time. No systematic errors were applied for HEXTE data.

The observations of XTE J1701-462 were contaminated with a small amount of diffuse Galactic emission within the large field of view of the PCA (∼1°) [Fridriksson et al., 2009]. Count rates near the end of the outburst, between Modified Julian Day (MJD) 54321 and 54342, reached a constant level, ∼2 counts/s/PCU (after the normal background subtraction), due to this diffuse component. The next *RXTE* pointed observation of this source was nearly 5 months later and indicated a similar level of residual flux. To correct for the diffuse emission, we created a spectrum from the observations between MJD 54321 and 54342 and applied it as an extra background correction. We only did this for observations between MJD 54300 and 54321, when the source intensity was < 300 counts/s/PCU and the diffuse emission could skew the spectral results significantly.

In order to study the source evolution in a model-independent manner, we also examined the CDs/HIDs of XTE J1701-462. We calculated X-ray colors as described in LRH07. We normalized the raw count rates from PCU 2 using observations of the Crab Nebula, and we defined soft and hard colors as the ratios of the normalized background-subtracted count rates in the (3.6–5.0)/(2.2–3.6) keV bands and the (8.6–18.0)/(5.0–8.6) keV bands, respectively. Throughout the paper, all PCA intensity values are normalized and correspond

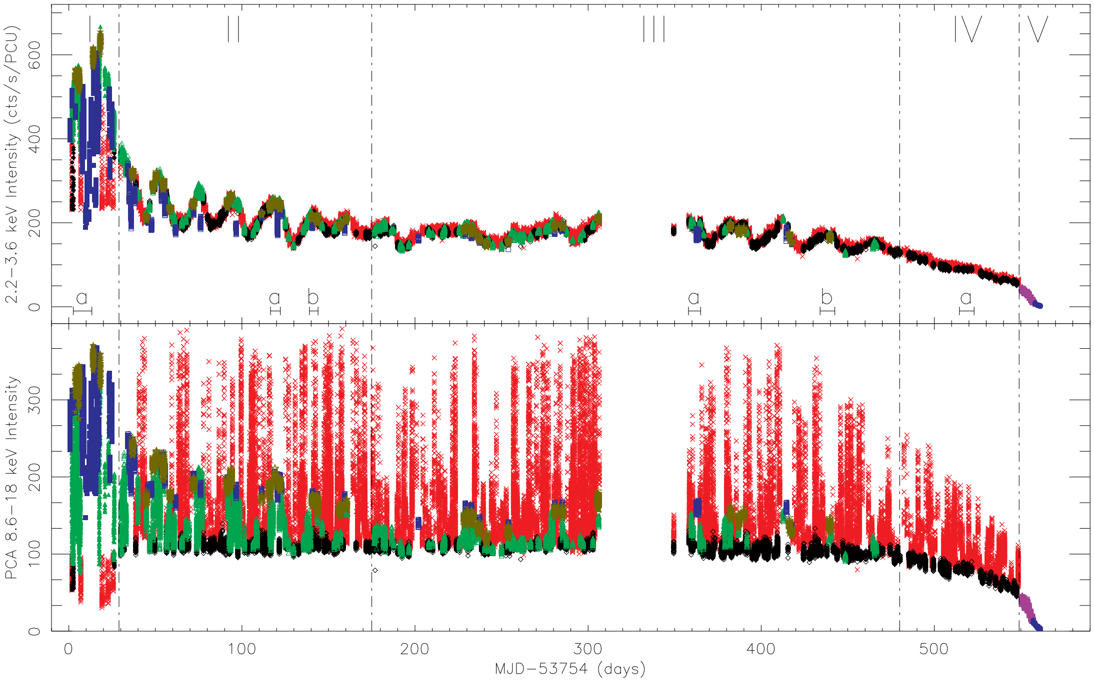

Figure 7-4: *RXTE* PCA 32-s light curves of XTE J1701–462 in two energy bands during the 2006–2007 outburst. The typical error bars are smaller than the symbol size. The outburst is divided into five stages. In stages I–IV, the source showed characteristics of Z source, with the HB, NB and FB marked by blue squares, green triangles, red crosses, respectively. We also mark the HB/NB and the NB/FB vertices by olive pentagrams and black diamonds, respectively (Figure 7-6). In stage V, the source showed characteristics of an atoll source, with the HS and SS marked by blue filled circles and purple hexagrams, respectively. The 'a' and 'b' in each stage mark the sample intervals for which detailed source properties are shown in §7.3.4 and §7.4.3.

to the sum count rate of these four energy bands. The difference between the normalized intensity and the raw total PCA count rate is normally <5%.

7.3 Light curves and color-color diagrams

7.3.1 Source state/branch classification

Normalized light curves, CDs and HIDs of the outburst of XTE J1701-462 are shown in Figures 7-4 and 7-5. The two light curves in Figure 7-4 have bin size 32 s, and they show count rates from the 2.2–3.6 and 8.6–18.0 keV energy bands, respectively. They are quite different, with the high-energy curve showing rapid and strong flaring, and the low-energy curve showing a ∼25-day modulation [Homan et al., 2007b] that varies in strength with time. The CDs and HIDs in Figure 7-5 were made from 960-s spectra to minimize the statistical uncertainties. The entire outburst is divided into five time stages, denoted by Roman numerals I-V. Their boundaries are marked by vertical dot-dashed lines in Figure 7-4, and the CDs and HIDs corresponding to each of the stages can be found in Figure 7-5. The boundaries between the stages are somewhat arbitrary, but are based on the following considerations: (I/II, MJD 53783) the source switches from Cyg-like to Sco-like Z source

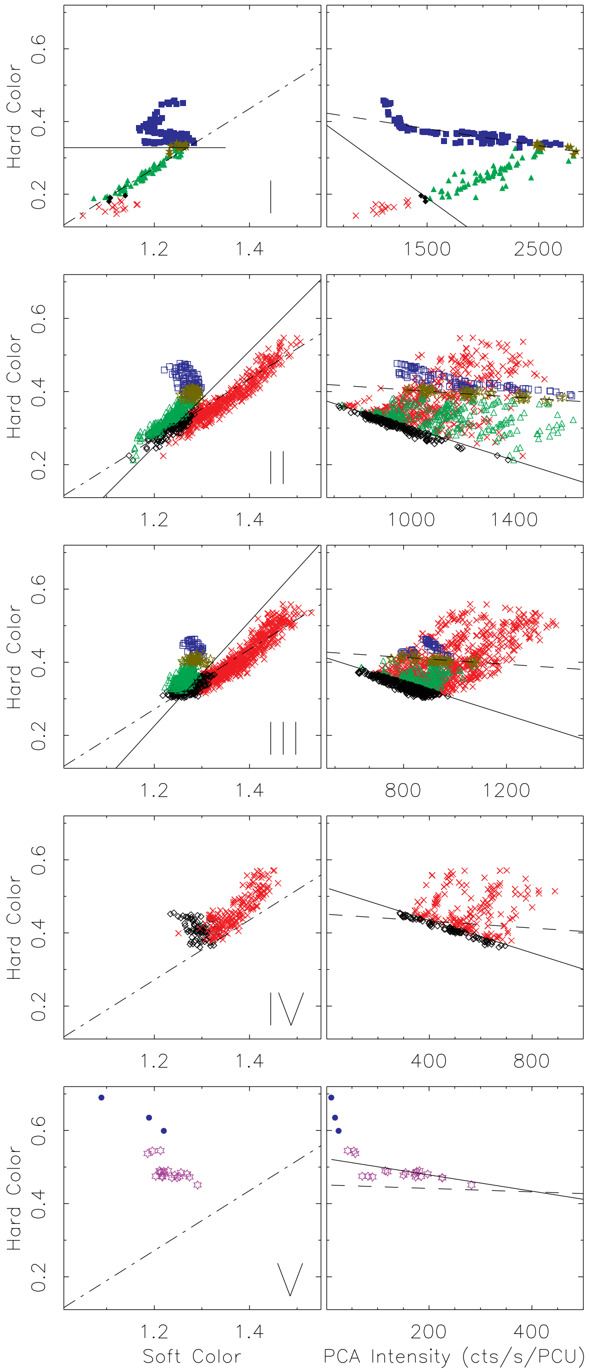

Figure 7-5: The CDs and HIDs for the five stages of the outburst defined in Figure 7-4. The bin size is ∼960 s for stages I–IV, while for stage V each data point corresponds either to one PCA observation or several observations combined (when the count rates are <30 counts/s/PCU). The meaning of the symbols are the same as in Figures 7-4 and 7-6. The solid and dashed lines are used to define the source branches. The typical error bars are smaller than the symbol size. The dot-dashed line is aligned with the NB in the CD of stage I and is shown in other panels of CDs for reference .

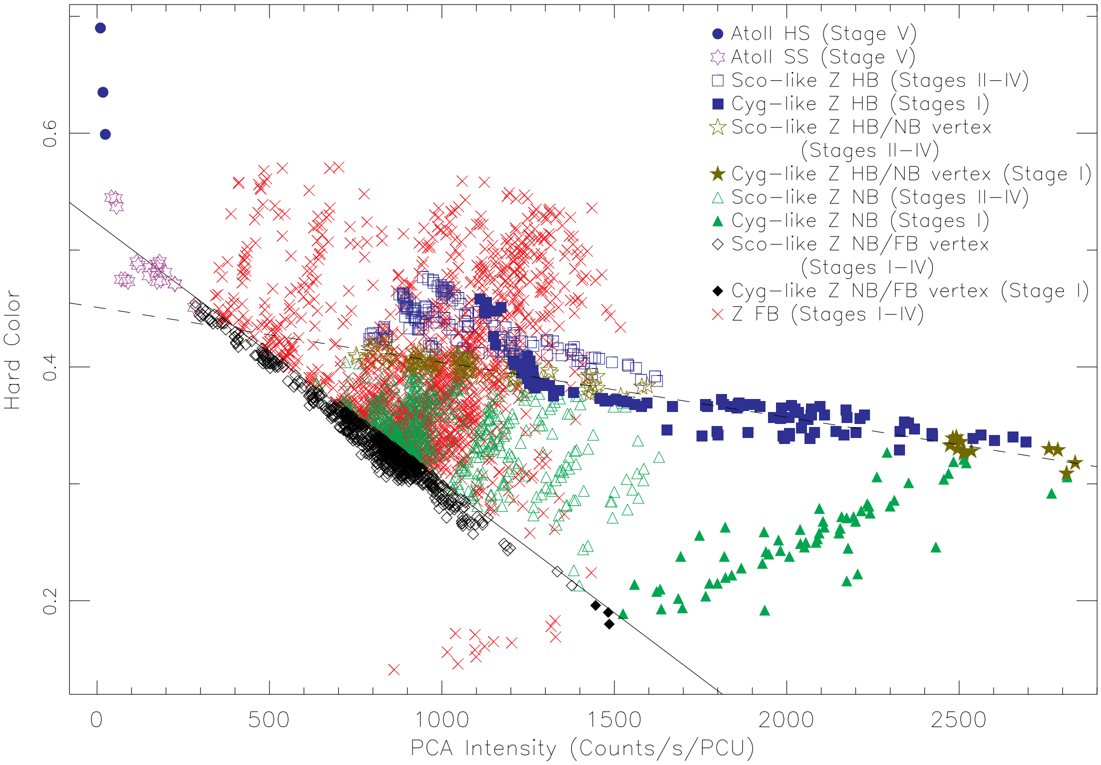

Figure 7-6: The complete HID of the outburst of XTE J1701–462. For reference, a legend of all different symbols is shown in the upper right corner; they apply to all other figures in this paper.

behavior in the CD, as reported in Homan et al. [2007b]; (II/III, MJD 53929) the long-term modulations at low energies become weaker and slower; (III/IV, MJD 54232) the long-term modulations disappear, and the final decay starts; (IV/V, MJD 54303) the flaring at high energies ends.

Most of the observations in stages I–II were analyzed in detail by Homan et al. [2007b] and shown to exhibit Z-source characteristics. Stage I is characteristic of a Cyg-like Z source, and stages II–III are similar to the Sco-like Z sources (Figure 7-5). In stage IV the source is similar to some of the bright atoll sources, such as GX 9+1 and GX 9+9 [Homan et al., 2007a]. While in those sources the observed flaring would be referred to as an upper banana branch, our analysis (see below) shows that it is simply a lower luminosity version of the flaring branch. In our view, the flaring is one of the defining characteristics that separate the Sco-like Z sources from the atoll sources. Thus we group stage IV with stages I–III and refer to them as the Z (source) stages. In stage V, XTE J1701-462 showed characteristics of an atoll source [Homan et al., 2007c], and we will refer to this stage as the atoll (source) stage. Finally, we note that the secular changes in stages II and III are mainly the result of the long-term modulations.

An important step toward understanding the evolution of the source is the classification of the observations in terms of states and branches. For sources showing substantial secular changes, this is normally done by dividing the data sets into smaller subsets, in order to identify clear tracks in the CDs/HIDs [e.g., Wijnands et al., 1997b, Homan et al., 2007b]. The observations of XTE J1701-462 are not long and dense enough (typically one hour per day) to do this for the entire data set, as the secular changes often smear the Z tracks before they are completely covered. A different way of classification is therefore necessary. Fortunately, we can take advantage of the fact that each branch shows systematic evolution in the CDs/HIDs of each of the stages. The HID for the entire outburst is shown in Figure 7-6; the position of the Z vertices throughout the outburst is marked by the solid and dashed lines, and the plot symbols that we use to differentiate the states/branches are given for reference (see below). We note that clear vertex lines are still seen if we define colors using the different energy bands that were used in Homan et al. [2007b].

The atoll stage V is divided into the HS (blue filled circle, with HC > 0.55) and SS (purple hexagram). Since little short-time variation is seen in stage V, each data point in Figure 7-5 corresponds to one entire PCA observation, and we also combine several observations when the source intensity is <30 counts/s/PCU. These same data intervals for stage V are used for spectral analysis in §7.4.

The branch classification strategy for Z stages proceeds as follows. Stages II–IV are Sco-like, and we focus on them first. In these stages, the HB, NB, FB, HB/NB vertex and NB/FB vertex are marked by (open) blue square, green triangle and red cross, olive pentagram and black diamond symbols, respectively (Figure 7-6). We made a preliminary branch classification in the CDs by hand, using data in $\sim$10-day time intervals, and found that the NB/FB vertex always hovers near the bottom of the corresponding HID. During the outburst the motion of this vertex is described well by a single line (i.e., the solid line) in the HID of Figure 7-6. Data below this line are identified as NB/FB vertex in stages II–IV. This line is also shown in the HIDs of stages I and V in Figure 7-5 for reference. The FB in stages II–IV is most easily identified in the CDs; it can be separated from other branches by simple lines (solid lines in the CDs of Figure 7-5 for stages II–III), while excluding the NB/FB vertex points described above. In stage IV, the HB and NB are absent, and the FB consists of all the points that remain after the NB/FB vertex points are identified.

For stages II and III, the HB, NB and HB/NB vertex classifications still need to be

Table 7.1. Statistics for observation time of the source in different states/branches

	observation time in ks and (percentage of the total)				
Source state/branch	I	II	III	IV	V
HB	96 (55)	90 (9)	40 (3)	0 (0)	—
HB/NB vertex	10 (6)	42 (4)	33 (3)	0 (0)	—
NB	52 (31)	228 (24)	178 (14)	0 (0)	—
NB/FB vertex	2 (1)	201 (21)	291 (24)	77 (33)	—
FB	12 (7)	408 (42)	687 (56)	156 (67)	—
SS	—	—	—	—	54 (58)
HS	—	—	—	—	40 (42)

defined. We first manually identified HB/NB vertex points based on the CDs and HIDs for a few short intervals (~10 days). Again, we found that they lie near a single line in the HIDs, i.e., the dashed line in Figure 7-6. This dashed line is also shown for reference in the HIDs of Figure 7-5. We identify the observations with a HC value within 0.01 of this line as the HB/NB vertex, excluding those on the FB, which were identified earlier. The other observations above and below this line were identified as the HB and NB respectively. At this point, the branch classification for Sco-like Z stages II–IV is complete. The classification process can be summarized as follows: the NB/FB vertex is identified by a line near the bottom of HIDs, the FB is separated from other branches in the CDs, and the HB/NB vertex lies around a single line in the HIDs, above and below which are the HB and NB respectively (excluding the FB and NB/FB vertex).

Cyg-like stage I spans about one month and mainly consists of two tracks. It shows strong dips (lower panel in Figure 7-4). The solid line which limits the NB/FB vertex in stages II–IV in the HIDs also applies to this stage (Figure 7-5), with the 'dipping' FB falling below the line, rather than above it. The boundary between the HB and NB is defined by a constant HC line in the CD. The HB/NB vertex points for the two main tracks are identified by hand. They fall close to the extension of the vertex line found for stages II–IV, as shown in Figure 7-6 (dashed line). The HB, NB, FB, HB/NB vertex and NB/FB vertex in this stage are marked by (filled) blue square, green triangle and red cross, olive pentagram and black diamond symbols, respectively (Figure 7-6).

7.3.2 Source evolution and relations between source types

With the classification of the source states/branches in place, we now investigate the global evolution of XTE J1701-462 during this outburst. Table 7.1 gives a summary of the amount of time that the source is observed in the different branches/states of each stage. Although these values are somewhat dependent on the definition of the boundaries between the source states/branches, it is quite clear that the fractions of time that the source stays on the HB and NB decrease with the evolution of the outburst with that on the HB decreasing faster. The source stays on the NB/FB vertex and the FB more and more frequently from stage I to stage IV. Moreover, while the source spends most of the time (>90%) on the HB and NB in stage I, it is not observed on the HB and NB at all in stage IV. We note that during each stage, the source often moves back and forth along the NB or the FB without entering another branch (Figure 7-4). Although there are no discontinuous jumps from one branch to another, the source often reverses its direction within a branch. We do not see a clear constraint as to when a source enters a specific branch, which seems to be random. The only exception is the occurrence of the HB during stages II and III, which appears mostly, but not exclusively, around the peaks of the long term modulation as observed in the low-energy light curve (Figure 7-4).

Following the disappearance of the HB and NB during stage IV, the FB disappears in stage V, and the original NB/FB vertex smoothly evolves into an atoll track. This is reflected both in the light curves (Figure 7-4) and in the HID (Figure 7-6). Moreover, there is no observational evidence that suggests that the HB evolves into the atoll SS or the atoll HS as $\dot{m}$ decreases [Muno et al., 2002, Gierliński and Done, 2002a, Homan et al., 2007b]. Another interesting phenomenon seen in Figure 7-6 is that the distance between the HB/NB vertex and the NB/FB vertex in the HID decreases with intensity (or equivalently, the NB shortens as the intensity decreases). In the HID, the HB/NB vertex line crosses that of the NB/FB vertex near the point where the FB disappears and the atoll track starts.

The Cyg-like HB/NB and NB/FB vertices seem to be natural extensions of Sco-like ones at high intensity (Figure 7-6). The Cyg-like NB also resembles the Sco-like ones. However, there are clear differences between the Cyg-like dipping FB and Sco-like strong FB. The HB in the Cyg-like stage is also very distinctive. It spans a much larger range of intensity than in other stages (Figure 7-6). However, in contrast with the FB, whose pointing direction switches from downward to upward in the HID as soon as the source enters stage II, the HB seems to transit more slowly, as it is still nearly horizontal and has significant range of intensity in stage II, especially at high intensity (Figure 7-5). This can be seen more clearly from sample intervals in §7.3.4. The HB becomes vertical only when the intensity is ∼800-1300 counts/s/PCU (Figure 7-6). It is interesting to see in Figure 7-6 that the nearly horizontal part of the Cyg-like HB (excluding the upturn) is closely aligned with the line traced out by the HB/NB vertex. This might hint at some connection between that part of the Cyg-like HB and the HB/NB vertex in the Sco-like Z stages. The upturn of the HB of the Cyg-like stage happens to have an intensity similar to the Sco-like HB. Considering that they are both vertical in the HID, they might be related, which we investigate based on spectral and timing properties later in this work.

7.3.3 Evolution speed along branches

Clues regarding the physical origin of each Z branch might be reflected in the timescales on which the source evolves along it. We therefore measure the speed at which XTE J1701-462 moves along its Z track. Such speed measurements have been made in the past for other Z sources [e.g., Wijnands et al., 1997b, Homan et al., 2002]. These authors used a rank number to track the source position along the Z track, which is scaled to the full length of the NB. This is very difficult to implement for XTE J1701-462, as it shows large secular changes of the tracks in the CDs/HIDs, making it hard to universally assign a rank number for all tracks. Instead, we measure the speed for each branch separately, by choosing a quantity X that changes substantially and is suitable for tracing the position along that branch. The normalized position in that branch can then be expressed as $S = (X - X_{\rm min})/(X_{\rm max} - X_{\rm min})$, where the maximum ($X_{\rm max}$) and minimum ($X_{\rm min}$) values are obtained in a time-dependent manner. When sequential data points have position numbers S_i and S_{i+1} and centroid temporal separation Δt, the speed at position $(S_i + S_{i+1})/2$ is calculated as $|S_{i+1} - S_i|/\Delta t$. This method is hereafter referred to as the rank-shift method. Using the normalized position in a branch, we also calculate a second measure of evolution speed, which is the inverse value of the fraction of the time that the source spends at each position of the branch. This

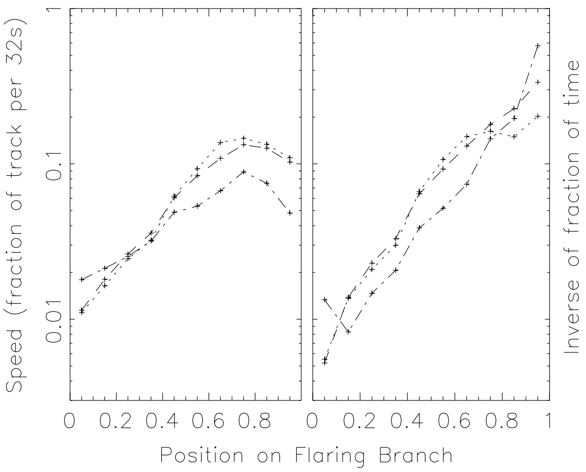

Figure 7-7: Left panel: the speed of the source along the FB, expressed as the average fraction of the FB track that the source goes through in 32 s. The FB is normalized to have length one, with the NB/FB vertex set to be 0.0. The position on the FB is based on the 8.6-18.0 keV intensity. The statistical error is very small, but the sample standard deviation is about as large as the speed itself. Right panel: inverse of the fraction of time in each segment (the normalization is arbitrary). This quantity is an alternative measure of the speed of the source along the FB (§7.3.3).

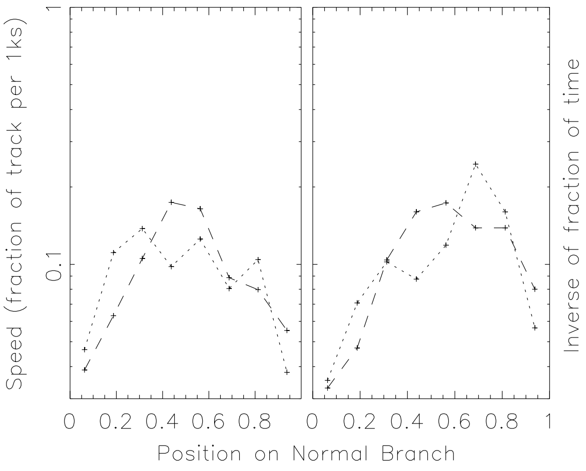

Figure 7-8: Same as Figure 7-7 but for the NB. The NB/FB vertex has a position value of 0.0, and the HB/NB vertex is 1.0. Time bins of 960 s are used for this plot.

method is valid under the assumption that our sampling does not bias the results.

For the FB and the NB/FB vertex, our speed measurement utilizes the intensity in the energy band 8.6-18.0 keV, since it shows strong changes (Figure 7-4). The source moves very fast along the FB, and 32-s spectra are used. We find that the intensity in this band maintains nearly constant minimum (∼100 counts/s/PCU) and maximum levels (∼350 counts/s/PCU) during stages II–III. Thus we set $X_{\min} = 100$ counts/s/PCU and $X_{\max} = 350$ counts/s/PCU for stages II–III. For stage IV, the range of the intensity at 8.6-18.0 keV on the FB changes with time. Thus we divide stage IV into intervals of 20 days and dynamically define $X_{\min}$ and $X_{\max}$ for each interval. Stage I has few FB observations, which are all dipping; they are not investigated.

The rank-shift results for the FB are shown in the left panel of Figure 7-7, using dotted, dashed and dot-dashed lines for stages II, III, and IV respectively. The NB/FB vertex has position number 0.0. We average the speed for ten bins along the FB. The statistical errors are very small, but the sample standard deviations per bin have values of order the speed. It is clear that the speed increases by about an order of magnitude as the source ascends the FB. The plot shows a slight decrease in speed at the tip of the FB, but this may be an artifact of the source reversing its direction at this position; if the speed at the top of the FB is high, this can occur within the timescale of our 32-s measurements. Based on the measured speed, we estimate that it takes ∼10 minutes for XTE J1701-462 to cross the FB in one direction. The right panel of Figure 7-7 is the inverse of the fraction of the time that XTE J1701-462 spends at each position of the FB. This result resembles the rank-shift method, in support of our finding that the speed increases as XTE J1701-462 ascends the FB.

The situation for the NB is more complicated. Figure 7-4 suggests that the intensity at 8.6-18.0 keV is also a good tracer for the position along the NB; the NB is much more pronounced here than in the low energy band. Samples of the NB show that it takes much longer time, about several hours, for XTE J1701-462 to travel across the NB. Hence, we use 960-s spectra to reduce the effect of short-time fluctuations. We only select intervals with complete tracks of the NB, i.e., including both the HB/NB and NB/FB vertices. Only stages II and III are considered, since only these two stages provide sufficient data. The results are shown in Figure 7-8. Because of its shorter range, the NB is divided into eight bins. Again we show the rank-shift method on the left and the method of the inverse fraction of time on the right. The NB/FB and HB/NB vertices have position numbers 0.0 and 1.0, respectively. Both stages and both methods give a common result: the speeds at the HB/NB and NB/FB vertices are much smaller than in the middle of the NB. Based on the speed measured here, we estimate that it takes about 3 hours for the source to cross the NB (excluding the first and last bins, assumed to be occupied by the vertices). The NB and FB branch crossing times have been independently confirmed from light curves and CDs/HIDs.

It is harder to measure the speed along the HB. Data samples (§7.3.4) show that it takes ∼a day for the source to trace out the HB, a timescale at which the secular changes of Z tracks become significant. The intensity decreases at high energy, but increases at low energy as the source climbs up the HB from the HB/NB vertex (§7.3.4). This suggests that a broad hardness ratio like (2.2–3.6 keV)/(8.6-18.0 keV) can be an effective means to track the source position on the HB. However, even this quantity only changes by at most 20% in stages II–III. Moreover, the end point of the HB is not well defined, which impedes our efforts to measure the evolution speed along the HB.

In summary, for the Sco-like Z branches it takes ∼10 minutes, ∼3 hours, and ∼a day for the source to go through the FB, NB, and HB respectively. The NB/FB vertex appears to represent a point of increased stability, compared to the adjoining branches, since the source evolves much slower when it enters this vertex. Figure 7-8 shows that the source slows down as it enters the HB/NB vertex from the NB, but we do not know whether the evolution speeds up as the source leaves the HB/NB vertex along the HB. Figures 7-7 and 7-8 can be interpreted to suggest that the FB and NB are unstable configurations relative to their ending vertices. We cannot say much about the Cyg-like Z stage I, due to insufficient observations, but a few samples also shows that the source moves much slower on the HB than on the NB or FB.

7.3.4 Selection of spectra for spectral fits

In this section, we examine the variability of XTE J1701-462 in different energy bands. The variability results will guide the data selection for our spectral fits, to be conducted over the entire outburst. We also investigate in detail the properties of a few sample intervals that exhibit evolution along Z branches. These samples will also be used later for our spectral analysis, to help us understand the physical causes of evolution along each branch.

Variability in different energy bands

The spectra in the atoll stage V show little variation within a typical PCA observation (Figure 7-4), and the spectrum of complete observations can be used for spectral fitting. However, variations are more significant and faster during the Z stages I–IV. We quantify the variations of the spectra within the time span of each 960-s spectrum using the 32-s spectra that it contains (see §7.2). We calculate the sample standard deviations (σ_s) and the means (μ) of the source intensity in the low and high energy bands and plot the fraction of variability (σ_s/μ) in Figure 7-9. In the low energy band the intensity varies little (~2%) within ~960 s in all branches, except for stage I where it varies up to ~25% on the dipping FB.

In the high energy band, the source intensity on the FB can vary up to 30% within ~960 s, while the HB and the NB typically show <10% variability. Also plotted in Figure 7-9 is the sample standard deviation of the hard color (σ_{HC}), again using the quanta of 32-s spectra within a given 960-s spectrum. Its variability is similar to the source intensity at high energy: σ_{HC} is <0.02 (~4%) except on the FB where it can be up to 0.08 (~15%).

For a 960-s spectrum we adopt the following criteria for steady conditions: $\sigma_{\mathrm{HC}} \leq 0.02$ and σ_{s}/μ $(8.6 - 18.0\mathrm{keV}) \leq 10\%$. The steady 960-s spectra generally have excellent statistics for spectral modeling. We obtain 2374 such spectra in the Z stages, about 79% of the total. Almost all non-steady intervals are on the FB.

Sample intervals

We now examine several sample Z tracks from the time intervals marked in Figure 7-4, corresponding to MJD 53756.6–53767.3, 53870.5–53876.2, 53893.0–53898.0, 54112.0–54119.0, 54188.0–54196.5, 54268.5–54277.0, and 54290.0–54299.0, respectively. These intervals span about five to ten days and are selected based on their small secular changes in the CDs/HIDs. Their light curves, CDs and HIDs are shown in Figure 7-10; the first and second columns are the light curves and CDs, respectively, and HIDs are plotted in the third and fourth columns. The light curves have bin size 32 s as in Figure 7-4, but in this case the intensity is the sum of all four energy bands (2.2–18.0 keV). From the light curves, we see that the

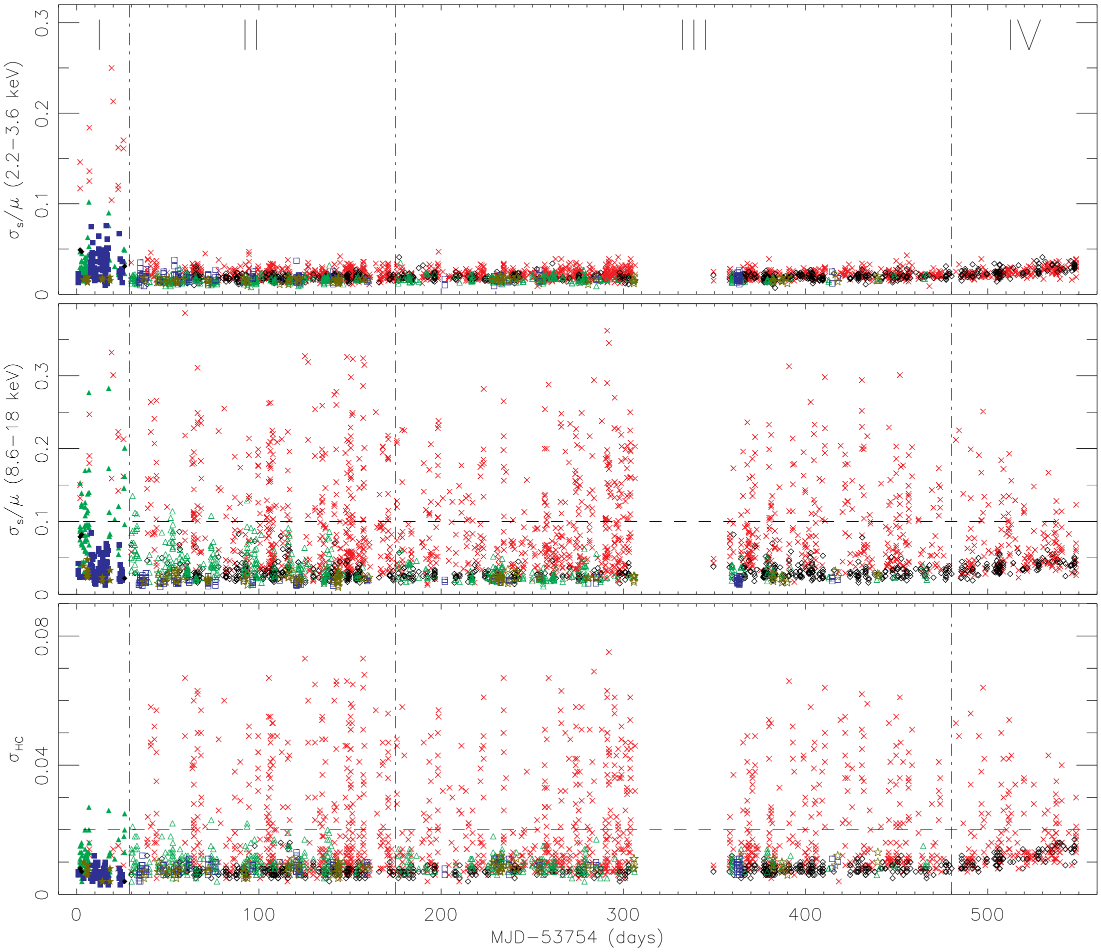

Figure 7-9: Different measures of spectral variability during the Z stages. Each point corresponds to one 960-s spectrum. The top two panels show the fraction of variability in two energy bands, using quanta of 32-s spectra for each point. The bottom panel is the corresponding sample standard deviation of the hard color.

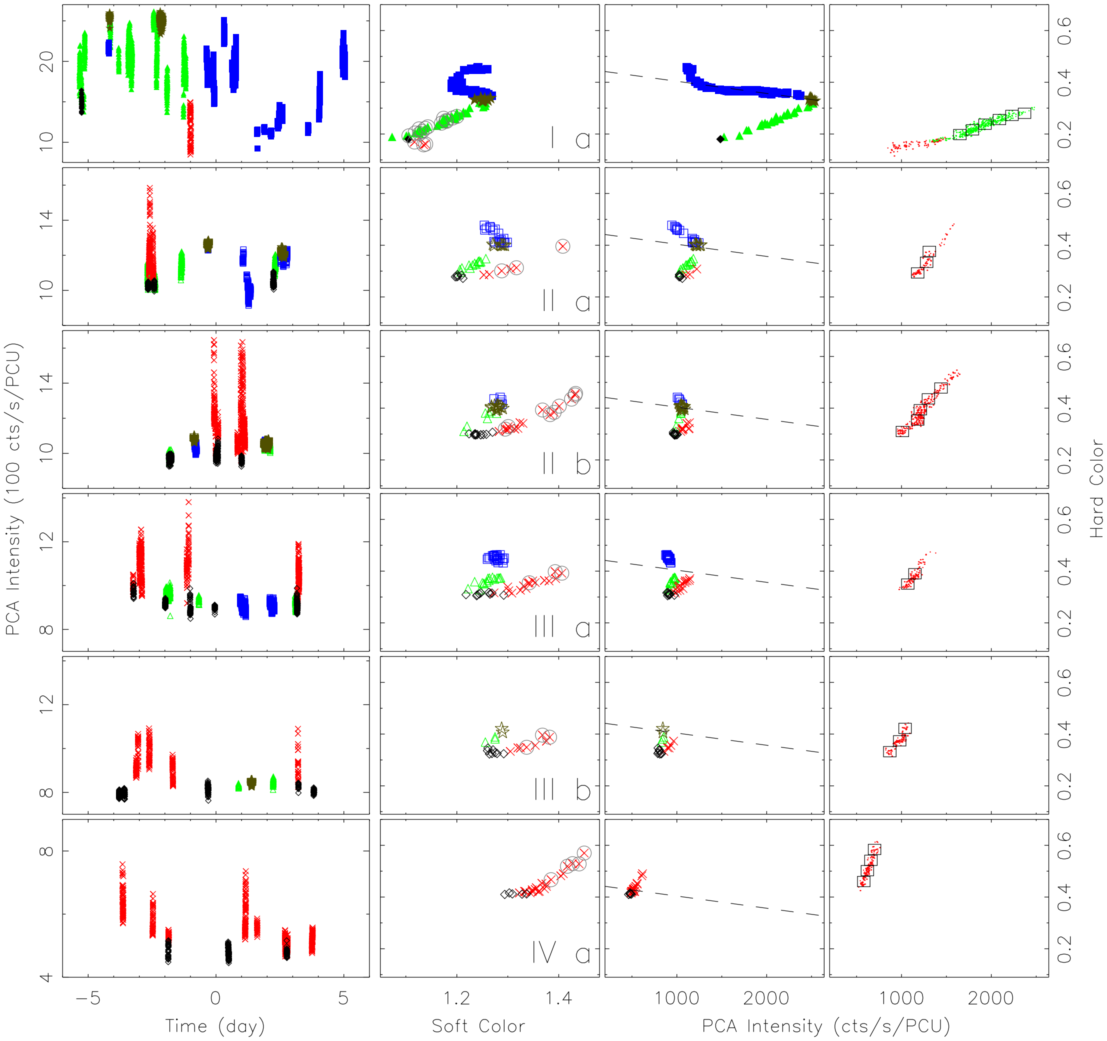

Figure 7-10: Light curves, CDs and HIDs of the sample intervals marked in Figure 7-4. The light curves are from 32-s spectra and the CDs from ∼ 960-s spectra. The HIDs for the steady (§7.3) and non-steady spectra (circled in the CDs) are shown in the third and fourth columns, respectively. The non-steady HIDs use the 32-s subintervals, and spectra within each box shown in these HIDs are combined to form a spectrum used for spectral fitting in §7.4.3.

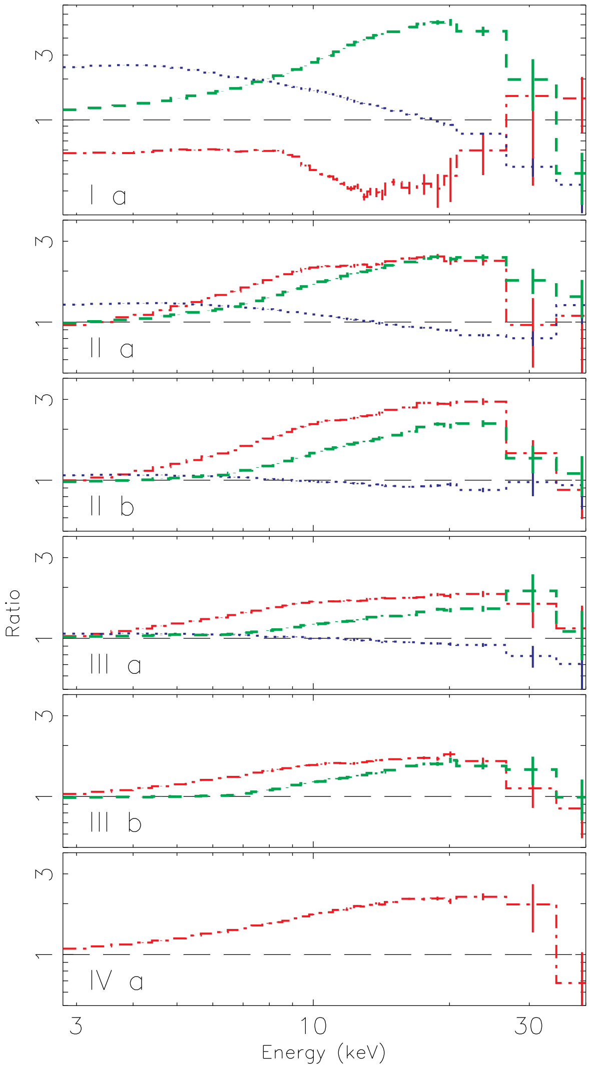

Figure 7-11: Comparison of the PCA spectra of XTE J1701-462 in key positions along the Z tracks from the sample intervals (§7.3.4). Blue dotted lines represent the ratio of the spectra at the HB/NB vertex relative to the left end of the HB. Green dashed lines show the ratio of the spectra at the HB/NB vertex relative to the NB/FB vertex. Red dot-dashed lines show the ratio of the spectra at the outer end of FB relative to the NB/FB vertex.

source evolves back and forth between different branches more than once in each sample interval. However, the corresponding CDs and HIDs (960-s bin size) each show only a single track. We therefore conclude that the secular changes in each sample interval are small. For the HIDs we differentiate two types of 960-s spectra. Data points from steady intervals are plotted in the third column. The steady 960-s spectra are used for spectral fitting without further grouping. We circle the non-steady 960-s spectra in the CDs and show their corresponding HIDs in the fourth column using their 32-s subintervals. To gain statistical precision, while avoiding spectral variability, we use boxes in the HIDs to group similar 32-s spectra and produce one spectrum per box (with exposures >300 s) for spectral fitting in §7.4.

We can compare the CDs/HIDs of the sample intervals from XTE J1701-462 with those from other Z sources (Figure 7-1). To aid in this comparison we plot in Figure 7-11 the ratios of spectra from key positions along the Z tracks in these sample intervals, analogous to what is displayed in Figure 7-2. The blue dotted lines correspond to the ratio of the spectra at the HB/NB vertex relative to the open end of the HB, the green dashed lines show the ratio of the spectra at the HB/NB vertex relative to the NB/FB vertex, and the red dot-dashed lines show the ratio of the spectra at the outer end of the FB relative to the NB/FB vertex. The ratios are defined to divide spectra with higher PCA intensity by ones with lower PCA intensity. The comparison of Figures 7-10–7-11 with Figures 7-1–7-2 confirms that stage I is consistent with being Cyg-like, while stages II–IV are Sco-like.

Figure 7-11 (blue dotted lines) shows that when the source descends the HB toward the HB/NB vertex, the intensity increases at low energies, but decreases at high energies. The pivot point is $\sim$20 keV in interval Ia, decreasing to $\sim$10 keV in the later intervals. We note that the HB in the interval IIa seems to represent conditions that are still in transition from a Cyg-like to a Sco-like Z source based on such spectrum ratio. This is consistent with the fact that the HB in this interval spans a large intensity range and appears horizontal in the HID, similar to Cyg-like sources (Figures 7-1). The increase in the intensity as the source moves from the NB/FB vertex to the HB/NB vertex (green dashed line) reaches maximum at energies > 10 keV. Moreover, in later intervals the intensity is almost constant below 7 keV. As for the FB, in interval Ia the intensity decreases as the source evolves along the FB from the NB/FB vertex, signifying a ‘dipping’ FB [Homan et al., 2007b]. This is different from the typical Cyg-like Z sources (Figures 7-1–7-2), where intensity initially increases from the NB/FB vertex along the FB, sometimes followed by dips that appear midway along the FB. The FB of XTE J1701-462 in stage I only shows dipping. This dipping increases suddenly at energies between 10–20 keV (Figure 7-11), perhaps indicating some type of occultation effect. In the Sco-like stages, the FB is quite long in the CDs/HIDs and the source intensity increases when moving away from the NB/FB vertex, most obviously in the high energy band 10–30 keV. All these details support the conclusion that stages II–IV are Sco-like.

7.4 Spectral modeling

7.4.1 Spectral models and assumptions

We used the hybrid model from LRH07 (Model 6) to fit the X-ray spectra of XTE J1701-462. In this model, the soft-state spectra are fit with a combination of MCD, BB, and CBPL. The CBPL component is a constrained broken power-law ($E_{\mathrm{b}} = 20$ keV and $\Gamma_1 \leq 2.5$) that can assume the role of weak Comptonization. The atoll hard-state spectra are fit with a

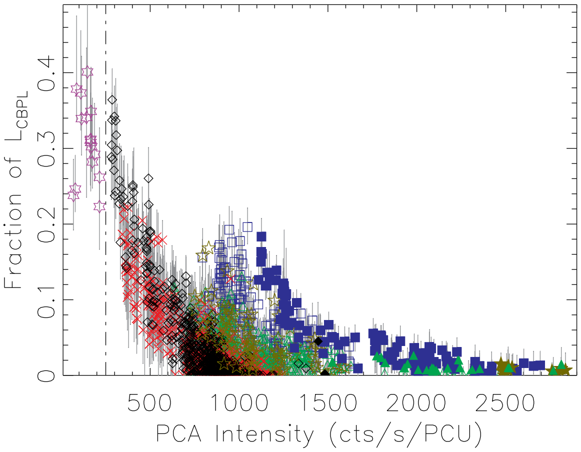

Figure 7-12: The fraction of the $L_{\rm CBPL}$ with one-σ error bars in the SS of atoll stage and in the steady spectra from all the Z stages.

combination of BB and BPL.

As in LRH07, the PCA and HEXTE pulse-height spectra were fitted jointly, with the normalization of the HEXTE spectrum relative to the PCA spectrum allowed to float between 0.7 and 1.3 (the average best-fitting value is 0.99±0.12). For the PCA spectra, we used energy channels 4–50, corresponding to 2.7–23 keV. For the HEXTE spectra, we used 20.0–80.0 keV for hard-state observations and 20.0–50.0 keV for soft-state ones. A Gaussian line was also included in the fit, with its central line energy constrained to be between 6.2–7.3 keV (the average best-fitting value is ∼6.5 keV) and the intrinsic width of the Gaussian line (σ) fixed at 0.3 keV. Interstellar absorption was taken into account with the hydrogen column density fixed at $N_{\rm H} = 2.0 \times 10^{22}$ cm^{-2}. The values of the hydrogen column density and the intrinsic width of the Gaussian line were based on joined fit of simultaneous observations of this source with *Swift* and *RXTE* .

The orbital inclination of the binary system cannot be very high ($\lesssim$75), as eclipses or absorption dips were not observed in this source. However, the Fe emission line is quite weak (equivalent width $\lesssim$50 eV), compared to other Z sources [e.g., White et al., 1986, Cackett et al., 2008b], and this could imply that the inclination is not very low, either [Fabian et al., 2000]. In this paper, a binary inclination of 70° was assumed. The luminosity and radius-related quantities were calculated using a distance of 8.8 kpc, inferred from type I X-ray bursts that showed photospheric radius expansion [Lin et al., 2007a, 2009a].

LRH07 showed that the CBPL component is only required at low-$L_{\rm X}$ soft-state observations. At higher $L_{\rm X}$, most spectra can be fit by the MCD+BB model. In Figure 7-12, we show the fraction of the $L_{\rm CBPL}$ using steady 960-s spectra in Z stages and all spectra in the atoll SS (§7.3.4). The $L_{\rm CBPL}$ was obtained by integrating from 1.5 keV to 200 keV. The choice of the upper limit is not critical since Γ_2 is normally >2. The majority (∼91%) of the steady spectra in the Z stages have $L_{\rm CBPL}$ that is less than 10% of the total luminosity. There are two situations when the CBPL component contributes significantly. The first is when the source intensity is low, at the end of the Z stage and in the atoll SS. The second is when the source enters the HB in the Sco-like Z stages or the upturn of the HB in the Cyg-like Z stage (∼800–1300 counts/s/PCU; Figure 7-6). In the top panel of Figure 7-13, we show a sample spectrum with a hard tail extending above 100 keV, from the upturn

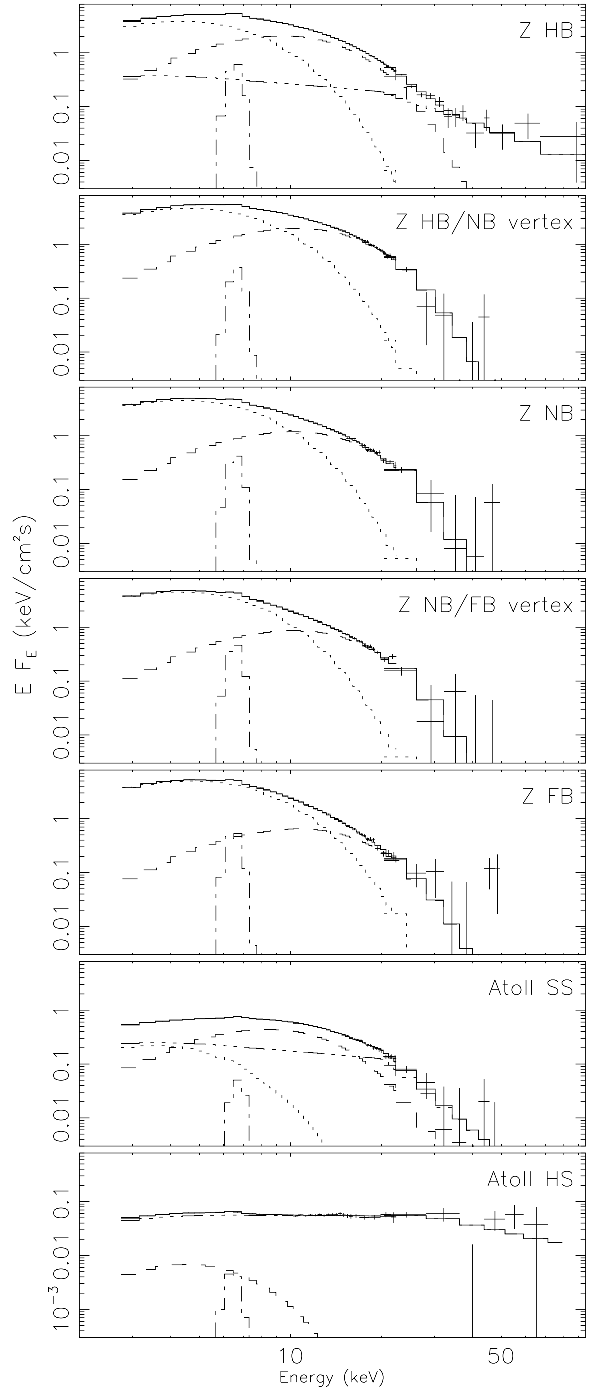

Figure 7-13: Examples of unfolded spectra at different states/branches. The total model fit is shown as a solid line, and it consists of an MCD component (dotted line), a BB (dashed line), a CBPL component (dot-dot-dashed line), and a Gaussian line (dot-dashed line). The spectrum at the top panel shows the detection of a hard tail on the HB.

of the HB in sample interval Ia. It is a combination of six observations made on 2006 February 2-3, with observation IDs 91106-02-02-12 and 91106-02-03-[01–05]. The combined spectrum has an total exposure of 15 ks, a hard color of 0.39 and an intensity near 1260 counts/s/PCU.

We also fit the steady 960-s spectra in the Z stages using the MCD+BB model, i.e. without the CBPL to account for a possible hard tail. About 90% of these spectra have an increase in the total χ^2 smaller than 4.6 (compared to the MCD+BB+CBPL model), a 90% confidence level criterion for the inclusion of the CBPL in the final fit for each spectrum. The initial photon index Γ_1 often reaches the hard limit in the fit of soft spectra so that the CBPL has only two free parameters in practice.

Figure 7-13 illustrates the unfolded spectra in different states/branches. The spectrum at the top panel is the one that we used to show the detection of a hard tail (see above). The sample spectra corresponding to the Z-source HB/NB vertex, NB, NB/FB vertex and FB are all from sample interval IIa, and all have exposures ∼960 s and intensities ∼1200 counts/s/PCU. There is no CBPL component in these unfolded spectra, because the inclusion of such a component does not improve the χ^2 (see above). The spectrum corresponding to the atoll-source SS is from observation 93703-01-02-11, with an exposure of 6155 s and an intensity of 181 counts/s/PCU. The spectrum corresponding to the atoll-source HS is a combination of observations 93703-01-03-14 and 93703-01-03-16, with an exposure of 13 ks and an intensity of 17 counts/s/PCU.

The spectral fit results are shown in the following sections. For clarity, we only plot data points with small error bars, i.e., if the difference between the upper and lower limits (90% confidence) of the temperature of the thermal components is smaller than 0.7 keV. In the end, 1.1% and 2.4% of the data points for the MCD and BB components are omitted, respectively.

7.4.2 Atoll source stage

Since our spectral model was developed for observations of transient atoll sources, we begin the fitting process of XTE J1701-462 with the atoll stage (V). We compare our results with those from LRH07, to see whether the spectral evolution in stage V is consistent with the behavior of other atoll sources. The CD and HID for this stage are shown in the bottom panel of Figure 7-5. The spectral fits show that the fraction of the $L_{\rm CBPL}$ can reach more than 30% in the SS (Figure 7-12). The HS observations are very faint and are dominated by the BPL component (∼95%) with initial photon index ∼2. The spectral fit results for the MCD and BB components are shown in Figure 7-14.

The left panel shows the luminosity of each thermal component versus its color temperature, $kT_{\rm BB}$ or $kT_{\rm MCD}$. For reference, we also show the lines for constant radius, assuming $L_{\rm X} = 4\pi\sigma_{\rm SB}R^2T^4$. The NS radius (8 km), inferred from type I X-ray bursts for an assumed distance of 8.8 kpc [Lin et al., 2009a, Chapter 8], is shown with dot-dot-dashed lines in Figure 7-14. The dot-dashed lines correspond to $R = 6.0$ km, and the dashed lines to $R = 1.7$ km. These latter two values are derived from the fit to the obtained best-fitting $R_{\rm MCD}$ and $R_{\rm BB}$ values, respectively. The inner disk radius is comparable with the inferred NS radius. However, we note that these values have large systematic uncertainties, since accurate measurements require knowledge of the distance, inclination, and other parameters such as the hardening factors for the disk and burst spectra.

The most remarkable result seen in Figure 7-14 is that the disk and boundary components evolve roughly along $L_{\rm X} \propto T^4$ tracks, consistent with LRH07 results for Aql X-1

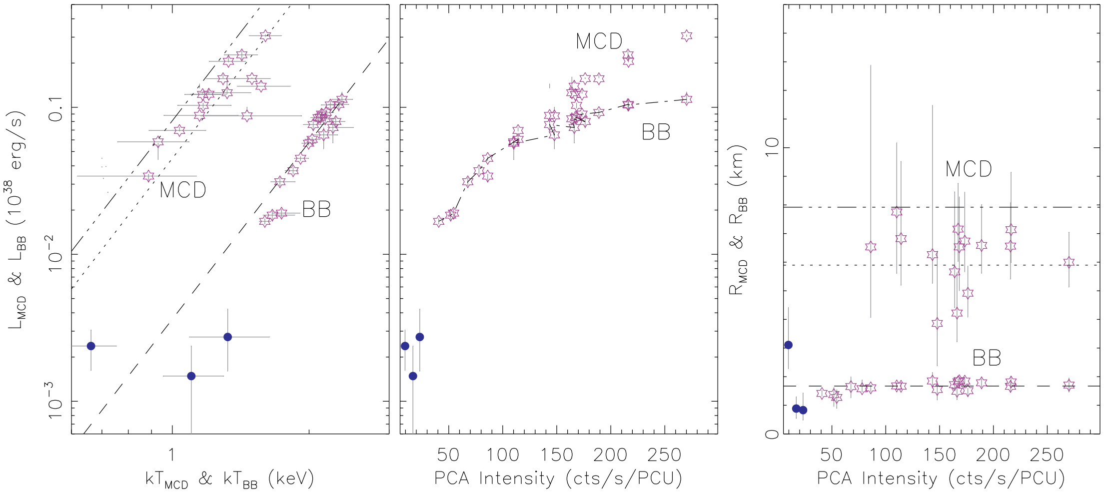

Figure 7-14: Spectral fitting results for the atoll stage of the outburst (stage V), using MCD+BB+CBPL for the SS and BB+BPL for the HS. There is no MCD component for the HS, and the blue filled circles correspond to the BB in all panels. The luminosities of the thermal components (MCD/BB) are plotted against their characteristic temperatures and the PCA intensity in the left and middle panels, respectively. The data points for the BB component in the SS in the middle panel are connected by a dot-dashed line for clarity. The right panel shows the characteristic emission size of the thermal component versus the PCA intensity. The dot-dot-dashed line corresponds to the size of the NS inferred from type I X-ray bursts. The dotted and dashed lines correspond to $R = 6.0$ km and $R = 1.7$ km, respectively, assuming $L_{\rm X} = 4\pi R^2 \sigma_{\rm SB} T^4$.

and 4U 1608-52. Moreover, the boundary layer is small and remains nearly constant in size throughout the SS. This can be seen in the right panel of Figure 7-14, which shows the best-fitting $R_{\rm MCD}$ and $R_{\rm BB}$ versus the source intensity. $R_{\rm BB}$ cannot be constrained very well in the HS, but its values are marginally consistent with those from the SS.

In the middle panel of Figure 7-14, we show the luminosity of each component (the MCD and BB) versus the PCA intensity. This plot makes it easy to link the spectral results to the HID in Figure 7-5. To help distinguish the two spectral components, the data points for the BB results in the SS are connected by a dot-dashed line.

7.4.3 Z Source Stages

The spectral evolution in the Z stages is more complex. To understand the physical processes that drive the evolution of Z sources along different branches, we carried out spectral fits for the samples of the Z tracks that were discussed earlier (time intervals marked in Figure 7-4 and light curves, CDs and HIDs shown in Figure 7-10). As explained in §7.3.4, we fit steady 960-s spectra directly, and we use box selections in the HIDs to combine 32-s spectra accumulated from the non-steady intervals. The spectral fitting results for the sample intervals are shown in Figure 7-15, one row for each interval. The quantities plotted in the three panels of each row are the same as for Figure 7-14. The results are discussed below, one Z branch or vertex at a time.

In addition to our consideration of these sample intervals, we also fit all the steady 960-s spectra of the four Z stages. The results are shown in Figure 7-16 for each branch/vertex. Some spectral results for non-steady observations in the sample intervals are also included

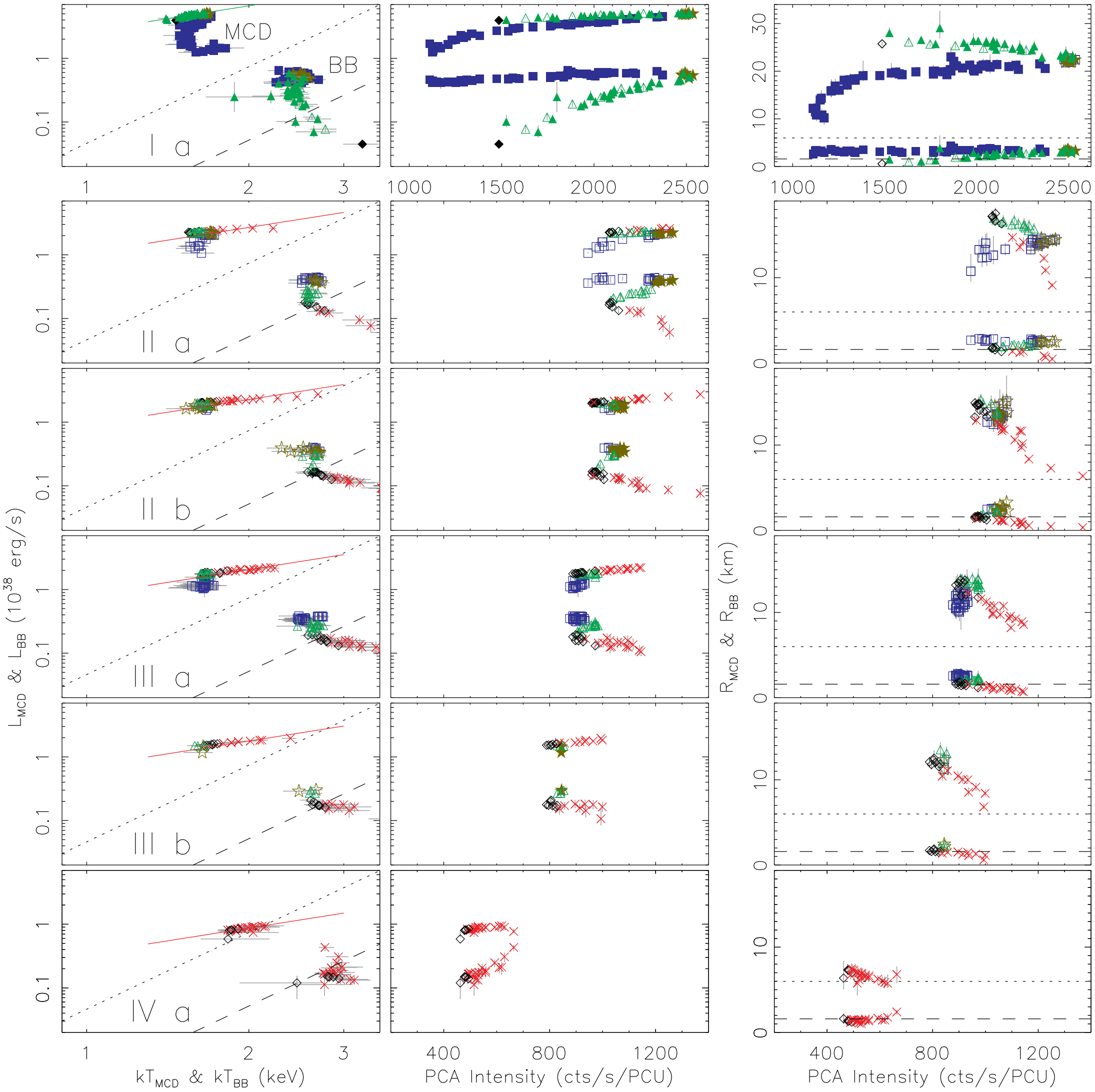

Figure 7-15: The spectral fitting results for the sample intervals (see §7.3.4). As in Figure 7-14, the luminosities of thermal components (MCD/BB) are shown versus their characteristic temperatures and versus the PCA intensity. The right column shows the characteristic emission size of the thermal component versus the PCA intensity. Each row of panels corresponds to one sample interval. The dotted line and dashed line in Figure 7-14 are replotted here for reference. In each panel, results of the MCD are always at the top, and those of the BB at the bottom.

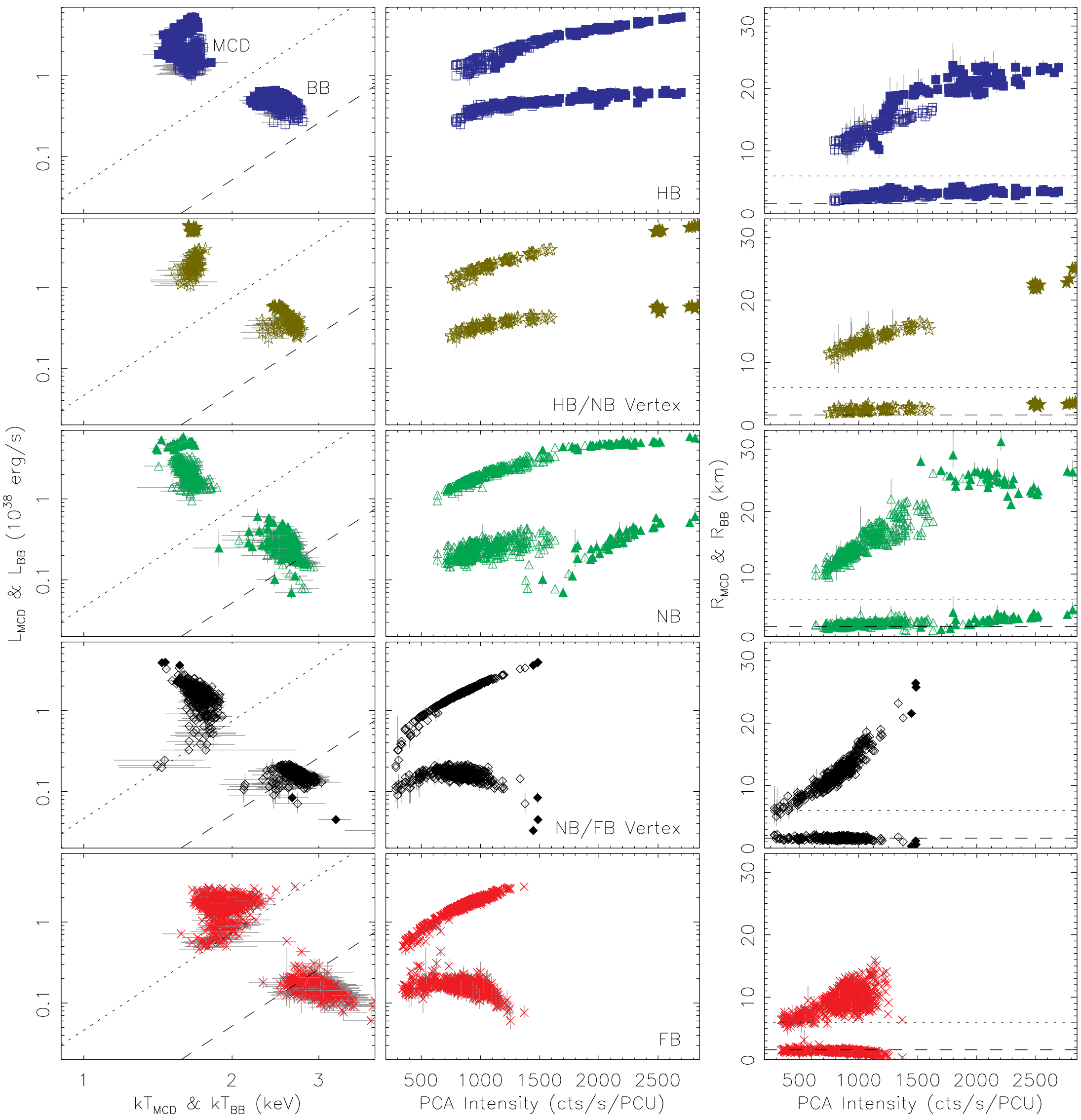

Figure 7-16: The same as Figure 7-15, but combining all observations throughout the Z stages of the outburst. From the top to the bottom, the rows correspond to the HB, HB/NB vertex, NB, NB/FB vertex, and FB respectively. The results are derived from the steady 960-s spectra plus the spectra created from the boxes shown in Figure 7-10.

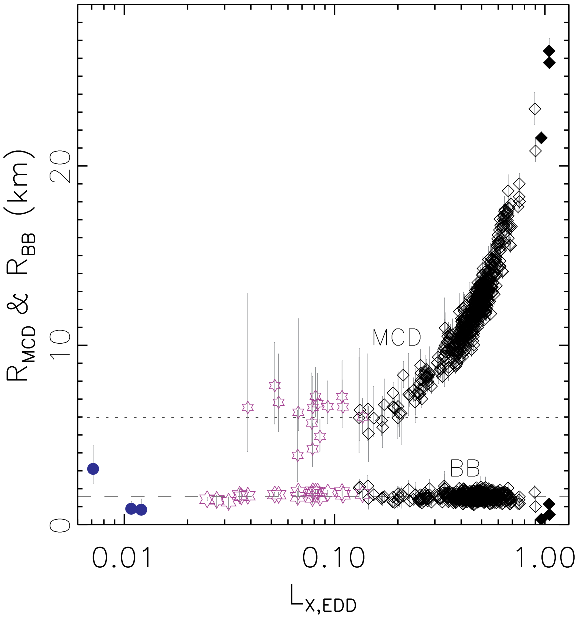

Figure 7-17: The emission sizes of the thermal components versus the total L_X for the NB/FB vertex and the atoll source stage V.

in this figure. The dotted and dashed constant radius lines from Figure 7-14 are again shown in Figures 7-15 and 7-16 for reference.

The NB/FB vertex

We begin the assessment of our spectral results for the Z stages by considering the evolution of the NB/FB vertex (black diamond symbols), which is globally shown to be well organized in Figure 7-16. When the Z-source behavior departs from the atoll track (Figure 7-14), the disk no longer follows the $L_{\rm MCD} \propto T_{\rm MCD}^4$ relationship, and $R_{\rm MCD}$ begins to increase with intensity.

To see this effect more clearly, we plot the radii of the thermal components versus the total L_X in units of $L_{\rm EDD}$ for the NB/FB vertex in Figure 7-17, with the results from the atoll track in stage V also included for comparison. $L_{\rm EDD}$ is taken to be 3.79×10^{38} erg/s. This value was estimated to be the Eddington luminosity for NS type I X-ray bursts showing photospheric radius expansion [Kuulkers et al., 2003]. This value was also used to infer the distance of 8.8 kpc for XTE J1701-462 [Lin et al., 2009a, Chapter 8]. We note that the same results would be obtained if we take the net flux from the spectral fit, while correcting the MCD term by inclination effect, and then divide by the average maximum flux measured for the two radius expansion bursts. Finally, we note that $L_{\rm X,EDD}$ is a quantity that is useful for scaling purposes only, since proper considerations of the Eddington limit should consider the disk and boundary layer of Z sources separately (§7.6), and, in addition, it is likely that a portion of the BB flux is obscured by the disk (LRH07).

In Figure 7-17, we see that the inner disk radius remains constant, at a value presumed to represent the innermost stable circular orbit (ISCO), until L_X reaches ~0.2 $L_{\rm EDD}$. Above this luminosity, the inner disk radius increases with luminosity. This is quite possibly a signature of the local Eddington limit in the disk and will be further discussed in §7.6.

When XTE J1701-462 deviates from the $L_{\rm MCD} \propto T^4_{\rm MCD}$ track, its evolution is consistent with $L_{\rm MCD} \propto T^{-4}_{\rm MCD}$, or equivalently $L_{\rm MCD} \propto R_{\rm MCD}$, with $T_{\rm MCD}$ slightly decreasing with $L_{\rm MCD}$.

In contrast to the behavior of the disk radius, the boundary layer ($R_{\rm BB} \sim 1.7$ km) maintained its small (nearly constant) size from the atoll stage to all observations in the NB/FB vertex, with luminosity ranging from ~0.01 to 1 $L_{\rm EDD}$. These results suggest an intimate relation between the atoll track and the NB/FB vertex.

The FB

The behavior of the FB is evaluated from the results of the sample intervals, shown in red cross symbols in Figures 7-15. Besides the two constant radius lines, we also plot solid lines for which $L_{\rm MCD} \propto T^{4/3}_{\rm MCD}$. These lines describe the relationship between disk luminosity and inner disk temperature when the source has a variable inner disk radius at a constant accretion rate, as shown in the following. The disk temperature T at radius R is [Hayakawa, 1981]

$$T(R) = \left(\frac{3GM\dot{m}}{8\pi\sigma_{\rm SB}R^3}\right)^{1/4} \tag{7.1}$$

where M is the mass of the NS. Evaluating the above equation at the inner disk radius and considering that $L_{\rm MCD} = 4\pi\sigma_{\rm SB}R^2_{\rm MCD}T^4_{\rm MCD}$ [Mitsuda et al., 1984], we obtain

$$L_{\rm MCD} = 4\pi\sigma_{\rm SB}\left(\frac{3GM\dot{m}}{8\pi\sigma_{\rm SB}}\right)^{2/3} T^{4/3}_{\rm MCD}. \tag{7.2}$$

A constant $\dot{m}$ then leads to $L_{\rm MCD} \propto T^{4/3}_{\rm MCD}$, as represented by the red solid lines in Figure 7-15.

This figure shows that the FB tracks closely follow the red solid lines, implying that the disk evolution is consistent with an inner disk radius varying under the condition of a constant $\dot{m}$. In the NB/FB vertex the disk is truncated at a larger radius than in the atoll stage. The FB is traced out when the disk refills temporarily and the inner radius shrinks to the value seen in the atoll stage, which is presumed to be the ISCO. As $\dot{m}$ increases, the disk in the NB/FB vertex is truncated at a progressively larger radius, thereby shifting and lengthening the constant $\dot{m}$ line along which the disk evolves on the FB. The superposition of these tracks can be seen in the left bottom panel of Figure 7-16.

The BB component contributes less as the source ascends the FB, especially in the intervals from stages II–III. At the same time, the temperature appears to increase, while the effective radius sharply decreases. We have no interpretation for these effects, and it is also possible that the results are affected by systematic problems with our model when one component (BB, in this case) contributes a small fraction of the flux. The FB of interval Ia is of the dipping type, and its spectra cannot be fit well by the MCD+BB+CBPL model. Therefore, the results for the FB of this interval are not shown.

The NB

Results from the sample intervals (Figure 7-15) show that, as the source ascends the NB in the Sco-like stages II–III, the MCD component seems to remain unchanged, while the BB radius increases at constant temperature. The latter effect causes an increase in the source intensity at energies around 10–30 keV, with almost no change at energies <7 keV (green

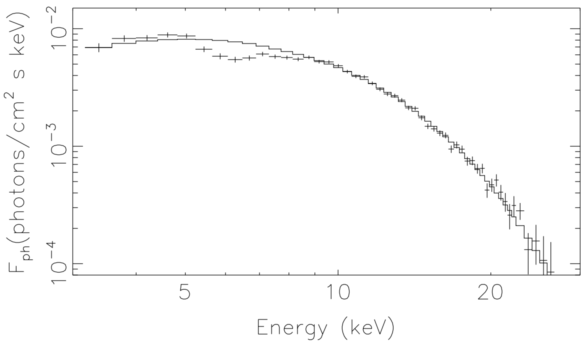

Figure 7-18: The difference of spectra for the two ends of the NB during interval IIIa. The spectrum is fit with a BB model (solid line) excluding the region 4.5–8 keV around the Fe line. The success of this model confirms that the evolution along the NB during this Sco-like Z stage is mostly due to the changes of the boundary layer emission area.

dashed lines in Figure 7-11). Since the NB is mainly the result of a changing BB radius, it is interesting to see whether the difference of the spectra from the two ends of the NB can be fit by a BB model. We test this on the NB in sample interval IIIa. Excluding the region around the Fe line near 6.4 keV, the resulting spectrum (Figure 7-18) can indeed be fit by a BB, with temperature $kT_{\rm BB} = 2.71 \pm 0.03$ keV. This temperature is close to that of the individual spectra on this particular NB, confirming that the source evolution along the NB is mostly due to an increase in the normalization of the BB at constant temperature. The difference spectrum shows a dip around the Fe line, indicating that the Fe line emission is stronger at the lower part of the NB, despite the fact that the source intensity at the lower part of the NB is lower.

On the NB of interval Ia the BB still changes very significantly, but in that case there is also a clear change in the MCD parameters, roughly consistent with evolution at a constant $\dot{m}$ through the disk (Figure 7-15). From the NB/FB vertex toward the HB/NB vertex, $L_{\rm MCD}$ and $kT_{\rm MCD}$ increase while $R_{\rm MCD}$ decreases. The $L_{\rm BB}$ and $R_{\rm BB}$ also increase. All this results in a large increase in the source intensity, at energies around 10-30 keV (Figure 7-11).

The possible origins of the BB increase on the Sco-like NB are discussed in §7.6. The coupled changes in the MCD and BB components for the Cyg-like NB seem to be complicated, and we have no simple picture of the corresponding physical changes.

The HB/NB vertex

Similar to the NB/FB vertex, the behavior of HB/NB vertex in the HID is well organized, i.e., it evolves along a single line in Figure 7-6. Since there is little change in the MCD component on the NB of the Sco-like stages, the differences between the MCD quantities of the HB/NB vertex and those of the NB/FB vertex are small (Figure 7-15). Only when the luminosity increases above a certain value do their differences become significant. This is reflected in the global spectral results for the HB/NB vertex in Figure 7-16: $kT_{\rm MCD}$ in the HB/NB vertex hovers around 1.6 keV, whereas $kT_{\rm MCD}$ in the NB/FB vertex shows a slight decrease at high luminosity.

Both $R_{\rm BB}$ and $R_{\rm MCD}$ increase with intensity. The visible BB effective radius always appears smaller than the disk radius and never reaches the values of the inner disk radius seen in the atoll stage. Both $L_{\rm MCD}$ and $L_{\rm BB}$ increase with intensity, but $L_{\rm MCD}$ increases

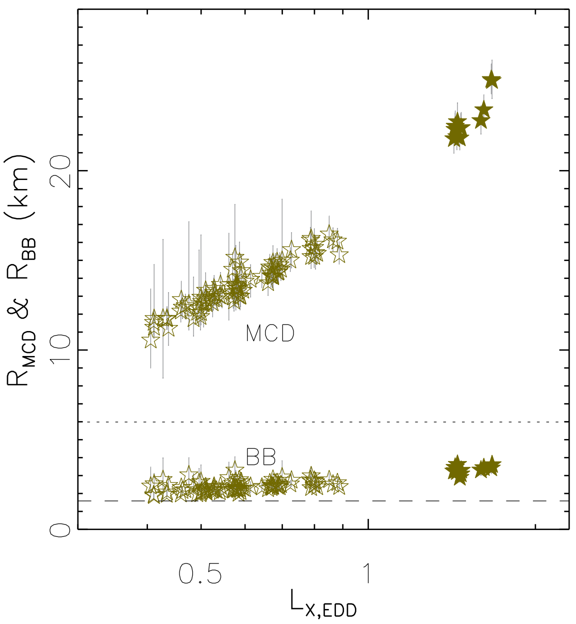

Figure 7-19: The emission sizes of the thermal components versus the total L_X for the HB/NB vertex.

much faster.

Although the Cyg-like and Sco-like Z tracks are quite different, the data points of HB/NB vertex in Cyg-like Z stage I seem to lie along the high-L_X extension of the points of the HB/NB vertex in the Sco-like Z stages II–IV. Figure 7-19 shows the emission sizes R_{MCD} and R_{BB} of the thermal components with respect to the total L_X, instead of the intensity. The HB/NB vertex extends from ∼0.4 to 1.7 Eddington luminosity, and the R_{MCD} and R_{BB} both increase with luminosity. However, there is a gap between 0.9–1.4 L_{EDD}.

The HB

The HB is first investigated using the sample observations (Figure 7-15). In general, L_{MCD} decreases as the source ascends the HB away from the HB/NB vertex. This causes changes in the spectrum at low energies, as shown in Figure 7-11 (blue dotted lines). The BB component, however, varies little. In contrast with the decrease in the intensity at low energy, there is an increase in the intensity at high energies, going out along the HB. This is mostly due to an increase of the Comptonized component (Figure 7-12), which for the Cyg-like Z stage mostly occurs on the upturn of the HB. The significant detection of Comptonization on the HB of the Z stages is consistent with a series of discoveries of hard tails in other Z sources [Paizis et al., 2006, Farinelli et al., 2005, Di Salvo et al., 2001, D'Amico et al., 2001, Di Salvo et al., 2000b], although there are claims of hard tail detections on branches other than the HB in some of these reports.

To illustrate the coupled behavior between the MCD and the CBPL components on the HB more quantitatively, we plot in Figure 7-20 the fractions of the L_{MCD} (upper panels) and the $L_{MCD} + L_{CBPL}$ (lower panels) for sample intervals Ia and IIIa. The results for all observations on the HB and HB/NB vertex are also plotted, on the right. We can see that while the fraction of the L_{MCD} on the HB changes by 20% (upper panels), the fraction

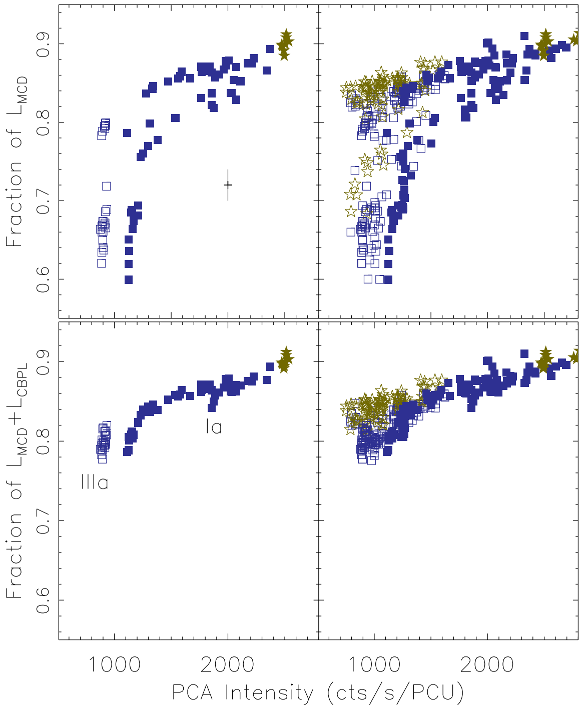

Figure 7-20: The fractions of the L_{MCD} (upper panels) and $L_{\mathrm{MCD+CBPL}}$ (lower panels) on the HB and the HB/NB vertex. Left panels show sample intervals Ia and IIIa, while the right panels show the entire outburst.

of the $L_{\mathrm{MCD}} + L_{\mathrm{CBPL}}$ maintains a much smoother track over the Sco-like Z tracks. On shorter timescales, the quantity $L_{\mathrm{MCD}} + L_{\mathrm{CBPL}}$ changes also very little over a typical Sco-like HB, e.g., only 5% for interval IIIa. The above results imply that in the Sco-like Z stages, as the source climbs up the HB, thermal emission from the disk is converted into a hard component by Comptonization. This is also true for the upturn of the HB in the Cyg-like Z stage. Thus the similarity between the Sco-like HB and the upturn of the Cyg-like HB is supported by both the fraction of Comptonization and the coupling between the MCD and CBPL luminosities.

7.5 Broadband variability

Although this work mostly focuses on the spectral properties of XTE J1701-462, timing properties are important tools for understanding the evolution along atoll and Z tracks. In LRH07 we used a measure of the broadband variability to compare the results of our spectral fits to those obtained for black hole systems. In particular, we focused on the relation between the fraction of Comptonized flux and the strength of the variability, as measured by the integrated (fractional) rms in the power density spectrum (PDS; 0.1–10 Hz).

In Figure 7-21 we plot the integrated rms versus the PCA intensity for XTE J1701-462. Similar to the classical atoll sources, the power is very weak in the atoll SS (<6%) and increases in the atoll HS. In the Z stages, except for the HB, the power is always very weak, with typical rms of 2%. Although the Sco-like HB typically has a small intensity

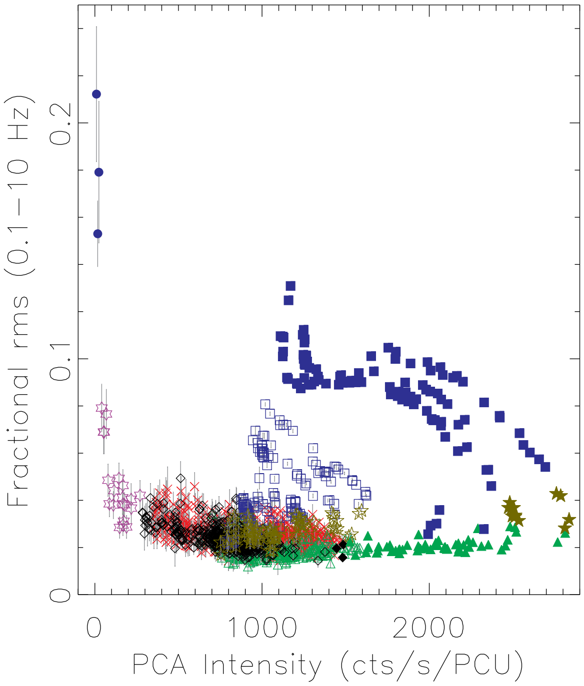

Figure 7-21: The rms from 0.1–10 Hz for the entire outburst. Elevated continuum power (i.e., rms > 5%) in the PDS is limited to the Z source HB and atoll source HS.

range (∼ 100 counts/s/PCU), the rms can increase quite significantly, by up to 4%, from the HB/NB vertex to the tip of the HB. We attribute this rms increase to the growing importance of Comptonization on the HB. This is consistent with the result in LRH07, in which we found that the rms is strongly tied to the fraction of the Comptonized component for both atoll sources and black hole binaries.

On the upturn of the Cyg-like HB the rms increases significantly, another aspect that makes it similar to the Sco-like HB. However, the rms on the upturn of the Cyg-like HB is higher than on the Sco-like HB. Moreover, on the non-upturn part of the Cyg-like HB, the rms already increases strongly, even though the Comptonization fraction remains low (Figure 7-20). The analysis of the frequency resolved spectroscopy on the typical Cyg-like Z sources [Gilfanov et al., 2003] indicated that this boost in rms seems to arise from the boundary layer.

7.6 Discussion

7.6.1 Secular evolution of XTE J1701-462 and the role of $\dot{m}$

During its 2006-2007 outburst, XTE J1701-462 successively shows characteristics of Cyg-like Z, Sco-like Z, and atoll sources, and the stages for each source type are clearly correlated with the X-ray luminosity. The Z tracks move substantially in the HID, while creating distinct lines for the upper (HB/NB) vertex and the lower (NB/FB) vertex, respectively (Figure 7-6). The line for the lower vertex smoothly connects to the atoll track. XTE J1701-462 shows a large dynamic range in luminosity that is typical of X-ray transients, and the overall shape of the broad band light curve is expected to represent the temporal evolution of $\dot{m}$. It is then straightforward to examine Figure 7-3 and Table 7.1 and conclude that the transitions between source types and the secular changes in the HID are both driven by the changes in $\dot{m}$.

A more detailed accounting of $\dot{m}$ can be derived from the results of our particular X-ray spectral model, which tracks the contributions from the MCD, the BB, and weak Comptonization. We first focus on the MCD, since the disk radiation is always the strongest component in the spectrum, except for the atoll hard state, and the origin of the radiation is upstream of any effects of the Eddington limit. We can infer $\dot{m}$ from the MCD model through [Frank et al., 1985]

$$\dot{m} = \frac{2L_{\mathrm{MCD}}R_{\mathrm{MCD}}}{GM}. \tag{7.3}$$

Figure 7-16 shows that for each of the vertices, both L_{MCD} and R_{MCD} increase with intensity, implying that $\dot{m}$ changes monotonically along each of the two vertex lines. If we use $\dot{m}$ for the MCD at the upper luminosity end of the atoll stage as a reference value, then there is a factor ~30 increase in $\dot{m}$ in the lower vertex at the upper luminosity end of the Sco-like Z stage (i.e., near 1400 counts/s/PCU), and factors ~40 and ~60 increase at the brightest points in the lower and upper vertices, respectively, of the Cyg-like Z stage. These ratios are larger than the corresponding ratios in luminosity or PCA intensity, because, for the same $\dot{m}$, an increasingly truncated disk produces radiation with decreasing efficiency. These accretion rates would amplify the sense in which XTE J1701-462 is seen to be an extraordinary X-ray transient.

Our spectral results for the MCD also provide insights as to how the Eddington limit might affect the behavior of Z source. In the atoll stage, R_{MCD} remains constant, and the value is presumably close to the radius of the ISCO. In the Z stages, R_{MCD} increases with L_{MCD} (and $\dot{m}$) along the NB/FB vertex line (Figure 7-17). One may interpret this result as the effect of the local Eddington limit in the disk. The Eddington limit is reached when the radiation pressure overcomes the force of gravity. For a spherical case, both gravity and radiation forces vary as r^{-2}, and the Eddington limit has a single value that covers all radii. However, in a disk system, both the gravity and radiation forces depend more complicatedly on r, and the Eddington limit should be reached locally [Katz, 1980, Fukue, 2004]. In a standard disk (Equation 7.1), the locally generated luminosity varies as r^{-3}, and radiation pressure most effectively moves matter in the vertical direction, while the vertical component of gravity force roughly varies as r^{-2}, if we assume that the thickness of the disk scales linearly with r. When $\dot{m}$ increases to a certain point, the inner disk must adjust to the radius where the local Eddington limit is reached, while at larger radii the disk can continue to produce thermal radiation [Katz, 1980, Fukue, 2004].

Detailed considerations of super-Eddington mass flows in accretion disks have shown $\dot{m}$ regimes in which the disk is thickened, an advective or quasi-radial accretion flow dominates the region inside the inner disk radius, and substantial mass may be driven out of the system [Katz, 1980, Watarai et al., 2000, Mineshige et al., 2000, Fukue, 2004, Ohsuga and Mineshige, 2007]. Such accretion solutions are often referred to as "slim disk" models. Structural changes for the slim disk will modify the $T(r)$ function, so that the emergent spectrum will no longer resemble the MCD model. However, the divergence between these models might not be apparent until $\dot{m}$ is much larger than the critical value that first brings the inner disk to the Eddington limit at the ISCO [Mineshige et al., 2000].

Slim disk models depend on the mass of the compact object and the accretion rate, and there are additional considerations required for effects of general relativity and of radiative transfer through the thick disk. Furthermore, such models are usually applied to accreting black holes, which are free from the additional emission from the boundary layer and its illumination of the inner disk. In black hole studies, observers look for evidence of slim disks in high-luminosity soft-state observations in which the MCD model does not fit the data well, while a more generic disk model based on the function, $T \propto r^{-p}$, constrains p to be somewhat lower than the value ($p = 0.75$) required for the MCD [Okajima et al., 2006]. Application of a slim disk model for XTE J1701-462, which requires careful considerations of the NS boundary layer, is beyond the scope of this investigation. We note, however, that we do not see a χ^2 barrier for our spectral model when the source is very bright, which suggests that the deviations between the disk spectrum and the MCD model are not large in the observed bandpass (3–50 keV).

We have seen that both the upper and the lower vertices evolve along two distinct lines respectively in the HID over a large overlapping intensity range (Figure 7-6). However, the variations of the MCD and BB components along the upper vertex line are different from those along the lower vertex line (Figure 7-16). This might imply that the system is able to respond to the variations in accretion rates in two different ways along these two vertex lines. We have discussed two possible disk solutions above (i.e., standard thin disk versus slim disk), and thus it is possible that the two vertices assume these two different solutions for disk accretion respectively. This idea will be further discussed in the next section in terms of the behavior of the source along the NB, which bridges these two vertices.

Our model fits additionally track the apparent conditions in the NS boundary layer, via the spectral parameters for the BB component. At the lower vertex, it is apparent that $L_{\rm BB}$ increases much more slowly than $L_{\rm MCD}$ and even decreases at the highest intensity in the Z-source stages (Figure 7-16). In addition, there is no evidence for BB radius expansion during the evolution that spans the atoll stage and the lower vertex in the Z stages (Figure 7-17). Thus, we can find no clear evidence on the lower vertex track for any critical point at which Eddington limit is reached in the BB, which is expected to expand and evolve in spectral shape as the luminosity passes through the Eddington limit [Inogamov and Sunyaev, 1999, Popham and Sunyaev, 2001]. This casts doubt on the idea that the gradual expansion of the disk with increasing luminosity at the lower vertex might be some type of disruption caused by the emission from boundary layer. On face value, our spectral results imply that significant mass outflow from the inner disk edge (in the Z stages) limits $L_{\rm BB}$ to levels below or near the Eddington limit at the surface of the NS.

Other investigations have looked for an Eddington signature in the behavior of the BB temperature. A value of $kT_{\rm BB} \sim 2.4$ keV was found to be a high-luminosity limit for accreting NSs that were studied with the Fourier-frequency resolved spectroscopy technique [Gilfanov et al., 2003, Revnivtsev and Gilfanov, 2006]. This value is close to the peak temperature seen in radius expansion bursts [Galloway et al., 2008], while a peak value $\sim$2.7 keV is found for two such bursts from XTE J1701-462 [Lin et al., 2009a, Chapter 7]. In both Z-vertices, the NB, and the HB (Figure 7-16), $kT_{\rm BB}$ hovers near 2.7 keV, with a trend toward slightly lower temperature and slightly larger $R_{\rm BB}$ at highest $L_{\rm BB}$. Thus, unless there is variable obscuration of the BB region that masks more substantial changes in conditions there, we surmise that at the lower vertex the BB hovers near its Eddington limit and that the BB inherits an increasingly smaller fraction of the $\dot{m}$ that flows through the disk, as $\dot{m}$ increases.

Once the inner disk radius is set by the Eddington limit in the lower (NB/FB) vertex, the only branch that tries to reverse this condition is the FB. In the upper vertex, there is a second evolution track for secular variations in which both $R_{\rm MCD}$ and $R_{\rm BB}$ expand with increases in luminosity. It is therefore possible that the mechanism for the NB (i.e., the addition of quasi-radial flow or some other mechanism) might bring the system to super-Eddington conditions in both the disk and the boundary layer in the upper (HB/NB) vertex, while only the disk experiences such conditions in the lower vertex. Our use of the term "super-Eddington" means, respectively, disk $\dot{m}$ in excess of the Eddington limit when the inner disk radius is at the ISCO, and boundary layer $\dot{m}$ in excess of the accretion limit at which the optical surface still coincides with the NS surface.

7.6.2 Physical processes along the Z branches of XTE J1701–462

We have found that spectral evolution along the Sco-like FB is consistent with a shrinking of the inner disk radius, while $\dot{m}$ remains constant (Figure 7-15). When we combine the interpretations for the FB and the NB/FB (lower) vertex, with further consideration of the increasing evolution speed along the FB (Figure 7-7), we arrive at the following scenario. For a given value of $\dot{m}$, the Sco-like Z sources accrete matter through a truncated disk, with inner radius set by a local Eddington limit (not by the ISCO). The FB is an instability that springs from the NB/FB vertex, and it represents a temporary push by the inner disk toward the ISCO. The entire FB can be traced out in ∼10 minutes, but the evolution is much faster at the top than at the bottom of the FB (Figure 7-7). Variations at timescales of ∼seconds can easily be seen in the light curve at the top of the FB. Such timescales are of order the viscous timescales of the inner disk for a viscosity parameter of 0.01 [Frank et al., 1985, Equation 5.69]. For the dipping FB in the Cyg-like Z stage, limited data and poor spectral fits prevent us from deriving any conclusions about its nature.

The NB bridges the upper and lower vertices of the Z. The Sco-like NB is traced out as the result of changes in the BB emission size, while the MCD properties remain nearly constant. Similar BB changes are seen on the Cyg-like NB, but here the disk also changes, shrinking in radius at constant $\dot{m}$ similar to the changes seen for the Sco-like FB. Taken literally, an increase of $\dot{m}$ onto the boundary layer, with no observable change in $\dot{m}$ for the disk, could suggest the onset of a radial or advective flow as a secondary accretion component. This would require that the total $\dot{m}$ increases slightly (i.e., by 10% or less) as the source ascends the NB from the lower vertex. This conjecture might be of further interest toward understanding why NS radio jets begin to be seen when a Z source begins to ascend the NB, while the jets become stronger and more steady on the HB [Migliari and Fender, 2006, and references below]. An alternative explanation for the Sco-like NB is that $\dot{m}$ remains constant, but the measured BB area increases as the result of the geometric changes associated with the boundary layer and/or our line of sight to it. While there are probably other explanations as well, it is important to point out one important constraint: the range of the NB at a specific $\dot{m}$ is not arbitrary, as we can see from the two vertex lines (Figure 7-6). Moreover, the process responsible for tracing out the NB appears to be another type of instability, as the source evolves faster on the NB than in the two vertices (§7.3.3).

In §7.6.1 we pointed out that the upper and lower vertices might assume two different solutions for the disk accretion, as they evolve along two distinct lines in the HID over a large overlapping intensity range, while the best-fitting results for the two main components MCD and BB are different. In addition, the two vertices appear to be stable compared with the evolution along the NB, and the upper vertex is most often seen at higher luminosity (Figures 7-17 and 7-19). Both the standard and slim disks are possible stable accretion disk solutions at high accretion rates with the slim disk associated with higher accretion rates and an increased amount of radial advection flow (see references in §7.6.1). Also considering that the increase of the BB emission size along the NB might be explained by an additional radial flow, we hypothesize that in the upper vertex the disk assumes a slim disk solution while the disk in the lower vertex is a standard thin disk. In that case, the NB is formed as the additional radial flow turns on and the source begins the transition to the slim disk.

As demonstrated in §7.4.3, the Sco-like HB is traced out as the thermal emission in the disk is converted into a hard component by Comptonization, while the combined luminosity from the disk and Comptonization (i.e., $L_{\rm MCD} + L_{\rm CBPL}$) remains roughly constant. In the most variable case, which is sample IIa, the combined luminosity varies by 10% relative to the mean HB value, and we have shown that this early Sco-like HB has some lingering characteristics of the Cyg-like stage. Thus it remains quite possible that the Sco-like HB is traced out at constant $\dot{m}$ through the disk. The Cyg-like HB consists of a long horizontal line in the HID, plus an upturn at the far end. The upturn portion exhibits an increase in Comptonization, in common with the Sco-like HB. However, the non-upturn part of the Cyg-like HB remains puzzling. Its track in the HID resembles the secular drift in the upper vertex, which might suggest that it is not a true HB track. However the power continuum shows strongly elevated continuum power, which is a clear signature of the HB, but from that standpoint the lack of Comptonization is very surprising. Further investigations of Cyg-like HB tracks for other sources are needed. Finally, as noted above, radio emission has been detected on the HB, presumably to be due to jet formation [Fender et al., 2007, Migliari et al., 2007, Fender and Hendry, 2000, Penninx et al., 1988]. For the Sco-like HB and the upturn portion of the Cyg-like HB, the association of increased Comptonization with radio flux follows a general convention for X-ray binaries. However, while the spectrum in the atoll HS is dominated by Comptonization, only modest Comptonization fractions are found for the HB in Z sources.

Given the variations in $R_{\rm MCD}$ along the FB and the Comptonization on the HB, we must use the value of $(R_{\rm MCD} \times (L_{\rm MCD} + L_{\rm CBPL}))$ to trace $\dot{m}$ through the disk for Z sources. Our overall conclusion is that for Sco-like Z tracks, $\dot{m}$ remains constant to the level of 10% or less [see also Homan et al., 2002]. The role of $\dot{m}$ in the evolution along the Z tracks has been in debate for decades (§7.1). In our analyses, what distinguishes the Z branches is not $\dot{m}$ but the different mechanisms that spring from the Z vertices, which are the more stable reference points along the Z track. The three branches are associated with different forms of spectral evolution, and our physical interpretations are different from the concept that Z track evolution is driven by changes in any single parameter.

Unstable nuclear burning was invoked as a mechanism for the FB by Church et al. [2008], using observations of Cyg-like Z sources. In their scenario, there are no changes in $\dot{m}$. We cannot determine whether this explanation works for the Cyg-like dipping FB of XTE J1701-462, but it clearly does not work for the FB in the Sco-like stages. We note that one type I X-ray burst has been observed in a FB during its decay back to the NB/FB vertex [Lin et al., 2009a, Chapter 7]. We further test this explanation on stage IV as follows. For a solar abundance, the ratio of the nuclear and gravitational energies is only about 2.5% [Strohmayer and Bildsten, 2006]. However, the Sco-like FB is frequent (Table 7.1), and the luminosity variations are very strong. We calculate the net flaring fluence on the FB in stage IV by subtracting the associated lower vertex flux from each FB flux measurement and integrating over time, and the non-flaring fluence is simply the total fluence minus the flaring fluence. Their ratio turns out to be very high, ∼33% for stage IV.

7.6.3 Comparison with other NS LMXBs

Stage I was shown to be very similar to the typical Cyg-like Z sources, especially GX 5-1 and GX 340+0, by Homan et al. [2007b] based on the CDs/HIDs and variability. The major difference is in the FB. Cyg X-2 is similar to XTE J1701-462 in that it also has substantial secular changes and sometimes even changes between source types [Kuulkers et al., 1996, Wijnands et al., 1997b]. A more detailed comparison between these two sources could be valuable.

In Sco-like stages II–III, XTE J1701-462 is very similar to the Sco-like Z sources. The color and spectral similarities between XTE J1701-462 and the typical Sco-like Z sources, shown in Figures 7-2 and 7-11, imply that the spectral fitting results for XTE J1701-462 should also apply to the Sco-like Z sources.

In stage IV, the HB and NB are no longer observed, and the CDs/HIDs resemble those of the bright persistent GX atoll sources GX 9+1,GX 9+9, and GX 3+1. These sources are believed to accrete at accretion rates between those of the classical atoll sources (like Aql X-1 and 4U 1608-52) and those of the Z sources [Hasinger and van der Klis, 1989, van der Klis, 2006]. Based on patterns traced out in the CDs, they are very similar to XTE J1701-462 in the Z stage IV. We classify such patterns in the CD/HID for XTE J1701-462 into the NB/FB vertex and the FB, while the bright persistent atoll sources have typical names "lower banana" and "upper banana" respectively [Hasinger and van der Klis, 1989, van der Klis, 2006]. It is possible that the lower banana in the GX atoll sources is simply the NB/FB vertex and the upper banana is the FB. This can be investigated with spectral fits, e.g., to see whether the upper banana shows evidence for typical FB spectral evolution, as shown in Figure 7-15.

In the brief atoll stage, XTE J1701-462 resembles the classical transient atoll sources Aql X-1 and 4U 1608-52 from the CDs/HIDs and spectral fits (LRH07). The emission size of the boundary layer remains constant across the states, and the inner disk radius remains constant in the SS. The increase of the Comptonization in the HS is also accompanied by an increase in continuum power, i.e., the integrated rms in the PDS. We also note that XTE J1701-462 in the atoll stage has a peak luminosity of $\sim$0.2 L_{EDD}, while Aql X-1 and 4U 1608-52 show maxima of $\sim$0.35 L_{EDD} (LRH07). We note that these values are scaling estimates only, as there might be large corrections required to infer intrinsic emission for some components, e.g., the BB which might be partially obscured.

7.7 Conclusions

Our results offer a major departure from the classical view of Z sources. The Sco-like Z track is traced out at nearly constant $\dot{m}$, while the three branches are tied to different physical mechanisms that function like instabilities tied to the more stable Z vertices. On the other hand, the secular changes, which are driven by variations in $\dot{m}$, unite, in sequence, all of the subclasses of atoll and Z sources.

The conclusions 3–6 below are primarily derived from our chosen spectral model, especially from the MCD component. The behavior of the BB component is more difficult to understand, as this component might be significantly affected by mass loss, obscuration, etc. We acknowledge the need to test this model on the persistent Z sources to determine whether such conclusions can be generalized. We also acknowledge the need to further consider systematic problems associated with the model and with the literal interpretation of physical quantities derived from the spectral parameters. Finally, there are alternative spectral models that convey different physical interpretations for the mechanisms of Z branches [e.g., Church et al., 2008], and detailed comparisons are required for these models and their associated predictions.

1. In the nearly-20-month-long outburst in 2006–2007, XTE J1701-462 evolves through the characteristic behaviors of the Cyg-like Z, Sco-like Z, and atoll sources as its luminosity decreases from super-Eddington values toward quiescence. Our spectral fits suggest that as $\dot{m}$ decreases NS LMXBs change from Cyg-like Z, via Sco-like Z, to atoll sources.

2. As the $\dot{m}$ decreases, the HB disappears first, followed by the NB, and finally by the FB. Despite the substantial secular changes during the outburst, the HB/NB and NB/FB vertices trace out two distinct lines in the HID. With the disappearance of the FB, the NB/FB vertex smoothly evolves into the atoll track traced out at the lowest accretion rate, beginning at $L_{\rm X} \sim 0.2\ L_{\rm EDD}$. The full length of the NB shortens with the decrease in luminosity.

3. In the atoll SS, the disk maintains a constant inner radius, at a value presumed to match the ISCO, and the spectral evolution follows $L_{\rm MCD} \propto T_{\rm MCD}^4$. Deviations from this behavior, in the form of increasing $R_{\rm MCD}$ with $\dot{m}$, are found in the NB/FB (lower) vertex during the Z-source stages. The truncated disk at larger radius is attributed to the effect of reaching the local Eddington limit at the inner disk radius.

4. The Sco-like FB is traced out when the disk shrinks back toward the atoll stage value at constant $\dot{m}$. This appears to be an instability in which the disk temporarily moves to reverse the truncation level set by the NB/FB vertex. The Cyg-like FB, which is of the "dipping" type in this source, cannot be satisfactorily fit with our spectral model, and its nature is unknown.

5. As the source evolves along the NB from the upper to lower vertices, the main spectral variation is the apparent size of the BB emission. This might be due to additional matter supplied to the boundary layer via the onset of a radial flow. Alternatively, there might be geometric effects that alter our view of the boundary layer while the source transverses the NB at constant $\dot{m}$. The NB seems to represent another type of instability in Z sources, since spectral evolution is faster on the NB than in its two connecting vertices.

6. The Sco-like HB is traced out when some of the energy in the disk is converted into a hard X-ray component, presumably via Comptonization, while the disk $\dot{m}$ remains roughly constant. Increasing continuum power in the PDS is also detected. The Cyg-like HB is much longer than the Sco-like one. Its upturn resembles the Sco-like HB in intensity range, strong Comptonization, and continuum power. Thus the upturn of the Cyg-like HB probably has the same nature as the Sco-like HB. The non-upturn part of the Cyg-like HB lies along the same line traced by the HB/NB vertex in the HID. Only weak Comptonization is detected, but there is also strong continuum power, making this particular portion of the Cyg-like HB to appear unique and puzzling.

7. Finally we speculate as to how these results can tie into theoretical investigations of accretion disks at high luminosity. Like the lower vertex, the upper vertex appears to be a more stable source condition than the Z branches. The upper vertex is

more commonly seen when the source is at the highest levels of luminosity, and it is associated with an increased efficiency in the disk for passing matter through to the boundary layer. These same properties distinguish the slim disk model from the standard thin disk. We therefore hypothesize that the two vertices coincide with the two disk models and that evolution up the NB represents the transition to the slim disk. The HB association with a stronger jet can then be interpreted as an apparent requirement that the slim disk be in place before the jet is able to attain higher luminosity, which is coupled to the appearance of increased Comptonization.

Chapter 8

Type I X-ray Bursts from the Neutron-star Transient XTE J1701-462

Abstract

The neutron-star X-ray transient XTE J1701-462 was observed for ∼3 Ms with *RXTE* during its 2006-2007 outburst. Here we report on the discovery of three type-I X-ray bursts from XTE J1701-462. They occurred as the source was in transition from a Z source to an atoll source, at ∼ 10% of the Eddington luminosity. The first burst was detected in the Z-source flaring branch; the second in the vertex between the flaring and normal branches; and the third in the atoll-source soft state. The detection of the burst in the flaring branch cast doubts on earlier speculations that the flaring branch is due to unstable nuclear burning of accreted matter. The last two of the three bursts show photospheric radius expansion, from which we estimate the distance to the source to be 8.8 kpc with a 15% uncertainty. No significant burst oscillations in the range 30 to 4000 Hz were found during these three bursts.

This chapter is adapted from the paper "Type I X-ray Bursts from the Neutron-star Transient XTE J1701-462" by Dacheng Lin, Ronald A. Remillard, & Jeroen Homan, published in The *Astrophysical Journal*, 2009, Vol. 699, p. 60-65.

8.1 Introduction

As accreting H/He-rich matter accumulates on the surface of a neutron star (NS), it is compressed and heated, occasionally leading to violent thermonuclear burning, a phenomenon known as type I X-ray bursts. Such bursts were discovered during the mid-1970s [Grindlay et al., 1976, Belian et al., 1976], and many theoretical studies have been made to investigate their detailed properties [e.g., Joss, 1977, Lamb and Lamb, 1978, Narayan and Heyl, 2003, Woosley et al., 2004, Cooper and Narayan, 2006]. For reviews, see Lewin et al. [1993], Cumming [2004], and Strohmayer and Bildsten [2006]. Recently, Galloway et al. [2008] presented a large sample of bursts (1187 in total) observed by *RXTE* over a time interval of more than ten years.

The bursts typically rise very rapidly (<2 s), followed by a slower exponential decay (∼10 s to several minutes). The burst spectra can be fit with a single blackbody (BB)

[Swank et al., 1977, Hoffman et al., 1977, Galloway et al., 2008]. Burst properties do depend on the mass accretion rate ($\dot{m}$) and the composition of the accreting matter (See Table 1 by Galloway et al. [2008] and references therein and above). Roughly, for solar metallicities, the bursts mostly burn helium and have a fast rise when $\dot{m}$ is about 1–10% of the Eddington limit ($\dot{m}_{\rm Edd}$). At higher or lower $\dot{m}$, they burn mixed hydrogen and helium and have a slower rise and decay. The accreted matter is expected to burn stably at $\dot{m}$ close to or above $\dot{m}_{\rm Edd}$ (although bursts are seen in some Z sources, see below). In bright bursts, the photospheric layer can be lifted off the NS surface by radiation pressure when the local X-ray luminosity reaches the Eddington limit. Under certain assumptions, these bursts can then be used as distance estimators [Basinska et al., 1984, Kuulkers et al., 2003, Galloway et al., 2003].

Bursts are most frequent in the atoll sources, a class of NS low-mass X-ray binaries (LMXBs) with $\dot{m}$ typically $< 0.5\dot{m}_{\rm Edd}$. In contrast, among the six classical Z sources, a class of NS LMXBs with $\dot{m}$ close to or above $\dot{m}_{\rm Edd}$, only GX 17+2 has exhibited type I X-ray bursts, and no bursts have been reported to be in the Z-source flaring branch [Kahn and Grindlay, 1984, Tawara et al., 1984, Sztajno et al., 1986, Kuulkers et al., 2002]. There are burst events in Cyg X-2, but their thermonuclear origin is still inconclusive [Kuulkers et al., 1995, Wijnands et al., 1997b, Galloway et al., 2008]. In this letter, we report an analysis of X-ray bursts from the NS X-ray binary XTE J1701-462 during its 2006-2007 outburst. XTE J1701-462 is a unique source in that it is the first NS transient that shows Z-source characteristics [Homan et al., 2007b, Lin et al., 2009b, Chapter 7]. During the decay of the outburst, it transformed into an atoll source [Lin et al., 2009b, Homan et al., 2009]. The analyses of comprehensive pointed observations of this outburst by *RXTE* have improved our understanding of LMXB subclasses and the physical processes associated with the three Z-source branches. Our analysis of its bursts is another part of our campaign to understand this source.

Preliminary results of the bursts from XTE J1701-462 have been given in Homan et al. [2007a,c] and Lin et al. [2007a]. In §8.2, we first carry out a systematic search of the *RXTE* archive for bursts from this source. We then present the spectral fit results of the bursts and estimate the distance of this source in §8.3. We describe our search for burst oscillations in §8.4. Finally we discuss our results and summarize our conclusions in §8.5.

8.2 Observations and burst search

We carried out a systematic search for bursts from XTE J1701-462 during its 2006-2007 outburst. We used all 866 pointed observations (∼3 Ms) of XTE J1701-462 made with the Proportional Counter Array [PCA; Jahoda et al., 1996] on board *RXTE*. We used the same scheme as that used by Remillard et al. [2006a], which is briefly described as follows. PCA 1-s light curves were created for each observation from "standard1" data mode, which integrates over the full energy range of the instrument (effectively 2–40 keV). For a time bin t, with intensity $C(t)$, we computed the mean b_1 and the sample standard deviation σ_1 using 1-s data in a "background" interval $t-280$ to $t-20$ and corresponding values (b_2 and σ_2) in another "background" interval $t+180$ to $t+280$ after it. Then we tested the joint condition $[C(t)-b_1] > 5\sigma_1$ and $[C(t)-b_2] > 5\sigma_2$. If this condition is satisfied for three sequential data points (at $t-1$, t and $t+1$), then we claim to find a burst candidate at t. Candidates are rejected if they are due to detector breakdowns; see http://heasarc.gsfc.nasa.gov/docs/xte/recipes/pca_breakdown.html for more information.

Table 8.1. Three bursts from XTE J1701-462 observed by *RXTE*

	Burst number	I	II	III
	Observation ID	93703–01–01–01	93703–01–02–00	93703–01–02–08
Persistent emission	Count rate (cts s^{-1} PCU^{-1})	396	301	176
	Soft color	1.35	1.28	1.22
	Hard color	0.46	0.44	0.49
	Source branch/state[a]	FB	NB/FB vertex	atoll SS
	flux (2.5–25 keV, 10^{-9} erg $\mathrm{cm}^{-2}\,\mathrm{s}^{-1}$)	4.45±0.07	3.38±0.04	1.99±0.02
	flux (Bolometric, 10^{-9} erg $\mathrm{cm}^{-2}\,\mathrm{s}^{-1}$)	6.17±0.12	4.90±0.10	2.94±0.05
	Dimensionless flux	0.150±0.004	0.119±0.003	0.072±0.002
Burst[b]	Start time (UT)	2007/07/17 12:24:22	2007/07/20 14:14:04	2007/07/25 13:39:24
	Rise time (s)	0.5	1.5	1.5
	Decay time scale τ_1 (s)	4.1±0.3	2.6±0.2	3.4±0.3
	Decay time scale τ_2 (s)	10.6±5.0	5.6±1.9	8.5±4.7
	Characteristic time scale τ (s)	5.6±0.2	5.5±0.2	6.4±0.2
	Peak count rate (cts s^{-1} PCU^{-1})	2248	3382	3465
	Peak flux (10^{-9} erg $\mathrm{cm}^{-2}\,\mathrm{s}^{-1}$)	27.2±1.0	39.2±1.1	42.9±1.2
	Fluence (10^{-7} erg cm^{-2})	1.52±0.03	2.16±0.03	2.76±0.04
	Asymptotic radius (km, at 8.8kpc)	7.9±1.5	8.0±1.6	7.9 ±1.3
	Radius expansion?	N	Y	Y
	Pulsed fraction upper limit	37.9%	14.6%	51.4%

[a] The source branch/state classification is from Lin et al. [2009b, Chapter 7]. FB: flaring branch; NB/FB vertex: the transition between the normal and flaring branches; atoll SS: atoll-source soft state

[b] Persistent emission subtracted

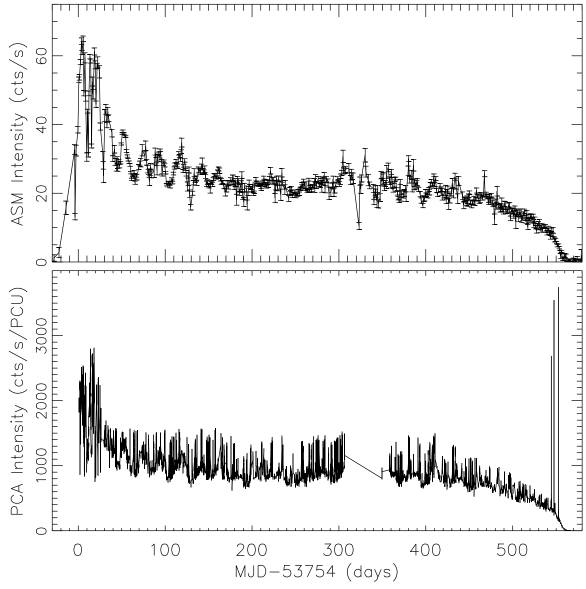

Figure 8-1: The one-day ASM light curve (upper panel) and 32-s PCA light curve (lower panel). The three prominences in the decay of the PCA light curve are type I X-ray bursts, where 1-s data are used.

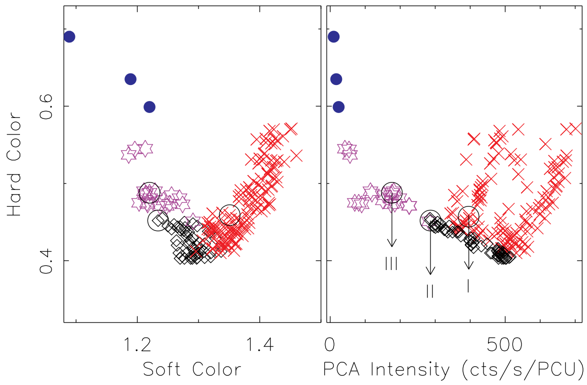

Figure 8-2: The color-color and hardness-intensity diagrams for observations between MJD 54260 and 54315 in the decay of the 2006-2007 outburst of XTE J1701-462. Blue filled circles for atoll-source hard state, purple hexagram for atoll-source soft state, red cross for Z-source flaring branch and black diamond for the normal/flaring branch vertex. The circled points mark the location of the bursts.

Using the above scheme we find three burst candidates. They are on 2007 July 17, 20, and 25, during observations 93703–01–01–01, 93703–01–02–00, and 93703–01–02–08. We number them I, II, and III, respectively (see Table 8.1 for details). All three bursts have the above condition satisfied for $\sim$20 sequential data points. The upper panel of Figure 8-1 shows the one-day light curve from the All-Sky Monitor [ASM; Levine et al., 1996], while the lower panel shows the 32-s light curve from the Proportional Counter Unit (PCU) 2 of the PCA, with 1-s bin size used for the three observations with bursts detected to show these bursts more clearly. The three bursts occur around the transition of XTE J1701-462 from the stage characteristic of a Z source to that of an atoll source.

Figure 8-2 shows the color-color diagram and hardness-intensity diagram for observations from Modified Julian Day (MJD) 54260 to 54315 in the decay of the outburst. The soft color and hard color are the count rate ratios in the (3.6–5.0)/(2.2–3.6) keV bands and the (8.6–18.0)/(5.0–8.6) keV bands, respectively. Each data point has an integration time $\sim$960 s for observations before MJD 54304, but corresponds to an entire observation for later observations, which show little spectral variability. Several observations are further combined when intensity is $<$30 counts s^{-1} PCU^{-1}. The figure is symbol-coded: blue filled circles for atoll-source hard state, purple hexagrams for atoll-source soft state, red crosses for Z-source flaring branch (FB) and black diamonds for the transition between the Z-source normal branch and the flaring branch (NB/FB vertex). The classification of the states/branches is from Lin et al. [2009b, Chapter 7].

During the time interval for data shown in Figure 8-2, the source is not observed to enter the Z-source NB or horizontal branch. The longest FB sequences in this interval show the same spectral evolution and timing properties as the FB at higher luminosity when all Z-source branches observed [Lin et al., 2009b, Homan et al., 2009]. Given the shape of the color track shown in Figure 8-2 and in view of the low persistent luminosity ($\sim$10% of L_{EDD}, see below), one could also classify the FB in Figure 8-2 as the atoll-source upper banana branch. The evolution of the color tracks shown in Lin et al. [2009b, Chapter 7] and Homan et al. [2009] suggests that the atoll-source upper banana branch and the Z-source FB as defined by Hasinger and van der Klis [1989] describe a similar phenomenon, albeit at different luminosities. In this paper, we will follow the state/branch classification scheme

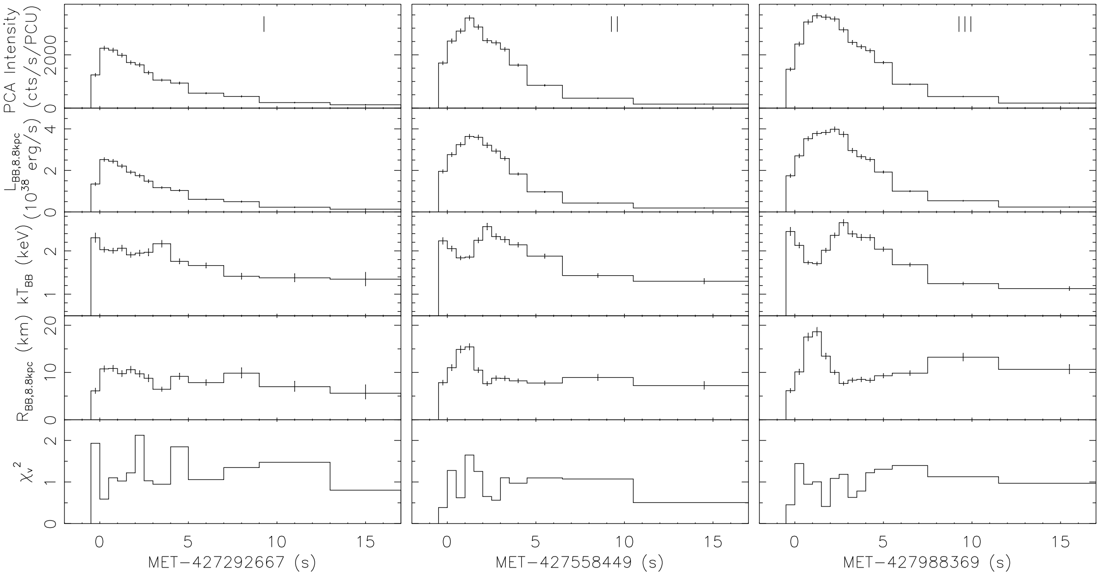

Figure 8-3: The results of the spectral fits of time-resolved spectra of the three bursts detected from XTE J1701-462 during its 2006-2007 outburst. The latter two bursts show photospheric radius expansion.

by Lin et al. [2009b, Chapter 7], in which the Z-source FB phenomenon can be observed down to luminosities typically associated with atoll sources.

In Figure 8-2, we circle the data points where the bursts are detected. Burst I is in the FB. In fact, it occurs in the decay of a flare, as the source is moving down the FB in the direction of the NB/FB vertex. Burst II is in the NB/FB vertex, and burst III in the atoll-source soft state. The count rate, soft color, hard color, and flux of the persistent emission are also given in Table 8.1. The flux is estimated using a model of a multi-color disk plus a single-temperature blackbody (BB) [Lin et al., 2009b, Chapter 7], with both 2.5–25 keV and bolometric values given. The conversion of flux to luminosity is complicated by uncertainties in several important parameters, such as the source distance, the disk inclination and the occultation factor of the BB, and is therefore not carried out here. Instead, we give in Table 8.1 the dimensionless flux, i.e., the ratio of the bolometric persistent flux to the Eddington flux inferred from the radius expansion bursts (see below). Based on this parameter, the $\dot{m}$ when the bursts are detected is roughly 10% of $\dot{m}_{\rm Edd}$.

8.3 Burst spectral fits

We used a standard procedure to do spectral fits of the three bursts: create time-resolved spectra, use the persistent emission around the burst as background, and fit the spectra with a BB model [e.g., Galloway et al., 2008]. We used a 15-s interval that ended 35 s before the burst to define the persistent emission. Event mode data with 64 channels and 125-μs time resolution were used. Only PCUs 0 and 2 were on during the observations in which the above three bursts were detected. Considering that the spectral calibration of PCU 0 has been bad at energies lower than 10 keV since the loss of the propane layer in 2000, we only used data from PCU 2. We note that Lin et al. [2007a] used data from both PCUs. The peak count rates of these bursts are quite high (~3500 counts/s/PCU), but by comparing

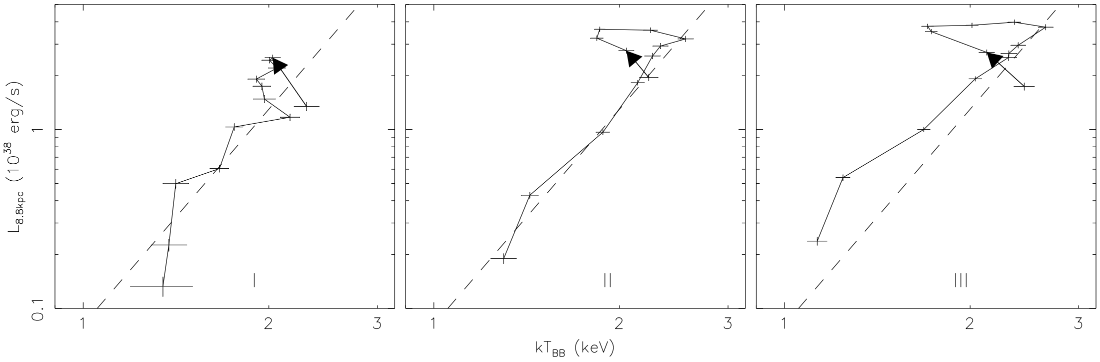

Figure 8-4: The burst luminosity versus blackbody temperature. The arrows show the direction of burst evolution. The dashed lines correspond to $R_{\mathrm{BB}} = 8$ km.

with the count rates from "standard1" mode data, we found no telemetry saturation in the event mode data. The integration time of the spectra was set to be 0.5 s around the peak and increased as the count rate decreased to maintain sufficient statistics to constrain the spectral parameters. An energy range of 3.5–20 keV was used, and 0.8% systematic errors were applied. Deadtime corrections were also made as suggested by *RXTE* team. The response files were created using HEAsoft version 6.4. A hydrogen column density $N_{\mathrm{H}} = 2.0 \times 10^{22}$ cm^{-2} was assumed; it was inferred from spectral fitting of the persistent emission [Lin et al., 2009b, Chapter 7].

The results of our spectral fits are shown in Figure 8-3. There are five panels for each burst (all with persistent emission background subtracted); PCA intensity, bolometric luminosity, BB temperature kT_{BB}, BB radius R_{BB}, and reduced χ^2 are all shown versus time. The luminosity and radius were calculated at a distance of 8.8 kpc (see below). The low values of reduced χ^2 suggest that the net burst spectra are well fit by a BB. The fast rise and slow cooling decay confirm that these bursts are bona fide type I X-ray bursts.

The most important feature that Figure 8-3 shows is that the two brightest bursts (II and III) show photospheric radius expansion, as indicated by the anti-correlation between the temperature and radius when the luminosity reaches its peak: the temperature decreases from ~2.5 keV to ~1.8 keV while the radius increases from ~10 km to ~20 km. Radius expansion bursts are also often studied in terms of the BB luminosity versus the temperature, as shown in Figure 8-4. In this figure, the arrows indicate the direction of the temporal evolution. As shown in the panels for bursts II and III, the source tends to evolve along a horizontal line (constant luminosity) during the radius expansion/contraction phase but along a (dashed) diagonal line (constant radius) during the cooling decay phase.

We use these radius expansion bursts to estimate the distance to XTE J1701-462. The peak flux in bursts II and III are given in Table 8.1 with an average value of $41.1\pm0.8 \times 10^{-9}$ erg cm^{-2} s^{-1}. Using the empirically determined Eddington luminosity $3.79 \pm 0.15 \times 10^{38}$ erg s^{-1} for bursts showing photospheric radius expansion [Kuulkers et al., 2003, with uncertainty 15%], we derive a distance of 8.8 kpc. Using a theoretical expression for the Eddington limit (see equation 8 in Galloway et al. [2008]) and assuming a 1.4 solar-mass NS with a radius of 10 km, we obtain a distance of 7.3±0.1 kpc for H-poor case (H-fraction $X = 0$) and 5.6±0.1 kpc for H-rich case ($X = 0.7$). We assumed that the peak luminosity is reached when the photosphere has settled back on the NS surface [Galloway et al., 2008], which is roughly true in this case (Figure 8-3). Hereafter, we use the value derived by the empirical method, i.e., 8.8 kpc.

The other properties of the bursts are listed in Table 8.1. The start time was defined to be the time when the burst flux first exceeded 25% of the peak flux, and the rise time is the interval that it takes for the burst flux to increase from 25% to 90% of the peak value [Galloway et al., 2008]. We see that all three bursts rise very rapidly, i.e., within ∼1 s. Such bursts are probably due to Helium burning, which is consistent with the $\dot{m}$ (∼10% of $\dot{m}_{\rm Edd}$) during these bursts (§8.1). The bursts show exponential decays but cannot be fit with a single exponential curve. Thus, as in Galloway et al. [2008], we divide the decay (using the bolometric flux curve) into two parts and fit each with an exponential curve with independent decay constants τ_1 and τ_2. These bursts decay rapidly, on time scales of several seconds. The fluence in Table 8.1 is estimated by summing the fluxes over the burst and integrating the final exponential curve to account for the additional flux beyond the data window. The characteristic time scale τ is the fluence divided by the peak flux. It is ∼6 s for all bursts.

As the bursts decay, the radius tends to remain at an asymptotic value, as also shown in Figure 8-4. We calculate the asymptotic radius in the burst tails using data when the burst flux decays from 80% to 20% of the peak value. The asymtotic radius for each burst is also listed in Table 8.1 with an average of 8±1 km at a distance of 8.8 kpc (corresponding to the dashed line in Figure 8-4). We note that there is a slight increase in emission area in burst III as the decay progresses, as can be seen in Figure 8-4, the cause of which is unknown. The effects of redshift and spectral hardening should be corrected for in order to obtain the actual size of the NS [Lewin et al., 1993]. If a 1.4 solar-mass NS and a hardening factor of 1.4 [e.g. Madej et al., 2004] are assumed, then the actual size of the NS is ∼ 13 km.

8.4 Burst oscillation search

We searched each burst for coherent pulsations in the frequency range 30 to 4000 Hz using Fourier techniques. We computed power spectra throughout each burst using sliding 1, 2, 3 and 4-s windows with a step of 0.125 s. The investigated energy bands were 2–60, 2–10, and 10–30 keV. We found no significant signal. To estimate the upper limits, we used the set of Leahy-normalized power spectra [Leahy et al., 1983] with a 1-s window so as to take into account possible frequency drifts.

The upper limit for each burst was then determined as follows [see also Vaughan et al., 1994]: (1) we searched for the largest observed power P_{max} in the 2–60 keV band; (2) we fit the noise powers of the power spectrum in which we found P_{max} with a constant plus power law model; (3) we divided by the continuum model and multiplied by 2 to re-normalize the power spectrum [see, e.g., Israel and Stella, 1996, Watts and Strohmayer, 2006] and (4) we estimated the upper limits at a 99% confidence level using the Groth distribution [Groth, 1975, Vaughan et al., 1994]. The pulsed fraction upper limits are listed in Table 8.1. They are relatively high and not very constraining, compared with the typically observed amplitudes of oscillations of a few ten percent [Strohmayer and Bildsten, 2006].

8.5 Discussions and conclusions

We find three type I X-ray bursts from the 866 *RXTE* pointed observations (∼3 Ms) of the NS transient XTE J1701-462 during its 2006-2007 outburst. These bursts are detected during the decay of the outburst. The persistent emission of the observations containing these three bursts is weak, with fluxes $\sim 10\%$ of the Eddington limit. Based on the source state/branch classifications by Lin et al. [2009b, Chapter 7], the first burst is detected in the Z-source flaring branch; the second in the flaring/normal branch vertex; and the third in the atoll-source soft state.

Detailed spectral fits confirm these bursts as type I X-ray bursts. The last two of the three bursts show strong photospheric radius expansion with a peak flux of $41.1 \pm 0.8 \times 10^{-9}$ $\mathrm{erg\,cm^{-2}\,s^{-1}}$. Assuming an Eddington luminosity of $3.79 \pm 0.15 \times 10^{38}$ $\mathrm{erg\,s^{-1}}$ [Kuulkers et al., 2003], we estimate a distance of 8.8 kpc for XTE J1701-462 with 15% systematic uncertainty. We find no significant burst oscillations between 30–4000 Hz.

The distance to XTE J1701-462 was initially estimated by Homan et al. [2007b]. They gave a distance of 14.7 ± 3 kpc by comparing the flux in the NB/FB vertex in a Sco-like Z-source interval with that of Sco X-1 (which has a distance of 2.8 ± 0.3 kpc, as determined by radio parallax measurements). This value is higher than that derived here using radius expansion bursts. A possible explanation for such a discrepancy is a difference in the inclination of these two systems. The orbital inclination of Sco X-1 is $\sim 40^\circ$ [Fomalont et al., 2001, Steeghs and Casares, 2002]. The above discrepancy can be explained if XTE J1701-462 has orbital inclination of 70°, as roughly estimated by Lin et al. [2009b, Chapter 7] based on the weak iron emission lines detected, assuming that the flux is dominated by the disk emission.

The occurrence of the burst near the end of the outburst is consistent with XTE J1701-462 turning into an atoll source. Atoll source are known to be much more prolific bursters than Z sources. Among the six classical Z sources, only GX 17+2 has exhibited type I X-ray bursts (§8.1). These sources accrete at high $\dot{m}$, close to or above $\dot{m}_{\mathrm{Edd}}$, as inferred from its radius expansion bursts. GX 17+2 has both short ($\tau \lesssim 10$ s) and long ($\tau > 100$ s) bursts. Burst-like events from Cyg X-2 are very short ($\tau \sim 3$ s), and many of them do not show cooling during burst decay. Thus their thermonuclear origin is inconclusive [Kuulkers et al., 1995, Wijnands et al., 1997b, Galloway et al., 2008]. XTE J1701-462 is different in that its bursts are detected when it accretes at low $\dot{m}$, $\sim 10\%$ of $\dot{m}_{\mathrm{Edd}}$ and that all bursts are short ($\tau \sim 6$ s). From the $\dot{m}$ and the burst profiles (fast rise and short duration), these bursts are consistent with Helium burning. Such bursts are often seen in the atoll sources in their banana branch [Galloway et al., 2008].

So far no bursts have been detected in the FB (except in the NB/FB vertex) from GX 17+2 [Kuulkers et al., 2002], while the thermonuclear origin of the Burst-like events from Cyg X-2 is inconclusive (see references above). While the detection of burst I from XTE J1701-462 in a low luminosity FB might not be unique, given the abundance of burst in the atoll upper banana branch [Galloway et al., 2008], it does cast doubt on the speculation that the Z-source FB is caused by unstable nuclear burning [Church et al., 2006]. Lin et al. [2009b, Chapter 7] offered an additional argument that the FB cannot be due to unstable nuclear burning, as the energy released to produce the FB would require a much higher $\dot{m}$ than is observed. Lin et al. [2009b, Chapter 7] propose an alternative explanation for the FB, in which the inner disk radius contracts temporarily from an Eddington-expanded value toward the innermost stable circular orbits.

The burst rate of XTE J1701-462 over the entire outburst is $\sim 1\ \mathrm{Ms}^{-1}$. However, the burst rate depends on $\dot{m}$ and is expected to be zero at $\dot{m}$ close to $\dot{m}_{\mathrm{Edd}}$ [Remillard et al., 2006a, Galloway et al., 2008]. While this result is consistent with the fact that we do not observe bursts during the bright phase of the outburst for XTE J1701-462 and in most of Z sources, it does raise the question of why the Z source GX 17+2 shows type-I X-ray bursts. One possible explanation could be that bursts are possible at high $\dot{m}$, but only in the narrow $\dot{m}$-range occupied by GX 17+2. We test this hypothesis by estimating the expected number of bursts from XTE J1701-462, for the duration when it was similar to GX 17+2. We estimate that XTE J1701-462 has ~0.5-Ms of exposure when it resembles GX 17+2, i.e., with all three Sco-like Z branches traced out, and thus has a similar $\dot{m}$ as well. However, XTE J1701-462 has no burst detected in this ~0.5-Ms interval, while we would have expected to see ~6 bursts, based on the burst rate of GX 17+2 (12 bursts observed in 1 Ms with *RXTE* [Galloway et al., 2008]). Thus the burst rate in GX 17+2 is much higher than XTE J1701-462 at similar $\dot{m}$. It suggests that bursts in GX 17+2 are not only due to its specific $\dot{m}$, but might also depend on other factors such as the NS parameters or the chemical composition of the accreted material.

The three bursts are detected at $\dot{m} \sim 10\%\ \dot{m}_{\rm Edd}$, with the burst rate about one per ten hours, considering that the source is observed for several tens of hours around such $\dot{m}$. This is consistent with the average value, ~12 hours from Galloway et al. [2008] or ~6 hours from Remillard et al. [2006a], corresponding to the above $\dot{m}$.

This research has made use of data obtained from the High Energy Astrophysics Science Archive Research Center (HEASARC), provided by NASA's Goddard Space Flight Center. TB acknowledges support from ASI through grant I/088/06/0.

Chapter 9

Spectral Properties of GX 17+2

Abstract

RXTE observed Sco X-1-like Z source GX 17+2 extensively between MJD 51454.1 and 51463.3, with 67 pointed observations made (∼270 ks). The spectral properties of this source strongly depend on the positions on the Z track. The spectral modeling shows that its three branches of Z track might be traced out due to three different mechanisms that are likely to operate at constant mass accretion rate. The horizontal branch is due to the increase of Comptonization. The most obvious change in the normal branch from our model is the boundary layer emission layer area, which might be the result of the additional radial/advective flow. The source climbs up the flaring branch as the inner disk radius decreases at constant mass accretion rate. All this is consistent with the study of XTE J1701–462 by Lin et al. [2009b, Chapter 7].

9.1 Introduction

Six of the persistently bright neutron star (NS) low-mass X-ray binaries (LMXBs) are classified as Z sources, named after the patterns that they trace out in X-ray color-color diagrams (CDs) or hardness-intensity diagrams (HIDs), based on the timing and spectral properties [Hasinger and van der Klis, 1989, van der Klis, 2006]. These sources are Sco X–1, GX 17+2, GX 349+2, GX 340+0, GX 5–1, and Cyg X–2. The upper, diagonal and lower branches of the Z-shaped tracks for these Z sources are called horizontal, normal and flaring branches (HB/NB/FB), respectively. Based on the shape and orientation of the Z tracks, these Z sources are further divided into two subgroups, with the first three called Sco-like Z sources and the latter three called Cyg-like [Kuulkers et al., 1994]. The Sco-like Z sources have the more vertical HB and the stronger FB than the Cyg-like types. The Z tracks can also move in the CDs/HIDs (secular changes), most substantially in Cyg X–2.

Recent studies of a transient Z source XTE J1701–462 significantly improve our understanding of the evolution in Z sources and their links to the atoll transients, another class of NS LMXBs with lower L_X than Z sources [Homan et al., 2007b, Lin et al., 2009b, Chapter 7, hereafter LRH09]. XTE J1701–462 experienced a long outburst in 2006-2007, and it showed characteristics of Cyg-like Z, Sco-like Z and atoll sources successively [Homan et al., 2007b, Lin et al., 2009b]. Although XTE J1701–462 experienced substantial secular changes of Z tracks, the upper (HB/NB) and lower (NB/FB) vertices each evolve in the HID in a well organized way, along two distinct lines respectively (LRH09). The HB, NB, and FB disappear successively, with the lower vertex finally left and forming the atoll soft-state track. Using the spectral model that was successfully applied to the atoll transients [Lin et al., 2007b, Chapter 4], LRH09 showed that it is the mass accretion rate ($\dot{M}$) that drives the secular changes of Z tracks and the transitions of source types. While the inner disk radius remains constant in the atoll stage, the inner disk in Z stage shows a luminosity-dependent expansion, which was interpreted as effects of the local Eddington limit. However, the motion along the Z branches appears to be caused by three different mechanism that, especially for Sco-like types, may operate at roughly constant $\dot{M}$ (LRH09). The source climbed up the HB as Comptonization of the disk emission increased, up the NB as the the apparent size of the boundary layer increases, and up the FB as the inner disk radius decreases toward the value seen in the atoll soft state, presumably the innermost stable circular orbit.

In this work, we concentrate on the spectral modeling of the Sco-like Z source GX 17+2 with the goal to check whether its spectral evolution is similar to the Sco-like Z stage in XTE J1701-462. Figure 9-1 is one-day-averaged light curve of GX 17+2 from *RXTE* All-Sky Monitor [ASM; Levine et al., 1996] and shows a quite constant intensity (∼45 counts/s) except occasional flares. This might indicate the overall properties of GX 17+2 do not vary over a long time scale. Indeed, the secular changes of the Z track in GX 17+2 are observed to quite small [Wijnands et al., 1997a, Homan et al., 2002]. Thus we concentrate on its one specific Z track from the 67 pointed observations (∼270 ks) during MJD 51454.1–51463.3. In this work, we fit the spectra of GX 17+2 with the model consisting of a single-temperature blackbody (BB), used to describe the boundary layer, a multicolor disk blackbody (MCD), and a broken power-law (CBPL) for weak Comptonization. We have used this model to fit the soft spectra of atoll transients and those of XTE J1701–462 (LRH09).

Spectral fits of GX 17+2 have been carried out for GX 17+2 in several other studies. Di Salvo et al. [2000b] fit a *BeppoSAX* observation covering the HB and NB with a BB plus a Comptonized component for the continuum spectra. They found a hard tail in the HB, which was fit by a power law and contributed ∼8% of the source flux. This component gradually faded as the source moved toward the NB, where it was no longer detectable. Similar conclusions were drawn from the analyses of another *BeppoSAX* observation by Farinelli et al. [2005]. The detection of the hard tail on the HB is consistent with the spectral fit results from LRH09 for XTE J1701-462 though a different model was used, as mentioned above. From the model used by Di Salvo et al. [2000b], the spectral evolution across the HB to the lower NB was ascribed mainly to a monotonic decrease of the electron temperature and optical depth of the Comptonized component. No conclusion on the nature of the FB was made as their observation did not cover this branch.

Detailed timing analyses of GX 17+2 were made before [Kuulkers et al., 1997, Wijnands et al., 1997a, Homan et al., 2002]. The timing studies of Homan et al. [2002] covered the observations analyzed in this work, while here we concentrate on the spectral modeling. In §9.2, we describe the reduction of the data and present the CDs/HIDs, with the procedure for the creation of the spectra for modeling also given. The spectral fit results are given in §9.3. Finally we discuss and conclude our results.

9.2 Observations and color-color diagrams

RXTE observed GX 17+2 extensively between MJD 51454.1 and 51463.3, with 67 pointed observations made (∼270 ks). A clean Z track was traced out from these observations, as shown in the following, and was analyzed in detail in this study. We used data made with the Proportional Counter Array [PCA; Jahoda et al., 1996] and the High Energy X-ray

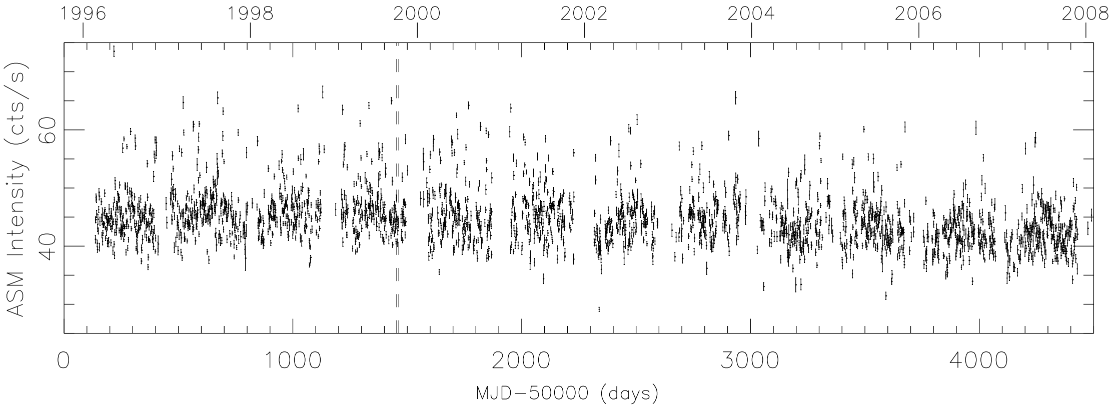

Figure 9-1: *RXTE* ASM one-day-averaged light curves of GX 17+2 spanning ~12 years. The dashed lines mark the interval MJD 51454.1–51463.3, during which PCA pointed observations are analyzed in details in this work.

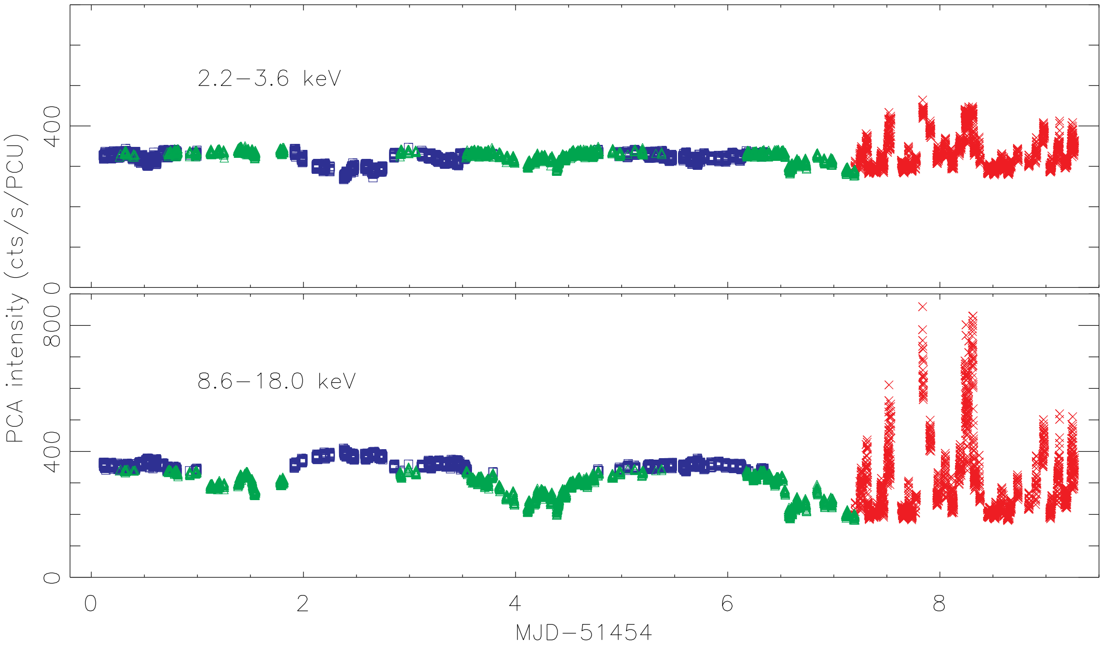

Figure 9-2: *RXTE* PCA 32-s light curves of GX 17+2 during MJD 51454.1–51463.3 in two energy bands. The typical error bars are smaller than the symbol size. The HB, NB and FB are marked by blue squares, green triangles, red crosses, respectively.

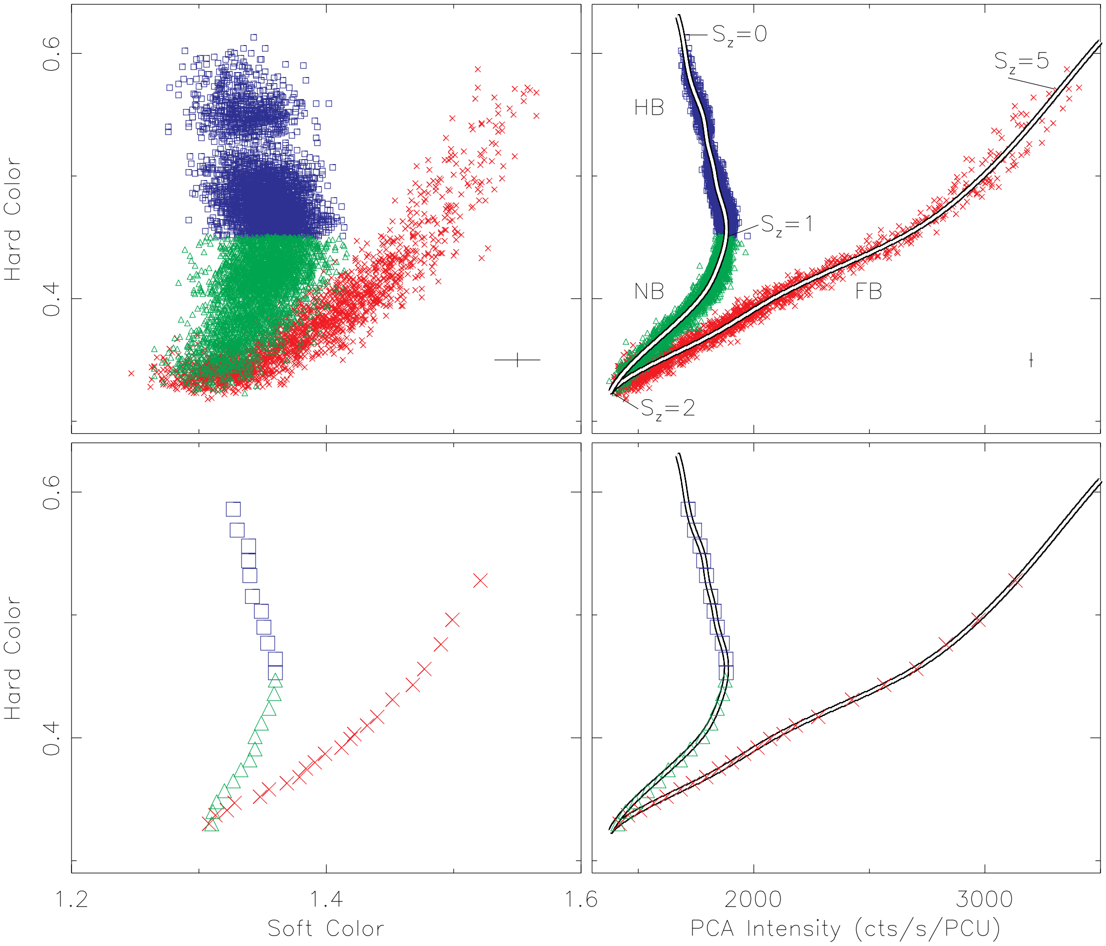

Figure 9-3: The color-color and hardness-intensity diagrams for observations of GX 17+2 between MJD 51454 and 51464. Upper panels: 32-s spectra are used, and the splines that are used for the S_z parameterization are shown. Lower panels: S_z-resolved spectra are used, and the splines are repeated here for reference.

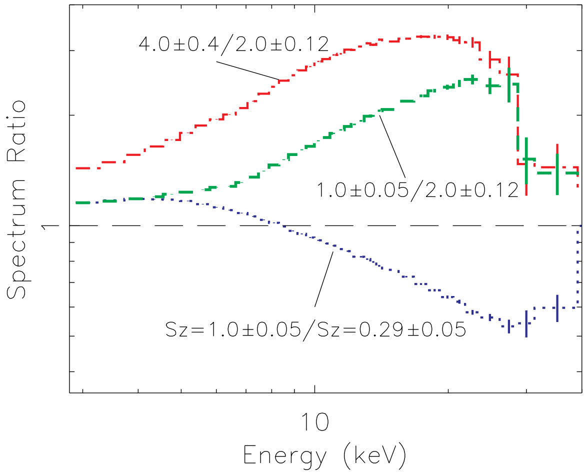

Figure 9-4: The ratios of the spectra on the two ends of each branch. Spectra with high total PCA intensity are divided by those with lower total PCA intensity in order to show that on each branch the intensity increases in a different energy range.

Timing Experiment [HEXTE; Rothschild et al., 1998] instruments. The best-calibrated detector units of each instrument were utilized, which are Proportional Counter Unit 2 (PCU 2) for the PCA and Cluster A for the HEXTE. We used the same standard criteria to filter the data as described in [Lin et al., 2007b, Chapter 4]. Background was estimated using the bright background model as the source always had very high intensity, >1000 counts/s/PCU, during these observations. Dead time corrections for the PCA and HEXTE data were also applied.

In order to study the source evolution in a model-independent manner and to create spectra for later spectra modeling, we also examined the CD/HID of GX 17+2. We calculated X-ray colors as described in [Lin et al., 2007b, Chapter 4], with the soft and hard colors (SCs/HCs) defined as the ratios of the Crab-Nebula-normalized background-subtracted count rates in the (3.6–5.0)/(2.2–3.6) keV bands and the (8.6–18.0)/(5.0–8.6) keV bands, respectively.

We first created the spectra with exposure of 32 s from “standard 2” data of PCU 2 and show the light curves in Figure 9-2 and the CD and HID in the upper panels of Figure 9-3. The light curves in Figure 9-2 show the (normalized) PCA intensities in two energy bands (2.2–3.6 keV and 8.6–18.0 keV). The HB, NB, and FB is denoted by the blue square, green triangle, and red cross symbols, respectively. The NB and FB are quite mixed in the CD/HID. Fortunately, the source entered the FB only between MJD 51461.2 and 51463.3, as can be seen from the light curves, and thus data points in this time interval are identified as the FB. We note that the source might in fact still enter the NB occasionally, based on the occasional detection of normal branch oscillations (NBOs) at ∼7 Hz, during this interval. The NBOs is at lower frequency than the flaring branch oscillations (FBOs, $\gtrsim$14 Hz), and they are not observed to occur simultaneously [Homan et al., 2002]. Thus they may be indicators of the NB and FB, respectively. Using the NBOs and FBOs to classify the NB and FB requires very detailed timing analyses and is out of the scope of this paper. The transition from the HB to the NB is quite smooth. Their boundary is defined to be HC $\simeq 0.45$ (strictly $S_z = 1$, see below).

The data points are normally assigned a rank number to track the position along the Z track [Hasinger et al., 1990, Hertz et al., 1992]. This can be done by creating the splines along the Z track, and the rank number S_z along the splines depends on the spline length, which is scaled to the full length of the NB. The rank number for each data point is obtained by projecting to the splines. This was normally done in the CD. Considering that the scattering is quite large in the CD in the current case, we create the splines in the HID instead and show them in the top right panel of Figure 9-3. We note that there is large overlap of lower parts of the FB and the NB in the HID. Considering that the FB can be mostly separated from the other branches in time (see above), we create a spline for the FB (FB spline) and another one for the portion of the track consisting of the HB and NB (HB/NB spline) separately. These two splines are independent except a common normal point. All the normal points for these splines are assigned by hand. S_z in the common normal point of these two splines is set to be 2.0, while the point with HC 0.45 in the HB/NB spline has S_z assigned to be 1.0. S_z at other points in the splines are determined by their distances along the splines to these two points. Considering the different units of HC and intensity, we divide them by their characteristic number first, 0.45 for the HC 2000 cts/s/PUC, before calculating the distances. Finally, the values of S_z for data points in the FB and data points in the HB and NB are determined by projecting onto the FB and the HB/NB spines, respectively. The boundary between the HB and NB is defined to be $S_z = 1$.

We create spectra for spectral fit based on S_z. The CD and HID of these S_z-resolved spectra are shown in the bottom panels. As in LRH09, we calculate the ratios of spectra in different branches in order to investigate how the spectral changes depend on the energy in each branch. These ratios are shown in Figure 9-4, with the ranges of S_z for the spectra used to create these ratios also labeled. The blue dotted line corresponds to the HB and shows that the intensity increases at energies below ∼9 keV but decreases at higher energies as the source descends the HB. This is reflected on the anti-correlated variations of the HB data points in the light curves in Figure 9-2, most obviously around MJD 51457. The green dashed line corresponds to the NB. Although the intensity increases over the whole energy range shown as the source evolves up the NB, the increase becomes dramatically only above ∼7 keV. This can also be seen in the light curves in Figure 9-2, where the 2.2–3.6 keV light curve varies much less than the 8.6–18.0 keV one in the NB (green triangles). The increase of the intensity in the FB is also in the high energies 10–30 keV (red dot-dashed line), but is smoother over all the energies relative to the NB. The properties of GX 17+2 described above are quite similar to XTE J1701–462 in the Sco-like stage (LRH09).

9.3 Spectral modeling

We carried out the spectral fit of the S_z-resolved spectra by the PCA and the HEXTE jointly, with the normalization of the HEXTE spectrum relative to the PCA spectrum allowed to float between 0.7 and 1.3. The creation of PCA spectra has been described above. We used channels 4–50 (numbering from 1 to 129; ∼2.8–23.0 keV) for our spectral fitting and applied systematic errors of 0.8% for channels 4–39 (below 18 keV) and 2% for channels 40–50. We created the HEXTE spectra to match the PCA spectra in observation time. No systematic errors were applied for HEXTE data. Only 20.0–50.0 keV was used for HEXTE spectra.

The model MCD+BB+CBPL was used, with a Gaussian line and interstellar absorption also included. The central line energy of the Gaussian line was fixed at 6.7 keV, and the

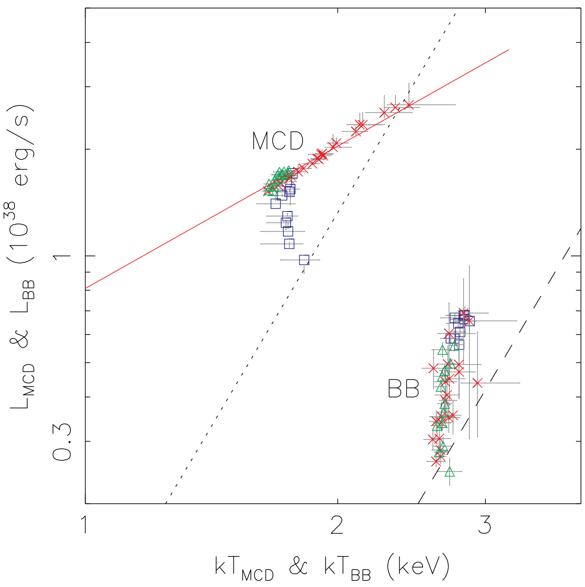

Figure 9-5: The results of the spectral fit of S_z-resolved spectra. The luminosities of the thermal components (MCD/BB) are plotted against their characteristic temperatures. The dotted line is a constant radius line inferred from the Type I X-ray bursts, while the red solid line is a constant $\dot{M}$ line.

intrinsic width was constrained to be smalled than 1 keV [Ercan, 1988, Di Salvo et al., 2000b, Farinelli et al., 2005]. The hydrogen column density was fixed at $N_{\mathrm{H}} = 2.4 \times 10^{22}$ cm^{-2}, which was based our joined fit of simultaneous observations of this source with *BeppoSAX* and *RXTE* using the above model.

The results of spectral fit are shown in Figures 9-5–9-6. Figure 9-5 plots the luminosities of the thermal components MCD and BB versus their characteristic temperatures, while Figure 9-6 plots the spectral fit results as a function of the rank number S_z. All error bars given are at 90% confidence level, and the error bar of the rank number for each data point in Figure 9-6 corresponds to the range of S_z of each S_z-resolved spectrum. L_{MCD} and L_{BB} are bolometric, and L_{CBPL} is calculated by integrating from 1.5 to 200 keV. The source distance of 8 kpc is used [Kuulkers et al., 2002], and disk inclination is assumed to be 60°. The doted and dashes lines in Figures 9-5 are constant radius lines of $R = 8$ km and $R = 2$ km, respectively, assuming $L_{\mathrm{X}} = 4\pi\sigma_{\mathrm{SB}}R^2T^4$. They are shown here for reference.

These two figures show that in the HB L_{MCD} decreases as the source climbs up the HB, while L_{BB} changes relatively much less. In contrast, L_{CBPL} increases correspondingly. In panel 4 of Figure 9-6, the filled blue squares show the sum of L_{MCD} and L_{CBPL}, which is changed $\lesssim$16%, much less than either individual component, in the HB. Using the assumptions that we have, the Comptonization can account for ~60% of the variations of the MCD in the HB. The estimate of the amount that the Comptonized component can account for the variations of the MCD component in the HB requires the precise factors like the disk inclination, the exact form of Comptonization, and the lower energy boundary used to integrate the luminosity of the Comptonized component. Considering all these uncertainties, it is possible that the source evolves above the HB due to Comptonization.

Figures 9-5–9-6 show that compared with the MCD and CBPL components, the BB component, especially its normalization, changes the most (a factor of two) in the NB. In

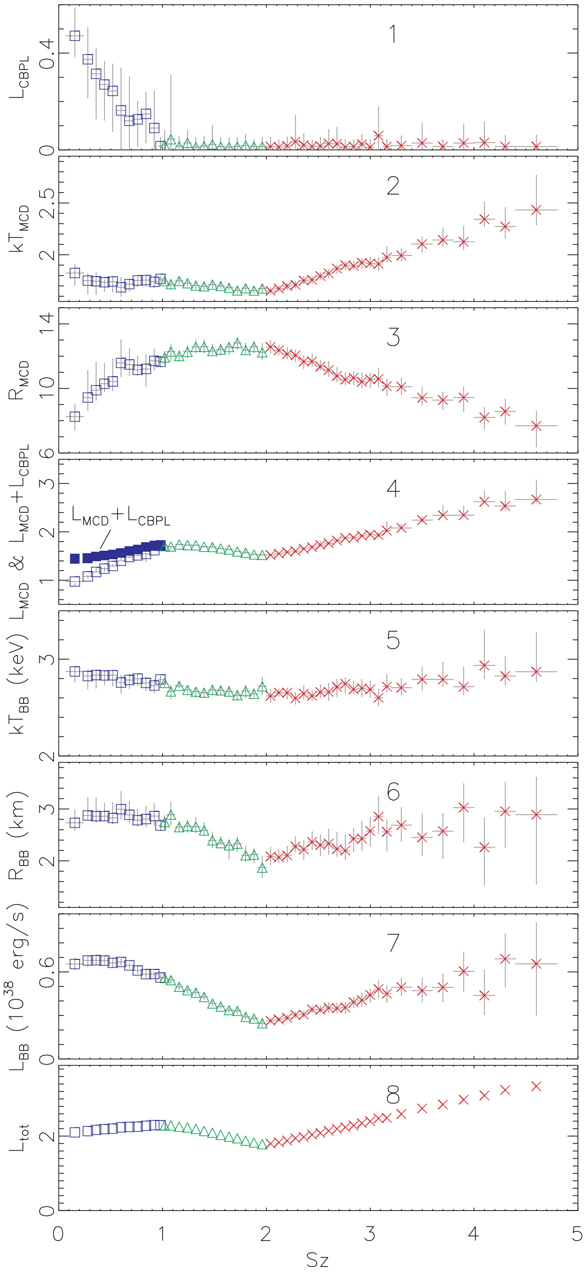

Figure 9-6: The results of the spectral fit of S_z-resolved spectra as a function of the rank number S_z.

fact, the CBPL component is almost undetectable in the NB (panel 1 in Figure 9-6). Thus based on our model, the change of intensity above ∼7 keV (green line in Figure 9-4) is mostly due to the BB component. However, the BB is just a small component, and thus the total luminosity (panel 8 in Figure 9-6) is changed by ∼20% only in the NB.

The variations of the MCD component in the FB follow a red solid line in Figure 9-5. This line describes the relation between L_{MCD} and T_{MCD} with varying R_{MCD} at constant $\dot{M}$, i.e., $L_{\mathrm{MCD}} \propto T_{\mathrm{MCD}}^{4/3}$ (LRH09), indicating that the FB is traced out due to the variation of the inner disk radius at constant $\dot{M}$, within 16% for this case. R_{MCD} decreases from ∼12 km to ∼8 km, while T_{MCD} increases from ∼1.7 keV at the lower vertex to 2.5 keV at the tip of the FB. The emission of the BB component also increases as the source climbs up the FB, mostly due to the normalization. As in the NB, there is little detection of the CBPL component in the FB (panel 1 in Figure 9-6).

9.4 Conclusions and discussions

GX 17+2 is well covered by *RXTE* between MJD 51454.1 and 51463.3, with 67 pointed observations made (∼270 ks). Analyses of these observations show that GX 17+2 has very similar spectral properties to XTE J1701–462 in the Sco-like stage. Our application of model MCD+BB+CBPL leads to conclusions as follows.

The Comptonization is only significantly detected in the HB. This is consistent with the study of the HB and NB by Di Salvo et al. [2000b], while our results also show little detection of Comptonization in the FB. From our model, the BB component is almost unchanged, while L_{MCD} varies and is strongly anti-correlated with L_{CBPL}, in the HB. As there is little change of $L_{\mathrm{MCD}} + L_{\mathrm{CBPL}}$ ($\lesssim$16%) in the HB, we surmise the HB is traced out due to the increase of Comptonization at roughly constant accretion rate.

The NB is most characterized by the variation of the emission area of the boundary layer, with other spectral parameters including the boundary layer temperature seldom changed. The total luminosity also shows little change, $\lesssim$20%. This was suggested to be due to onset of some radial/advective flow in LRH09. The cause of the additional flow is uncertain. One possibility was suggested in LRH09 to be the transition of a standard thin disk in the lower vertex to a slim disk in the upper vertex.

The disk in the FB seems to be due to the decrease of R_{MCD} at constant $\dot{M}$, within 16%. This was interpreted as an instability that proceeds off the lower vertex in LRH09. The study of XTE J1701–462 suggested that at the high accretion rate, the disk truncates at a radius outside the innermost stable circular orbit (ISCO), maybe due to the local Eddington limit effect, at the lower vertex in this case. The FB is then traced out as the inner disk radius decreases from the value set at the lower vertex toward the ISCO at constant $\dot{M}$.

From our model, the inferred accretion rate stays roughly (within ∼20%) constant over the whole track. This is consistent with the 0.1–200 keV flux from the study of the HB and NB by Di Salvo et al. [2000b], even if a different spectral model was used. We note, however, that the flux in the FB does vary substantially, for a factor of two. Based on the little variation of the total flux in the HB and NB and the comparison with the black hole candidates, Homan et al. [2002] suggested that $\dot{M}$ along the Z track might be constant while the spectral changes were ascribed to an unknown parameter. From the results of the spectral analyses above, we have suggested that the Z track is traced out by three types of mechanism that might operate at constant $\dot{M}$.

The BB component on the whole track seems to stay at a nearly constant temperature,

$\sim$2.6-2.9 keV while the emission area can vary for a factor of two. This might hint that the boundary layer reaches the local Eddington limit on the surface of the NS. This explanation is further supported by the following two results. First, the above temperature is very close to the peak temperature observed in the radius-expansion bursts from this source [Kuulkers et al., 2002]. Second, it is also very close to the temperature of $\sim$2.4 keV inferred from the study of a set of sources that span a large range of accretion rate, including GX 17+2, using the Fourier-frequency resolved spectroscopy technique [Gilfanov et al., 2003, Revnivtsev and Gilfanov, 2006].

Chapter 10

Physical Interpretations of Accretion in NS LMXBs

Abstract

In this chapter, we first give a high-level summary of the main results of this thesis. Then we give a detailed description of results from our spectral studies regarding the different classes of NS LMXBs, first in the context of color-color and hardness-intensity diagrams, and then on the basis of spectral fits that use our new spectral model. In the following section, the physical origins of spectral evolution and the physical properties of NS LMXBs are discussed. This chapter is written to be as self-contained as possible, with references to previous chapters liberally given.

10.1 Brief summary of results of this thesis

This thesis investigates the thirty-year-old problem of spectral decomposition for weakly magnetized NS LMXBs. Although many models could fit their spectra, the inferred spectral parameters did not describe behavior that was self-consistent with the physics of an accretion disk: the disk did not follow the $L \propto T^4$ relation, and sometimes had a too small inner radius. Comptonization was inferred to be very strong in the soft state, which was inconsistent with the timing/spectral properties of accretion disks in black hole binaries, where soft X-ray spectra and low values of continuum power (in power density spectra) are associated with low fraction of Comptonization.

Based on studies of thousands of *RXTE* observations of one subclass of weakly magnetized NS LMXBs, i.e., atoll sources, we offer a way of modeling the X-ray spectrum of NS LMXBs that does yield $L \propto T^4$ behavior. We further derive a Comptonization fraction that does scale with rms continuum power. This same model goes on to provide new pictures of the spectral states of atoll sources, physical interpretations for the three branches of Z sources, an explanation that the Z and atoll subclasses are simply related by the mass accretion rate, and a signature for the effects of reaching the local Eddington limit in the inner part of the disk for Z sources. This new model also provides an interesting connection of kHz QPOs with spectral properties of the disk, which makes it promising to reveal the origins of kHz QPOs. This work revises our understanding of the similarities and differences between NS and black hole accretion disks. Finally, a proper understanding of the way to deconvolve the disk continuum and the boundary layer in NS LMXBs is an essential step toward our learning how to use continuum spectra to constrain the equation of state of NS.

Our understanding of the accretion process in weakly magnetized NS LMXBs begins with our new way of modeling the spectra of atoll and Z sources in their soft state (see also Chapter 4). The main difference between the new and the classical models is that our new model has double thermal components that dominate the soft-state spectra. Comptonization in the form of a weak power law (and the third spectral component) is only on the low-luminosity power of the soft state. Based on this model, we have the following interpretations of spectral states of atoll sources: the disk is truncated at a constant radius, presumably the ISCO in most of the soft state, while the boundary layer also has a roughly constant emission area over the large range in luminosity that bridges the hard and the soft states. Weak Comptonization is seen in the soft state, which makes their timing/spectral properties more aligned with those of black hole X-ray binaries. In the hard state, strong Comptonization is found, and it is probably due to a jet. We also find that the disk seems to be truncated at a larger radius in the part of the soft state that coincides with frequent occurrences of kHz QPOs, which contributes evidence relevant to solving the origin of kHz QPOs.

Based on a spectral study of a new transient source, XTE J1701–462, we find that different subclasses of weakly magnetized NS LMXBs are due to different mass accretion rates (see also Chapter 7). At high mass accretion rates, the source behaves as a Z source, and the change of accretion rates results in secular changes (i.e., pattern shifts) in the HID. At low accretion rates, the source behaves as an atoll source. The inner disk radius is not constant but increase with luminosity in the stage when the source behaves as a Z source. In the lower Z vertex, this effect is attributed to the maintaining of the local Eddington limit in the inner part of the disk. In the upper Z vertex, the disk appears to be truncated by advection from a slim disk. We have new explanations for three spectral branches of Z sources: they seem to be due to three different physical mechanisms that might operate at constant mass accretion rates. Rapid evolution along these branches suggests a nature of instability, compared to the vertices. The flaring branch is traced out as the inner part of the disk temporarily refills, with the inner disk radius decreasing from the value found in the adjacent lower vertex. The normal branch is characterized by change of the emission area of the boundary layer, and we suggest that it is due to the switch from a standard thin disk to a slim disk. The horizontal branch is formed due to increase in Comptonization, consistent with strong radio emission detected in this branch.

10.2 Detailed summary of the spectral study results

10.2.1 Color-color and hardness-intensity diagrams

Color-color and hardness-intensity diagrams (see Chapter 1) are useful tools to characterize and differentiate different classes of NS LMXBs. For all plots in this section, we normalize the count rates in the four energy bands 2.2–3.6, 3.6–5.0, 5.0–8.6, and 8.6–18.0 keV to those of the Crab Nebula, and define the soft and hard colors as the ratios of the count rates in the (3.6–5.0)/(2.2–3.6) and (8.6–18.0)/(5.0–8.6) keV energy bands. The intensity is the sum count rate in these four energy bands. All data in this section are from *RXTE* , averaging over all available PCUs.

Figure 10-1 (see also Figure 6-2) shows the color-color and hardness-intensity diagrams for four atoll sources, and Figure 10-2 (see also Figure 7-1) for two Z sources. Atoll and Z sources, being two main classes of weakly magnetized NS LMXBs, show different patterns in

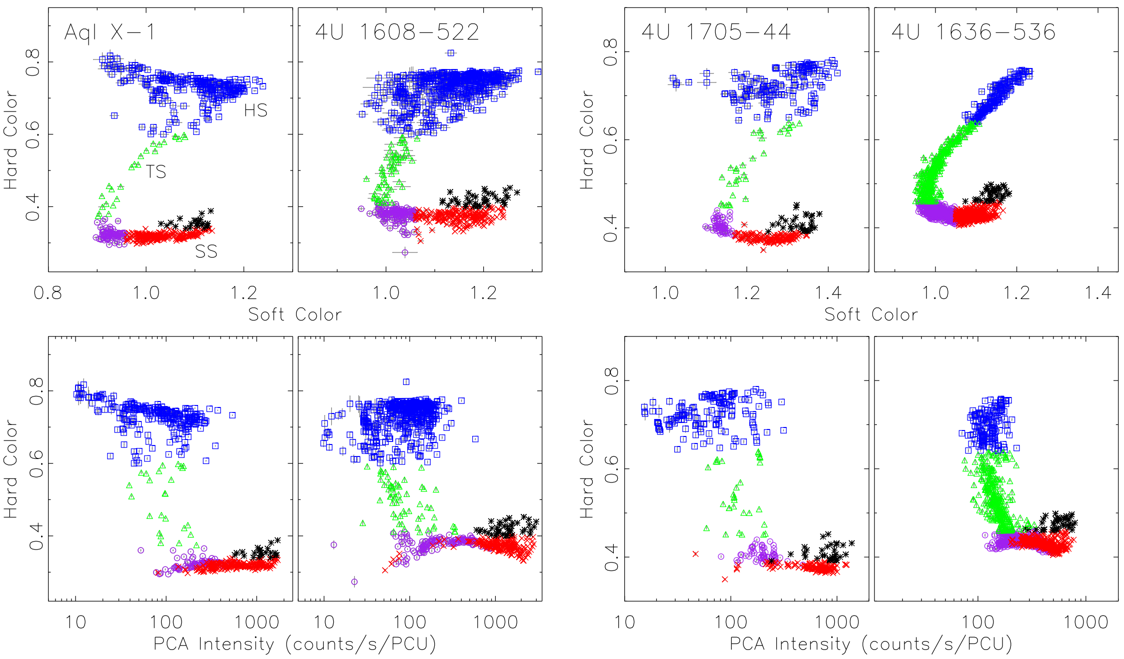

(a) (b)

Figure 10-1: Color-color and hardness-intensity diagrams of transient (a) and persistent (b) atoll sources. The bin size is constrained to be < 4 ks. The atoll-source states (HS: hard state (blue squares); TS: transitional state (green triangles); SS: soft state (purple circles, red crosses, and black stars)) are labeled in the color-color diagram for Aql X–1. See also Figure 6-2.

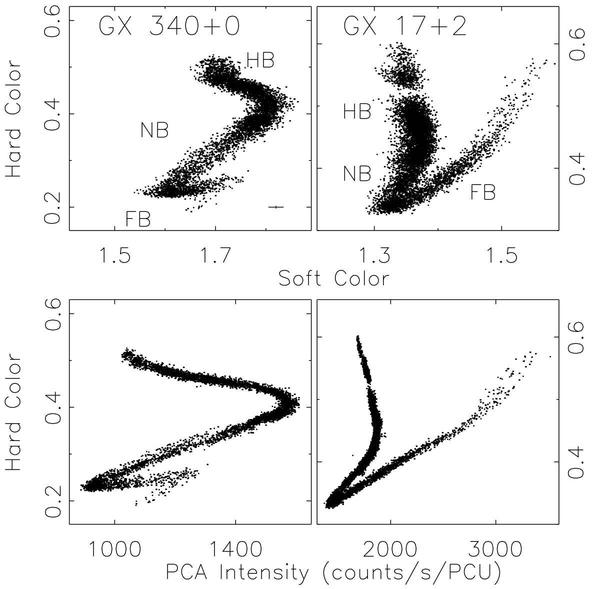

Figure 10-2: Color-color and hardness-intensity diagrams of the Cyg-like Z source GX 340+0 (MJD 51920–51925) and the Sco-like Z source GX 17+2 (MJD 51454–51464), with bin size 32 s. The typical error bars for the colors are shown in the top left panel; errors in the intensity are negligible. The Z-source branches (HB, NB, and FB) are labeled in the color-color diagrams. See also Figure 7-1.

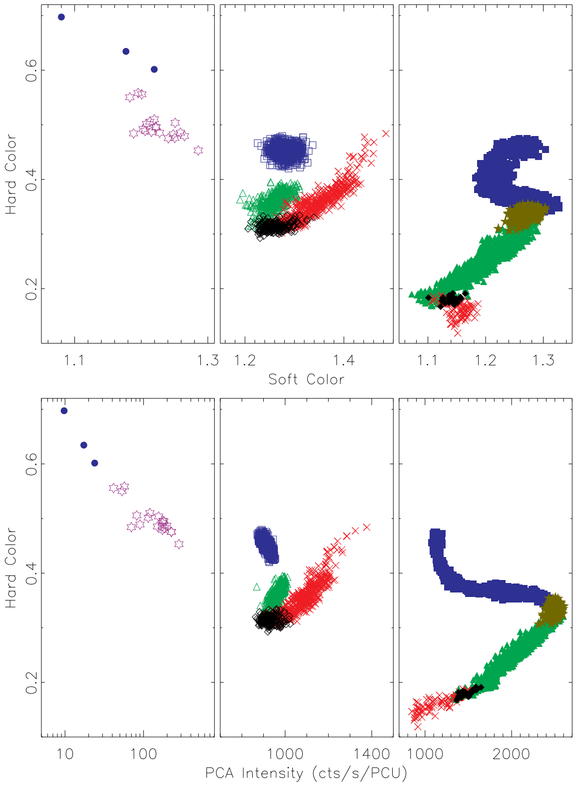

Figure 10-3: Color-color and hardness-intensity diagrams of the transient Z source XTE J1701–462 in three time intervals. Panels in the first column are from MJD 54303–54315.3, when the source behaves as an atoll source. Panels in the second column are from MJD 54112–54119, when the source behaves as a Sco-like Z source. Panels in the last column are from MJD 53756.6–53767.3, when the source behaves as a Cyg-like Z source. The bin size is 32 s for the second and last columns, while for the first column, it is a whole observation or longer. For the meaning of symbols, refer to Figure 10-4

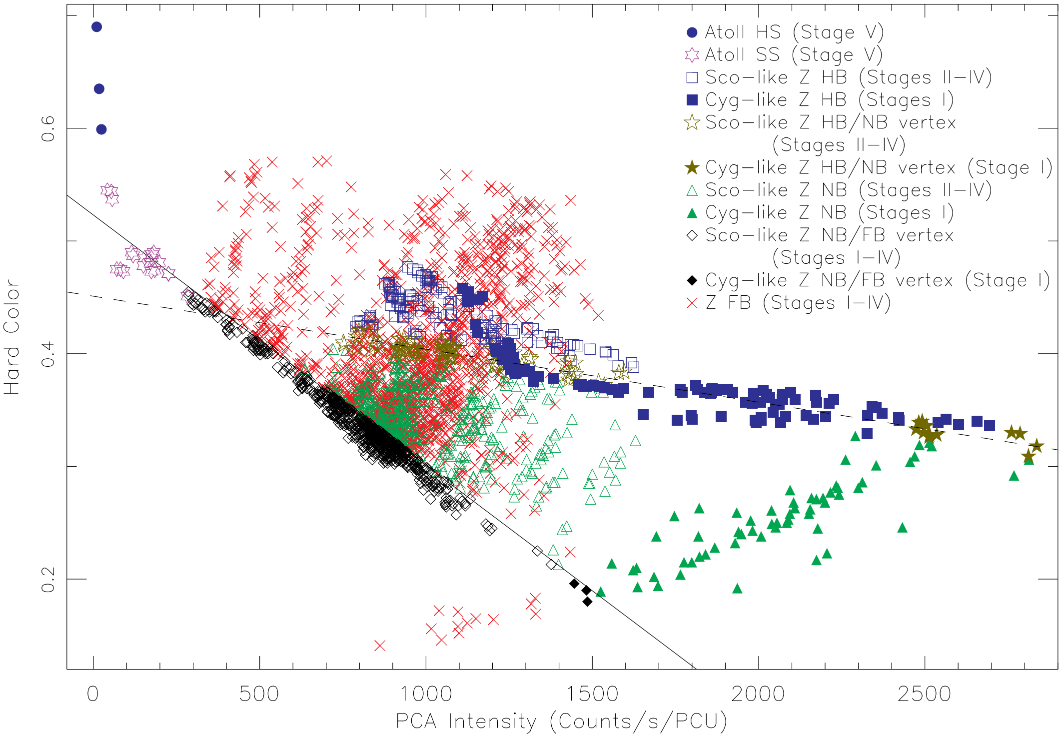

Figure 10-4: The complete HID of the outburst of XTE J1701–462 in 2006–2007. For reference, a legend of all different symbols is shown in the upper right corner. The solid and dashed lines mark the rough track that the lower and upper Z vertices follow, respectively. The bin size is 960 s for data when the source behaves as a Z source, and it is a whole observation or longer when the source behaves as an atoll source. See also Figure 7-6

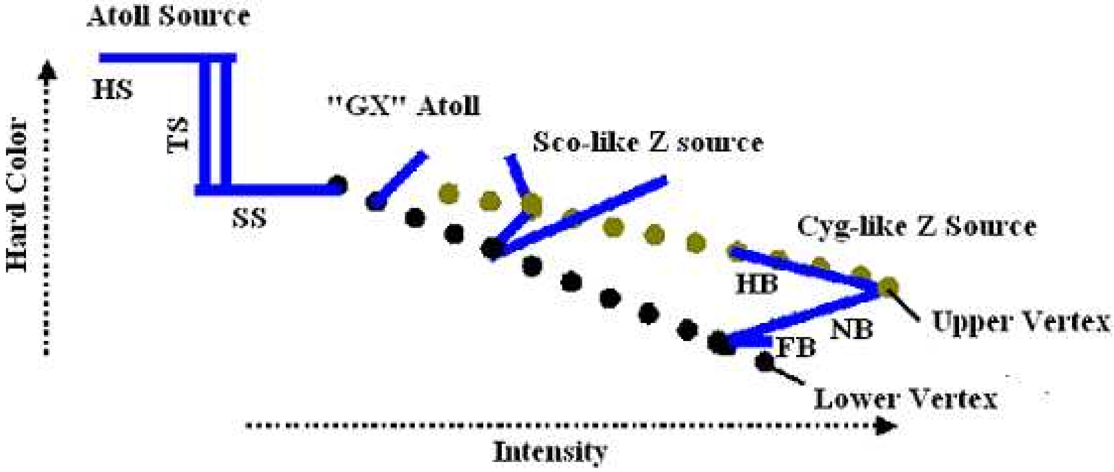

Figure 10-5: Source evolution in the hardness-intensity diagram. This links the behavior of the atoll and Z subclasses as a function of source luminosity.

the color-color and hardness-intensity diagrams. Atoll sources have relatively slow spectral evolution (weeks to months), and span low luminosity (∼0.001–0.5 $L_{\rm Edd}$). They have a hard state (HS; spectra are dominated by a power law with photon index ∼1.7) and a soft state (SS; spectra decrease exponentially above 10 keV), plus a transitional state (TS). Z sources have faster spectral evolution (days to weeks) and emit at high luminosity ($\sim L_{\rm Edd}$). They have three distinctive branches (horizontal, normal and flaring branches (HB/NB/FB); Figure 10-2). Although spectra on all three branches are mostly soft, these three branches are different from each other in many aspects (e.g., evolution timescales, radio emission, fast variability). Z sources are further classified into two subgroups based on the length and orientation of their "Z" tracks (Figure 10-2): Cyg-like (Cyg X–2, GX 340+0, and GX 5–1) and Sco-like (Sco X–1, GX 17+2, and GX 349+2).

Some special notes follow. For atoll sources (Figure 10-1), the three states, i.e., hard, transitional, and soft states, are also called in the literature extreme island, island, banana states, respectively. The banana state is further divided into lower left banana (with twin kHz QPOs), lower banana (with several 10 Hz band limited noises), and upper banana (dominated by a $<$ 1 Hz power-law noise). They are denoted as purple circles, red crosses, and black stars, respectively, in Figure 10-1 (see Chapter 6).

For Z sources, the "Z" tracks for some sources move little over years in the color-color and hardness-intensity diagrams (e.g., gx340+0), but for others, the "Z" tracks can move fast, over timescales of days to weeks, especially Cyg X–2 and the recently discovered transient Z source XTE J1701–461, which we discuss now.

XTE J1701–461 experienced a long outburst in 2006-2007. In Figure 10-3 (see also Figures 7-5 and 7-10), samples of the color-color and hardness-intensity diagrams of this source in three time intervals are shown. The source was first observed at high luminosity, and it behaved as a Cyg-like Z source (compare the panels of the last column in Figure 10-3 with the panels of the first column in Figure 10-2). As the source luminosity decreased, tracks similar to those of the Sco-like Z sources were traced out (compare the panels of the second column in Figure 10-3 with the panels of the second column in Figure 10-2). As the source luminosity decreased further, the source shows behaviors typical of an atoll source (compare the panels of the first columns in Figure 10-3 with Figure 10-1). Thus this source clearly shows that different classes of Z sources are due to different levels of mass accretion rates.

The hardness-intensity diagram for this whole outburst is shown in Figure 10-4 (see also Figure 7-6), with a legend of all different symbols denoting different spectral states/branches included (note that different bin sizes are used, compared with Figure 10-3). The overall intensity decreases with the outburst. In this diagram, we see that the lower (black diamonds) and upper (olive pentagrams) Z vertices (transitions between branches) lie along two distinct lines, with the lower vertex smoothly evolved into the atoll track traced out at the lowest luminosity. The upper vertex disappears earlier than the lower vertex in this outburst, and no direct connection between the upper vertex and the atoll track is observed. However, the normal branch seems to shorten in this diagram, i.e., the two vertices become close, as the source intensity decreases. Figure 10-5 sketches the source evolution in the hardness-intensity diagram based on the above behavior of XTE J1701–461.

10.2.2 Summary of spectral fit results

In this section, spectral fit results for several NS LMXBs using our new spectral model are collected from previous chapters to be compared and summarized. In our model, atoll

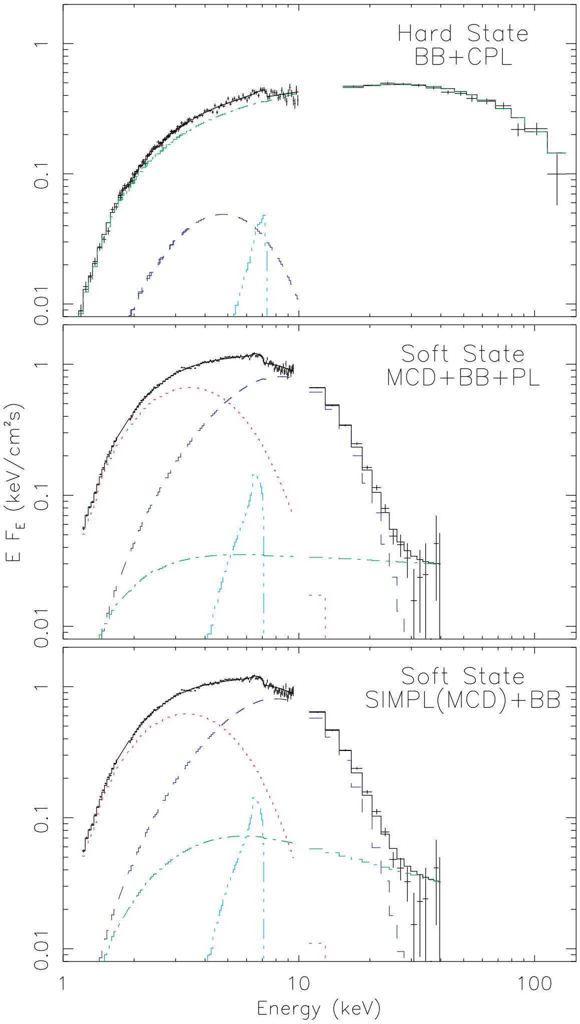

Figure 10-6: Example of unfolded spectra at different states using different models. The total model fit is shown as a black solid line. The MCD component (if included) is shown by a red dotted line, the BB component by a blue dashed line, the PL/CPL/SIMPL component by a green dot-dashed line, and a Fe line (modeled by the diskline model) by a cyan triple-dot-dashed line. For the SIMPL(MCD)+BB model, the MCD component shown is the unscattered part, and the plotted SIMPL component refers to the scattered part. See also Figure 5-3.

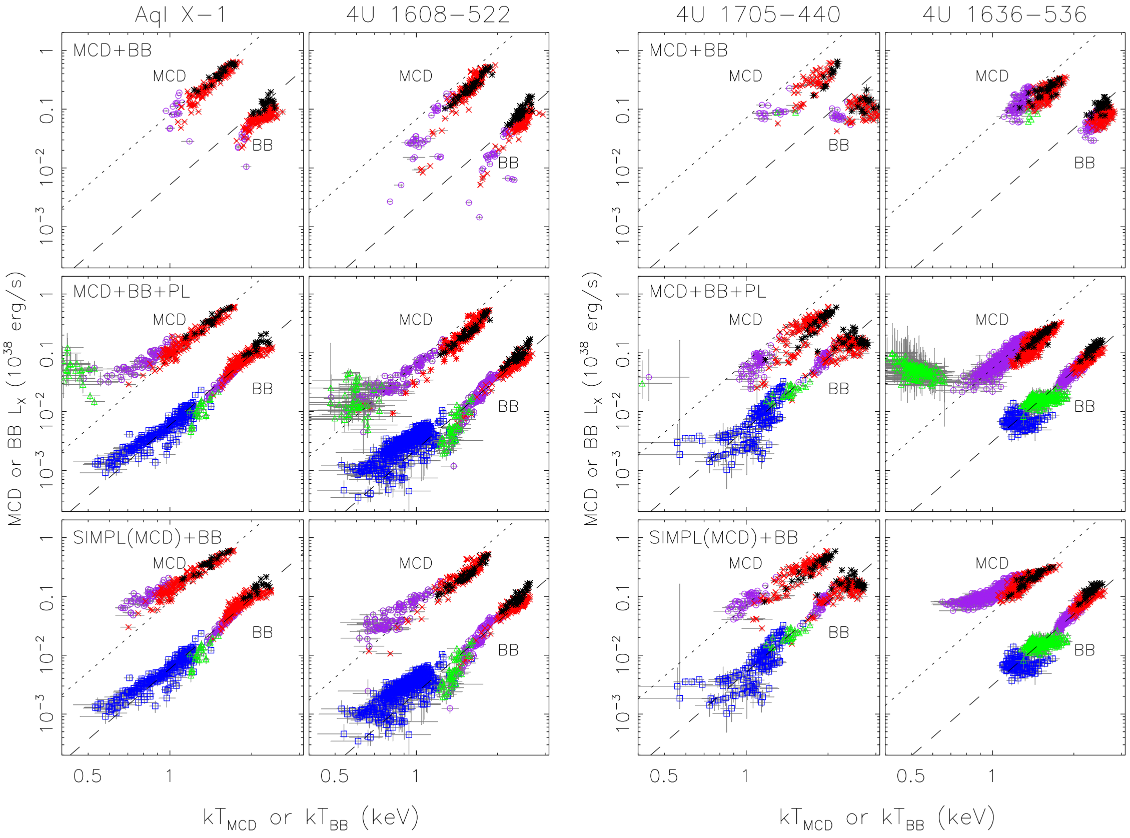

(a) (b)

Figure 10-7: Spectral fit results of transient (a) and persistent (b) atoll sources. The bin size is constrained to be < 4 ks. The data here correspond to those in Figure 10-1. See also Figure 6-6.

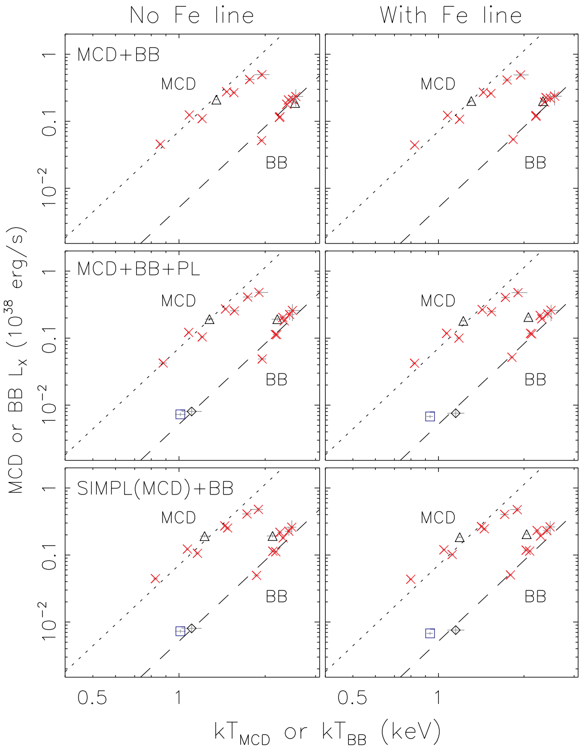

Figure 10-8: Fit results of broad-band spectra of 4U 1705–44 observed by *Suzaku* and *BeppoSAX*. The panels in the left column show the results of the fit with the Fe line region (4.2–8.2 keV) excluded, while the panels in the right column show the fitting results with the Fe line modeled by the diskline model. The symbols in each panel denote different spectral states and different observatories: *BeppoSAX* hard (black diamond) and soft (black triangle) states, and *Suzaku* hard (blue square) and soft (red crosses) states. For the case of Model SIMPL(MCD)+BB, the MCD component shown refers to the original (before scattering) emission. The dotted lines correspond to the NS burst radius of 7.4 km, and the dashed lines correspond to $R = 2.0$ km, assuming $L_X = 4\pi R^2 \sigma T^4$. See also Figure 5-4.

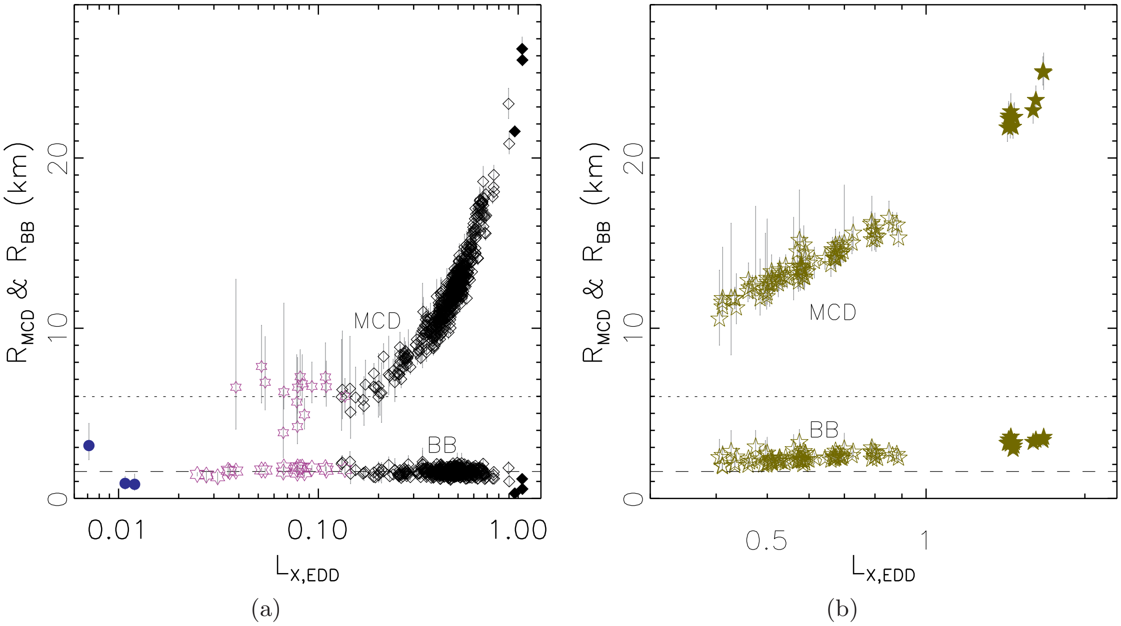

(a) (b)

Figure 10-9: Spectral fit results of transient source XTE J1701–462. Only results of the atoll hard state (filled blue circles), atoll soft state (purple hexagrams), the lower Z vertex (black diamonds), and the upper Z vertex (olive pentagrams) are shown. See also Figures 7-17 and 7-19.

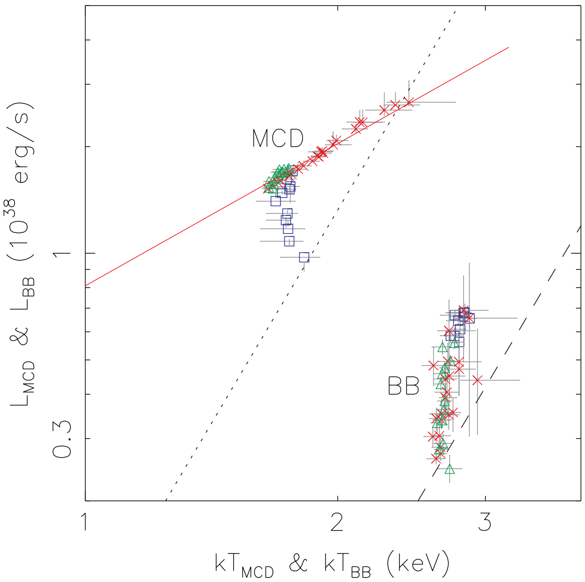

Figure 10-10: The results of the spectral fit of Z source GX 17+2. The spectra were obtained by rebinning data according their position in the hardness-intensity diagram shown in Figure 10-2. The luminosities of the thermal components (MCD/BB) are plotted against their characteristic temperatures. The dotted line is a constant radius line inferred from the Type I X-ray bursts, while the red solid line is a constant $\dot{M}$ line. see also Figure 9-5.

hard-state spectra are described by a single temperature blackbody (BB), presumed to model emission from the boundary layer where the accreted material impacts on the NS surface, and a strong Comptonized component, modeled by a cutoffpl power law (CPL; Figure 10-6). Atoll soft-state spectra are described by two thermal components, i.e., a multicolor disk (MCD) and a BB, with additional weak Comptonized component, modeled by a single power law or by a simple convolution Comptonization model (SIMPL) by Steiner et al. [2008]. Compared with the classical two-component models (one thermal and the other Comptonized), our model gives results of the thermal component much closer to the $L \propto T^4$ track (constant apparent emission area) and requires only a small fraction of Comptonization in the soft state, as shown in the following (see also Chapters 4–6).

Figure 10-7 (see Chapter 6) shows the spectral fit results for the four atoll sources shown in Figure 10-1. The first row in Figure 10-7 shows the results from model MCD+BB, i.e., no Comptonized component. Only fits with values of reduced χ^2 smaller than 2.0 are shown. A majority of the soft-state spectra can be fit with this model, with a slight sign that both MCD and BB roughly follow the $L \propto T^4$ track. The second row in Figure 10-7 shows the results of soft-state data modeled by MCD+BB+PL, combined with those of the hard-state data modeled by BB+CPL. We see that the MCD in the soft state (excluding the lower left banana, where kHz QPOs are detected; see below) evolves close to the $L \propto T^4$ track. The BB is also close to the $L \propto T^4$ track, from the hard to the soft states. All this is in contrast with the results from the classical two-component models, which has the thermal components roughly maintaining at constant temperatures in the soft state (see Chapter 4). We note that although both MCD and BB have constant emission areas on the whole, there are scatters in the results whereby individual measurements can differ by 30–40%. Whether this is real or due to systematic uncertainties is unknown to us. We cannot quantitatively estimate the systematic deviation from the $L \propto T^4$ track using *RXTE* data, in part because of the lack of spectral response < 2 keV. The similarity of results for modeling the weak Comptonization modeled by SIMPL or by PL is a common conclusion and is not further discussed here.

The atoll-source lower left banana is special in that a lot of kHz QPOs are detected (see Chapter 6). We see in Figure 10-7 that the MCD systematically has larger best-fitting inner disk radius in the lower left banana than in other parts of the soft state. This might hint on the close relation between the accretion disk and kHz QPOs in accreting NSs.

The results of the fit of the broad-band energy spectra of 4U 1705–44 observed by *Suzaku* and *BeppoSAX* is shown in Figure 10-8 (see Chapter 5). The BB appears to follow the $L \propto T^4$ track. The MCD component instead shows a deviation in which $L \propto T^{3.2}$. This deviation from $L \propto T^4$ can be explained by the luminosity-dependent spectral hardening factor. Spectral hardening arises when the electron scattering dominates over absorption as photons escape the disk through a hot atmosphere. In such a situation, the local specific flux in the disk appears as a simple dilute blackbody with a color temperature higher than the effective temperature by a factor of $f_{\rm col}$ [Shimura and Takahara, 1995]. This factor slightly increases with luminosity/temperature [Davis et al., 2006]. We also note that the above deviation might be real in some observations associated with kHz QPOs (their occurrences are hard to check using *Suzaku* data).

We also apply our spectral model to the transient source XTE J1701–462, which shows both Z and atoll source behavior as shown above (see Chapter 7). In Figure 10-9 (see also Figures 7-17 and 7-19), we show the spectral fit results. Only results of the atoll hard state (filled blue circles), the atoll soft state (purple hexagrams), the lower Z vertex (black diamonds; left panel), and the upper Z vertex (olive pentagrams; right panel) are shown.

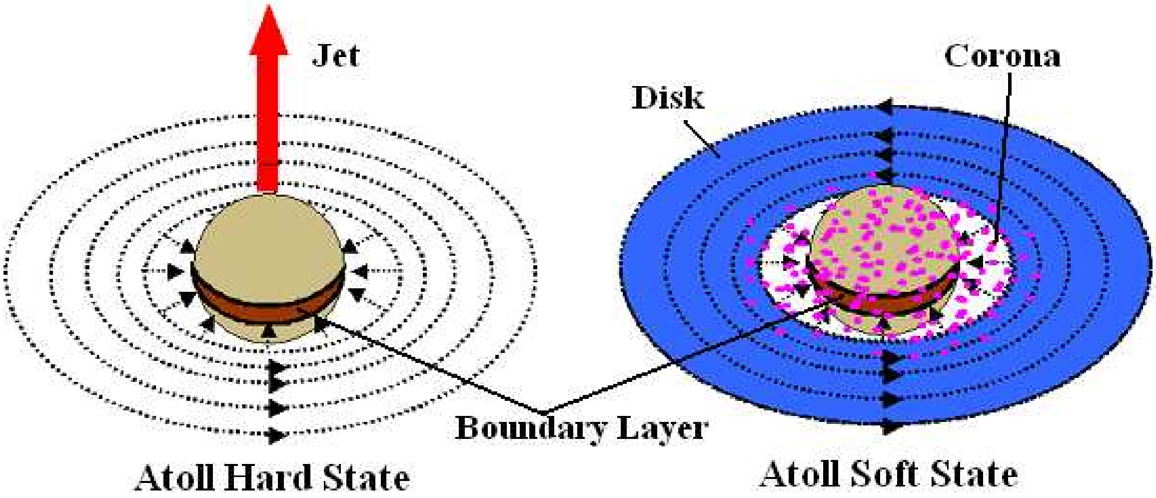

Figure 10-11: The sketches of the atoll source states based on our spectral study of several atoll sources. The radiative regions are colored. In the hard state, the disk is not seen, perhaps because the temperature is lower than the limit of instrumental sensitivity, and the inner radius of the disk in the hard state is therefore uncertain.

As we showed above, the two Z vertices lie along two distinct lines in the hardness-intensity diagram, with the lower vertex directly connected to the atoll track. The vertices can track the secular move of the "Z" track for Z sources. Thus this plot shows the connection between atoll and Z sources. Figure 10-9 shows that the inner disk radius is roughly constant when the source behaves as an atoll source, but in the vertices, it increases with luminosity. The BB emission area is seldom changed from the atoll hard to the soft state, and also in the lower vertex. However, in the upper vertex, it increases with luminosity. We note that the track of the MCD/BB for the lower vertex is different from that for the upper vertex, which might imply that they belong to two different accretion configurations.

To understand the spectral evolution in the Z-source branches, we show in Figure 10-10 (see also Figure 9-5) the fit results of the Sco-like Z source GX 17+2, which has better data quality than XTE J1701–462 for a single track. The red line in this figure shows a constant $\dot{M}$ line, i.e., $L_{\mathrm{MCD}} \propto T_{\mathrm{MCD}}^{4/3}$. This shows the relation between disk luminosity and the temperature at the inner disk radius when the inner disk varies in radius under a constant $\dot{M}$ (assuming a standard thin disk). This figure shows that the MCD in the flaring branch (red crosses) follows this line. In the normal branch (green triangles), the disk is little changed, but the BB emission area increases from the lower vertex to the upper vertex, under a nearly constant temperature. In the horizontal branches (blue squares), the MCD changes obviously, but it is not the case for the BB. It can be shown that the total luminosity of the MCD plus the Comptonized component (PL) is roughly constant, to within 20%. We note that the above results apply to Sco-like Z sources. For Cyg-like Z sources, the spectral evolution appears to be more complicated.

10.3 Physical interpretations derived from spectral analyses

10.3.1 A new spectral model for weakly magnetized NS LMXBs

One of the most important results of this thesis is that we obtain a new way to model the spectra of weakly magnetized NS LMXBs. In this model, the soft state is described by two main thermal components, i.e., a MCD and a BB (for the boundary layer), with additional weak Comptonization, while the hard state is described by a strong Comptonization component and a BB (Thus far, there is no evidence that the MCD can be seen in the hard state). The scenario that the new model describes can be illustrated in Figure 10-11. This new model gives spectral fit results for weakly magnetized NS LMXBs physically more reasonable than the classical two-component models. The value of the inner disk radius from our new model is consistent with being about or larger than the NS radius. The disk roughly follows a $L \propto T^4$ track in most of the soft state. The Comptonization fraction is small ($\lesssim$30%) in the soft state, which makes the timing/spectral properties of weakly magnetized NS LMXBs more aligned with BH X-ray binaries. None of classical two-component models can reproduce all the above results [Lin et al., 2007b, Chapter 4].

10.3.2 The accretion disk inner radius and the boundary layer effective area in atoll sources

Now we discuss the physical implications from our spectral study of weakly magnetized NS LMXBs, with most of physics being covered in Chapter 3. We start with atoll sources. Our model suggests that for several atoll sources the MCD in the soft state (excluding the lower left banana where kHz QPOs occur) roughly follows a $L \propto T^4$ track, allowing for small deviation due to the luminosity-dependent spectral hardening. The apparent inner disk radius is comparable to the apparent size of the NS inferred from the Type I X-ray burst. Thus the disk in the atoll soft state is probably a standard thin disk. In the hard state, PCA data have lower energy boundary around 2.7 keV and do not allow us to constrain the MCD component. When we use the broad-band spectra from 4U 1705–44 observed by *Suzaku* and *BeppoSAX*, which cover energies down to ~1 keV, we find the color temperature of the disk must be less than 0.2 keV if there is any visible accretion disk.

The boundary layer, described as a BB in our model, follows a $L \propto T^4$ track from the atoll hard to soft states. The boundary layer area is roughly 1/16 of the whole NS surface, based on simple comparison between the apparent BB areas from the persistent emission and those from the bursts. Its luminosity is about 10% or less of the total source luminosity in the hard state, but is comparable to the MCD luminosity in the soft state. One interpretation of this difference is the strong mass outflow in the hard state. This seems to be consistent with the radio detection of jets in the atoll hard state. Based on the above results, we can speculate the accretion scenario as shown in Figure 10-11.

10.3.3 NS radius vs. the ISCO in atoll sources

In a summary, our spectral model for the atoll sources suggests that the disk might be truncated at a constant radius in most of the soft state and that the boundary layer area is small but is also nearly constant from the hard to soft states. If these results are correct, then there is a question of whether the disk is truncated by the ISCO or by the NS surface. The main difficulty in determining whether the accretion disk is truncated by the NS surface or at the ISCO is that the ISCO is quite close to the surface of the NS. The above two cases can be differentiated if the NS confined inside its ISCO or not can result in quite different spectral evolution behavior of the boundary layer and the accretion disk. If the accretion disk extends all the way down to the surface of the NS, the boundary layer and the disk are dynamically coupled. Popham and Sunyaev [2001] modeled the boundary layer as part of the disk, using the slim disk equations and Newtonian approximation, and found that the transition radius of the accretion disk to the boundary layer increased with the accretion rate. Our results suggest that the increase in the luminosity of the boundary layer and the accretion disk mostly results in increase in characteristic temperatures, instead of in emission areas, and might suggest that the boundary layer is not fully coupled with the accretion disk. Thus the accretion is quite probably truncated by the ISCO. The small size of the boundary layer might require that the disk is always geometrically thin. Based on the disk luminosity above, the ratio of the disk maximum thickness to the distance to the NS center is about less than 0.1 from McClintock et al. [2006]. Besides, Abramowicz et al. [1978] showed the existence of the cusp of the equipotential surface with the presence of the ISCO, resulting in the sharp cusp on the inner edge of the accreting disk. Thus the thickness of the disk can be forced to be small near the ISCO. All the above pictures need to be confirmed by modeling the accretion disk and boundary layer together, with the general relativistic effect taken into account.

10.3.4 Magnetic fields of the NS in atoll sources

No matter whether the disk is truncated at the ISCO or by the NS surface, the magnetic field of the NS should be dynamically unimportant, if the thermal accretion disk goes all the way down to near the NS. This requires the Alfvén radius $r_{\rm A}$, the radius at which the magnetic pressure is roughly the sum of the ram and gas pressure, should be smaller than the inner disk radius. Based on Equations 6.19–6.20 in Frank et al. [1985], we have

$$r_{\rm A} \sim 7.5 \left(\frac{k_{\rm A}}{0.5}\right) \left(\frac{M_{\rm NS}}{M_\odot}\right)^{1/7} \left(\frac{R_{\rm NS}}{10~{\rm km}}\right)^{10/7} \left(\frac{L}{10^{37}~{\rm erg/s}}\right)^{-2/7} \left(\frac{B}{10^8~{\rm G}}\right)^{4/7}~{\rm km}, \qquad (10.1)$$

where B is the magnetic field strength at the surface of the NS and $k_{\rm A}$ is the correction from the spherical accretion to disk accretion and is about 0.5. This formula assumes a dipole-like magnetic field. Now we assume the NS mass to be 1.4 solar mass and radius 10 km, and assume the disk is truncated at the radius of the ISCO. Using the lowest luminosity of 10^{37} erg/s (0.04 $L_{\rm Edd}$) of 4U 1705–44 in the soft state (from *Suzaku*/*RXTE* observations; see Chapter 5–6), the magnetic field strength at the surface of the NS in 4U 1705–44 should be less than about 1.9×10^8 G. The soft-state lowest luminosity for Aql X–1, 4U 1608–522 and 4U 1636–536 are about 0.02, 0.01, and 0.07 and should have magnetic fields weaker than 1.2, 1.0, 2.5 $\times 10^8$ G, respectively, at the surface of the NS in their systems. Considering that the boundary layer area is seldom changed from the hard to the soft state, the magnetic field might be even weaker than the above value. The hard-state lowest luminosity is <0.004, <0.004, 0.01, and 0.05 $L_{\rm Edd}$, which corresponds to upper limit of the magnetic field of 0.6, 0.6, 1.0, 2.1 $\times 10^8$ G from the above equation, for Aql X–1, 4U 1608–522, 4U 1705–44, and 4U 1636–536, respectively.

Some special notes follow. The above estimates are based on some simplified assumptions, without addressing the questions of whether the stellar magnetic field is dipolar, whether the magnetic moment is parallel to the NS spin axis, etc. [Psaltis and Chakrabarty, 1999]. The inferred magnetic field for the above atoll sources is roughly consistent with other reports [e.g., Psaltis and Lamb, 1998, Di Salvo and Burderi, 2003, Casella et al., 2008]. Little coherent pulsation is detected from persistent emission of these sources (see, however, detection of coherent millisecond X-ray pulsation lasting for $\sim$150 s from Aql X–1 by Casella et al. [2008]). The millisecond X-ray pulsars are also reported to have comparable magnetic fields [e.g., Psaltis and Chakrabarty, 1999, Cackett et al., 2009a]. Different accretion rates might be an important factor in explaining the detection of coherent pulsation from millisecond X-ray pulsars but not from nonpulsing atoll sources though they have comparable magnetic fields, considering that millisecond X-ray pulsars are almost the faintest class in NS LMXBs [van der Klis, 2006]. However, there might be other factors (viewing angles, alignment of magnetic moment with NS spin axis, etc. [Psaltis and Chakrabarty, 1999]).

We also note that our results do not seem to support the explanation of "propeller" effect for the hard state [e.g., Zhang et al., 1998a, Chen et al., 2006]. This explanation suggests that the transition from the soft to hard states in accreting NSs is due to the centrifugal barrier of the magnetic field. It is based on the observations of significant decrease of the BB flux and overall flux, which is argued against by Rappaport et al. [2004], and hardening of the power-law component (the spectra are fit with BB+PL). Although our results do not violate these observations, we find that the BB emission area are essentially similar from the hard to the soft state. If the propeller effects take place, we should observe significantly different BB emission area. Our results are more consistent with the jet explanation of the hard state (see above).

10.3.5 Investigation of kilohertz quasi-periodic oscillations in atoll sources

Atoll sources are known to exhibit kHz QPOs in the lower left banana branch in the soft state. This part is normally the final stop of the source in the soft state before entering the transitional state and returning back to the hard state (it is hard to observe the transition from the hard to the soft states). We note that (lower) kHz QPO frequency normally decreases from 700–900 Hz in this part to < 500 in the transitional state and can show shifts on timescales of hours. We also note that such kHz QPOs are not observed in black-hole X-ray binaries.

A lot of models have been suggested for kHz QPOs, including beat-frequency, relativistic precession and relativistic resonance models [van der Klis, 2006]. Our spectral results show interesting behavior related to kHz QPOs, which thus might shed light on their origin. In our fit of four atoll sources (see Chapter 6), we find that the apparent inner disk radius appears to be larger in the lower left banana than in other parts of the soft state. There is a sign (that still needs to be confirmed) that the inner disk radius might increase as the source gets close to the transitional state. Thus our results suggest a close relation between kHz QPOs in atoll sources and the accretion disk. It is well known that kHz QPOs in the accreting NS has larger fractional root-mean-square at higher photon energies [van der Klis, 2006]. In their study of 4U 1608-522 and GX 340+0 using Fourier frequency resolved X-ray spectroscopy, Gilfanov et al. [2003] argued that the kHz QPOs in accreting NSs should be from emission from the boundary layer. Based on the above results, one explanation for the kHz QPOs in accreting NSs is that they are due to modulation of the accretion rate into the boundary layer [van der Klis, 2006]. This new information still needs to be combined with the existing models for kHz QPOs, such as the beat-frequency model by Miller et al. [1998], in order to understand their origins in the end.

10.3.6 Relation between source types and the role of mass accretion rates

XTE J1701–462 is a unique source to study the relation between source types (see Chapter 7). It experiences the behavior of a Cyg-like Z source, a Sco-like Z source, and an atoll source as the overall intensity decreases in its 2006-2007 outburst. This hints on the picture that the change of source behavior from one type to another and the secular changes (seen in the color-color/hardness-intensity diagrams) are due to changes in the mass accretion rate $\dot{M}$. Its two vertices of Z-source tracks move along two distinct lines in the hardness-intensity diagrams with the lower vertex directly connected to the atoll track at low luminosity. We can use the vertex lines plus the atoll track to trace the source spectral evolution. Using the MCD component in our model, we see that $\dot{M} \sim 2L_{\rm MCD}R_{\rm MCD}/GM$ decreases monotonically along the lower vertex line toward the atoll track and along the upper vertex line, supporting the idea that the secular changes of Z tracks and the change of the source behavior from a Cyg-like Z source, a Sco-like Z source, to an atoll source are due the changes in $\dot{M}$.

10.3.7 Accretion disk and boundary layer in Z sources and the Eddington limit

Again using its Z vertices and atoll track of XTE J1701–462, we can examine its overall behavior of the accretion disk and boundary layer (see Chapter 7). Our spectral results show that the disk is probably truncated at the ISCO when the source behaves as an atoll source in the soft state. However, in the Z vertices, the apparent inner disk radius increases with luminosity. This might be because the inner part of the disk is reaching the Eddington limit. That is, when $\dot{M}$ increases to some point, the temperature at the inner disk radius becomes too high, and the local Eddington limit in the disk vertical direction is reached so that there is mass outflow in that direction while the mass can still continue to accrete (see Chapter 3). As $\dot{M}$ increases, more and more part of the inner disk reaches the local Eddington limit, and we see increase in the inner disk radius. If this is true, we expect hot gas outflow. We note that the increase of the apparent inner disk radius might also be due to the thickness of the disk and thus domination of the advection as the cooling mechanism. Advection makes the accretion become radiatively less effective in the inner part of the disk and thus can make the inner disk radius appear to increase, which we discuss below.

The boundary layer in XTE J1701–462 appears to maintain at a constant emission area in the atoll track, similar to our results for the typical atoll sources. In the lower vertex, the boundary layer appears to change little (temperature and area). The temperature there is about the peak value seen in the atoll track, which is about 2.7 keV and is about the peak value seen in the type I X-ray bursts showing photospheric expansion from this source [Lin et al., 2009a]. As shown in Chapter 3, such a temperature is about the Eddington temperature on the NS surface. The area is small and is about the value seen in the atoll track. All this might suggest that the accretion flow onto the NS surface is not thick and that the local Eddington limit in the boundary layer has influence on the accretion flow so that the accretion rate onto the boundary layer is maintained at a constant level.

In the upper vertex, the boundary layer emission area increases with luminosity, with the temperature still maintains at about 2.7 keV. This is a strong sign that the boundary layer reaches the local Eddington limit. We note that the peak value of the boundary layer emission area in the upper vertex is smaller than the whole NS surface inferred from type I X-ray bursts. We also note that although the boundary layer in the upper vertex also reaches the local Eddington limit but has more area than in the lower vertex, it does not necessarily mean that it should have very strong influence on the accretion flow like the behavior of the lower vertex suggested above. This is because in the upper vertex, the accretion flow might be thick and have a lot of mass flow in at high velocity. In this case, large mass accretion rates onto the boundary layer forces the boundary layer to expand but stay at the Eddington temperature.

10.3.8 Speculations for different disk solutions for the vertices of Z sources

We continue to address the Z vertices. They draw our attention above because they can be used to track the secular changes of Z tracks. Now we focus them further because they appear to represent stable accretion configurations. This is based on the observation that the source seems to evolve slower in the vertices than in the branches (at least the flaring and normal branches; see Chapter 7). Our spectral fit results further suggest that the accretion configuration is different in different vertices (the MCD and BB components behave in different ways; e.g., the BB is little changed in the lower vertex, but has the emission area increase with luminosity in the upper vertex). Thus we have the idea that the accretion system in the two vertices represents two different stable accretion configurations, while the branches are due to some types of instabilities.

We now speculate as to how these results can tie into theoretical investigations of accretion disks at high luminosity. Based on the study of the normal branch, which connects the upper and lower vertices, there appears to be more mass accreted onto the boundary layer in the upper vertex than in the lower vertex, when the mass accretion rate into the disk from outside is similar. Combined this and the above results, we hypothesize that the disk in the upper vertex is a slim disk while in the lower vertex it is a standard thin disk. Then the evolution up the normal branch represents the transition to the slim disk.

A brief summary of the picture that we have concerning the two Z vertices follows. The upper vertex represents a slim disk with advection dominated in the inner disk. The lower vertex represents a standard thin disk, with the inner disk experiencing hot gas outflow due to local Eddington limit. Thanks to the above different accretion flows, the boundary layer in the upper vertex have more emission area, though the accretion rate into the disk from outside is similar for these two vertices.

10.3.9 The physical nature of different branches in Z sources

Finally, we address the physical interpretations for different branches of Z sources. We only concentrate on Sco-like Z sources, as Cyg-like Z tracks show more complicated behavior and their origins are more difficult to understand. The flaring branch of Z sources is connected to the other part of Z track at the lower vertex. Our spectral modeling suggests that it is traced out when the disk shrinks back at constant $\dot{M}$ toward the value assumed when the source is atoll-like (presumably the ISCO). As mentioned above, the disk is truncated at a larger radius in the lower vertex than the value seen when the source is atoll-like. The flaring branch evolves on timescales of 10 minutes and much faster (seconds) at the end of the flaring branch. This is about the thermal timescale in the disk around NSs (see Chapter 3). Thus the flaring branch appears to be an instability in which the disk temporarily moves to reverse the truncation level set by the NB/FB vertex.

As the source evolves along the NB from the upper to lower vertices, the main spectral variation is the apparent size of the BB emission. This might be due to additional matter supplied to the boundary layer via the onset of a radial flow. This is possible from the picture that we have for the two vertices that the normal branch connects. The Sco-like horizontal branch is traced out when some of the energy in the disk is converted into a hard X-ray component, presumably via Comptonization, while the disk $\dot{m}$ remains roughly constant. Strong radio emission has been observed in this branch.

We have seen that these three branches of (Sco-like) Z tracks represent three different physical mechanisms, which appear to operate at a nearly constant $\dot{M}$ for a single Z track. They probably represent three different instabilities that origin from the two relatively stable Z vertices.

Appendix A

Timing Analyses

This appendix describes the Fourier transform technique that is commonly used in the X-ray timing study. Some terminologies will also be introduced. Suppose there are a sequence of N numbers x_k (k = 0, 1, ..., $N-1$). In X-ray timing study, x_k is normally the X-ray photon counts per time step τ. The discrete Fourier transform of this sequence is defined as,

$$a_j = \Sigma_{k=0}^{N-1} x_k \mathrm{e}^{2\pi ijk/N}, \qquad j = -N/2, ..., N/2-1, \tag{A.1}$$

where i is the imaginary number with $i^2 = -1$. The inverse discrete Fourier transform is given by

$$x_k = \frac{1}{N} \Sigma_{j=-N/2}^{N/2-1} a_j \mathrm{e}^{-2\pi ijk/N}, \qquad k = 0, ..., N-1. \tag{A.2}$$

The Parseval's theorem states,

$$\Sigma_{k=0}^{N-1} |x_k|^2 = \frac{1}{N} \Sigma_{j=-N/2}^{N/2-1} |a_j|^2. \tag{A.3}$$

The variance for the sequence (assumed to be real numbers) is given by

$$\mathrm{var}(x_k) \equiv \frac{1}{N} \Sigma_k (x_k - \bar{x})^2 = \frac{1}{N^2} \Sigma_{j=-N/2, j\neq 0}^{N/2-1} |a_j|^2. \tag{A.4}$$

Some definitions follow. The sample period T is defined to be $N\tau$. The frequency (in unit of hertz) is $\nu_j = j/T$. The maximal frequency is called Nyguist frequency, which is equal to $N/2T$. The total number of photons is $N_{\mathrm{ph}} = \Sigma_k x_k = a_0$.

The power spectrum, following the normalization by Leahy et al. [1983], is defined as,

$$P_j \equiv \frac{2}{N_{\mathrm{ph}}} |a_j|^2, \qquad j = -N/2, ..., N/2-1. \tag{A.5}$$

The power density spectrum is defined as $P_j T$.

The variance is related to the power spectrum as,

$$\mathrm{var}(x_k) = \frac{N_{\mathrm{ph}}}{N^2} \left(\Sigma_{j=1}^{N/2-1} P_j + \frac{1}{2} P_{N/2} \right). \tag{A.6}$$

The fractional root-mean-square (rms) variation is defined as,

$$r = \frac{\sqrt{\mathrm{var}(x_k)}}{\bar{x}} = \sqrt{\frac{\Sigma_{j=1}^{N/2-1} P_j + \frac{1}{2} P_{N/2}}{N_{\mathrm{ph}}}}. \tag{A.7}$$

For the rms over some frequency range, one just needs to set the sum range to the corresponding frequency range. In practice, deadtime correction has to be made first, and the Poisson noise is subtracted.

Bibliography

M. Abramowicz, M. Jaroszynski, and M. Sikora. Relativistic, accreting disks. A&A, 63: 221–224, February 1978.

M. A. Abramowicz, B. Czerny, J. P. Lasota, and E. Szuszkiewicz. Slim accretion disks. ApJ, 332:646–658, September 1988.

V. K. Agrawal and P. Sreekumar. X-ray spectral evolution of low-mass X-ray binary GX 349+2. MNRAS, 346:933–939, December 2003.

M. L. Alme and J. R. Wilson. X-Ray Emission from a Neutron Star Accreting Material. ApJ, 186:1015–1026, December 1973.

K. A. Arnaud. XSPEC: The First Ten Years. In G. H. Jacoby and J. Barnes, editors, Astronomical Data Analysis Software and Systems V, volume 101 of Astronomical Society of the Pacific Conference Series, pages 17–+, 1996.

K. Asai, T. Dotani, F. Nagase, and K. Mitsuda. Iron K Emission Lines in the Energy Spectra of Low-Mass X-Ray Binaries Observed with ASCA. ApJS, 131:571–591, December 2000.

T. Augusteijn, F. van der Hooft, J. A. de Jong, M. H. van Kerkwijk, and J. van Paradijs. Phase-resolved spectroscopy of the low-mass X-ray binaries 1636-536/V 801 Arae and 1735-444/V 926 Scorpii. A&A, 332:561–568, April 1998.

S. A. Balbus. Enhanced Angular Momentum Transport in Accretion Disks. ARA&A, 41: 555–597, 2003.

S. A. Balbus and J. F. Hawley. A powerful local shear instability in weakly magnetized disks. I - Linear analysis. II - Nonlinear evolution. ApJ, 376:214–233, July 1991.

D. Barret. The broad band x-ray/hard x-ray spectra of accreting neutron stars. Advances in Space Research, 28:307–321, 2001.

D. Barret and J.-F. Olive. A Peculiar Spectral State Transition of 4U 1705-44: When an Atoll Looks Like a Z. ApJ, 576:391–401, September 2002.

D. Barret, J. F. Olive, L. Boirin, C. Done, G. K. Skinner, and J. E. Grindlay. Hard X-Ray Emission from Low-Mass X-Ray Binaries. ApJ, 533:329–351, April 2000.

D. Barret, J. F. Olive, and T. Oosterbroek. Simultaneous BeppoSAX and Rossi X-ray timing explorer observations of 4U 1812-12. A&A, 400:643–647, March 2003.

D. Barret, J.-F. Olive, and M. C. Miller. Supporting evidence for the signature of the innermost stable circular orbit in Rossi X-ray data from 4U 1636-536. MNRAS, 376: 1139–1144, April 2007.

E. M. Basinska, W. H. G. Lewin, M. Sztajno, L. R. Cominsky, and F. J. Marshall. X-ray observations of the burst source MXB 1728 - 34. ApJ, 281:337–353, June 1984.

R. D. Belian, J. P. Conner, and W. D. Evans. The discovery of X-ray bursts from a region in the constellation Norma. ApJ, 206:L135–L138, June 1976.

M. Berger, M. van der Klis, J. van Paradijs, W. H. G. Lewin, F. Lamb, B. Vaughan, E. Kuulkers, T. Augusteijn, W. Zhang, F. E. Marshall, J. H. Swank, I. Lapidus, J. C. Lochner, and T. E. Strohmayer. Discovery of 800 HZ Quasi-Periodic Oscillations in 4U 1608-52. ApJ, 469:L13+, September 1996.

G. Boella, R. C. Butler, G. C. Perola, L. Piro, L. Scarsi, and J. A. M. Bleeker. BeppoSAX, the wide band mission for X-ray astronomy. A&AS, 122:299–307, April 1997a.

G. Boella, L. Chiappetti, G. Conti, G. Cusumano, S. del Sordo, G. La Rosa, M. C. Maccarone, T. Mineo, S. Molendi, S. Re, B. Sacco, and M. Tripiciano. The medium-energy concentrator spectrometer on board the BeppoSAX X-ray astronomy satellite. A&AS, 122:327–340, April 1997b.

E. Boldt. The cosmic X-ray background. Phys. Rep., 146:215–257, 1987.

H. V. Bradt, R. E. Rothschild, and J. H. Swank. X-ray timing explorer mission. A&AS, 97:355–360, January 1993.

E. F. Brown, L. Bildsten, and R. E. Rutledge. Crustal Heating and Quiescent Emission from Transiently Accreting Neutron Stars. ApJ, 504:L95+, September 1998.

E. M. Cackett, J. M. Miller, S. Bhattacharyya, J. E. Grindlay, J. Homan, M. van der Klis, M. C. Miller, T. E. Strohmayer, and R. Wijnands. Relativistic Iron Emission Lines in Neutron Star Low-Mass X-Ray Binaries as Probes of Neutron Star Radii. ApJ, 674: 415–420, February 2008a.

E. M. Cackett, J. M. Miller, J. Raymond, J. Homan, M. van der Klis, M. Méndez, D. Steeghs, and R. Wijnands. Investigating the Nature of Absorption Lines in the Chandra X-Ray Spectra of the Neutron Star Binary 4U 1820-30. ApJ, 677:1233–1240, April 2008b.

E. M. Cackett, D. Altamirano, A. Patruno, J. M. Miller, M. Reynolds, M. Linares, and R. Wijnands. Broad Relativistic Iron Emission Line Observed in SAX J1808.4-3658. ApJ, 694:L21–L25, March 2009a.

E. M. Cackett, J. M. Miller, D. R. Ballantyne, D. Barret, S. Bhattacharyya, M. Boutelier, M. C. Miller, T. E. Strohmayer, and R. Wijnands. Relativistic Lines and Reflection from the Inner Accretion Disks Around Neutron Stars. ArXiv e-prints, August 2009b.

E. M. Cackett, J. M. Miller, J. Homan, M. van der Klis, W. H. G. Lewin, M. Méndez, J. Raymond, D. Steeghs, and R. Wijnands. A Search for Iron Emission Lines in the Chandra X-Ray Spectra of Neutron Star Low-Mass X-Ray Binaries. ApJ, 690:1847–1855, January 2009c.

P. Casella, D. Altamirano, A. Patruno, R. Wijnands, and M. van der Klis. Discovery of Coherent Millisecond X-Ray Pulsations in Aquila X-1. ApJ, 674:L41–L44, February 2008.

S. Chandrasekhar. The Stability of Non-Dissipative Couette Flow in Hydromagnetics. Proceedings of the National Academy of Science, 46:253–257, February 1960.

P. A. Charles and M. J. Coe. Optical, ultraviolet and infrared observations of X-ray binaries, pages 215–265. April 2006.

X. Chen, S. N. Zhang, and G. Q. Ding. Propeller-driven Spectral State Transition in the Low-Mass X-Ray Binary 4U 1608-52. ApJ, 650:299–302, October 2006.

D. J. Christian and J. H. Swank. The Survey of Low-Mass X-Ray Binaries with the Einstein Observatory Solid-State Spectrometer and Monitor Proportional Counter. ApJS, 109: 177–+, March 1997.

M. J. Church and M. Balucińska-Church. Results of a LMXB survey: Variation in the height of the neutron star blackbody emission region. A&A, 369:915–924, April 2001.

M. J. Church, N. A. Inogamov, and M. Bałucińska-Church. A comparison of neutron star blackbody luminosities in LMXB with the theory of accretion flow spreading on the stellar surface. A&A, 390:139–146, July 2002.

M. J. Church, G. S. Halai, and M. Bałucińska-Church. An explanation of the Z-track sources. A&A, 460:233–244, December 2006.

M. J. Church, M. Balucinska-Church, N. K. Jackson, and A. Gibiec. A model for the Z-track phenomenon, jet formation and the kilohertz QPO based on Rossi-XTE observations of the Z-track sources. ArXiv e-prints, November 2008.

R. L. Cooper and R. Narayan. A Two-Zone Model for Type I X-Ray Bursts on Accreting Neutron Stars. ApJ, 652:584–596, November 2006.

A. Cumming. Thermonuclear X-ray bursts: theory vs. observations. Nuclear Physics B Proceedings Supplements, 132:435–445, June 2004.

A. D'Aí, P. Życki, T. Di Salvo, R. Iaria, G. Lavagetto, and N. R. Robba. Broadband Spectral Evolution of Scorpius X-1 along Its Color-Color Diagram. ApJ, 667:411–426, September 2007.

F. D'Amico, W. A. Heindl, R. E. Rothschild, and D. E. Gruber. High-Energy X-Ray Timing Experiment Detections of Hard X-Ray Tails in Scorpius X-1. ApJ, 547:L147–L150, February 2001.

S. W. Davis and I. Hubeny. A Grid of Relativistic, Non-LTE Accretion Disk Models for Spectral Fitting of Black Hole Binaries. ApJS, 164:530–535, June 2006.

S. W. Davis, C. Done, and O. M. Blaes. Testing Accretion Disk Theory in Black Hole X-Ray Binaries. ApJ, 647:525–538, August 2006.

T. Di Salvo and L. Burderi. Constraints on the neutron star magnetic field of the two X-ray transients SAX J1808.4-3658 and Aql X-1. A&A, 397:723–727, January 2003.

T. Di Salvo, R. Iaria, L. Burderi, and N. R. Robba. The Broadband Spectrum of MXB 1728-34 Observed by BeppoSAX. ApJ, 542:1034–1040, October 2000a.

T. Di Salvo, L. Stella, N. R. Robba, M. van der Klis, L. Burderi, G. L. Israel, J. Homan, S. Campana, F. Frontera, and A. N. Parmar. The Discovery of a State-Dependent Hard Tail in the X-Ray Spectrum of the Luminous Z Source GX 17+2. ApJ, 544:L119–L122, December 2000b.

T. Di Salvo, N. R. Robba, R. Iaria, L. Stella, L. Burderi, and G. L. Israel. Detection of a Hard Tail in the X-Ray Spectrum of the Z Source GX 349+2. ApJ, 554:49–55, June 2001.

T. Di Salvo, R. Farinelli, L. Burderi, F. Frontera, E. Kuulkers, N. Masetti, N. R. Robba, L. Stella, and M. van der Klis. On the spectral evolution of Cygnus X-2 along its color-color diagram. A&A, 386:535–547, May 2002.

T. Di Salvo, R. Iaria, M. Méndez, L. Burderi, G. Lavagetto, N. R. Robba, L. Stella, and M. van der Klis. A Broad Iron Line in the Chandra High Energy Transmission Grating Spectrum of 4U 1705-44. ApJ, 623:L121–L124, April 2005.

T. Di Salvo, A. D'Ai', R. Iaria, L. Burderi, M. Dovčiak, V. Karas, G. Matt, A. Papitto, S. Piraino, A. Riggio, N. R. Robba, and A. Santangelo. A relativistically smeared spectrum in the neutron star X-ray Binary 4U 1705-44: Looking at the inner accretion disc with X-ray spectroscopy. ArXiv e-prints, April 2009.

C. Done and M. Gierliński. Observing the effects of the event horizon in black holes. MNRAS, 342:1041–1055, July 2003.

C. Done, P. T. Życki, and D. A. Smith. The X-ray spectrum of Cyg X-2. MNRAS, 331: 453–462, March 2002.

C. Done, M. Gierliński, and A. Kubota. Modelling the behaviour of accretion flows in X-ray binaries. Everything you always wanted to know about accretion but were afraid to ask. A&A Rev., 15:1–66, December 2007.

E. N. Ercan. The X-ray spectrum of the bright galactic bulge source X1813 - 14 = GX17 + 2. Ap&SS, 147:145–156, August 1988.

A. C. Fabian, M. J. Rees, L. Stella, and N. E. White. X-ray fluorescence from the inner disc in Cygnus X-1. MNRAS, 238:729–736, May 1989.

A. C. Fabian, K. Iwasawa, C. S. Reynolds, and A. J. Young. Broad Iron Lines in Active Galactic Nuclei. PASP, 112:1145–1161, September 2000.

R. Farinelli, F. Frontera, A. A. Zdziarski, L. Stella, S. N. Zhang, M. van der Klis, N. Masetti, and L. Amati. The transient hard X-ray tail of GX 17+2: New BeppoSAX results. A&A, 434:25–34, April 2005.

R. Fender. in Compact Stellar X-ray Sources, pages 381–419. eds. W. Lewin & M. van der Klis, Cambridge University Press, April 2006.

R. P. Fender and M. A. Hendry. The radio luminosity of persistent X-ray binaries. MNRAS, 317:1–8, September 2000.

R. P. Fender, M. Dahlem, J. Homan, S. Corbel, R. Sault, and T. M. Belloni. The variable radio counterpart and possible large-scale jet of the new Z source XTE J1701-462. MNRAS, 380:L25–L29, September 2007.

M. Fiocchi, A. Bazzano, P. Ubertini, and P. Jean. Disk-Jet Coupling in the Low-Mass X-Ray Binary 4U 1636-53 from INTEGRAL Observations. ApJ, 651:416–420, November 2006.

M. Fiocchi, A. Bazzano, P. Ubertini, and A. A. Zdziarski. The First Detection of Compton Reflection in the Low-Mass X-Ray Binary 4U 1705-44 with INTEGRAL and BeppoSax. ApJ, 657:448–452, March 2007.

E. B. Fomalont, B. J. Geldzahler, and C. F. Bradshaw. Scorpius X-1: The Evolution and Nature of the Twin Compact Radio Lobes. ApJ, 558:283–301, September 2001.

E. C. Ford, M. van der Klis, and P. Kaaret. Discovery of Kilohertz Quasi-periodic Oscillations in the Atoll X-Ray Binary 4U 1705-44. ApJ, 498:L41+, May 1998.

J. Frank, A. R. King, and D. J. Raine. Accretion power in astrophysics. Cambridge and New York, Cambridge University Press, 1985, 283 p., 1985.

J. Frank, A. King, and D. J. Raine. Accretion Power in Astrophysics: Third Edition. February 2002.

Fridriksson et al. RXTE Observations of the Neutron Star Low-Mass X-Ray Binary GX 17+2: Correlated X-Ray Spectral and Timing Behavior. in preparation, 2009.

F. Frontera, E. Costa, D. dal Fiume, M. Feroci, L. Nicastro, M. Orlandini, E. Palazzi, and G. Zavattini. The high energy instrument PDS on-board the BeppoSAX X–ray astronomy satellite. A&AS, 122:357–369, April 1997.

J. Fukue. Critical Accretion Disk. PASJ, 56:569–580, June 2004.

D. K. Galloway, D. Psaltis, D. Chakrabarty, and M. P. Muno. Eddington-limited X-Ray Bursts as Distance Indicators. I. Systematic Trends and Spherical Symmetry in Bursts from 4U 1728-34. ApJ, 590:999–1007, June 2003.

D. K. Galloway, D. Psaltis, M. P. Muno, and D. Chakrabarty. Eddington-limited X-Ray Bursts as Distance Indicators. II. Possible Compositional Effects in Bursts from 4U 1636-536. ApJ, 639:1033–1038, March 2006.

D. K. Galloway, M. P. Muno, J. M. Hartman, D. Psaltis, and D. Chakrabarty. Thermonuclear (Type I) X-Ray Bursts Observed by the Rossi X-Ray Timing Explorer. ApJS, 179: 360–422, December 2008.

R. Giacconi, H. Gursky, F. R. Paolini, and B. B. Rossi. Evidence for x Rays From Sources Outside the Solar System. Physical Review Letters, 9:439–443, December 1962.

M. Gierliński and C. Done. A comment on the colour-colour diagrams of low-mass X-ray binaries. MNRAS, 331:L47–L50, April 2002a.

M. Gierliński and C. Done. The X-ray spectrum of the atoll source 4U 1608-52. MNRAS, 337:1373–1380, December 2002b.

M. Gierliński, A. Maciołek-Niedźwiecki, and K. Ebisawa. Application of a relativistic accretion disc model to X-ray spectra of LMC X-1 and GRO J1655-40. MNRAS, 325: 1253–1265, August 2001.

M. Gilfanov, M. Revnivtsev, and S. Molkov. Boundary layer, accretion disk and X-ray variability in the luminous LMXBs. A&A, 410:217–230, October 2003.

I. Goldman. General relativistic effects and the radius and mass of X-ray bursters. A&A, 78:L15+, September 1979.

M. Gottwald, F. Haberl, A. Langmeier, G. Hasinger, W. H. G. Lewin, and J. van Paradijs. X-ray bursts from 4U 1705-44 - Another case of burst properties dependent on the strength of the persistent emission. ApJ, 339:1044–1053, April 1989.

J. Grindlay, H. Gursky, H. Schnopper, D. R. Parsignault, J. Heise, A. C. Brinkman, and J. Schrijver. Discovery of intense X-ray bursts from the globular cluster NGC 6624. ApJ, 205:L127–L130, May 1976.

E. J. Groth. Probability distributions related to power spectra. ApJS, 29:285–302, June 1975.

M. Guainazzi, A. N. Parmar, A. Segreto, L. Stella, D. dal Fiume, and T. Oosterbroek. The comptonized X-ray source X 1724-308 in the globular cluster Terzan 2. A&A, 339: 802–810, November 1998.

O. H. Guseĭnov, A. T. Saygac, A. Allakhverdiev, H. Caliskan, S. Ozdemir, S. K. Yerli, and A. Ankay. A Preliminary Version of a Catalog of High- Low-Mass X-ray Binaries. Astronomy Letters, 26:725–729, November 2000.

F. Haberl and L. Titarchuk. On the distance and mass-radius relation of neutron stars in X-ray burst sources. A&A, 299:414–+, July 1995.

S. Hands. The phase diagram of QCD. Contemporary Physics, 42:209–225, April 2001.

G. Hasinger and M. van der Klis. Two patterns of correlated X-ray timing and spectral behaviour in low-mass X-ray binaries. A&A, 225:79–96, November 1989.

G. Hasinger, M. van der Klis, K. Ebisawa, T. Dotani, and K. Mitsuda. Multifrequency observations of Cygnus X-2 - X-ray observations with GINGA. A&A, 235:131–146, August 1990.

S. Hayakawa. X-ray irradiated accretion disk. PASP, 33:365–372, 1981.

P. Hertz, B. Vaughan, K. S. Wood, J. P. Norris, K. Mitsuda, P. F. Michelson, and T. Dotani. X-ray variability of Scorpius X-1 during a multiwavelength campaign. ApJ, 396:201–218, September 1992.

J. A. Hoffman, W. H. G. Lewin, and J. Doty. Observations of the X-ray burst source MXB 1636-53. ApJ, 217:L23–L28, October 1977.

J. Homan, M. van der Klis, P. G. Jonker, R. Wijnands, E. Kuulkers, M. Méndez, and W. H. G. Lewin. RXTE Observations of the Neutron Star Low-Mass X-Ray Binary GX 17+2: Correlated X-Ray Spectral and Timing Behavior. ApJ, 568:878–900, April 2002.

J. Homan, T. Belloni, R. Wijnands, M. V. D. Klis, J. Swank, E. Smith, D. Pereira, and C. Markwardt. First detection of a type-I X-ray burst from the transient Z source XTE J1701-462. The Astronomer's Telegram, 1144:1–+, July 2007a.

J. Homan, M. van der Klis, R. Wijnands, T. Belloni, R. Fender, M. Klein-Wolt, P. Casella, M. Méndez, E. Gallo, W. H. G. Lewin, and N. Gehrels. Rossi X-Ray Timing Explorer Observations of the First Transient Z Source XTE J1701-462: Shedding New Light on Mass Accretion in Luminous Neutron Star X-Ray Binaries. ApJ, 656:420–430, February 2007b.

J. Homan, R. Wijnands, D. Altamirano, and T. Belloni. Rapid decay of the neutron star transient XTE J1701-462. The Astronomer's Telegram, 1165, August 2007c.

J. Homan, D. L. Kaplan, M. van den Berg, and A. J. Young. A Variable Near-Infrared Counterpart to the Neutron-Star Low-Mass X-Ray Binary 4U 1705-440. ApJ, 692:73–80, February 2009.

Homan et al. RXTE Observations of the Neutron Star Low-Mass X-Ray Binary GX 17+2: Correlated X-Ray Spectral and Timing Behavior. in preparation, 2009.

R. Iaria, T. di Salvo, N. R. Robba, G. Lavagetto, L. Burderi, L. Stella, and M. van der Klis. The BeppoSAX 0.1-18 keV spectrum of the bright atoll source GX 9+1: an indication of the source distance. A&A, 439:575–583, August 2005.

S. Ichimaru. Bimodal behavior of accretion disks - Theory and application to Cygnus X-1 transitions. ApJ, 214:840–855, June 1977.

N. A. Inogamov and R. A. Sunyaev. Spread of matter over a neutron-star surface during disk accretion. Astronomy Letters, 25:269–293, May 1999.

G. L. Israel and L. Stella. A New Technique for the Detection of Periodic Signals in "Colored" Power Spectra. ApJ, 468:369–+, September 1996.

K. Jahoda, J. H. Swank, A. B. Giles, M. J. Stark, T. Strohmayer, W. Zhang, and E. H. Morgan. In-orbit performance and calibration of the Rossi X-ray Timing Explorer (RXTE) Proportional Counter Array (PCA). In Proc. SPIE, 2808, pages 59–70, October 1996.

K. Jahoda, C. B. Markwardt, Y. Radeva, A. H. Rots, M. J. Stark, J. H. Swank, T. E. Strohmayer, and W. Zhang. Calibration of the Rossi X-Ray Timing Explorer Proportional Counter Array. ApJS, 163:401–423, April 2006.

P. C. Joss. X-ray bursts and neutron-star thermonuclear flashes. Nature, 270:310–314, November 1977.

S. M. Kahn and J. E. Grindlay. Evidence for weak X-ray burst emission from Cygnus X-2 and GX 17 + 2. ApJ, 281:826–829, June 1984.

J. I. Katz. Acceleration, radiation and precession in SS 433. ApJ, 236:L127–L130, March 1980.

W. Kluzniak and R. V. Wagoner. Evolution of the innermost stable orbits around accreting neutron stars. ApJ, 297:548–554, October 1985.

W. Kluzniak and J. R. Wilson. Hard X-ray spectra from gap accretion onto neutron stars. ApJ, 372:L87–L90, May 1991.

K. Koyama, H. Inoue, K. Makishima, M. Matsuoka, T. Murakami, M. Oda, Y. Osgawara, T. Ohashi, N. Shibazaki, Y. Tanaka, F. J. Marshall, I. S. Kondo, S. Hayakawa, H. Kunieda, F. Makino, K. Masai, F. Nagase, Y. Tawara, S. Miyamoto, H. Tsunemi, and K. Yamashita. Discovery of X-ray bursts from Aquila X-1. ApJ, 247:L27–L29, July 1981.

K. Koyama, H. Tsunemi, T. Dotani, M. W. Bautz, K. Hayashida, T. G. Tsuru, H. Matsumoto, Y. Ogawara, G. R. Ricker, J. Doty, S. E. Kissel, R. Foster, H. Nakajima, H. Yamaguchi, H. Mori, M. Sakano, K. Hamaguchi, M. Nishiuchi, E. Miyata, K. Torii, M. Namiki, S. Katsuda, D. Matsuura, T. Miyauchi, N. Anabuki, N. Tawa, M. Ozaki, H. Murakami, Y. Maeda, Y. Ichikawa, G. Y. Prigozhin, E. A. Boughan, B. Lamarr, E. D. Miller, B. E. Burke, J. A. Gregory, A. Pillsbury, A. Bamba, J. S. Hiraga, A. Senda, H. Katayama, S. Kitamoto, M. Tsujimoto, T. Kohmura, Y. Tsuboi, and H. Awaki. X-Ray Imaging Spectrometer (XIS) on Board Suzaku. PASJ, 59:23–33, January 2007.

I. Kreykenbohm, J. Wilms, W. Coburn, M. Kuster, R. E. Rothschild, W. A. Heindl, P. Kretschmar, and R. Staubert. The variable cyclotron line in GX 301-2. A&A, 427: 975–986, December 2004.

A. Kubota and C. Done. The very high state accretion disc structure from the Galactic black hole transient XTE J1550 - 564. MNRAS, 353:980–990, September 2004.

A. Kubota, Y. Tanaka, K. Makishima, Y. Ueda, T. Dotani, H. Inoue, and K. Yamaoka. Evidence for a Black Hole in the X-Ray Transient GRS 1009-45. PASJ, 50:667–673, December 1998.

E. Kuulkers, M. van der Klis, T. Oosterbroek, K. Asai, T. Dotani, J. van Paradijs, and W. H. G. Lewin. Spectral and correlated timing behaviour of GX 5-1. A&A, 289:795–821, September 1994.

E. Kuulkers, M. van der Klis, and J. van Paradijs. Burstlike Events in the Z Source Cygnus X-2. ApJ, 450:748–+, September 1995.

E. Kuulkers, M. van der Klis, and B. A. Vaughan. Secular variations in the Z source CygnusX-2. A&A, 311:197–210, July 1996.

E. Kuulkers, M. van der Klis, T. Oosterbroek, J. van Paradijs, and W. H. G. Lewin. GX17+2: X-ray spectral and timing behaviour of a bursting Z source. MNRAS, 287: 495–514, May 1997.

E. Kuulkers, J. Homan, M. van der Klis, W. H. G. Lewin, and M. Méndez. X-ray bursts at extreme mass accretion rates from GX 17+2. A&A, 382:947–973, February 2002.

E. Kuulkers, P. R. den Hartog, J. J. M. in't Zand, F. W. M. Verbunt, W. E. Harris, and M. Cocchi. Photospheric radius expansion X-ray bursts as standard candles. A&A, 399: 663–680, February 2003.

D. Q. Lamb and F. K. Lamb. Nuclear burning in accreting neutron stars and X-ray bursts. ApJ, 220:291–302, February 1978.

D. A. Leahy, W. Darbro, R. F. Elsner, M. C. Weisskopf, S. Kahn, P. G. Sutherland, and J. E. Grindlay. On searches for pulsed emission with application to four globular cluster X-ray sources - NGC 1851, 6441, 6624, and 6712. ApJ, 266:160–170, March 1983.

A. M. Levine, H. Bradt, W. Cui, J. G. Jernigan, E. H. Morgan, R. Remillard, R. E. Shirey, and D. A. Smith. First Results from the All-Sky Monitor on the Rossi X-Ray Timing Explorer. ApJ, 469:L33, September 1996.

W. H. G. Lewin and M. van der Klis. Compact stellar X-ray sources. April 2006.

W. H. G. Lewin, J. van Paradijs, and R. E. Taam. X-Ray Bursts. Space Science Reviews, 62:223–+, 1993.

W. H. G. Lewin, J. van Paradijs, and E. P. J. van den Heuvel. X-ray Binaries. January 1997.

L.-X. Li, E. R. Zimmerman, R. Narayan, and J. E. McClintock. Multitemperature Blackbody Spectrum of a Thin Accretion Disk around a Kerr Black Hole: Model Computations and Comparison with Observations. ApJS, 157:335–370, April 2005.

D. Lin, J. Homan, R. Remillard, and R. Wijnands. Radius expansion bursts from the neutron star transient XTE J1701-462; a new distance estimate. The Astronomer's Telegram, 1183, August 2007a.

D. Lin, R. A. Remillard, and J. Homan. Evaluating Spectral Models and the X-Ray States of Neutron Star X-Ray Transients. ApJ, 667:1073–1086, October 2007b.

D. Lin, D. Altamirano, J. Homan, R. A. Remillard, R. Wijnands, and T. Belloni. Type I X-ray Bursts from the Neutron-star Transient XTE J1701-462. ApJ, 699:60–65, July 2009a.

D. Lin, R. A. Remillard, and J. Homan. Spectral States of XTE J1701-462: Link Between Z and Atoll Sources. ApJ, 696:1257–1277, May 2009b.

T. J. Maccarone and P. S. Coppi. Hysteresis in the light curves of soft X-ray transients. MNRAS, 338:189–196, January 2003a.

T. J. Maccarone and P. S. Coppi. Spectral fits to the 1999 Aql X-1 outburst data. A&A, 399:1151–1157, March 2003b.

J. Madej, P. C. Joss, and A. Różańska. Model Atmospheres and X-Ray Spectra of Bursting Neutron Stars: Hydrogen-Helium Comptonized Spectra. ApJ, 602:904–912, February 2004.

D. Maitra and C. D. Bailyn. Evolution of Spectral States of Aquila X-1 during the 2000 Outburst. ApJ, 608:444–453, June 2004.

G. Manzo, S. Giarrusso, A. Santangelo, F. Ciralli, G. Fazio, S. Piraino, and A. Segreto. The high pressure gas scintillation proportional counter on-board the BeppoSAX X-ray astronomy satellite. A&AS, 122:341–356, April 1997.

S. Markoff, M. A. Nowak, and J. Wilms. Going with the Flow: Can the Base of Jets Subsume the Role of Compact Accretion Disk Coronae? ApJ, 635:1203–1216, December 2005.

H. L. Marshall. Constraints on the parameters of X-ray burster emission regions. ApJ, 260: 815–820, September 1982.

J. E. McClintock and R. A. Remillard. Black hole binaries, pages 157–213. Compact stellar X-ray sources. Edited by Walter Lewin & Michiel van der Klis. Cambridge Astrophysics Series, No. 39. Cambridge, UK: Cambridge University Press, ISBN 978-0-521-82659-4, ISBN 0-521-82659-4, DOI: 10.2277/0521826594, 2006, p. 157 - 213, April 2006.

J. E. McClintock, R. Shafee, R. Narayan, R. A. Remillard, S. W. Davis, and L.-X. Li. The Spin of the Near-Extreme Kerr Black Hole GRS 1915+105. ApJ, 652:518–539, November 2006.

S. Migliari and R. P. Fender. Jets in neutron star X-ray binaries: a comparison with black holes. MNRAS, 366:79–91, February 2006.

S. Migliari, J. C. A. Miller-Jones, R. P. Fender, J. Homan, T. Di Salvo, R. E. Rothschild, M. P. Rupen, J. A. Tomsick, R. Wijnands, and M. van der Klis. Linking Jet Emission, X-Ray States, and Hard X-Ray Tails in the Neutron Star X-Ray Binary GX 17+2. ApJ, 671:706–712, December 2007.

J. M. Miller. Relativistic X-Ray Lines from the Inner Accretion Disks Around Black Holes. ARA&A, 45:441–479, September 2007.

J. M. Miller, A. C. Fabian, R. Wijnands, C. S. Reynolds, M. Ehle, M. J. Freyberg, M. van der Klis, W. H. G. Lewin, C. Sanchez-Fernandez, and A. J. Castro-Tirado. Evidence of Spin and Energy Extraction in a Galactic Black Hole Candidate: The XMM-Newton/EPIC-pn Spectrum of XTE J1650-500. ApJ, 570:L69–L73, May 2002.

J. M. Miller, J. Homan, and G. Miniutti. A Prominent Accretion Disk in the Low-Hard State of the Black Hole Candidate SWIFT J1753.5-0127. ApJ, 652:L113–L116, December 2006a.

J. M. Miller, J. Homan, D. Steeghs, M. Rupen, R. W. Hunstead, R. Wijnands, P. A. Charles, and A. C. Fabian. A Long, Hard Look at the Low/Hard State in Accreting Black Holes. ApJ, 653:525–535, December 2006b.

M. C. Miller, F. K. Lamb, and D. Psaltis. Sonic-Point Model of Kilohertz Quasi-periodic Brightness Oscillations in Low-Mass X-Ray Binaries. ApJ, 508:791–830, December 1998.

S. Mineshige, T. Kawaguchi, M. Takeuchi, and K. Hayashida. Slim-Disk Model for Soft X-Ray Excess and Variability of Narrow-Line Seyfert 1 Galaxies. PASJ, 52:499–508, June 2000.

G. Miniutti, A. C. Fabian, and J. M. Miller. The relativistic Fe emission line in XTE J1650-500 with BeppoSAX: evidence for black hole spin and light-bending effects? MNRAS, 351:466–472, June 2004.

K. Mitsuda, H. Inoue, K. Koyama, K. Makishima, M. Matsuoka, Y. Ogawara, K. Suzuki, Y. Tanaka, N. Shibazaki, and T. Hirano. Energy spectra of low-mass binary X-ray sources observed from TENMA. PASJ, 36:741–759, 1984.

K. Mitsuda, H. Inoue, N. Nakamura, and Y. Tanaka. Luminosity-related changes of the energy spectrum of X1608-522. PASJ, 41:97–111, 1989.

K. Mitsuda, M. Bautz, H. Inoue, R. L. Kelley, K. Koyama, H. Kunieda, K. Makishima, Y. Ogawara, R. Petre, T. Takahashi, H. Tsunemi, N. E. White, N. Anabuki, L. Angelini, K. Arnaud, H. Awaki, A. Bamba, K. Boyce, G. V. Brown, K.-W. Chan, J. Cottam, T. Dotani, J. Doty, K. Ebisawa, Y. Ezoe, A. C. Fabian, E. Figueroa, R. Fujimoto, Y. Fukazawa, T. Furusho, A. Furuzawa, K. Gendreau, R. E. Griffiths, Y. Haba, K. Hamaguchi, I. Harrus, G. Hasinger, I. Hatsukade, K. Hayashida, P. J. Henry, J. S. Hiraga, S. S. Holt, A. Hornschemeier, J. P. Hughes, U. Hwang, M. Ishida, Y. Ishisaki, N. Isobe, M. Itoh, N. Iyomoto, S. M. Kahn, T. Kamae, H. Katagiri, J. Kataoka, H. Katayama, N. Kawai, C. Kilbourne, K. Kinugasa, S. Kissel, S. Kitamoto, M. Kohama, T. Kohmura, M. Kokubun, T. Kotani, J. Kotoku, A. Kubota, G. M. Madejski, Y. Maeda, F. Makino, A. Markowitz, C. Matsumoto, H. Matsumoto, M. Matsuoka, K. Matsushita, D. McCammon, T. Mihara, K. Misaki, E. Miyata, T. Mizuno, K. Mori, H. Mori, M. Morii, H. Moseley, K. Mukai, H. Murakami, T. Murakami, R. Mushotzky, F. Nagase, M. Namiki, H. Negoro, K. Nakazawa, J. A. Nousek, T. Okajima, Y. Ogasaka, T. Ohashi, T. Oshima, N. Ota, M. Ozaki, H. Ozawa, A. N. Parmar, W. D. Pence, F. S. Porter, J. N. Reeves, G. R. Ricker, I. Sakurai, W. T. Sanders, A. Senda, P. Serlemitsos, R. Shibata, Y. Soong, R. Smith, M. Suzuki, A. E. Szymkowiak, H. Takahashi, T. Tamagawa, K. Tamura, T. Tamura, Y. Tanaka, M. Tashiro, Y. Tawara, Y. Terada, Y. Terashima, H. Tomida, K. Torii, Y. Tsuboi, M. Tsujimoto, T. G. Tsuru, M. J. L. . Turner, Y. Ueda, S. Ueno, M. Ueno, S. Uno, Y. Urata, S. Watanabe, N. Yamamoto, K. Yamaoka, N. Y. Yamasaki, K. Yamashita, M. Yamauchi, S. Yamauchi, T. Yaqoob, D. Yonetoku, and A. Yoshida. The X-Ray Observatory Suzaku. PASJ, 59:1–7, January 2007.

M. P. Muno, R. A. Remillard, and D. Chakrabarty. How Do Z and Atoll X-Ray Binaries Differ? ApJ, 568:L35–L39, March 2002.

N. Nakamura, T. Dotani, H. Inoue, K. Mitsuda, Y. Tanaka, and M. Matsuoka. TENMA observation of X-ray bursts from X1608-52. PASJ, 41:617–639, 1989.

R. Narayan and J. S. Heyl. Thermonuclear Stability of Material Accreting onto a Neutron Star. ApJ, 599:419–449, December 2003.

R. Narayan and I. Yi. Advection-dominated accretion: A self-similar solution. ApJ, 428: L13–L16, June 1994.

L. Natalucci, A. Bazzano, M. Cocchi, P. Ubertini, J. Heise, E. Kuulkers, and J. J. M. in't Zand. Broadband Observations of the New X-Ray Burster SAX J1747.0-2853 during the 1998 March Outburst. ApJ, 543:L73–L76, November 2000.

K. Ohsuga and S. Mineshige. Why Is Supercritical Disk Accretion Feasible? ApJ, 670: 1283–1290, December 2007.

T. Okajima, K. Ebisawa, and T. Kawaguchi. A Stellar-Mass Black Hole in the Ultraluminous X-Ray Source M82 X-1? ApJ, 652:L105–L108, December 2006.

J.-F. Olive, D. Barret, and M. Gierliński. Correlated Timing and Spectral Behavior of 4U 1705-44. ApJ, 583:416–423, January 2003.

T. Oosterbroek, D. Barret, M. Guainazzi, and E. C. Ford. Simultaneous BeppoSAX and RXTE observations of the X-ray burst sources GX 3+1 and Ser X-1. A&A, 366:138–145, January 2001.

F. Özel. Soft equations of state for neutron-star matter ruled out by EXO 0748 - 676. Nature, 441:1115–1117, June 2006.

A. Paizis, R. Farinelli, L. Titarchuk, T. J.-L. Courvoisier, A. Bazzano, V. Beckmann, F. Frontera, P. Goldoni, E. Kuulkers, S. Mereghetti, J. Rodriguez, and O. Vilhu. Average hard X-ray emission from NS LMXBs: observational evidence of different spectral states in NS LMXBs. A&A, 459:187–197, November 2006.

A. N. Parmar, D. D. E. Martin, M. Bavdaz, F. Favata, E. Kuulkers, G. Vacanti, U. Lammers, A. Peacock, and B. G. Taylor. The low-energy concentrator spectrometer on-board the BeppoSAX X-ray astronomy satellite. A&AS, 122:309–326, April 1997.

A. N. Parmar, T. Oosterbroek, A. Orr, M. Guainazzi, N. Shane, M. J. Freyberg, D. Ricci, and A. Malizia. BeppoSAX Low-Energy Concentrator Spectrometer background subtraction techniques. A&AS, 136:407–418, April 1999.

W. Penninx, W. H. G. Lewin, A. A. Zijlstra, K. Mitsuda, and J. van Paradijs. A connection between the X-ray spectral branches and the radio brightness in GX17+2. Nature, 336: 146–148, November 1988.

W. Penninx, E. Damen, J. van Paradijs, J. Tan, and W. H. G. Lewin. EXOSAT observations of the X-ray burst source 4U 1608-52. A&A, 208:146–152, January 1989.

S. Piraino, A. Santangelo, T. di Salvo, P. Kaaret, D. Horns, R. Iaria, and L. Burderi. BeppoSAX observation of 4U 1705-44: detection of hard X-ray emission in the soft state. A&A, 471:L17–L20, August 2007.

R. Popham and R. Sunyaev. Accretion Disk Boundary Layers around Neutron Stars: X-Ray Production in Low-Mass X-Ray Binaries. ApJ, 547:355–383, January 2001.

D. Psaltis. Accreting Neutron Stars and Black Holes: A Decade of Discoveries. ArXiv Astrophysics e-prints, October 2004.

D. Psaltis and D. Chakrabarty. The Disk-Magnetosphere Interaction in the Accretion-powered Millisecond Pulsar SAX J1808.4-3658. ApJ, 521:332–340, August 1999.

D. Psaltis and F. K. Lamb. Magnetic Fields of Neutron Stars in Low Mass X-Ray Binaries. In N. Shibazaki, editor, Neutron Stars and Pulsars: Thirty Years after the Discovery, pages 179–+, 1998.

S. A. Rappaport, J. M. Fregeau, and H. Spruit. Accretion onto Fast X-Ray Pulsars. ApJ, 606:436–443, May 2004.

P. Reig, M. Méndez, M. van der Klis, and E. C. Ford. Correlated Timing and Spectral Variations of the Soft X-Ray Transient Aquila X-1: Evidence for an Atoll Classification. ApJ, 530:916–922, February 2000.

P. Reig, S. van Straaten, and M. van der Klis. Timing Properties and Spectral States in Aquila X-1. ApJ, 602:918–930, February 2004.

R. C. Reis, A. C. Fabian, and A. J. Young. Relativistically broadened iron line in the SUZAKU observation of the neutron star X-ray binary 4U 1705-44. ArXiv e-prints, April 2009.

R. A. Remillard and J. E. McClintock. X-Ray Properties of Black-Hole Binaries. ARA&A, 44:49–92, September 2006.

R. A. Remillard, D. Lin, R. L. Cooper, and R. Narayan. The Rates of Type I X-Ray Bursts from Transients Observed with RXTE: Evidence for Black Hole Event Horizons. ApJ, 646:407–419, July 2006a.

R. A. Remillard, D. Lin, and the ASM Team at MIT and NASA/GSFC. New X-ray Transient, XTE J1701-462. The Astronomer's Telegram, 696, January 2006b.

M. G. Revnivtsev and M. R. Gilfanov. Boundary layer emission and Z-track in the color-color diagram of luminous LMXBs. A&A, 453:253–259, July 2006.

C. E. Rhoades and R. Ruffini. Maximum mass of a neutron star. Physical Review Letters, 32:324–327, 1974.

R. E. Rothschild, P. R. Blanco, D. E. Gruber, W. A. Heindl, D. R. MacDonald, D. C. Marsden, M. R. Pelling, L. R. Wayne, and P. L. Hink. In-Flight Performance of the High-Energy X-Ray Timing Experiment on the Rossi X-Ray Timing Explorer. ApJ, 496: 538–+, March 1998.

R. E. Rutledge, L. Bildsten, E. F. Brown, G. G. Pavlov, and V. E. Zavlin. The Thermal X-Ray Spectra of Centaurus X-4, Aquila X-1 , and 4U 1608-522 in Quiescence. ApJ, 514: 945–951, April 1999.

R. E. Rutledge, L. Bildsten, E. F. Brown, G. G. Pavlov, and V. E. Zavlin. Quiescent Thermal Emission from the Neutron Star in Aquila X-1. ApJ, 559:1054–1059, October 2001.

E. S. Rykoff, J. M. Miller, D. Steeghs, and M. A. P. Torres. Swift Observations of the Cooling Accretion Disk of XTE J1817-330. astro-ph/0703497, March 2007.

R. Shafee, J. E. McClintock, R. Narayan, S. W. Davis, L.-X. Li, and R. A. Remillard. Estimating the Spin of Stellar-Mass Black Holes by Spectral Fitting of the X-Ray Continuum. ApJ, 636:L113–L116, January 2006.

R. Shafee, J. C. McKinney, R. Narayan, A. Tchekhovskoy, C. F. Gammie, and J. E. McClintock. Three-Dimensional Simulations of Magnetized Thin Accretion Disks around Black Holes: Stress in the Plunging Region. ApJ, 687:L25–L28, November 2008.

N. I. Shakura and R. A. Syunyaev. Black holes in binary systems. Observational appearance. A&A, 24:337–355, 1973.

S. L. Shapiro and S. A. Teukolsky. Black holes, white dwarfs, and neutron stars: The physics of compact objects. 1983.

T. Shimura and F. Takahara. On the spectral hardening factor of the X-ray emission from accretion disks in black hole candidates. ApJ, 445:780–788, June 1995.

N. R. Sibgatullin and R. A. Sunyaev. Energy Release During Disk Accretion onto a Rapidly Rotating Neutron Star. Astronomy Letters, 26:699–724, November 2000.

D. Steeghs and J. Casares. The Mass Donor of Scorpius X-1 Revealed. ApJ, 568:273–278, March 2002.

J. F. Steiner, R. Narayan, J. E. McClintock, and K. Ebisawa. A Simple Comptonization Model. ArXiv e-prints, October 2008.

T. Strohmayer and L. Bildsten. New views of thermonuclear bursts, pages 113–156. Compact stellar X-ray sources, April 2006.

V. Suleimanov and J. Poutanen. Spectra of the spreading layers on the neutron star surface and constraints on the neutron star equation of state. MNRAS, 369:2036–2048, July 2006.

R. Sunyaev and M. Revnivtsev. Fourier power spectra at high frequencies: a way to distinguish a neutron star from a black hole. A&A, 358:617–623, June 2000.

J. H. Swank, R. H. Becker, E. A. Boldt, S. S. Holt, S. H. Pravdo, and P. J. Serlemitsos. Spectral evolution of a long X-ray burst. ApJ, 212:L73–L76, March 1977.

M. Sztajno, J. van Paradijs, W. H. G. Lewin, A. Langmeier, J. Trumper, and W. Pietsch. X-ray bursts from GX 17+2 - A new approach. MNRAS, 222:499–511, November 1986.

T. Takahashi, K. Abe, M. Endo, Y. Endo, Y. Ezoe, Y. Fukazawa, M. Hamaya, S. Hirakuri, S. Hong, M. Horii, H. Inoue, N. Isobe, T. Itoh, N. Iyomoto, T. Kamae, D. Kasama, J. Kataoka, H. Kato, M. Kawaharada, N. Kawano, K. Kawashima, S. Kawasoe, T. Kishishita, T. Kitaguchi, Y. Kobayashi, M. Kokubun, J. Kotoku, M. Kouda, A. Kubota, Y. Kuroda, G. Madejski, K. Makishima, K. Masukawa, Y. Matsumoto, T. Mitani, R. Miyawaki, T. Mizuno, K. Mori, M. Mori, M. Murashima, T. Murakami, K. Nakazawa, H. Niko, M. Nomachi, Y. Okada, M. Ohno, K. Oonuki, N. Ota, H. Ozawa, G. Sato, S. Shinoda, M. Sugiho, M. Suzuki, K. Taguchi, H. Takahashi, I. Takahashi, S. Takeda, K.-I. Tamura, T. Tamura, T. Tanaka, C. Tanihata, M. Tashiro, Y. Terada, S. Tominaga, Y. Uchiyama, S. Watanabe, K. Yamaoka, T. Yanagida, and D. Yonetoku. Hard X-Ray Detector (HXD) on Board Suzaku. PASJ, 59:35–51, January 2007.

T. M. Tauris and E. P. J. van den Heuvel. Formation and evolution of compact stellar X-ray sources, pages 623–665. April 2006.

Y. Tawara, T. Hirano, T. Kii, M. Matsuoka, and T. Murakami. Long X-ray burst from GX 17 + 2. PASJ, 36:861–867, 1984.

L. Titarchuk. Generalized Comptonization models and application to the recent high-energy observations. ApJ, 434:570–586, October 1994.

M. van der Klis. in Compact Stellar X-ray Sources, pages 39–112. eds. W. Lewin & M. van der Klis, Cambridge University Press, April 2006.

S. van Straaten, M. van der Klis, and M. Méndez. The Atoll Source States of 4U 1608-52. ApJ, 596:1155–1176, October 2003.

B. A. Vaughan, M. van der Klis, K. S. Wood, J. P. Norris, P. Hertz, P. F. Michelson, J. van Paradijs, W. H. G. Lewin, K. Mitsuda, and W. Penninx. Searches for millisecond pulsations in low-mass X-ray binaries, 2. ApJ, 435:362–371, November 1994.

E. P. Velikhov. Stability of an Ideally Conducting Liquid Flowing Between Cylinders Rotating in a Magnetic Field. J. Exptl. Theoret. Phys, 36:1398–1404, August 1959.

S. D. Vrtilek, J. C. Raymond, M. R. Garcia, F. Verbunt, G. Hasinger, and M. Kurster. Observations of Cygnus X-2 with IUE - Ultraviolet results from a multiwavelength campaign. A&A, 235:162–173, August 1990.

K.-y. Watarai, J. Fukue, M. Takeuchi, and S. Mineshige. Galactic Black-Hole Candidates Shining at the Eddington Luminosity. PASJ, 52:133–+, February 2000.

A. L. Watts and T. E. Strohmayer. Detection with RHESSI of High-Frequency X-Ray Oscillations in the Tailof the 2004 Hyperflare from SGR 1806-20. ApJ, 637:L117–L120, February 2006.

N. E. White, A. Peacock, G. Hasinger, K. O. Mason, G. Manzo, B. G. Taylor, and G. Branduardi-Raymont. A study of the continuum and iron K line emission from low-mass X-ray binaries. MNRAS, 218:129–138, January 1986.

N. E. White, L. Stella, and A. N. Parmar. The X-ray spectral properties of accretion discs in X-ray binaries. ApJ, 324:363–378, January 1988.

R. Wijnands. Quasi-periodic oscillations and noise in neutron star and black-hole X-ray binaries. Advances in Space Research, 28:469–479, 2001.

R. Wijnands, J. Homan, M. van der Klis, M. Mendez, E. Kuulkers, J. van Paradijs, W. H. G. Lewin, F. K. Lamb, D. Psaltis, and B. Vaughan. Discovery of Kilohertz Quasi-Periodic Oscillations in GX 17+2. ApJ, 490:L157+, December 1997a.

R. A. D. Wijnands, M. van der Klis, E. Kuulkers, K. Asai, and G. Hasinger. GINGA observations of Cygnus X-2. A&A, 323:399–414, July 1997b.

R. A. D. Wijnands, M. van der Klis, J. van Paradijs, W. H. G. Lewin, F. K. Lamb, B. Vaughan, and E. Kuulkers. Discovery in 4U 1636-53 of Two Simultaneous Quasi-periodic Oscillations near 900 HZ and 1176 HZ. ApJ, 479:L141+, April 1997c.

S. E. Woosley, A. Heger, A. Cumming, R. D. Hoffman, J. Pruet, T. Rauscher, J. L. Fisker, H. Schatz, B. A. Brown, and M. Wiescher. Models for Type I X-Ray Bursts with Improved Nuclear Physics. ApJS, 151:75–102, March 2004.

S. N. Zhang, W. Cui, and W. Chen. Black Hole Spin in X-Ray Binaries: Observational Consequences. ApJ, 482:L155+, June 1997.

S. N. Zhang, W. Yu, and W. Zhang. Spectral Transitions in Aquila X-1: Evidence for "Propeller" Effects. ApJ, 494:L71+, February 1998a.

W. Zhang, I. Lapidus, N. E. White, and L. Titarchuk. Kilohertz Quasi-periodic Intensity Oscillations from 4U 1636-536. ApJ, 469:L17+, September 1996.

W. Zhang, K. Jahoda, R. L. Kelley, T. E. Strohmayer, J. H. Swank, and S. N. Zhang. Millisecond Oscillations in the Persistent and Bursting Flux of Aquila X-1 during an Outburst. ApJ, 495:L9+, March 1998b.